UNIVERSIDAD DE CHILE
FACULTAD DE CIENCIAS FÍSICAS Y MATEMÁTICAS
DEPARTAMENTO DE INGENIERÍA ELÉCTRICA

SOLAR MODULE CHARACTERIZATION VIA VISUAL INSPECTION IN THE FIELD, I-V CURVE AND THERMAL-IMAGE ANALYSIS

TESIS PARA OPTAR AL GRADO DE
MAGÍSTER EN CIENCIAS DE LA INGENIERÍA, MENCIÓN ELÉCTRICA

MEMORIA PARA OPTAR AL TÍTULO DE
INGENIERA CIVIL ELÉCTRICA

MARÍA IGNACIA DEVOTO ACEVEDO

PROFESOR GUÍA:
RODRIGO PALMA-BEHNKE

MIEMBROS DE LA COMISIÓN:
WILLIAMS CALDERÓN MUÑOZ
PABLO FERRADA MARTÍNEZ
PATRICIO MENDOZA ARAYA

SANTIAGO DE CHILE
JUNIO 2018

RESUMEN DE LA TESIS PARA OPTAR AL GRADO DE
MAGÍSTER EN CIENCIAS DE LA INGENIERÍA, MENCIÓN ELÉCTRICA,
Y AL TÍTULO PROFESIONAL DE INGENIERA CIVIL ELÉCTRICA
POR: MARÍA IGNACIA DEVOTO ACEVEDO
FECHA: JUNIO 2018
PROFESOR GUÍA: RODRIGO PALMA-BEHNKE

CARACTERIZACIÓN DE PANELES SOLARES MEDIANTE INSPECCIÓN VISUAL EN TERRENO, ANÁLISIS DE CURVA I-V E IMÁGENES TÉRMICAS

El desierto de Atacama anida abundantes recursos naturales en sus 105.000 km^2. Éste contiene las reservas más grandes de cobre y productos no metálicos del mundo, y los niveles mundiales de irradiancia más altos con un promedio anual de 2.500 kWh/m^2 de Irradiancia Horizontal Global (GHI), 3.500 kWh/m^2 de Irradiancia Directa Normal (DNI) y de 4.000 horas de sol. A pesar de tener muchas ventajas, también presenta desafíos importantes. A modo de ejemplo, se sabe que las dosis anuales de UV-B en el desierto de Atacama son cerca de un 40% más altas que las típicas del norte de África. Esta parte del espectro no genera más electricidad y podría perjudicar los materiales utilizados en los módulos fotovoltaicos (FV), reduciendo su vida útil. Por ende, un módulo vidrio/vidrio (bifacial) especialmente diseñado para nuestro desierto es parte de la I+D+i FV en el programa solar nacional. Para materiales y diseños de módulos FV ya existentes, datos acerca de observaciones sobre su degradación son variables en su nivel de detalle, consistencia, calidad y significancia estadística. Además, la información disponible acerca de fallas típicas de módulos FV instalados en el desierto de Atacama es escasa o inexistente.

A partir del contexto señalado, el objetivo principal de esta tesis es diseñar e implementar una herramienta de inspección para recolectar datos (IDCTool, por sus siglas en inglés), con el fin de evaluar módulos FV que operan en condiciones climáticas desérticas y caracterizarlos. La propuesta se basa en el estado-del-arte de prácticas en terreno junto con la definición de un conglomerado de criterios para su uso en soluciones FV de baja escala. Su implementación incluye el desarrollo de una encuesta, equipos y herramientas; y procedimientos para pruebas en terreno y análisis. IDCTool fue usada para una campaña en la región de Arica y Parinacota, la que es representativa de climas desérticos. Los resultados obtenidos fueron analizados de acuerdo con el procedimiento propuesto.

La propuesta metodológica de esta tesis se validó mediante la campaña de Arica. Los 15 sitios visitados (comuna de Arica) fueron clasificados en 4 zonas: la costa, el centro de la ciudad, el valle y el desierto. Durante la campaña se inspeccionó 95 módulos FV, de los cuales se encontraron 9 fabricantes distintos. Los módulos operando por más tiempo llevaban 13 años instalados, los más nuevos llevaban 2 años. Todos los módulos inspeccionados estaban compuestos por un vidrio frontal, una lámina polimérica trasera y marco de aluminio. Según los resultados, no se presentaron fallas en cables, conectores ni celdas solares. La falla más típica fue el efecto *soiling* con 52 casos de soiling ligero y 39 de soiling fuerte. Otras fallas típicas fueron corrosión menor de la puesta a tierra (18 casos) y corrosión del marco (12 casos). En relación a los parámetros eléctricos, la mayor degradación se observó en la potencia nominal con una caída máxima de 39,08% y una caída promedio de 13,19±6,22%. En relación a la diferencia de temperatura de operación de los módulos FV con respecto a la temperatura ambiente, la mayor diferencia fue 24,45°C con un promedio de 11,67°C. Se encontró que la celda más caliente de todo el universo inspeccionado operaba a 99,4°C, mientras que en promedio las celdas más calientes operaban a 64,0°C. Con respecto a las anormalidades térmicas, se encontraron 2 módulos FV con patrón PID y 12 módulos mostraron celdas homogéneamente muy calientes.

El trabajo realizado indica que la herramienta desarrollada, incluyendo la metodología para el análisis, entrega datos en formato estándar capaces de caracterizar módulos FV. Los datos analizados fueron estudiados mediante sus tendencias con el uso de herramientas estadísticas. Por ende, fue posible realizar conclusiones y recomendaciones. A pesar de esto, y debido a la falta de módulos inspeccionados, los fenómenos encontrados durante la campaña no pueden ser generalizados. En efecto, nuestro análisis no está validado por evidencia estadística sólida. En este contexto, el desarrollo de una base de datos significativa, mediante el uso de la IDCTool, será el mejor conjunto de datos como punto de partida para comenzar a hacer recomendaciones concluyentes para desarrollos en el ámbito FV.

ABSTRACT OF THE THESIS TO OBTAIN THE DEGREE OF
MASTER OF SCIENCE IN ELECTRICAL ENGINEERING,
AND THE PROFESSIONAL DEGREE OF ELECTRICAL ENGINEER
BY: MARÍA IGNACIA DEVOTO ACEVEDO
DATE: JUNE 2018
THESIS ADVISOR: RODRIGO PALMA-BEHNKE

SOLAR MODULE CHARACTERIZATION VIA VISUAL INSPECTION IN THE FIELD, I-V CURVE AND THERMAL-IMAGE ANALYSIS

The Atacama Desert, within its 105,000 km^2, harbors abundant natural resources. It contains the largest copper and non-metallic reserves in the world. Furthermore, it has the highest worldwide levels of solar irradiance with an annual average of 2,500 kWh/m^2 of Global Horizontal Irradiance (GHI), 3,500 kWh/m^2 of Direct Normal Irradiance (DNI) and 4,000 hours of sunlight. Although the Atacama Desert has a lot of advantages in this regard, it also presents important challenges. As an example, it is currently known that the annual UV-B doses in the Atacama Desert are about 40% greater than typical UV-B doses in northern Africa. This part of the spectrum cannot be used to generate more electricity and may be detrimental for the materials used in photovoltaic (PV) modules, reducing their lifetime. Thus, a new glass/glass (bifacial) PV module specially designed for our desert is one of our most important targets for PV R&D&I within the national solar program. For existing materials and design of PV modules, data regarding observations of degradation are variable in detail, consistency, quality, and statistical significance. Also, the available data of typical failures of PV modules installed in the Atacama Desert is scarce or non-existent.

With the above being said, the main objective of this thesis is to design and implement a tool (IDCTool) to evaluate PV modules operating in desert climate conditions and to characterize the samples. The proposal is based on the state-of-the-art in the field and the definition of a set of criteria for its use in small scale PV solutions. The implementation involves the development of a survey, equipment and tools, procedure for testing and analysis. IDCTool was used for a field campaign in the Arica and Parinacota Region, which is representative for desert climate conditions. The obtained results were analyzed following the proposed procedure. Thus, the main conclusions and future work were developed.

The proposed methodology of this thesis was validated with a case study, which was carried out in Arica and Parinacota Region. The 15 locations (all in Arica's commune) that were visited were separated into 4 zones: the coastal, the city center, the valley and the desert region. Considering the whole campaign, 95 PV modules were inspected in total. Modules were from 9 different manufacturers with the longest exposure of time being 13 years and the shortest being 2 years. All the inspected modules had front glass, rear-polymeric backsheet and aluminum frame. Results did not show any failure or defect in their wires, connectors or solar cells. Soiling in the glass was the most common visual failure with 52 cases of slight soiling and 39 cases of heavy soiling. The following visual defects that appeared the most were minor corrosion of the frame grounding (18 cases) and weathered/corroded frame (12 cases). Regarding to electrical parameters, most degraded parameter was the maximum power with a maximum drop of 39.08% and an average drop of 13.19±6.22%. In relation to temperature operation of the modules and the ambient temperature, the largest temperature difference found was 24.45°C with an average difference of 11.67°C. The hottest cell from the whole inspected universe was found to be operating around 99.4°C, while in average the hottest cells were operating at 64.0°C. Regarding the thermal abnormalities of the inspected modules, 2 modules showed PID pattern and 12 modules showed severely homogeneous hot cells.

The work carried out point out that the IDCTool in combination with the proposed analysis methodology gives standardized information and PV modules can be characterized. Analyzed data was studied by tendencies using statistical tools. Thus, it was possible to make conclusions and recommendations. However, due to the low amount of PV modules inspected, the phenomena found in the campaign cannot be generalized. In fact, our analysis is not supported by robust statistical evidence due to the small number of PV modules inspected. In this context, the development of a meaningful database, by the use of the IDCTool, will be the best set of information to start making conclusive recommendations for developments in the PV field.

"Here comes the sun"

The Beatles

Acknowledgments

Me gustaría comenzar por agradecer a mi hermosa madre que me crio con un preciado amor y me enseñó que estudiar no lo es todo en la vida. Gracias a ella, y otros, he sabido equilibrar mi vida y hacer de este trabajo algo bonito, llevadero y entretenido. Gracias a ella que me enseñó todo lo que es necesario para sobrevivir fuera del aula de clases y que me obligaba a salir a "carretear".

En segundo lugar, quiero agradecer a Daniela, mi pareja, por estar siempre presente y apoyándome en todas mis locuras—incluso las más ñoñas. Gracias a ella es que he podido recordar (aunque soy consciente de que a veces lo olvido) lo que mi madre, tan preciadamente, ha tratado de inculcarme—el valor de las personas, la familia (humana y perruna) y el amor. Ya que sin ellos éste trabajo no tendría el mismo valor. Quisiera también agradecerle a ella por lo "aperrada" que ha sido estos más de 4 años (no, sin saltito) y por aventurarse conmigo en cosas que jamás se me habrían ocurrido hacer en otros tiempos. ¡Seguimos siendo cheque a fecha!

Por otro lado, quiero agradecer a mi profesor guía, Rodrigo, que ha sido un verdadero guía. Con su carisma, sencillez y su carácter soñador ha despertado en mí las mismas ganas de ver un cambio en el mundo que vivimos, y comenzando por casa. Él ha sido una inspiración y alguien en quien he podido confiar y creer, lo que ha facilitado de muchas formas mi experiencia como estudiante universitaria. Me gustaría también agradecerle a él por toda la ayuda que me ha entregado en térmicos prácticos, sus cartas de recomendaciones, las redes de contacto, ¡mi primero trabajo!, la camaradería, esos cachitos que me daba para él salir de apuros, todas esas cosas que me han servido para entrar al mundo laboral de una manera mas sólida y más preparada. Me gustaría poder continuar con el legado que él ha dejado en la Universidad de Chile y hacer de la energía solar el motor de este país.

Además, quiero agradecer a mis profesores de comisión—Williams, Patricio y Pablo—por la ayuda que me han brindado en la depuración de este trabajo. Han sido, cada uno en su área de experiencia, un aporte necesario del cuál también he aprendido algunas cosas. En particular agradecerle a Pablo por su ayuda técnica-académica a lo largo de mi trabajo, pues es él quien me ha ayudado, quizás sin saberlo, a canalizar parte de mi tesis.

Para finalizar, quisiera agradecer la generosa ayuda financiera que me suministró Fondecyt N°1151438 "Optimal Storage Technology Mix in Power Systems with High Penetration of Variable Renewable Energy Sources", Fondap N°15110019 "Solar Energy Research Center (SERC-Chile)" y el Instituto Sistemas Complejos de Ingeniería (CONICYT – PIA – FB0816).

Contents

List of Tables

List of Figures

Chapter 1

Introduction

1.1 Motivation

The Atacama Desert, within its 105,000 km^2, harbors abundant natural resources. Moreover, it contains the largest copper and non-metallic reserves in the world. The national mining industry, which is the main productive and economic sector of Chile, is sustained by this vast desert. The annual copper production in Chile, which is the world's largest producer of this mineral, corresponds to 5.7 million tons. Furthermore, an annual electricity consumption of 34.1 TWh by the Chilean copper mining industry is projected by 2025. Additionally, the Atacama Desert has the highest levels of solar irradiance in the world with an annual average of 2,500 kWh/m^2 (GHI), 3,500 kWh/m^2 (DNI) and 4,000 hours of sunlight.[1]

The Atacama Desert not only presents advantages but also important challenges. According Cordero [1], the annual UV-B doses in the Atacama Desert are about 40% greater than typical UV-B doses in northern Africa. Mostly due to seasonal changes in the ozone, the differences between the Atacama Desert and northern Africa are expected to be about 60% in the case of peak UV-B levels. This, in combination with an annual average of 2 mm of rainfall (in the key zones of the desert) and an average temperature of more than 30°C in the summer, may lead to a fast degradation of the encapsulant materials of photovoltaic (PV) modules operating in the desert. The encapsulant materials not only allow us to have a solid structure to transport, manipulate and install the PV module but also maintain a safe electrical insulation of the device and protect its active layers against the environmental conditions. Therefore, the degradation of the encapsulant materials not only leads to the emanation of faults and subsequent degradation modes within the PV module, but also leads to serious safety problems. [1]

Comprehending failure modes of PV modules and their driving forces is a key factor in the design of PV modules. According to the current literature, the main root cause for PV mod-

[1] http://www.programaenergiasolar.cl/ The Chilean Solar Program is a Government initiative developed through CORFO and the Energy Ministry, who drafted a 2025 Road-map in a collaborative process with different public, corporate, academic and civil society representatives.

ule's degradation is the interaction between materials within the PV module [2]. Moreover, this interaction can be driven in a passive or an active environment. In the case of a passive environment, degradation interactions are due to uncontrolled manufacturing processes such as poorly cross-linked EVA encapsulant or too long lamination times. Concerning an active environment, degradation interactions are mainly driven by the combined effects of the material compounds with light, heat, water, moisture, wind, and chemical reactions.

Currently, in Chile, PV modules are mostly imported from and certificated in China, Europe or USA. Therefore, those PV modules are designed to operate in weather conditions that are normal/typical for those places. Likewise, international certification ensures that their products meet established quality and performance standards under most severe climatic conditions. Nevertheless, the climate conditions, severe or normal, in the Atacama Desert are not the same as North America or Europe. In conclusion, the special conditions in the Atacama Desert open new challenges and opportunities for the development of innovative energy solutions. For the time being, the development of an advanced solar power industry is on the way, and a glass/glass (bifacial) PV module specially designed for our desert is one of our most important targets for PV R&D&I within the national solar program.

In order to succeed in the development of a module adapted to the Atacama Desert conditions (bifacial PV module specially design for Atacama Desert conditions), it is imperative to have first-hand information about the typical faults experienced by PV modules that have been operating for several years in various areas within the Atacama Desert. Moreover, it is important that this information is reliable and standardized. Standardized information allows the use of statistical tools, the comparison between information extracted from different sources and the drawing of non-misguided conclusions. Hence, the development of a protocol that can be used to obtain data from PV modules operating in the field without taking them to a laboratory facility is imperative.

1.2 Research Hypothesis

For existing materials and designs of PV modules, data regarding (visual evaluation and electrical testing) observations of degradation are variable in detail, consistency, quality, and statistical significance. In this context, the regularization and standardization of the collected data by the means of an inspection data collection tool (IDCTool) will not only organize the data for statistical use but also give us more insights to determine the most critical failures that PV modules experience in the field.

As main hypothesis of this research work, it is established that the information of the performance of PV modules installed and operating in Atacama Desert constitutes key information for the development of adapted and more efficient PV modules. Likewise, it is expected to give guidance for the criteria of technology selection and for the development of standards for the country.

1.3 Objectives

1.3.1 General objectives

The general objective of this thesis is to design and implement a tool (IDCTool) to evaluate PV modules operating in desert climate conditions and to characterize samples. For their characterization, a methodology for the analysis is developed.

1.3.2 Specific objectives

1. Review of the state-of-the-art of failure modes and degradation mechanisms of PV modules.
2. Review of the state-of-the-art of standards/guidelines for outdoor testing of fielded PV modules.
3. Design and implement a filling form or survey, for data collection (visual and electronic data).
4. Define the equipment and tools needed to collect data.
5. Define and implement the procedures for field testing that ensure the health and safety of the worker in compliance with HSE requirements.
6. Design and implement a methodology for PV module characterization.
7. Carry out a campaign (case study) in a region, which must be representative for desert climate conditions, using the IDCTool.
8. Analyze and characterize the samples from the campaign according to the developed methodology.
9. Elaborate recommendations based on the analysis of the results from the campaign.

1.4 Structure of the Thesis

Chapter 2 starts with a review of the components of a conventional crystalline silicon (c-Si) PV module. The review includes a detailed description from the point of view of the materials that constitute the components and the main functions of such components. Typical failure modes and degradation mechanisms of c-Si PV modules depend on material composition and operating environmental conditions. Therefore, in Chapter 3, a review of the most common failure modes and their degradation mechanisms following the structure of the components of a c-Si PV module is presented. Now that a minimum number of failures are known and they are expected to be found at a particular region within the PV module, Chapter 4 reviews

current in-situ methods for the inspection of PV modules operating outdoor. Chapter 5 briefly explains the framework of this thesis followed by the description of the main criteria, scope and limitations within the framework. In this chapter, it is also given a detailed explanation of the IDCTool and the methodology for the analysis of the results. Chapter 6 describes the case study to validate the IDCTool, which includes a general description of the region where the data is collected, its climate and a detailed description of the inspected locations. In this chapter, it is also given the results from the campaign, the analysis of the results, and a discussion and recommendations based on the analysis. Finally, Chapter 7 summarizes the main conclusions of the research work and the recommendations for future work.

1.5 Scope of the Thesis

The design of the IDCTool and the case study in Arica consider the following limitations and delimitations:

- The IDCTool is designed only for c-Si PV modules, which is the technology most likely to be found operating in the Atacama Desert.

- Although the tool is sought to be easily extended or modified, it is designed to be applied with PV modules operating in desert climates. This is due to the intention of contributing to a long-term goal (although beyond the practical objectives of this thesis) that considers the creation of a database containing standardized information about all the PV modules operating within the Atacama Desert.

- The level of details of the survey is moderate in order to facilitate the work in the field and to minimize the data collection time. The intention of this tool is not to fully scan and determine all the failures that a PV module had experienced. This would generate large amounts of information that later must be treated and reduced. In addition, the application of such survey would require an specialized worker to conduct the survey.

- Since the IDCTool must be flexible and easy to be conducted, not all the field inspection methods that are reviewed in Section 4 are implemented in the tool. The reason for this limitation is twofold. On the one hand, there is a budget limitation for equipment. On the other hand, there is the complexity of implementing those methods, such as electroluminescence imaging that require expensive equipment, dark environment for imaging and skills for image processing.

- The equipment and tools used to conduct the survey must be low-cost devices. Three main reasons explain this decision. The first one is due to budget limitations. The second is because the tool is designed so that anyone (natural person, a small-scale company or a researcher, etc.) can use it. Finally, the last reason is because the studies to be carried out with this tool are qualitative and should not require sophisticated instruments of high resolution or high thermal precision.

Chapter 2

Crystalline Silicon Photovoltaic Module Components

To successfully understand the typical failure modes of a conventional c-Si PV module, it is important to recognize all the components of the module. The failure modes review is organized based on the structure and components of the module. This chapter breaks down the c-Si PV module into its most important component and describes these components in a very detailed way from the point of view of the materials that constitute them and of their main functions.

2.1 General Description of the Components

Figure 2.1 shows the most important components of a conventional c-Si PV module. The heart of the module is the silicon solar cell (Fig. 2.1 (A)) and its main purpose is to directly convert solar radiation into electricity. The physical principle of the solar cell is the photoelectric effect. Furthermore, to be able to extract the electricity (current of electrons), metallic conductors are incorporated on the cell. The metallic conductor system that interconnect the cells is called metallization (Fig. 2.1 (B)).

To obtain energy from the solar cells nothing more is needed. What come next are the components that protect the electrical system to withstand the environmental conditions in which the cells will operate. These extra components also provide mechanical support against external forces and they offer space to install a box where all the electrical protections can be placed.

The cell-metallization system is packed into two layers of encapsulant (Fig. 2.1(C)). Traditionally, this encapsulant is a polymer called ethylene-vinyl acetate (EVA). Its main purpose is to insulate the electric system and maintain the solar cell immovable. Following the encapsulant, we found the backsheet (Fig. 2.1 (D)). The backsheet can be a polymer or a glass, but polyvinyl fluoride (PVF) is the most common. PVF is a thermoplastic fluoropolymer material that protects the back of the module from environmental conditions.

Figure 2.1: General components of a c-Si PV module [3]. Components are: (A) silicon solar cell, (B) metallization, (C) encapsulant, (D) backsheet, (E) front glass, (F) frame and (G) junction box.

At the front side, the module is protected by glass (Fig. 2.1 (E)). Glass is chosen because is durable, protects the module from environmental conditions and hails, and at the same time is highly transparent in the visible range.

Finally, glass-polymer modules join their components with an aluminum frame (Fig. 2.1 (F)). The frame is commonly fixed with a sealing adhesive to prevent water entering the encapsulation. At the back, a junction box (Fig. 2.1 (G)) is glued. Inside the box are the bypass diodes and the positive and negative poles from the metallization system.

2.2 Detailed Description of the Components

2.2.1 c-Si solar cell

2.2.1.1 Standard c-Si solar cell

Si-based solar cells is the technology that covers more than 90% of the PV market. For this reason, this study focuses only in solar cells that are built on silicon wafer, specifically on

crystalline silicon (not amorphous). Fig. 2.2 shows a cross-section scheme of a Si-based solar cell which is also called *standard screen-printed p-type* Si *solar cell*. The operating principle of a solar cell shortly consist of:

1. Generation of electron-hole pairs within the cell by means of the photoelectric effect.

2. Diffusion of the electron-hole pairs to the p-n junction interface.

3. Separation of the electron-hole pairs by the built-in electric field at the space charge region.

4. Recollection of the electrons and holes at opposite contacts.

According to Wirth [4], the thickness of a traditional silicon solar cell is 180 μm (2013), which has not changed until today [5]. This thickness considers the anti-reflective (AR) coating, the emitter layer, the base layer and the back surface field (BSF), but no contacts. Mertens [6] describes, in a general way, the processes to produce Si-based solar cells in Fig. 2.3, which are: (1) slicing of wafers from crystalline ingots of p-type silicon, (2) polishing, cleaning and texturing the surface, (3) doping the silicon wafer with an n-type material to form the p-n junction, (4) deposition of the AR coating, (5) application of the front and back contact and (6) contact firing to create the BSF.

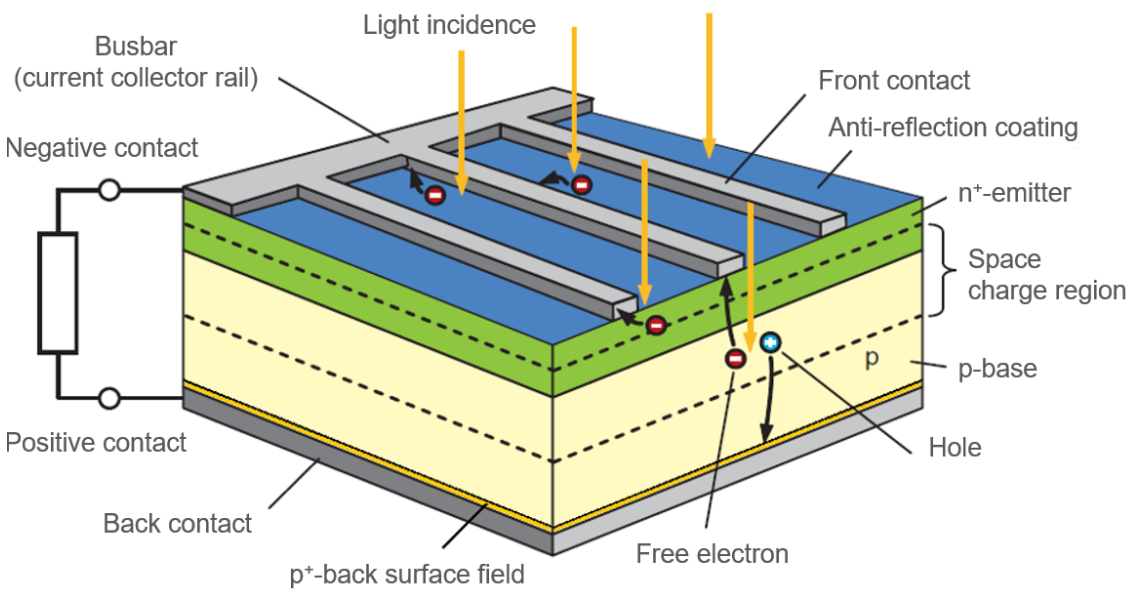

Figure 2.2: A cross-section scheme of typical Si-based solar cells. Adapted from [6].

The base can be fabricated of monocrystalline silicon (mono-Si) or poly-/multi-crystalline silicon (poly-/multi-Si). Single crystal ingots are commonly growth with *Czochralski method* shown in Fig. 2.4. In this method, pieces of poly-silicon are melted and a seed crystal is dipped into the melt. Then, it is withdrawn whereby fluid silicon attaches to it and crystallizes. The thickness of the ingot can be adjusted by temperature and withdrawal speed variation (for deeper explanation refer to [7, 8, 9]). Alternatively, the *float-zone method*, shown in Fig. 2.5, can be used. In this method, a seed crystal is placed under a vertical hanging poly-silicon rod. Then, a heating ring, moving upwards the rod, melts the poly-

silicon locally so that impurities are driven upwards during the crystallization (for deeper explanation refers to [7, 8, 9]).

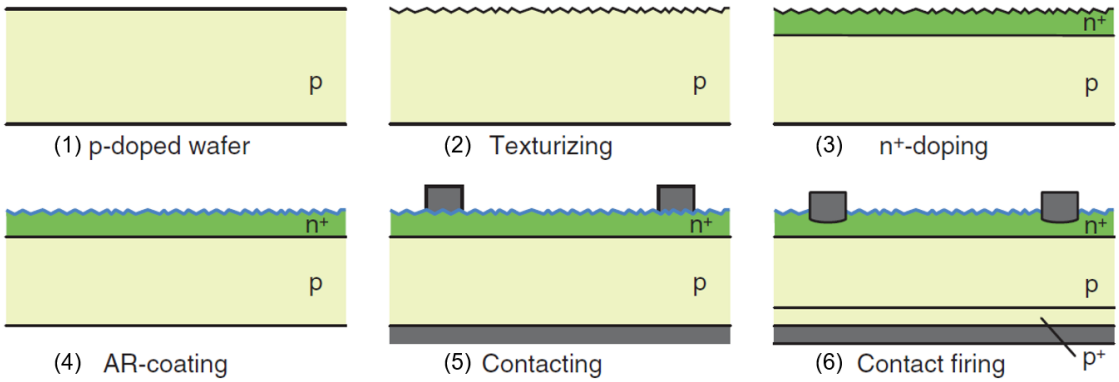

Figure 2.3: Process steps for the manufacture of mono-Si and multi-Si solar cells [6].

Multicrystal ingots are much easier to produce. The process, shown in Fig. 2.6, consists in melting the poly-silicon in a crucible. Then, letting the poly-silicon to cool down from the bottom. In the cooling process, several mono-crystals are formed at the bottom. These crystals grow in all directions until they touch each other at the sides. The zones where crystals touch each other are future recombination's centers in the cell.

After the ingots are ready, they are cut into individual sheets called wafers (step 1 from Fig. 2.3). This is normally done with wire saws of thickness 100-140 μm that move at high speed. Merterns [6] explains that once the wafers are cut, they are dipped into an etching bath to remove contaminants or defects at the surface. Additionally, Xiao and Xu [10] explain that the wafer's surface must be textured to enhance light absorption (step 2 from Fig. 2.3). According to Battaglia, Cuevas and De Wolf [11], the state-of-the-art for texturing the surface is wet chemical treatment, where the surface is etched by an alkaline solution for mono-Si cells and by an acidic solution for multi-Si cells. Battaglia also indicates that after texturization the wafers must be cleaned. This is done by a two-step process: first an oxidizing agent encapsulate the surface impurities and secondly the oxide is stripped off by de-ionized water.

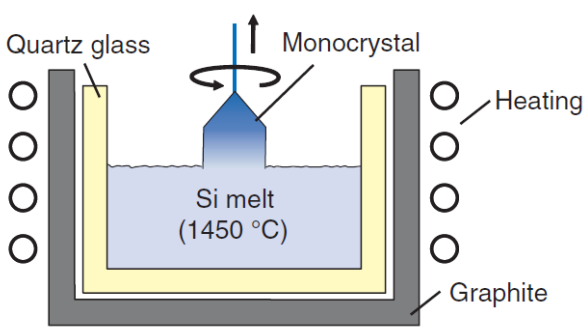

Figure 2.4: A scheme of Czochralski method for mono-Si growth [6].

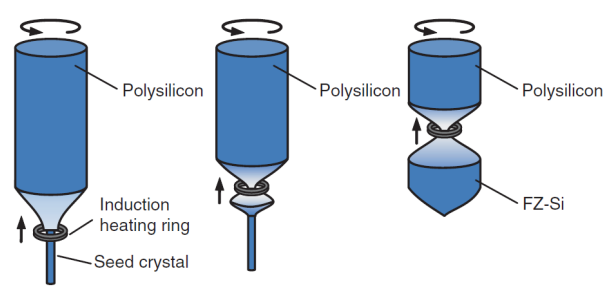

Figure 2.5: A scheme of float-zone method for mono-Si growth [6].

Following the surface texturing and cleaning comes the formation of the n^+-emitter and the p-n junction (step 3 from Fig. 2.3). To create the emitter, the surface of the p-type Si

is doped with atoms from group V (e.g. phosphorous) of the periodic table. As a result, the surface has a higher concentration of phosphorus than that of boron. This region is called emitter. The phosphorus continues its diffusion towards the p-type Si bulk. The p-n junction is formed where the concentration of phosphorous is the same as boron (at some place within the bulk). After the junction, the p-type Si contains higher concentration of boron than that of phosphorous. This region is called p-base.

According to Goswami [12], the most common method for n-type doping is phosphorus diffusion in the vapor phase while the back side of the wafer is covered. Additionally, Goswami also indicates that an alternative method is to deposit a solid layer of the dopant material on the top surface of the wafer and heating (800–900°C) the system, then the dopant will diffuse from the top. In brief, the p-n junction or base/emitter interface is made by boron-doped Si [11] (base) and phosphorous-doped Si (emitter).

A second purpose of the n^+-layer is to enable a metal-semiconductor junction. The interface between the semiconductor and the metal must have low resistance to minimize the energy losses, maintain a low temperature operation and enhance charge carrier flow. A low resistance is achieved with a high potential barrier at the semiconductor/metal interface. According to Battaglia et al. [11], a high concentration of phosphorous (typically $1 \times 10^{20} cm^{-3}$) is used to create this high potential barrier.

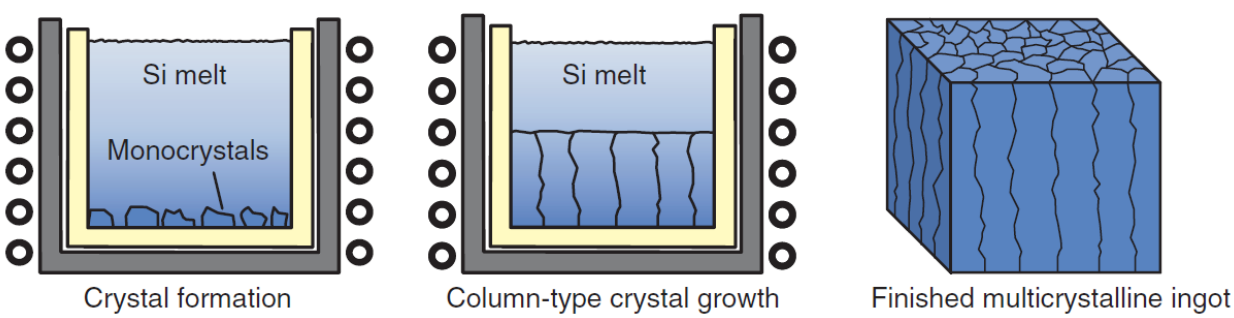

Figure 2.6: Growth of multi-Si ingots [6].

The next step in the manufacture processes of solar cells is the deposition of an AR coating (step 4 from Fig. 2.3). The reflection coefficient at the silicon/air interface is 30%[1], which is considered very high. The reflection of the light can be reduced by texturing the surface and/or by applying an AR coating to the surface. According to Mertens [6], standard cells use hydrogenated amorphous silicon nitride Si_3N_4, often just called silicon nitride, as AR coating. Additionally, Xiao and Xu [10] explain that not only SiN_x is transparent to the sun light but also thermally grown silicon dioxide SiO_2. Goswami [12] explains that the common methods of AR coating depositions are by vacuum vapor deposition, sputtering, or chemical spraying.

Following the AR coating deposition is the application of the contacts (step 5 from Fig. 2.3). The application of electrical contacts on the top surface of the doped wafer is made in a grid pattern that covers no more than 10% of the front surface. The pattern must cover a very small percent of the front surface because silver reflects light and shadows the cell.

[1] `http://www.pveducation.org/pvcdrom/anti-reflection-coatings`

According to Goswami [12], the front grid pattern is made by vacuum metal vapor deposition through a mask or by screen printing where a mask is placed on top of the doped wafer and a silver paste is brushed on. Additionally, the busbars contain copper-tin stripes on top [11]. At the rear side, silver pads are applied by using $AgAl$ paste to solder the connection wires and the rest is covered with a solid metallic sheet (aluminum). The aluminum also acts as a back mirror for part of the light that the silicon did not absorb in the previous passage.

The final step from Fig. 2.3 consists in contact firing (at 800°C) of the cell to lead to the sintering of Ag particles and contact formation. As a consequence of the firing, the BSF is created (see next paragraph). Meterns [6] also explains that after the BSF is created the cell must be insulated at the edges by etching or laser cutting process because the p-n junction is short-circuited at the edges due to phosphorous diffusion.

At this point we know the reason to why the silicon wafer is doped with phosphorous at the front side, but why the cell needs a p^+-layer at the metal-semiconductor interface on the rear side? Or more simple, why the cell needs a BSF? Electrons generated far from the p-n junction, that is in the bottom of the base, can easily recombine with holes in their way to the space charge region. This happens because electrons have short diffusion length (or lifetime) and they are the minority charge carriers inside the p-base. Therefore, to reduce the recombination probability a p^+-layer is needed. At the interface between the BSF layer and the base layer, an electric field (called BSF) is generated and is called back surface field. The BSF push back the electrons generated at the base so they can reach the space charge region faster and the probability of recombination decrease.

According to Xiao and Xu [10], the state-of-the-art of BSF for industrial screen-printed p-type Si solar cells is realized by the $p^+ - p$ junction using aluminum (Al). As a consequence of the firing (in the final step of the manufacture of solar cells), Al atoms from the rear contact diffuse into the p-doped base acting as p^+ acceptors creating the desired junction.

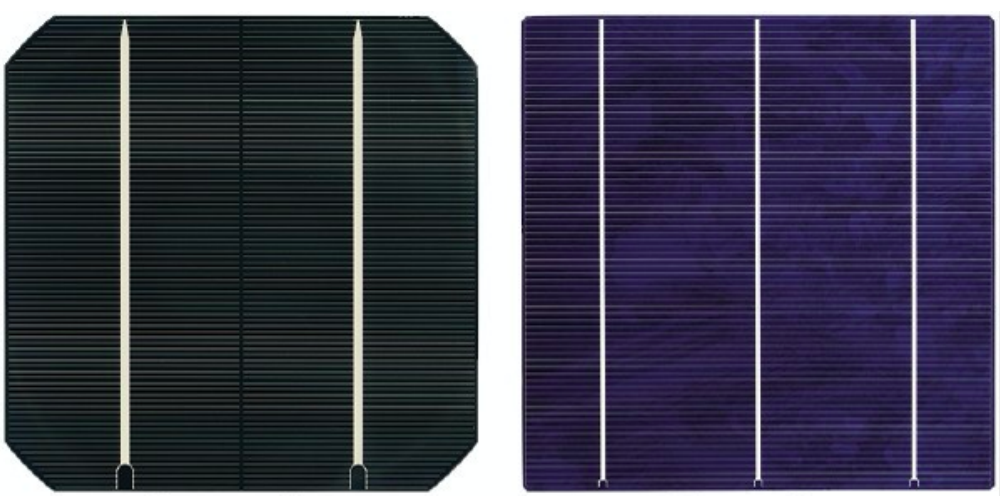

Figure 2.7: Mono-Si (left) and multi-Si (right) solar cell. Photo obtained from `http://www.sundirected.com/`

According to Battaglia et al. [11], silicon solar cells manufactured with the previously described process have efficiencies typically near 19.5% (mono-Si) and 17.8% (multi-Si). Fig. 2.7 shows how mono-Si and multi-Si solar cells looks like. Nowadays, AR coatings and

outer glass allow cell-to-module power ratios to be 100%, but the remaining components and interconnects drop down the module efficiency to be 1.5-2% lower than the cell efficiency.

Figure 2.8 shows both sides of a finished mono-Si solar cell. At the front side, the grid pattern can be recognized. The multiple horizontal silver lines are called grid-lines/fingers and the two vertical silver lines are called busbars. At the rear side, the two vertical silver lines are called rear-busbars. The typical dimensions for a (pseudo-square) mono-Si cell and (square) multi-Si cell are $125 \times 125mm^2$ and $156 \times 156mm^2$ respectively. According to Wirth [4], the front busbars of a mono-Si solar cell are typically 1.3-2 mm wide. Additionally, Werner [13] states that the width of rear-busbars of mono-Si solar cells is 3.2 mm.

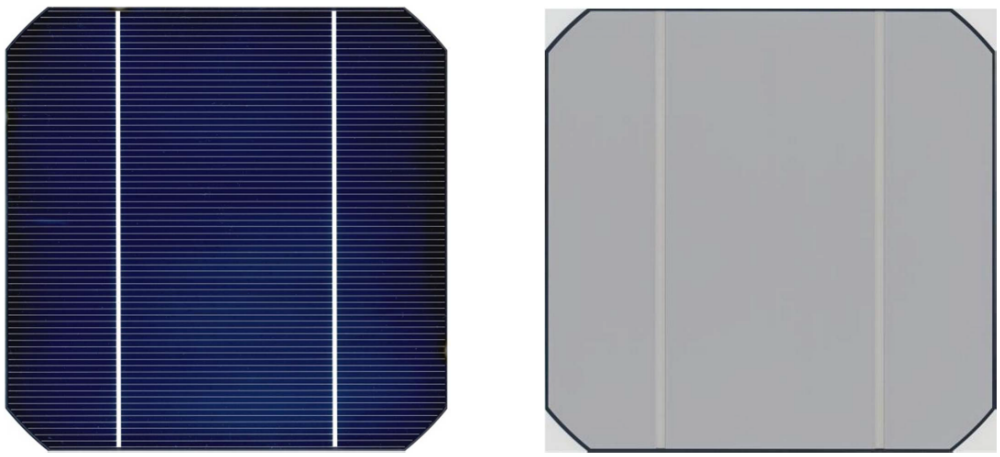

Figure 2.8: Front side (left) and rear side (right) of a mono-Si solar cell [13].

2.2.1.2 High-efficiency c-Si solar cells

The silicon solar cell has been industrially commercialized in large scale since 1990 and it reached its maturity in the past 10 years. Although the PV market is growing at an annual rate of 35-40% [10], the production costs of these cells are still high compared with conventional fossil-fuel-based technologies. Hence, researchers have been working on low-cost and high-efficiency technologies. Low-cost technologies focus on cost reduction in the manufacture of cells while high-efficiency technologies focus in the increase of power per unit area of cells. The increase in the output power density of a solar cell is mainly due to innovations in its design according to the following criteria:

- Optimization of the light absorption.
- Effective energy transfer from photons to electron-hole pairs.
- Effective electron-hole pair separation.
- Suppression of electron and hole recombination in the bulk and at the surface.
- Optimization of the recollection of electrons and holes at the contacts.

According to Xiao and Xu [10], the variety of high-efficiency Si-based solar cell devices

today are: Passivated Emitter and Rear Cell (PERC) devices, Passivated Emitter and Rear Locally diffused (PERL) cells, Passivated Emitter and Rear Totally diffused (PERT) cells, Pluto cells, PANDA cells, Interdigitated Back-Contacted (IBC) solar cells, Emitter-Wrap-Through (EWT) solar cells, Metallization-Wrap-Through (MWT) solar cells and Hetero-junction with Intrinsic Thin-layer (HIT) solar cells. Since Neuhaus and Münzer [14] state that HIT cells fabricated by Sanyo and IBC cells fabricated by SunPower were the most commercialized technologies at that time, HIT and IBC cells will be explained in detail.

Sanyo HIT solar cell

Figure 2.9 shows a schematic drawing of a HIT solar cell produced by Sanyo. This high-efficiency solar cell has symmetric layers, which are: upper TCO (Transparent Conductive Oxide) layer; upper thin a-Si (partially p-type doped and partially intrinsic) layer; n-type base; lower thin a-Si (partially intrinsic and partially n-type doped) layer and a lower TCO layer.

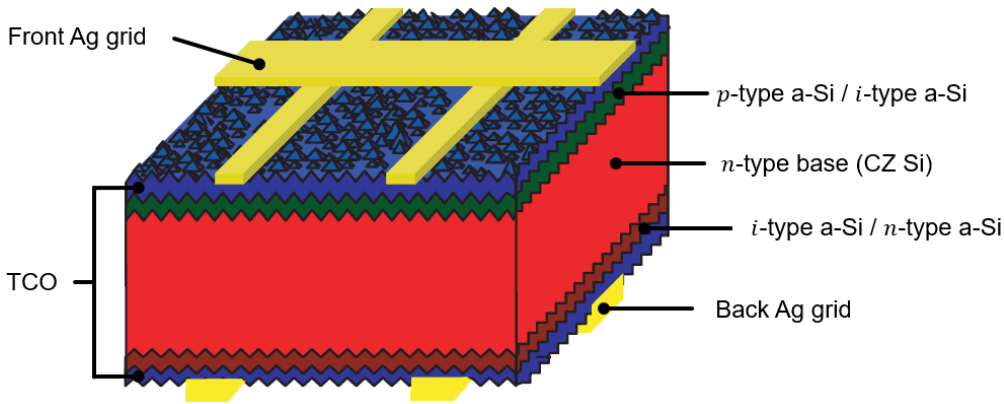

Figure 2.9: Schematic drawing of a HIT solar cell produced by Sanyo. Adapted from [14].

According to the construction steps of Sanyo shown in Table 2.1, the n-type silicon base is first textured and cleaned at both sides. Secondly, the hetero-junction emitter is formed by the sandwiched i-type a-Si layer between the p-type a-Si layer and the n-type Si substrate at the front side. The third step forms the BSF, which is the result of the sandwiched i-type a-Si layer between the n-type a-Si layer and the n-type Si substrate at the rear side. The fourth step consists in the deposition of the TCO at each sides by sputtering. Finally, the last step forms the Ag electrodes using the silkscreen-printing method. All the steps are performed at temperatures below 200°C.

One of the differences between HIT and standard cells is the use of TCO. The reason to why TCO is used is because the thin a-Si layer has a poor conductivity. According to Xiao and Xu [10], TCO layers guarantee charge transport to the metal contacts, low contact resistant between Ag/a-Si interface, and maximal optical transmission at the surface. Therefore, TCO works as AR coating. They also state that ITO (Indium Tin Oxide) and ZnO (Zinc Oxide) are the most common TCO materials.

Another difference is the use of a-Si. Although the device use a-Si, this technology is

Table 2.1: Inferred fabrication steps for HIT solar cells produced by Sanyo. Adapted from [14].

(1) Saw damage removal, texture and cleaning of n-type silicon wafer
(2) Deposition of i-type and p-type a-Si:H to the front side
(3) Deposition of i-type and n-type a-Si:H to the rear side
(4) Deposition of TCO to the front and rear sides
(5) Silver silk screen contact print to the front and rear sides

based on mono-Si wafers. According to Xiao and Xu [10], the use of a-Si is mainly due to the following three reasons: (1) enables surface passivation and creates a p-n junction simultaneously; (2) its low-temperature processes ($< 200°C$) can prevent bulk quality degradation; and (3) cells can obtain better temperature coefficient with high open-circuit voltage (V_{oc}). Amorphous silicon can be n-type (or p-type) doped using SiH_4, H_2, and B_2H_6 (or PH_3) precursors by a variety of deposition methods. They state that PECVD (Plasma Enhanced Chemical Vapor Deposition) is the most common method.

Finally, HIT cells can be either n-type or p-type. However, n-type substrate enables better cell performance. The open-circuit voltage of n-type HIT cells can exceed 700 mV, while p-type HIT cells are usually in the range of 660-690 mV [10].

SunPower IBC solar cell

Figure 2.10 shows a schematic drawing of an IBC solar cell produced by SunPower. This high-efficiency solar cell, which has metal contacts only at the rear side, has the following layers: front AR coating, front and rear passivation layers, front surface field (FSF) layer, n^+-type base, and p^+-type emitter and BSF layer.

According to the fabrication steps of IBC solar cells of SunPower shown in Table 2.2, the first part consist in the diffusion of boron at the rear side to selectively collect holes. Then, in the remaining part of the rear side, phosphorous is diffused to selectively collect electrons. This is followed by the deposition of the front AR coating and the deposition of the passivation layer at both sides. According to Xiao and Xu [10], the AR coating is usually a single SiN_x layer or SiO_2/SiN_x stack and the passivation layer is usually a single SiO_2 layer or SiO_2/SiN_x stack. Then, the passivation layer patterning generates a pattern of holes in the oxide layer at both boron and phosphorous areas. Later on, aluminum is deposited as first metal layer for better light reflectance and is patterned according to boron and phosphorous areas. This is followed by Ni and Cu plating for electrical conductivity and Ag plating for Cu protection. Finally, the metal contacts are applied by screen-printing or e-beam evaporation (annealing step).

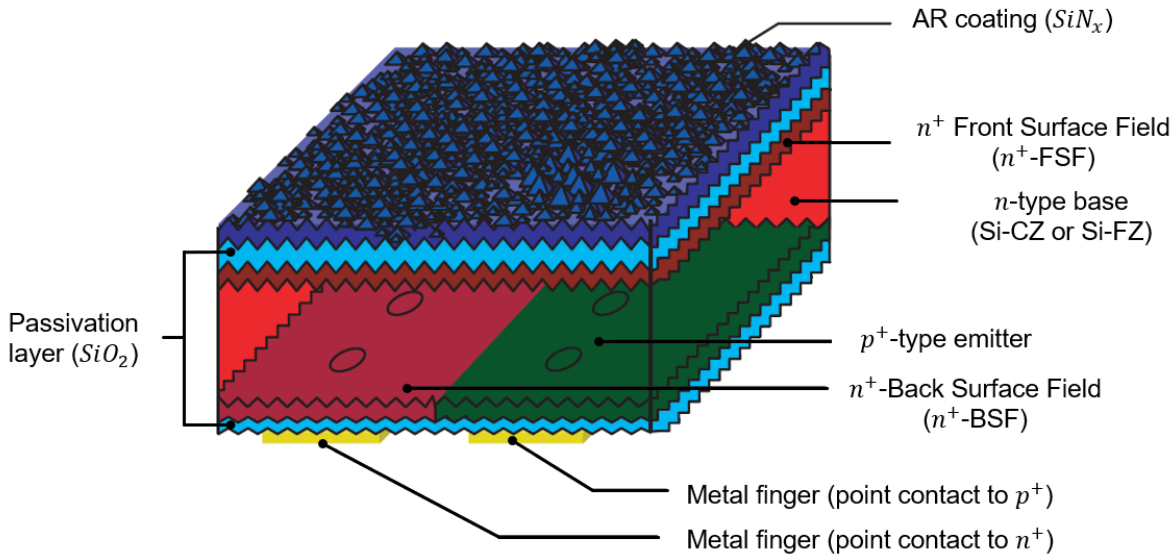

Figure 2.10: Schematic drawing of an IBC solar cell produced by SunPower. Adapted from [14].

Table 2.2: Inferred fabrication steps for IBC solar cells of SunPower [14].

(1) Saw damage removal and cleaning of n-type silicon wafer
(2) Boron diffusion
(3) Boron glass removal
(4) Rear-side SiN_x
(5) Front-side boron etching
(6) Oxidation
(7) Pattern of rear side for phosphorous diffusion
(8) Rear-side phosphorous diffusion
(9) Front-side oxide etching and texture
(10) Front-side phosphorous diffusion
(11) Diffusion glass removal
(12) Silicon nitride deposition on front and rear sides
(13) SiN_x patterning for contact points
(14) Aluminum sputtering
(15) Aluminum patterning
(16) Plating Ni, Cu, Ag
(17) Annealing

The main difference between IBC and standard cells is the location of the emitter and contacts at the rear side of the cell. The purpose of this structure is the elimination of light

reflectance at the front surface of the cell due to silver metallization. Another benefit of back contacts is that metal strips can fully cover the rear side. Therefore, stripes act as back mirror for the not absorbed light.

Finally, Battaglia et al. [11] state that IBC solar cell demonstrates excellent bulk lifetime, surface passivation and contact passivation with V_{oc} around 737 mV. However, HIT cells can provide better performance in terms of open-circuit voltage.

2.2.2 Metallization

The first step to assembly a PV module is to interconnect the solar cells in series. Fig. 2.11 shows how cells are interconnected in series. The ribbon strip is soldered along the length of the cell (on top of the busbars) and an extended part of the same ribbon strip is soldered to the back of a neighboring cell (series connection). When the cells are interconnected by soldering, the solder joint functions as electrical connection, mechanical support and thermal conduit.

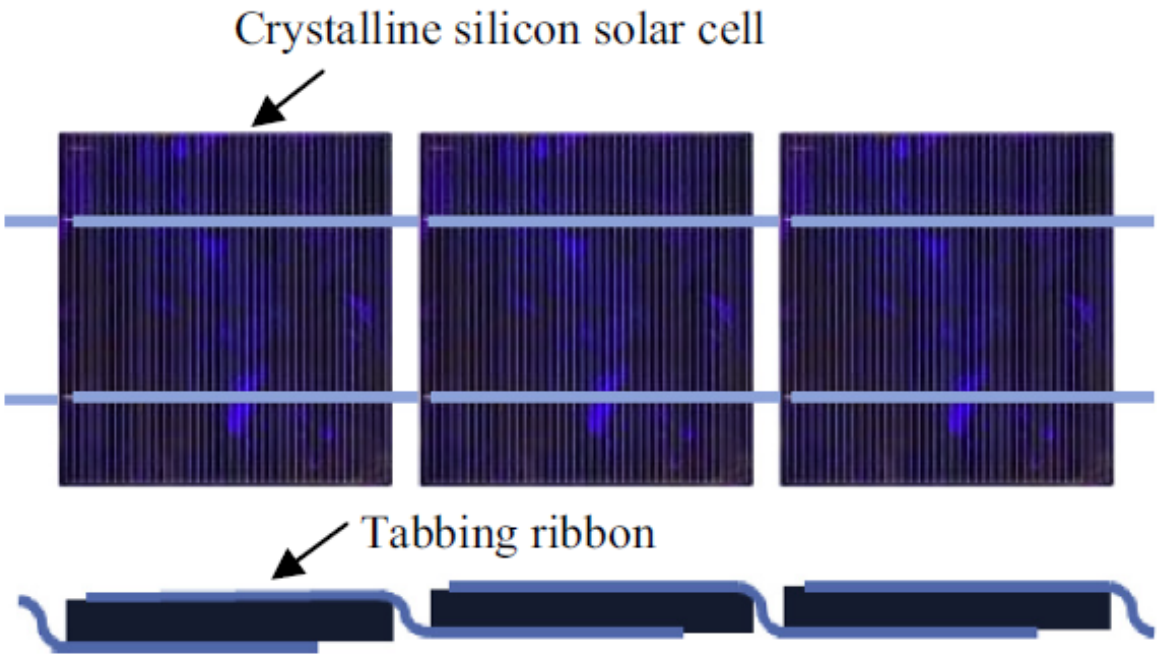

Figure 2.11: Solar cells interconnected in series with ribbon strips [15].

Figure 2.12 shows different spools of ribbon strips from Luvata company. Typically, the strips are copper-based ribbon and the solder material is lead-based. Since lead-based materials are toxic and have negative impact on human health and the environment, in the last years the industry has started to use lead-free solder materials for cell interconnection.

According to Zarmai [16], the most studied and widely used lead-free solder materials are $SnAg$ and $SnAgCu$ alloy.

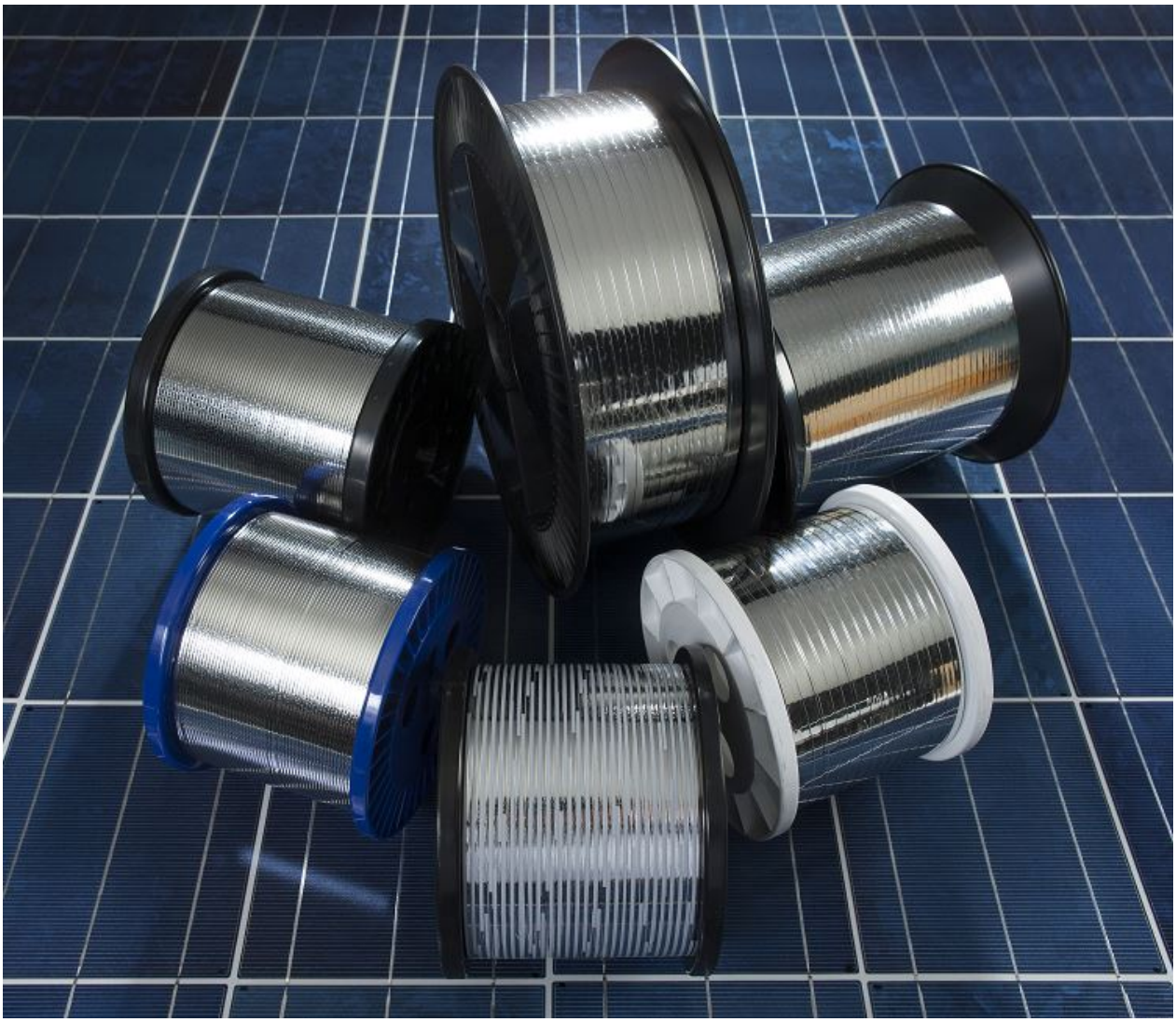

Figure 2.12: Ribbon spools from Luvata company.

Zarmai [16] explains that when copper ribbon strips are soldered onto the silver busbar of the silicon cell, inter-metallic compounds (IMCs) are formed at the solder/ribbon interface as well as at the solder/busbar interface through diffusion processes. Fig. 2.13 shows a schematic cross section of an encapsulated silicon cell and it makes zoom at the important interfaces. In his study, Zarmai used a lead-free $95.5Sn$-$3.8Ag$-$0.7Cu$ solder alloy to interconnect the solar cells. Consequently, the IMC formed at the Ag/solder interface was Ag_3Sn and at the solder/Cu interfaces were Cu_3Sn and Cu_6Sn_5. In general, the IMCs formed within the different interfaces depend on the composition of the solder, the temperature and the time [16]. The IMCs continue to growth in size through the service lifetime of the module as it operates in the field. According to Zarmai [16], the thickness of IMCs layers can grow from 0 to 12 μm depending on the type of solder (lead-based or lead-free) and other factors.

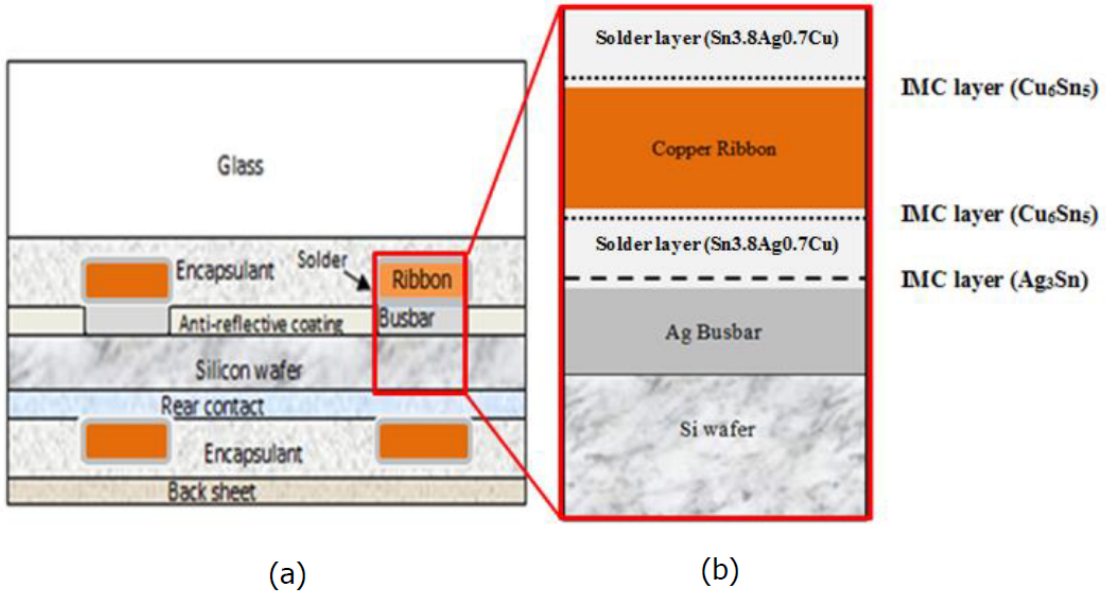

Figure 2.13: Schematic cross-section of typical c-Si assembly. (a) Encapsulated cell assembly. (b) Soldered interconnects including IMCs layers [16].

It is important to be careful with the terminology to be able to successfully identify failure modes in a solar module. For this purpose, the following terminology clarifications should be considered. Fig. 2.14 shows a single solar cell with its silver busbars and grid-lines/fingers. Additionally, Fig. 2.15 shows the ribbon for cell interconnects and the ribbon for string interconnects. In the latter case, two strings of 4 cells each are interconnected.

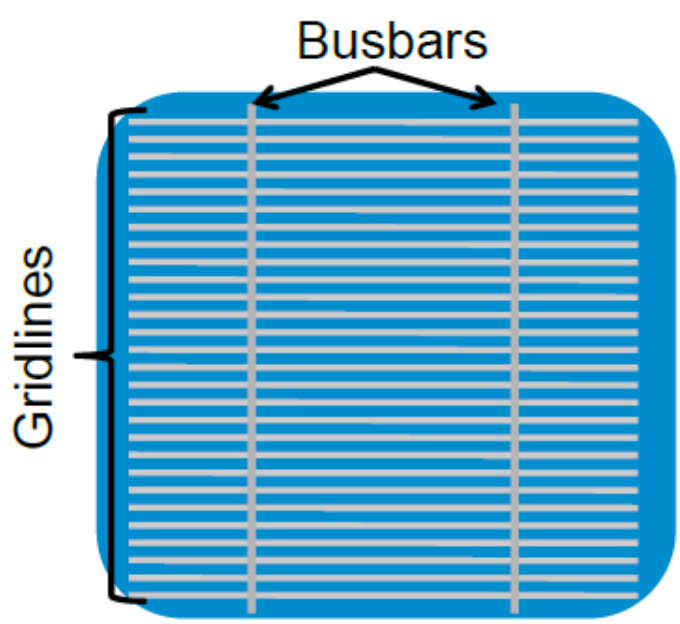

Figure 2.14: Grid-lines/fingers and busbars on a single solar cell [17].

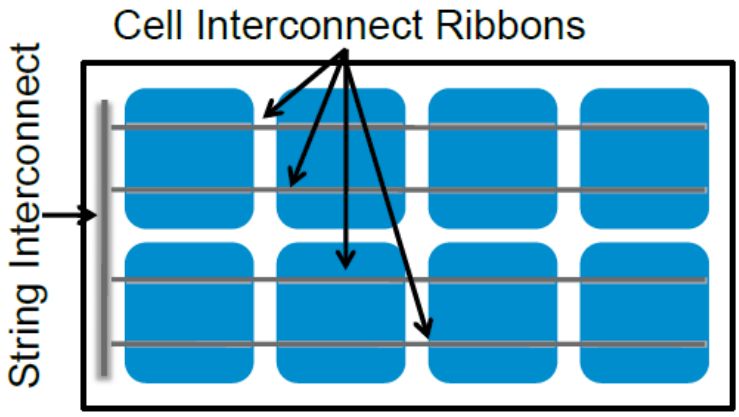

Figure 2.15: String interconnect ribbon and cell interconnect ribbons on a PV module[17].

2.2.3 EVA encapsulant

EVA is the most widely used encapsulant for glass-backsheet PV modules. Fig. 2.16 shows how unlaminated and uncured EVA looks like. Jiang, Wang, Zhang, Ding and Yu [18] describe few advantages of EVA, such as high transmittance coefficient (higher than 90%) and elasticity, low processing temperature, excellent melt fluidity, and good adhesive property. Since EVA is in contact with several components, such as the silicon cells, ribbon wire, glass and backsheet, it should have good compatibility with all these components and at the same time maintain its own features.

Figure 2.16: Unlaminated and uncured EVA.

EVA-encapsulant is a co-polymer of 73-67% polyethylene and 27-33% vinyl acetate (VA) [19]. Its formulation is adapted to withstand photo-oxidative stress. Köntges et al. [2] described the formulation of standard EVA as a polymer resin also containing cross-linking

agents (or curing agent), adhesion promoters, UV absorbers, and antioxidant agents. Furthermore, Blieske and Stollwerck [19] mentioned that standard EVA also contain UV and thermal stabilizers. Table 2.3 shows the composition's proportions of ELVAX 150 (standard EVA).

Table 2.3: Composition of ELVAX 150 [20].

Composition	**Proportions (%)**
Vinyl acetate	32-34
Curing agent	1.50
Photo-antioxidant	0.10
Thermo-antioxidant	0.20
UV absorber	0.25
Adhesive agent	1.00

Cross-linking agent is needed because when EVA is heated (during lamination) the agent lead to the formation of covalent bonds with the backsheet. Common EVA formulations use Lupersol as cross-linking agents, usually these agents are peroxides [2]. Köntges et al. [2] also mentioned that the common additives used in standard EVA are Cyasorb 531 and Tinuvin 234 as UV absorber; Tinuvin 123 and Tinuvin 770 as light stabilizer; Butylated hydroxytoluene (BHT), Irgafos 168 and Naugard P as antioxidant agents and Silane A 174/2530-85-0 as adhesive promoter. In the other hand, this standard formulation of EVA turns out into the properties shown in Table 2.4. The most important properties of EVA are its elasticity modulus, electrical resistivity and water absorption.

Table 2.4: EVA properties [20].

Properties	
Thickness	$\approx 0.45\ mm$
Density	$0.957\ g/cm^3$
Breakdown elongation	900-1100%
Elasticity modulus	$4.8\ MPa$
Electrical resistivity	$10^{14}\ \Omega cm$
Melt index (190°C/2.16kg)	$43\ g/10\ min$
Melting point	63°C
Water absorption	0.05-0.13%
Refractive index (average)	1.482

Jiang et al. [18] explain that the adhesion property of EVA is influenced by its structure and the surface treatment of the front glass and the backsheet. Additionally, according to Jiang, the bonding strength between EVA and front and back layers increases with the cross-linking curing reaction of EVA. Furthermore, high content of VA improves the flexibility of EVA at low temperatures and the adhesive property. Jiang indicates that the appropriate VA content is fixed between 28% to 33%.

The most common encapsulation process for PV modules is the vacuum laminating method. The aim of this process is to bond the multiple layers all together. The most important stage of the encapsulation process is the thermal treatment of the EVA. This treatment is performed in two steps: the lamination and the curing (polymerization cycle). The time under vacuum, the pressure applied and the duration of the lamination process affect the quality of the final result. Since the polymerization reaction is irreversible, the thermal treatment is crucial.

The process of encapsulation starts with the lamination cycle where the air is evacuated and the unlaminated module is heated up around 120°C. At this stage, the EVA flows and embeds the cells. Then, the upper chamber (see Fig. 2.17) is filled with air to press the laminate module. After this, the curing stage starts when the temperature is increased until 150°C. According to Luque and Hegedus [8], standard EVA needs 60 minutes to cure. During this period, the polymerization of the EVA occurs. This means that EVA cross-links forming chemical bonds and sealing the module components. The final step is the cooling and subsequently the unload of the laminated module from the laminator chamber.

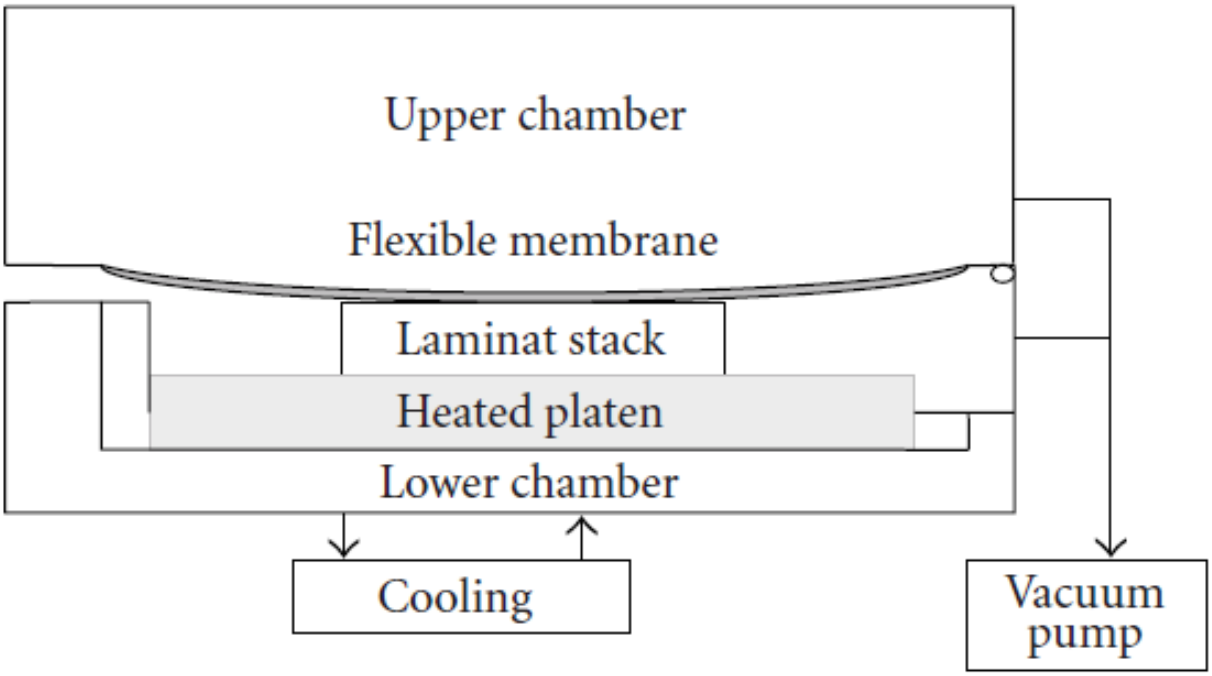

Figure 2.17: Scheme of the encapsulation chamber [20].

2.2.4 Polymeric backsheet

The most important objectives of the backsheet are: protects the module from moisture ingress and ensures electric insulation. Traditional c-Si modules can use either glass or polymeric films as a backsheet. The focus in this section will be on polymeric films because they are more widely used than glass. Polymeric films are also referred as "Tedlar-film" because they were mostly based on that type of film in the beginning of PV module manufacturing. Fig. 2.18 shows a spool of Tedlar from DuPont company. Due to a Tedlar material shortage these films evolved into more complex structures. Nowadays, polymeric backsheets have three layers (see Fig. 2.19) to fulfill different requirements. Each of these layers has a different function and they are glued together by adhesive layers.

Figure 2.18: Tedlar spool from DuPont company.

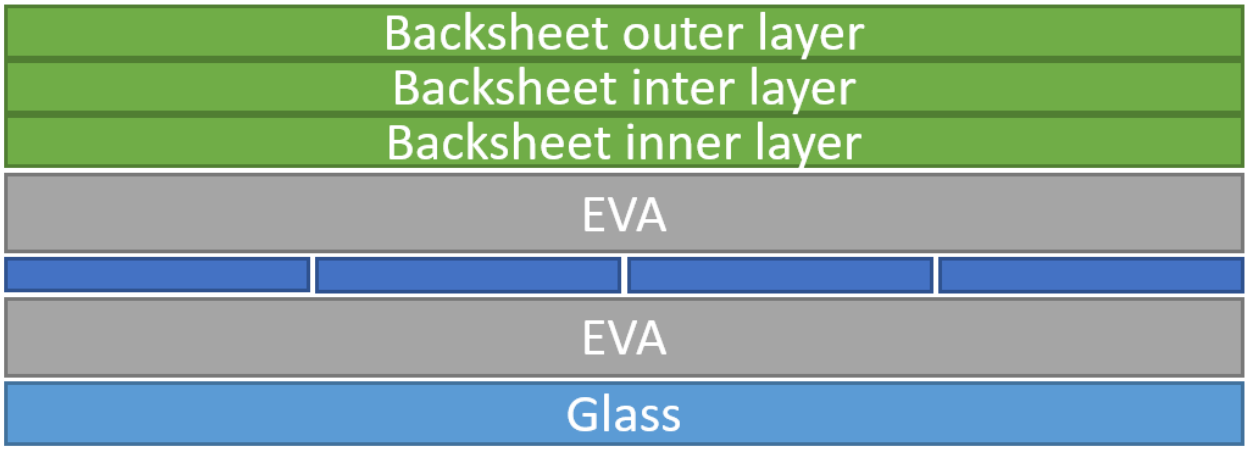

Figure 2.19: Scheme of the three layers of a backsheet. The outer layer is in direct contact with the environment and the inner layer is in direct contact with the EVA-encapsulant.

The oldest backsheet material is a three-layer combination of PET (Polyester or Polyethylene Terephthalate) stretched between PVF (Poly Vinyl Fluoride known as Tedlar). This combination is called TPT (see Fig. 2.20). According to Blieske and Stollwerck [19], PET

and PVF have a typical thickness of 200 μm and 40 μm respectively. PET is a good electrical insulator and it provides mechanical strength, but it needs stabilizing additives to resist long weathering cycles. Since PVF do not interact with UV and moisture and do not degrade at high temperatures, PVF was chosen to protect the PET. Some backsheets also have an additional thin aluminum layer ($\sim$ 8-12 μm) for high moisture requirements.

PVF is not the only alternative for fluoride layers in the backsheet. According to Blieske and Stollwerck [19], PVDF (Poly Vinylidene Fluoride) and THV (terpolymer of tetrafluoroethylene, hexafluoropropylene, and vinylidene fluoride) are also used in the solar industry. In Fig. 2.20, Dupont shows the most typical structures used nowadays. Tedlar®is a registered trademark from Dupont, fluoro-coating backsheets use PET as core layer and fluoropolymers as outer and inner layer. PET based backsheets can easily undergo hydrolysis, but they can be modified to be hydrolysis resistance (HPET).

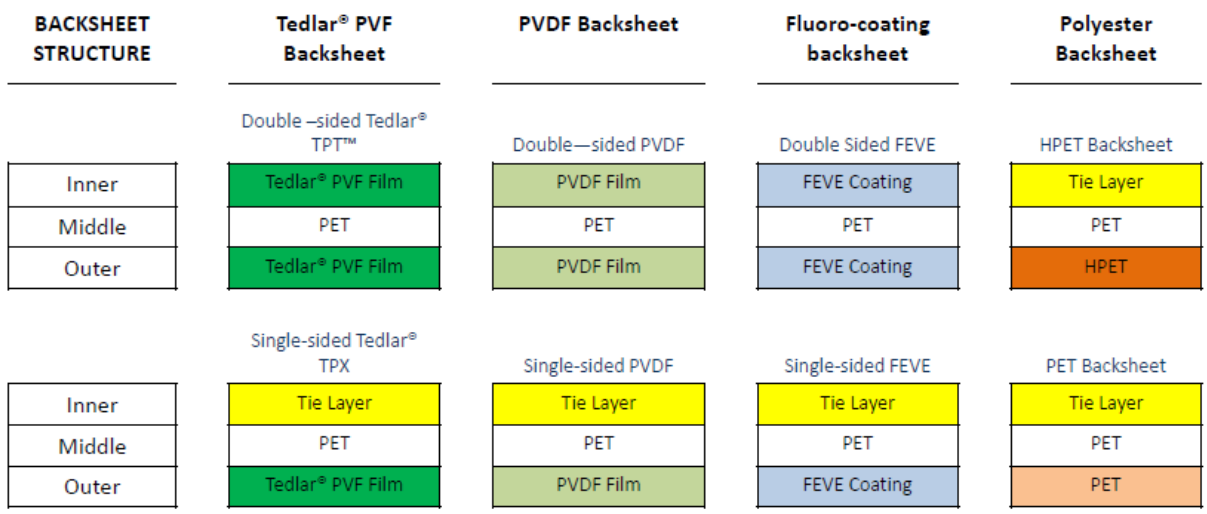

Figure 2.20: Typical PV backsheet structures. PVF:Poly Vinyl Fluoride Film, PVDF: Poly Vinylidene Fluoride Film, FEVE: Fluoroethylene-Alkyl Vinyl Ether Coating, HPET: Hydrolysis Resistance Polyester, PET (Polyester): Polyethylene Terephthalate and Tie-layer: EVA, Polyethylene, Polyolefin, Polyamide, Primer, Fluoro-coating, etc. [21].

Blieske and Stollwerck [19] explain that PVF is over-engineered because the inner layer of the backsheet is not in direct contact with the environment and the EVA has a UV-absorber. Thus, the inner layer main objective is to provide adhesion between the EVA and the backsheet, because EVA and PET do not adhere naturally. For all these reasons, the inner layer often consists of EVA, PE or a primer (Tie layer in Fig. 2.20). When the PET is stretched between EVA and PVF the combination is called TPE. In the other hand, Blieske and Stollwerck [19] state that some manufacturers replace the fluoride polymer (outer layer) with a non-fluoride coating that provides an equal weathering barrier for the PET and it is low cost. This combination with EVA as inner layer is called Polyester-Polyester-EVA (PPE).

The PET, EVA, PVF, PVDF and aluminum do not adhere each other, thus they must be glued together with adhesive. According to Blieske and Stollwerck [19], the adhesive

has special adhesion promoters for each interface PVF/PET, PET/EVA or PET/PET. The adhesive is a mixture of different chemical components that provides long-term stability and fast adhesion force build-up to the adhesive layer.

From an optical point of view, Blieske and Stollwerck [19] indicate that TPE backsheet has a higher reflection coefficient than TPT backsheet. From an environmental protection point of view, Tedlar/Al/Tedlar backsheet has the lowest moisture vapor transmission rate at 38°C followed by Tedlar/PET/EVA, THV/PET/EVA and PET/PET/PE.

2.2.5 Soda-lime front glass

Glass is one of the best options to provide protection against the environment, while at the same time light is allowed to pass unhindered to the solar cells. Glass is used because is transparent, hermetic, durable and has enough strength to resist 25 years or more; it also enhances light trapping. Glass is not the only option for this purpose, some transparent polymers has been proposed depending on the PV application, for example, for flexible or light-weight modules, but the traditional c-Si PV modules are assembled with soda-lime glass because this glass has the sufficient properties at the lowest costs.

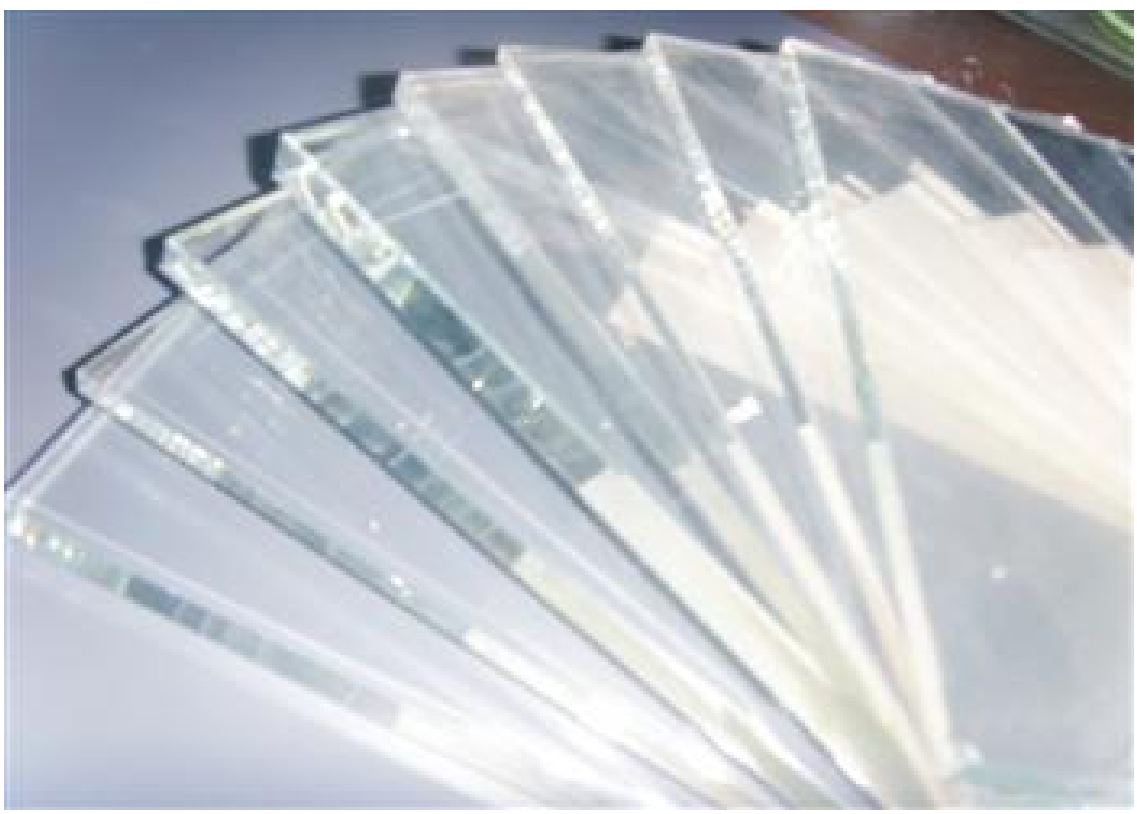

Figure 2.21: Low iron tempered soda-lime glass from the company AVIC.

Specifically for PV, low iron soda-lime glass is used. This type of glass is water resistant (liquid and vapor) and it can be very strong by heat strengthening. Soda-lime glass composition is shown in Table 2.5. This glass is mainly fabricated with silicon dioxide SiO_2 (called

silica) and sodium oxide Na_2O (called soda). Most of these chemical compounds (especially silicon dioxide) contain a significant amount of iron. Since iron leads to a strong absorption in the near infrared [19], low iron soda-lime glass has better transmission coefficient than standard soda-lime glass. Fig. 2.21 shows a low iron tempered soda-lime glass from the company AVIC.

According to Blieske and Stollwerck [19], soda-lime glass with a composition such as the one in Table 2.5 has a practical melting temperature of 1300°C that is relatively low temperature compared with pure silica glass. Typically, this glass is manufactured in cross fired furnaces by two major processes: (1) the float process or (2) the roller process. The first process results in a glass with a mirror-like surface and the second in a patterned glass surface. Both kind of glasses are non-tempered and their physical properties can be found in Table 2.6.

Table 2.5: Chemical composition in mass% of soda-lime glass used in solar glass production [19].

Chemical compound	**Composition (%) according to DIN**[2]	**Typical composition (%) according to Nölle** [22]
Silicon dioxide (SiO_2)	69-74	72
Sodium oxide (Na_2O)	10-16	14
Calcium oxide (CaO)	5-14	8
Magnesium oxide (MgO)	0-6	4
Aluminum oxide (Al_2O_3)	0-3	1.3
Others (e.g., K_2O or Fe_2O_3)	0-5	0.7

The tempering process of glass shown in Fig. 2.22, in few words, consists in cutting the non-tempered glass, grinding the edges, cleaning the glasses, drying them, heating (at >630°C) and finally cooling them. In the cooling stage, the center of the glass undergoes a relatively slower cooling process than its surface. This difference leads to a higher density in the center of the glass. Consequently, the volume experiences a tensile stress while the surface experiences a compressive stress. The high stress difference between the center of the glass and its surface increases its mechanical strength.

According to Blieske and Stollwerck [19], non-tempered soda-lime glass has a bending strength of 45 MPa (N/mm^2) while a fully tempered glass has 120 MPa or more. They also indicated that "tempered glass can withstand a heat difference of more than 100°C on the whole glass surface, whereas non-tempered glass will break at temperature differences of more than 40°C".

[2]DIN Deutsches Institut für Normung e.V., 2004. DIN EN 572-1 Glas im Bauwesen.

Table 2.6: Physical properties of (nontempered) soda-lime glass [19].

Property	**Symbol**	**Value and units**
Refractive index	n	1.5 (380-780 nm)
Density	ρ	2.5 g/cm^3
Elasticity modulus	E	70,000 N/mm^2
Poisson number	ν	0.2
Thermal expansion coefficient	χ_T	9 x 10^{-6} K^{-1}
Bending tensile strength	f_t	45 N/mm^2
Heat gradient tolerance		40 K

To reduce the glass surface reflections, two options have been used. The first option is texturization of the glass surface and the second option is the adhesion of an AR coating on the air/glass interface. According to Blieske and Stollwerck [19], current AR coatings for PV modules consist of porous SiO_2 with a refractive index of 1.23. The different processes to add AR coatings can be divided into two main categories: (1) deposition of the coating after annealing, but before tempering and (2) glass treated after tempering. The first category includes deposition techniques such as spraying, roller coating dipping, and chemical vapor deposition, whereas the second category is based in chemical arching in ammonium fluoride.

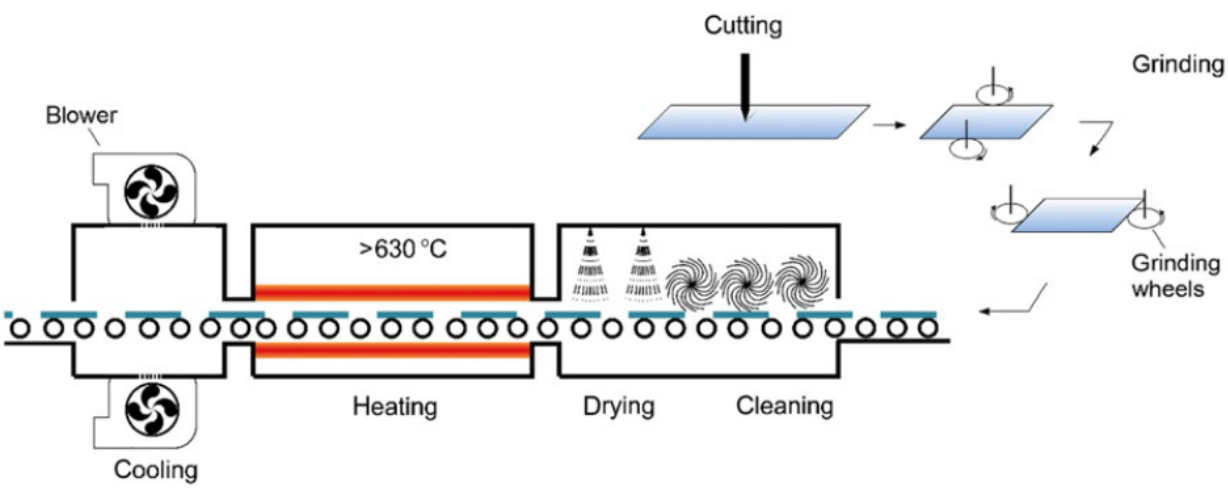

Figure 2.22: Schematic cross section of a fully integrated tempering line (includes cutting and grinding) [19].

2.2.6 Junction box and bypass diodes

The junction box is a container fixed at the back of the solar module which converts the string interconnects into module leads. Fig. 2.23 shows an example of a junction box. Inside

of this box, bypass diodes are incorporated to short-circuit strings in case of shading or severe current mismatch.

Figure 2.23: A TE Connectivity junction box.

2.2.6.1 Junction box enclosure and pottant

For the junction box to perform its function reliably and safely, the box must adhere to the back of the solar panel with strength and it must provide enough electrical insulation. Additionally, since bypass diodes dissipate the power according to the cell current, the box should have good heat transmission to the external ambient. Since internal connections could develop arcs, junction boxes must be nonflammable.

Polymers are used for both the junction box enclosures and pottants, but each of them has different material requirements. An enclosure is a non-waterproof open container and a pottant is an adhesive material. Schneller et al. [23] mention that junction box enclosures are typically made from Noryl or Xyron, which are made of polyphenylene and polystyrene, while Poliskie [24] explains that most widely used pottants are silicones and epoxies. According to FABRICO™[25], foam tapes are also used as sealing adhesives. Polyethylene and polyurethane foam tapes have been long used by solar manufacturers while acrylic foam tapes are relatively new in the solar industry.

Dow Corning [26], a worldwide company with more than 65 years of experience in PV adhesives and sealants, describes potting agents as solvent-less silicone materials with low

viscosity. When potting agents are properly cured, they form a coating that provides protection against moisture, dirt, shock and vibration. Additionally, pottants resist UV radiation and high temperatures.

In Table 2.7 and Table 2.8, Poliskie indicates the material specifications for polymeric enclosures and pottants that meet the requirements for a junction box.

Table 2.7: Material specifications for polymeric junction box enclosures used for Balance of System (BOS) components [24].

Material Parameter	**Specification**
Thermal	Relative temperature index (RTI) equal or above 363 K
Mechanical	Impact resistance >22.6 Nm
Electrical	Comparative tracking index (CTI)≤2
Flammability	Flammability rating of 5-VA, hot wire ignition (HWI)≤4, high-current arc ignition (HAI) 3-2
Weathering	f1 UL rating

Table 2.8: Material specifications for polymeric junction boxes pottants used for PV BOS components [24].

Material Parameter	**Specification**
Thermal	High thermal conductivity <0.4 $W/(m\ K)$, low coefficient of thermal expansion
Electrical	Volume resistivity 1016 to 1014 $\Omega\ cm$, comparative tracking index (CTI)≤2
Flammability	Flammability rating of HB, hot wire ignition (HWI) = 1 for HB materials, high-current arc ignition (HAI) = 1 for HB materials
Transmission rates	High water vapor transmission rate (WVTR) $< 10^{-1}\ g/m^2/\mathrm{d}ay$

2.2.6.2 Bypass diodes

Situations such as cell mismatch or cell shading can cause local hot-spots (see section 3.2.1.3). These hot-spots, caused by reverse biasing of cells, may induce thermal degradation of the PV module, because they can exceed 150°C. If PV modules operate in these conditions for long periods of time, then these PV modules could be irreversibly damaged. Bypass diodes are used to prevent these operating conditions.

In a PV module, cells are interconnected in series to form an individual string. Each of these strings are routed to the junction box with its own bypass diode. Depending on the module layout, bypass diodes are normally used for 20-24 cells [23]. Fig. 2.24 shows an example of a 60 cells solar panel with three bypass diodes. Each bypass diode has 20 cells connected in series.

According to Schneller et al. [23], the normal operation of the diodes is in reverse bias. Consequently, these diodes should have extremely low current leakage. As an immediate consequence, reverse breakdown voltage of the diode must be much higher than the voltage string. In other hand, when a string is partly shaded, the diode operates in forward bias. Additionally, bypass diodes must withstand over-voltage spikes such as the ones that occurs during an electrostatic discharge (ESD) when lightnings strike.

Firsts bypass diodes were *p-n* junction diodes because they meet the requirements for reverse bias operation. The problem with them is that in forward bias condition they overheat too much. Therefore, PV industry upgraded to Schottky diodes that exhibit lower power dissipation in forward bias condition but suffers with relatively high leakage currents in reverse bias. Fig. 2.25 shows an opened junction box with its bypass diodes.

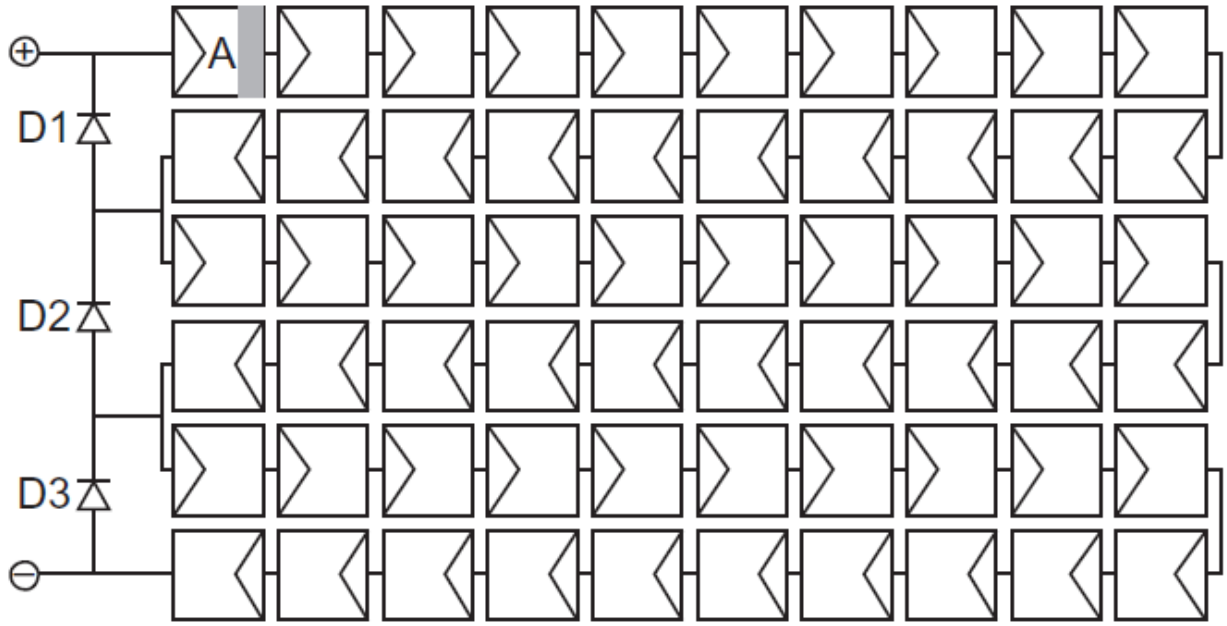

Figure 2.24: Module interconnection scheme of 60 cells in 3 strings where each string is protected by a bypass diode [4].

Figure 2.25: Bypass diodes inside an opened junction box.

Chapter 3

Failure Modes and Degradation Mechanisms for Fielded c-Si PV Modules

Failures and degradation mechanisms of PV modules depends on module construction and the climate where they operate. The available data of typical/dominant failures for c-Si PV modules in Atacama Desert, Chile, is scarce or non-existent. Most of the literature that focuses on failures modes of PV modules operating in desert climate conditions is based on studies of PV modules operating in Arizona, USA.

Due to this lack of data, this chapter first mentions the most common failure modes for PV modules operating in desert or hot-dry climate conditions. Secondly, the focus of attention change to the description of typical failure modes for c-Si PV modules no matter where they have been operating.

3.1 Operating in Desert Climatic Conditions

Kuitche, Pan and TamizhMani [27] investigated dominant failure modes for fielded c-Si PV modules under desert climate in Arizona, USA. They used the Failure Mode and Effects (Criticality) Analysis (FMEA/FMECA) technique for this purpose. They determined that solder bond failures and encapsulant discoloration are the dominant modes under the hot and dry climate of Arizona.

Berman, Biryukov and Faiman [28] evaluated a grid-connected PV system in Negev Desert, Israel. They observed browning EVA after 5 years of operation.

Shrestha et al. [29] evaluated 5900 c-Si glass/polymer modules fielded for 6 to 16 years in three different PV power plants under hot and dry desert climate in Arizona, USA. They concluded that the dominant failure was solder bond fatigue with/without grid-line contact fatigue.

Yedidi [30] evaluated two 16-year-old PV plants to ascertain degradation rates and various

failure modes in hot and dry climate. He suggested that the primary degradation mode was encapsulant browning leading to thermo-mechanical solder bond fatigue (cell/ribbon and ribbon/ribbon).

Mallineni [31] evaluated two PV power plants, one in Glendale and the other in Mesa, both from Arizona. Modules operated for 12 years under hot and dry climate conditions. She concluded that the major cause of degradation of modules from Glendale's power plant was high series resistance (probably due to solder/bond thermo-mechanical fatigue) and the failure mode ribbon/ribbon solder bond fatigue.

Suleske [32] investigated 1900 aged (10-17 years) grid-tied PV modules installed in the desert climatic condition of Arizona. He documented visual defects, infrared images and I-V curve measurements. He concluded that the browning of encapsulant was the largest issue followed by hot-spots.

Singh, Belmont and TamizhMani [33] analyzed the degradation of 1900 fielded PV modules operating for 12 to 18 years under hot and dry climate conditions. They wanted to identify potential induced degradation (PID) failure. For this purpose, all series strings at the power plant were positively biased with respect to the ground potential (negative). They indicate that modules do not appear to experience PID effect and they attribute this behavior to the dry climate of Arizona.

Table 3.1: Summary of dominant failure modes for c-Si PV modules operating in desert or hot-dry climate conditions.

Dominant failure modes
Solder bond failure (cell/ribbon)
Solder bond failure (ribbon/ribbon)
Encapsulant discoloration (browning or yellowing)
Hot-spots

3.2 Operating in Diverse Climatic Conditions

3.2.1 c-Si solar cell

3.2.1.1 Snail tracks/trails

Snail tracks, also called snail trails, corresponds to discoloration on grid-lines/fingers, which is visible to the naked eye. Fig. 3.1 shows how snail trails looks like in a real fielded PV module. They seem like black curves on top of the solar cell, like trails made by snails. These tracks can have different patterns, for example, in Fig. 3.2 silver fingers are only discolored at the edge while in Fig. 3.3 the pattern is random over the surface of the cell. In terms of

the origin of this failure, it was not very clear until recently. However, currently there are more insights about this failure mode.

Mohammed, Boumediene and Miloud [35] assessed the long-term degradation of modules in Adrar (southern Algeria) by visual inspection and Fan [36] modeled the formation of snail trails for PV modules under accelerating aging tests. They observed that the discoloration of the fingers is due to the formation of silver compounds. Specifically, Fan found that snail tracks contain dark silver acetate ($AgC_2H_3O_2$) and its abundance depends on the concentration of acetic acid from EVA. Additionally, Köntges et al. [37] speculated that additives or impurities of EVA may contain halogens and phosphor that could initiate reactions with silver. Furthermore, Duerr et al. [38] found that UV radiation and gas permeability were also degradation reactants leading to silver compounds. Finally, authors from [39, 35, 38], suggested that humidity and moisture assists the formation of snail trails.

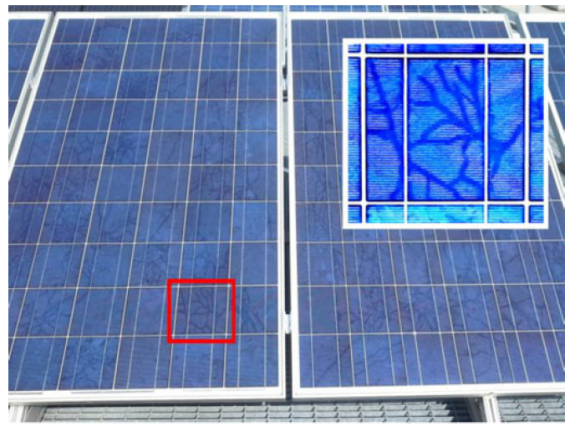

Figure 3.1: Fielded PV module with several cells with snail trails [34].

Recent investigations on snail trails formation have clarified the exact reason of the origin. Meyer et al. [40] observed that at the silver-finger/EVA-encapsulant interface a reaction occurs, which is triggered by moisture, temperature and an electric field. This reaction can lead to the formation of particles that contain silver, phosphorus and sulfur, which could migrate within the encapsulant. In another study, Meyer et al. [41] proposed the hypothesis that moisture diffusing through cell edges and micro-cracks could dissolve silver from fingers, which could diffuse into the encapsulant. They thought that a chemical reaction (probably triggered by phosphite) reduced the dissolved silver ions into metallic nano-particles displaying

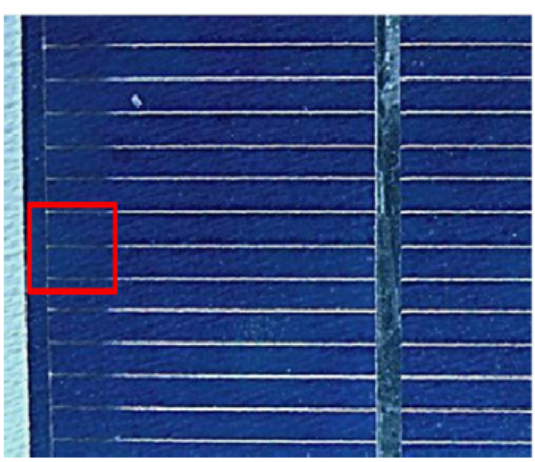

Figure 3.2: Discolored fingers at the left edge of a silicon cell [41].

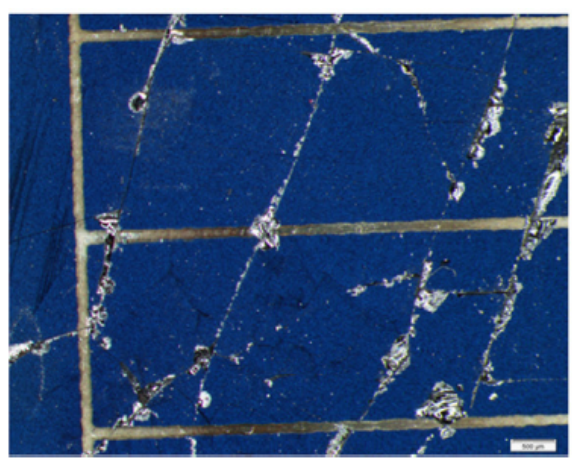

Figure 3.3: Random discoloration pattern of cell's surface after foil was removed [41].

brown color. This hypothesis was clarified by Peng et al. [42] even before Meyer et al. formulated it. They confirmed the Ag_2CO_3 nano-particles and explained that the brown color was because silver particles absorbed radiation.

Finally, Peng et al. added that "SiN films could act as secondary light trapping sites" and Meyer et al. [43] showed that polymeric films composition determines the predisposition of PV module's snail trails formation. Additionally, Liu, Huang, Lee, Yan and Lin [44] explained that EVA-encapsulant chemical additives and physical properties affect the discoloration processes of silver. Not only the encapsulant can affect the discoloration but the chemical binding with sulfur and/or phosphorus could lead to discoloration according to Richter, Werner and Hagendorf [45].

3.2.1.2 Cracks

Solar cells are so thin that cracks are very likely to occur. Severe cracks are visible to the naked eye, but thin cracks are not visible. Several studies have been carried out to investigate the patterns of cracks (origin and directions) and the growth. Fig. 3.4 shows the directions of the principal strains for cells within a PV module subjected to uniform mechanical load. Dendritic cracks have different orientations and are numerous within a cell and ± 45° cracks normally start at the busbar.

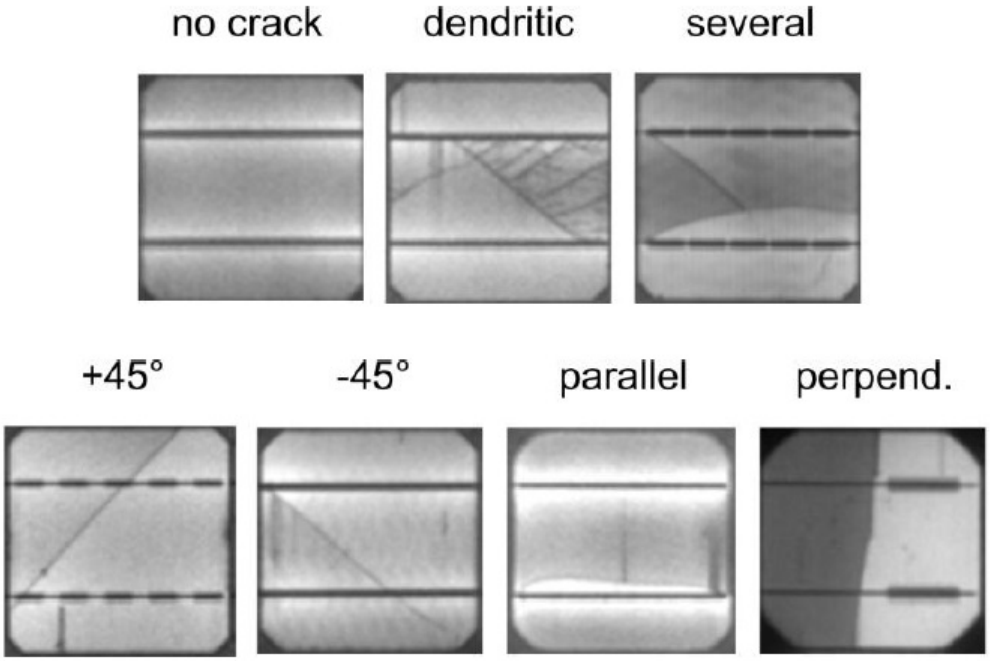

Figure 3.4: Direction of principal strain (black lines) on cells within a PV module subjected to uniform mechanical load [46].

Kajari-Schröder, Kunze, Eitner and Köntges [46] analyzed crack distributions in PV modules after being subjected to a uniform mechanical load. From a total universe of 27 PV modules (with 60 cells each), 41% of the cells were cracked. According to Kajari-Schröder et al., the most typical crack pattern is parallel to the busbars (50%) followed by diago-

nal cracks (20%), several directions (15%), dendritic cracks (14%) and perpendicular to the busbar (1%). From all these patterns, the ones resulting in highest separation cell area are parallel cracks (25% of separated area) and diagonal cracks (6.25% of separated area).

It is currently known, and expected, that mechanical and thermal stress induce cracks on cells within a PV module. Also, cracks can be the worsening of micro-cracks induced by poor manufacturing/handling or excess of stress in the soldering process. Schneller et al. [23] observed that stress over the busbar due to mismatch between the coefficient of thermal expansion (CTE) of silicon and copper lead to micro-cracks that ultimately lead to cell fracture due to mechanical and/or thermal stress from wind load and thermal cycling. Wendt, Träger, Mette, Pfennig and Jäckel [47] observed an increase number of interrupted (by busbars) silver fingers after thermal cycling. Additionally, Sander et al. [48] observed that PV modules exposed to thermal cycling and mechanical load mainly develop cracks at the beginning of the busbars and along them.

Finally, there is a certain correlation between snail trails and cracks; however, Köntges et al. [37] suggested that cracks are not the origin of snail tracks because cell edge can also be affected by snail tracks. They observed that "cell cracks in modules with framing turn into snail trails", but that did not happen to most of PV modules.

3.2.1.3 Hot-spots

The behavior of solar cells under partial shading or with a high amount of defects (such as process-induced defects, grown-in defects of material, or defects due to stress during operation) can be explained using an equivalent circuit of the solar cell. To successfully understand the equivalent circuit and the behavior of the solar cell under different circumstances, the operation of solar cells must be reviewed first. This review will cover the physics of the solar cell under illumination and dark conditions in combination with the relationship between these physical phenomena and the equivalent circuit. Hot-spots will be explained using the reviewed equivalent circuit.

Operation of a standard solar cell

The structure and the material used to fabricate solar cells was already reviewed in section 2.2.1. Based on this standard silicon solar cell structure, shown in Fig. 2.2, a scheme of the cross sectional area of the cell and all the possible places where light can be absorbed within the material is shown in Fig. 3.5. This scheme, which can be seen as a p-n junction, will be used to explain the physics of what is happening within the solar cell when the cell is under no bias, forward bias and reverse bias in dark and illuminated conditions.

Under dark conditions and with no bias applied, the junction between the n-type and p-type materials is a key region in the solar cell. Here, the attraction between the free charge carriers (free electrons and holes) is stronger than in any other region of the whole cell. Therefore, near the junction the free charge carriers recombine, annihilating themselves while forming the space charge region (SCR or depletion region). Although there are no

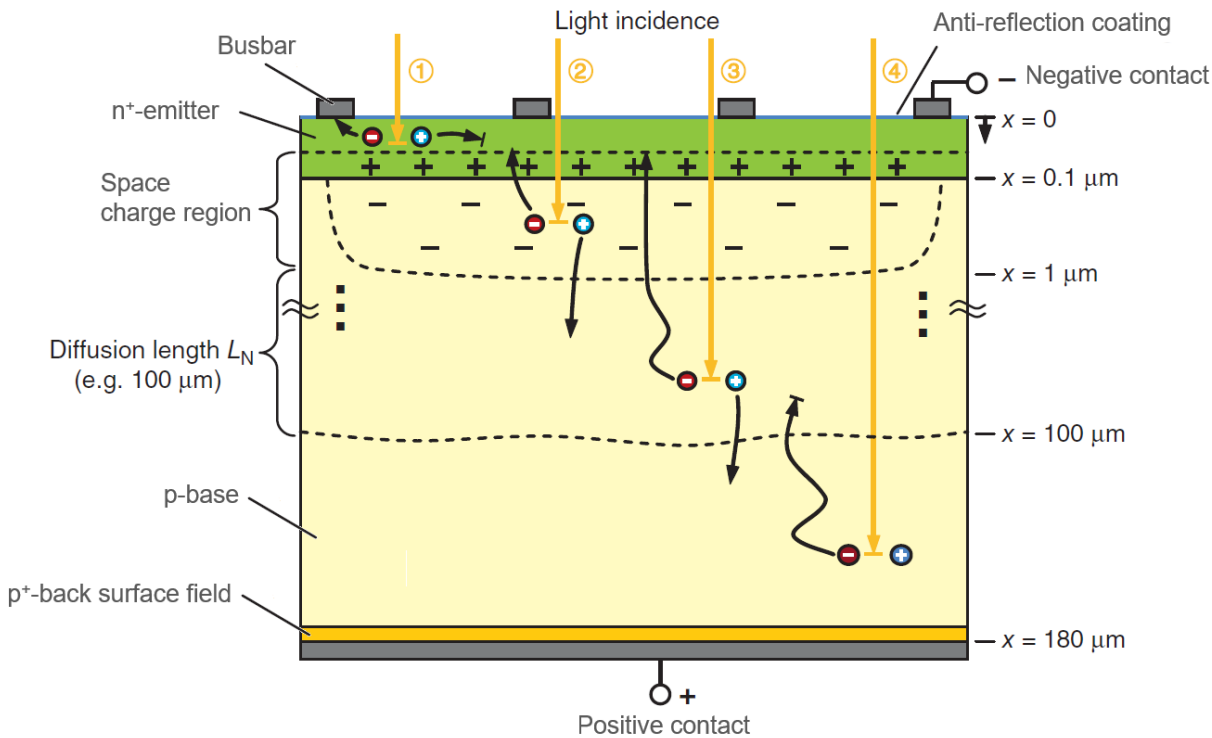

Figure 3.5: Scheme of the cross sectional area of a standard silicon solar cell. Adapted from [6].

free charge carriers in the SCR, the fixed nuclei from the dopant atoms are still present. Particularly in the SCR, these nuclei are positively ionized (due to loss of electrons) in the n^+-emitter and negatively ionized (due to the loss of holes) in the p-base. Therefore, these nuclei develops a field from n^+-emitter to the p-base. This field is almost zero at the edges of the SCR and has its maximum at the junction. This means that the field is almost negligible outside the SCR. The built-in potential is the integral of this field along the length of the SCR. Therefore, the built-in potential corresponds to the potential difference between the edges of the SCR.

At this point the cell develops two opposite currents: (1) the drift current and (2) the diffusion current. The drift current is the flow of free charge carriers due to the presence of the built-in potential. Therefore, the drift current flows from the n^+-emitter to the p-base. In contrast, the diffusion current, which is the flow of free charge carriers due to concentration differences, flows from the p-base to the n^+-emitter. Since there is no bias applied at the cell's terminal and there is no light, the opposite currents have equal magnitudes and the net current is zero. Furthermore, the net current is still zero even if the cell is circuit shorted. When the cell is shorted, there is no voltage drop between the cell's contacts. Therefore, there is not enough energy for the free charge carriers to reach the other side of the junction using the external circuit. Fig. 3.6(a) shows the dark characteristic of a p-n junction under no bias.

When a forward bias is applied under dark conditions, the built-in potential of the cell and the SCR region width is reduced. This happens because the electric field generated by

the external bias is in opposite direction to the electric field in the SCR. Since the field is lowered, the built-in potential is also reduced. Therefore, the drift current is also reduced and the diffuse current is exponentially increased depending on the external voltage magnitude as can be seen in Fig. 3.6(b). When the cell is reverse biased, on the contrary, the magnitude of the built-in potential and the width of the SCR region are increased. This results in the operation point shown by the dark characteristic of Fig. 3.6(c). In this case, the current is dominated by the enlarged electric field while the diffusion current is almost negligible. Although the drift current is dominant here, its magnitude is small.

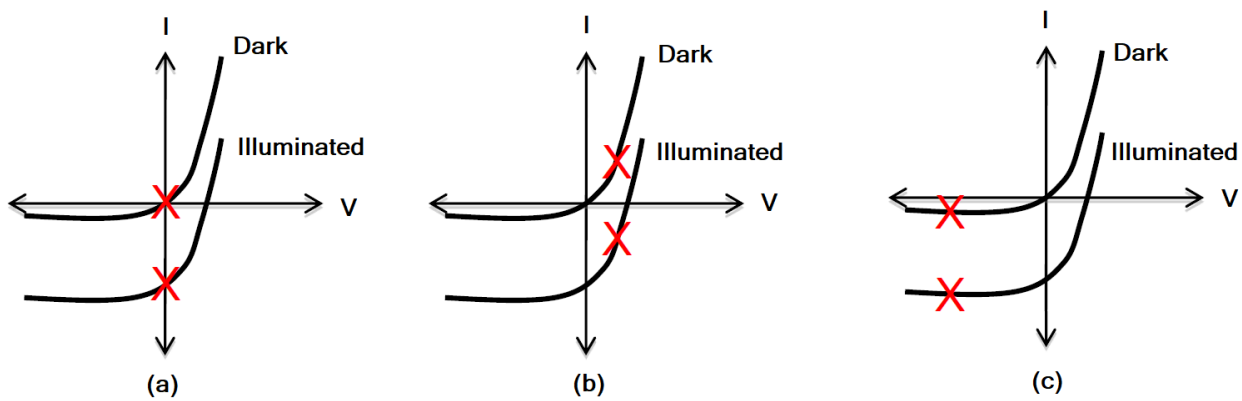

Figure 3.6: *I-V* curve of *p-n* junction under dark and illuminated conditions for the junction under (a) no bias, (b) forward bias and (c) reverse bias. Adapted from [49].

When the cell is illuminated, a new current develops within the device. This new current is called photo-current and depends on the power density of the light. In contrast to the dark current, the photo-current does not depend on the cell's voltage. Therefore, the illuminated characteristic of solar cell corresponds to the dark characteristic shifted on the current axis. This is shown in Fig. 3.6 for all the possible bias conditions. It is important to understand that the dark current not only flows in dark conditions but also in illuminated conditions. Furthermore, the dark current is in opposite direction to the photo-current. Hence, the total current that is delivered by the cell correspond to the sum of these two currents. Note that the dark current reduce the total current that the cell delivers to the load.

Classic and modified one-diode model for solar cells

Figure 3.7 shows the simplest equivalent circuit to model a real solar cell. The *current source* corresponds to the *photo-current* (I_{ph}) generated by the cell when light impacts on the cell's active surface. Note that is a current source not a voltage source, because the photo-current does not depend on cell's voltage. The *ideal diode* represents the *p-n* junction, which is basically the heart of the solar cell. The current flowing through this diode is called *diode current* (I_D). Through this diode flows the dark current in dark conditions —which also flows in illuminated conditions. The combination of the current source with the ideal diode represent the characteristic of an ideal solar cell. Real cells deviate from ideal cells due to two reasons:

1. the ohmic contacts and the inherent resistance from the silicon material induce a voltage

drop at the cell's terminal, which is represented by a *series resistance* (R_s),

2. and leakage current that flows through the edges of the cell and at small internal shorted paths, which is represented by a *shunt resistance* (R_{sh}).

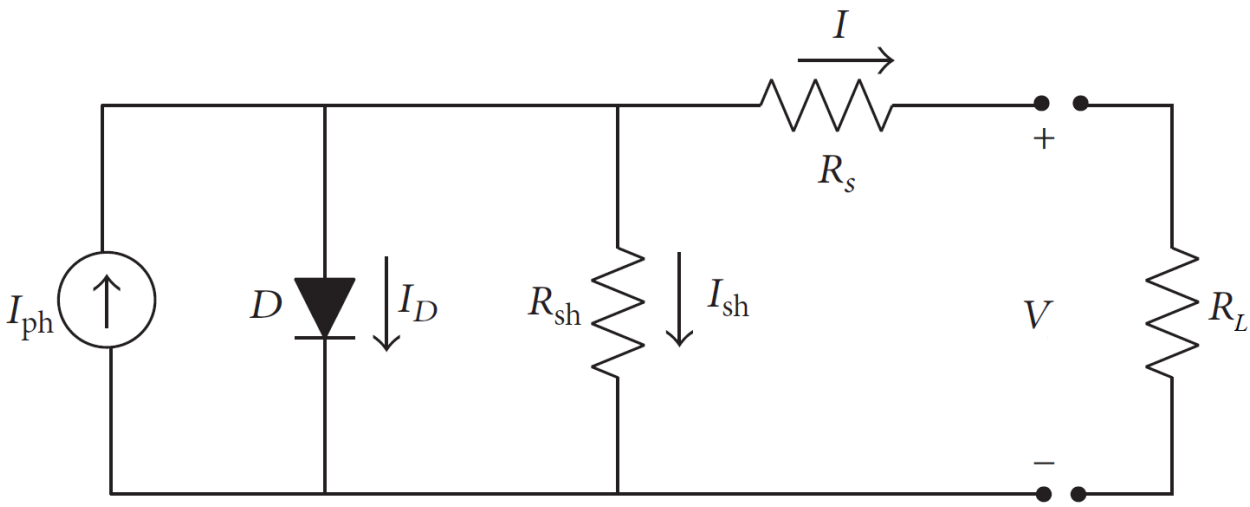

Figure 3.7: One diode model for solar cells. Adapted from [50].

Since there are many currents involved in the operation of real solar cells, it is important to use the right vocabulary when a current is addressed. The dark current, which was explained in the above paragraphs, not only flows through the ideal diode in Fig. 3.7 but also through the shunt resistance. Therefore, the total dark current consist in the ideal diode current plus the shunt current. Furthermore, the shunt current is also called leakage current, because this current represent the defects and dislocations where some of the cell's current is loss.

According to the equivalent circuit shown in Fig. 3.7, the current that will be delivered to the solar cell's load can be calculated as

$$I = I_{ph} - I_D - I_{sh} \tag{3.1}$$

The Shockley equation relates the voltage-current characteristic of a diode under dark conditions, which considering the voltage drop due to series resistance is expressed by [51, 52]

$$I_D = I_{sat} \cdot \left\{ \exp\left[\frac{q(V + I \cdot R_s)}{nkT}\right] - 1 \right\} \tag{3.2}$$

where I_{sat} is the reverse saturation current, q is the charge of an electron, k is the Boltzmann constant, T is the temperature (in K), and n is the diode ideality factor.

Regarding to the leakage current, this current can be calculated by the Kirchhoff's Voltage Law (KVL) in the last mesh and is given by

$$I_{sh} = \frac{V + I \cdot R_s}{R_{sh}} \tag{3.3}$$

This one-diode model is extensively use to study solar cells with low computer simulations resources. It is not very accurate but serves good for modelling the behavior of the cell in forward bias with low amount of defects and for typical environmental conditions. However, this model is not the best to explain hot-spots, partial shading or cell behavior under reverse bias condition. Hence, Bishop [52] introduced a new variable in the one-diode model to be able to explain certain behavior of solar cells. This new variable corresponds to $M(V_j)$ which is connected in series with the shunt resistance as shown in Fig. 3.8. $M(V_j)$ is a multiplication factor which basically represent a voltage controlled current source, because the shunt current is controlled by the voltage V_j.

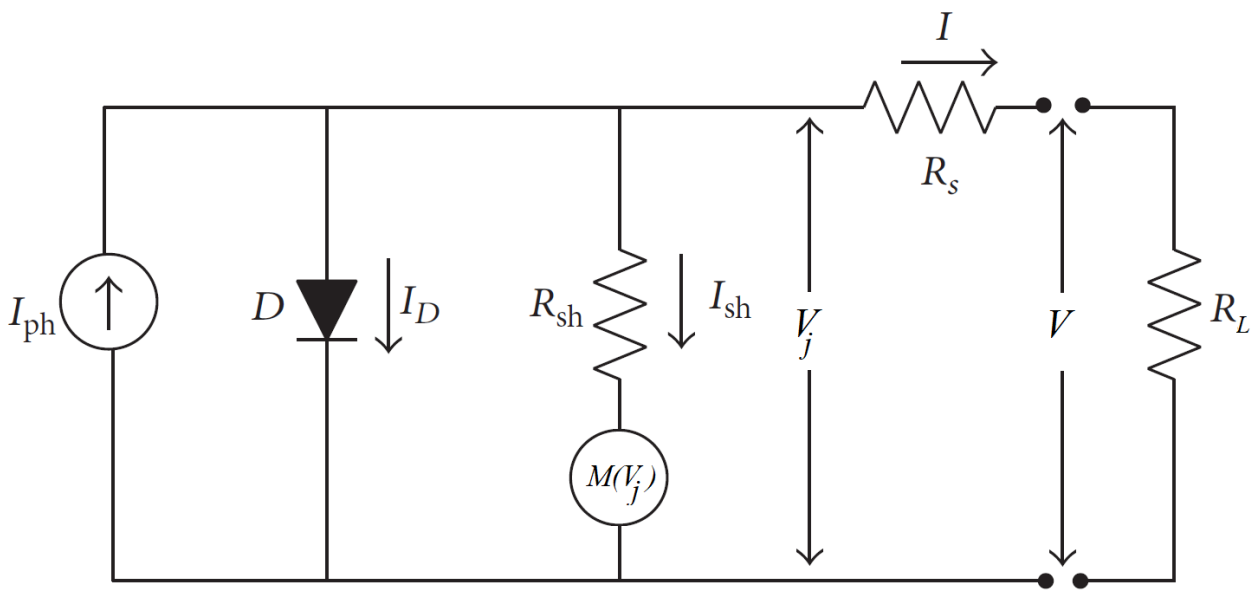

Figure 3.8: One diode model for solar cells adapted by Bishop [52] to simulate the effects of mismatches in photovoltaic cell interconnection.

The avalanche breakdown effect of the reverse characteristic of solar cells can be explained by the introduction of this non-linear multiplication factor, which is expressed as [52]

$$M(V_j) = 1 + a\left(1 - \frac{V_j}{V_{br}}\right)^{-m} \tag{3.4}$$

where V_j is the voltage across the junction, V_{br} is the junction breakdown voltage, a is the fraction of ohmic current involved in avalanche breakdown and m is the avalanche breakdown exponent.

Considering this new non-linear multiplication factor, the shunt current will be modelled as

$$I_{sh} = \frac{V + I \cdot R_s}{R_{sh}} \left\{ 1 + a \left(1 - \frac{V_j}{V_{br}} \right)^{-m} \right\} \tag{3.5}$$

Hence, the combination of equation 3.1, equation 3.2 and equation 3.5 gives

$$I = I_{ph} - I_{sat} \cdot \left\{ \exp \left[\frac{q(V + I \cdot R_s)}{nkT} \right] - 1 \right\} - \frac{V + I \cdot R_s}{R_{sh}} \left\{ 1 + a \left(1 - \frac{V_j}{V_{br}} \right)^{-m} \right\} \tag{3.6}$$

It can be seen that equation 3.6 requires iterative methods to be solved. However, Bishop [52] recognized that $V_j = V + I \cdot R_s$. Replacing this last expression into equation 3.6, the following expression is generated

$$I = I_{ph} - I_{sat} \cdot \left\{ \exp \left[\frac{q \cdot V_j}{nkT} \right] - 1 \right\} - \frac{V_j}{R_{sh}} \left\{ 1 + a \left(1 - \frac{V_j}{V_{br}} \right)^{-m} \right\} \tag{3.7}$$

which Bishop [52] used to calculate points of the I-V characteristic in two steps: (1) substitution of the value V_j into equation 3.7 to obtain the current I, and (2) evaluation of the cell terminal voltage as $V = V_j - I \cdot R_s$. To calculate a cell I-V characteristic, V_j is initially set equal to V_{br} and incremented by small amount δV_j. Equation 3.7 and $V = V_j - I \cdot R_s$ are then evaluated, and V_j is incremented again. V_j must sweep from left to right until terminating conditions are satisfied. According to Bishop [52], the number of points required to represent an I-V curve is minimized by making δV_j inversely proportional to the curvature $\mathrm{d}^2 I / \mathrm{d}V^2$.

Figure 3.9 shows the I-V curve of a cell, which is produced by Bishop [52] with the parameters shown in the same figure. It should be noted that the Y axis shows the current density in mA/cm^2 and the amount of points to simulate the knee of the curve is higher than for any other region of the curve. It can be seen that the curve, in Fig. 3.9 contain 3 regions that are easily distinguishable. At the right, there is a rapid increase of the dark current which rapidly overcomes the photo-current. At the left, the rapid increase is due to avalanche current while at the middle, where is little variation, the current is almost the same along a wide range of voltage. In the middle, the behavior is determined by the shunt resistance. For high shunt resistances, the slope is small and the curve is very flat. However, small shunt resistances will increase the slope increasing the reverse current.

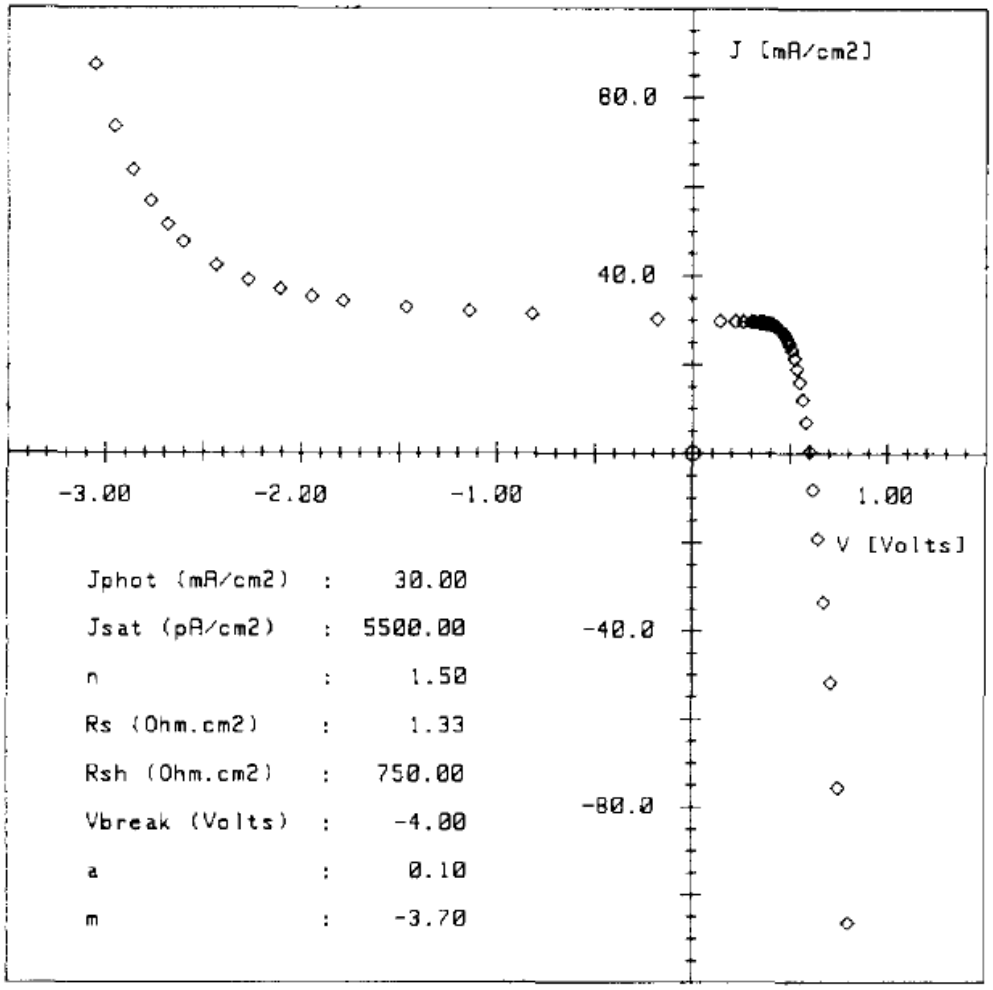

Figure 3.9: Cell *I-V* curve produced by Bishop [52] using the equivalent circuit in Fig. 3.8.

Hot-spot phenomenon

According to IEC 61215 [53], "hot-spot heating occurs in a module when its operating current exceeds the reduced short-circuit current of a shadowed or faulty cell or group of cells within it. When such a condition occurs, the affected cell or group of cells is forced into reverse bias and must dissipate power, which can cause overheating". When a cell within a string is shaded or faulty, the maximum power dissipation depends on (1) the string operating point (see Fig 3.10), (2) degree of mismatch and (3) cell reverse characteristic. How a cell can be reverse biased by its neighbouring cells can be explained either by the equivalent circuit shown in Fig. 3.7 or Fig. 3.8. However, the classical one-diode model cannot explain the high magnitude of the current of a shaded/faulty cell in reverse bias. Hence, it cannot explain its high power dissipation.

Figure 3.10 shows the operating point of each of the ten cells operating in a short-circuited series string. The cells that have a short-circuit current lower than the short-circuit current of the string are reverse biased. Furthermore, Fig. 3.11 shows the resulting characteristic of the same string with one cell grossly mismatched. It can be seen that the mismatched

cell is operating in reverse bias at the same current of the whole string. The other nine cells are operating in forward bias, at their maximum power point. The resulting characteristic, which is the string characteristic, is operating at short-circuit conditions and its maximum power point is lowered. In this situation, the mismatched cell is seen as a load by the other healthy nine cells. Therefore, all other nine cells are working together at their maximum power point, dissipating all their power on the mismatched cell.

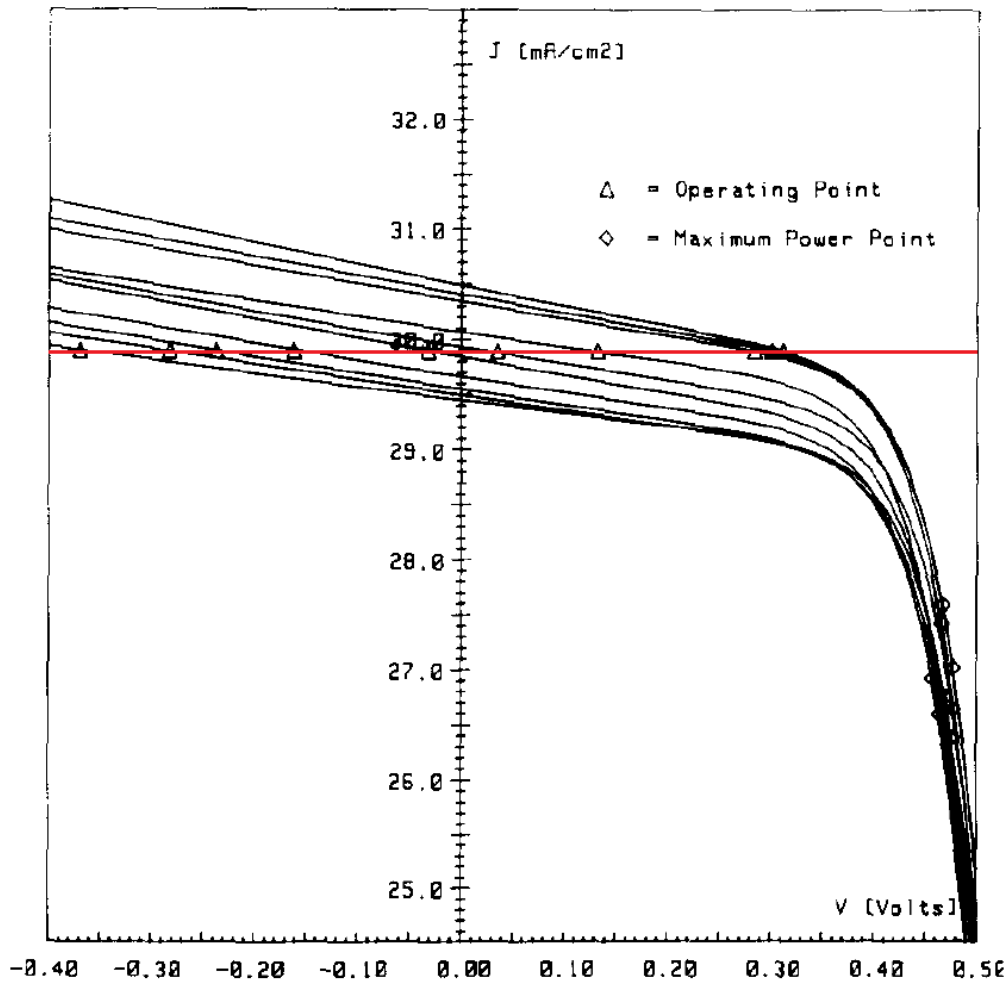

Figure 3.10: Cell operating points in a short-circuited series string (of ten cells) [52].

The situation described in Fig. 3.11 can be seen into more detail using the modified equivalent circuit of Bishop. Consider only two cells connected in series, both exposed at the same irradiation as shown in Fig. 3.12. When both cells are irradiated by the same light, they deliver the current $I = I_{ph_1} - I_{D_1} - I_{sh_1} = I_{ph_2} - I_{D_2} - I_{sh_2}$, which is defined by the load. This current flows through the load, thus there is a voltage drop across the load. Considering that the system is grounded at the bottom and that the load is chosen so the cells are operating at their maximum power point, the voltage at point B is 0.5 V while the voltage at point A is 1.0 V. Therefore, both cells are operating in forward bias condition with a voltage of 0.5 V each.

When the cell at the bottom of Fig. 3.12 is totally shaded, the situation changes to the one shown in Fig. 3.13. In this situation, the shaded cell cannot generate an output current.

Therefore, the current through the load is zero. Now, considering the ground of the system at the bottom, the voltage at point A is 0 V, because there is no voltage drop at the resistive load. Since the cell at the top is generating current due to the irradiation, it is still operating in forward condition. Hence, the voltage at point B is -0.5 V. This means that the shaded cell is reverse biased, which means that the dark current changed its flowing direction. The current $I = I_{ph_1} - I_{D_1} - I_{sh_1}$ is dissipated by the shaded cell, which is consuming a current $I = I_{D_2} + I_{sh_2} = -(I_{ph_1} - I_{D_1} - I_{sh_1})$.

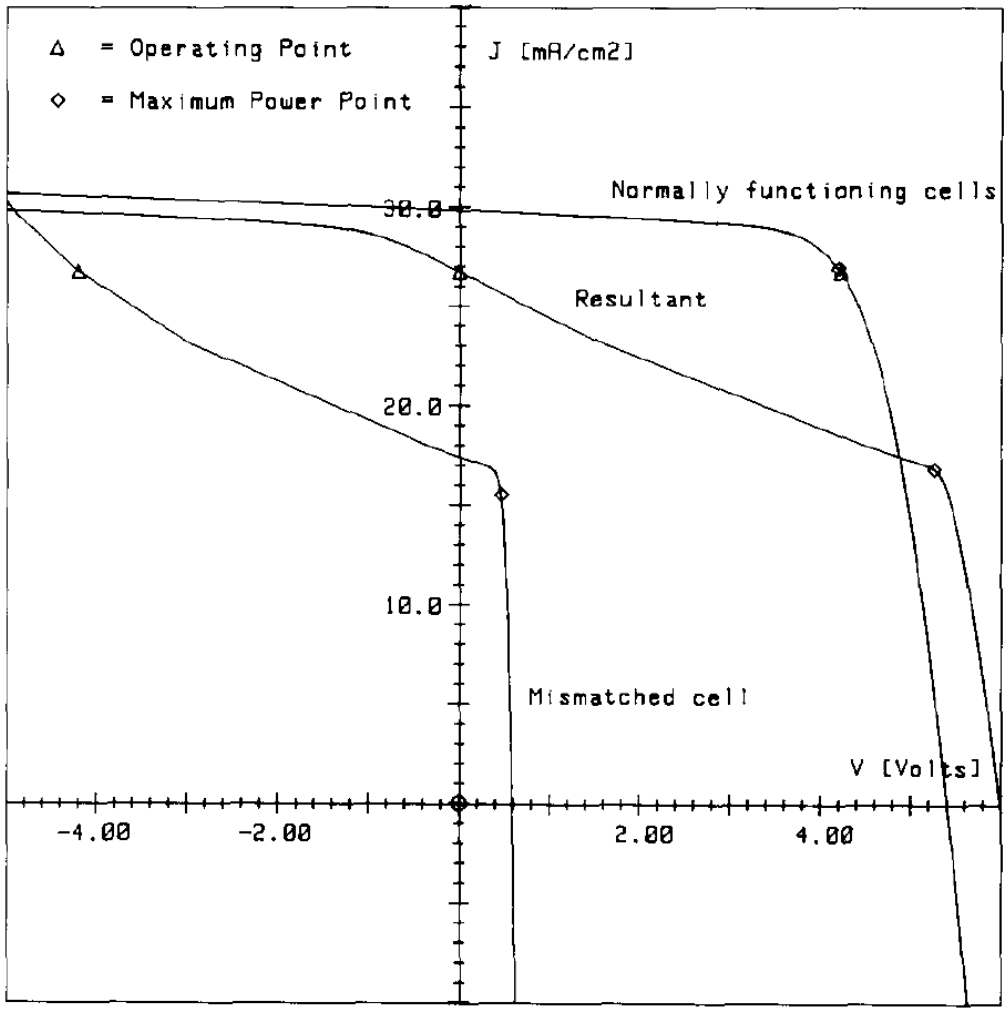

Figure 3.11: Resultant curve of the simulation of a shadowed cell within a short-circuited string of ten cells [52].

The situation described in Fig. 3.12 and Fig. 3.13 only considers two cells connected in series, but solar cells in commercial PV modules are connected in series in bigger strings. PV modules with 72 solar cells typically use 4 bypass diodes, where each bypass diode is connected in parallel to a string of 18 cells connected in series. In the case of PV modules with 60 solar cells, they use 3 bypass diodes with a string of 20 solar cells in series connected in parallel to each bypass diode. If we consider the situation shown in Fig. 3.13 with 20 cells connected in series where one cell is totally shaded, the shaded cell will be reverse biased with a voltage of $19 \times 0.5 = 9.5$ V. Now depends on the reverse characteristic of the shaded cell

how high will be the current dissipated. Depending on the shunt resistance and the avalanche breakdown voltage, the reverse dissipated current can be dominated by the leakage current or the avalanche current.

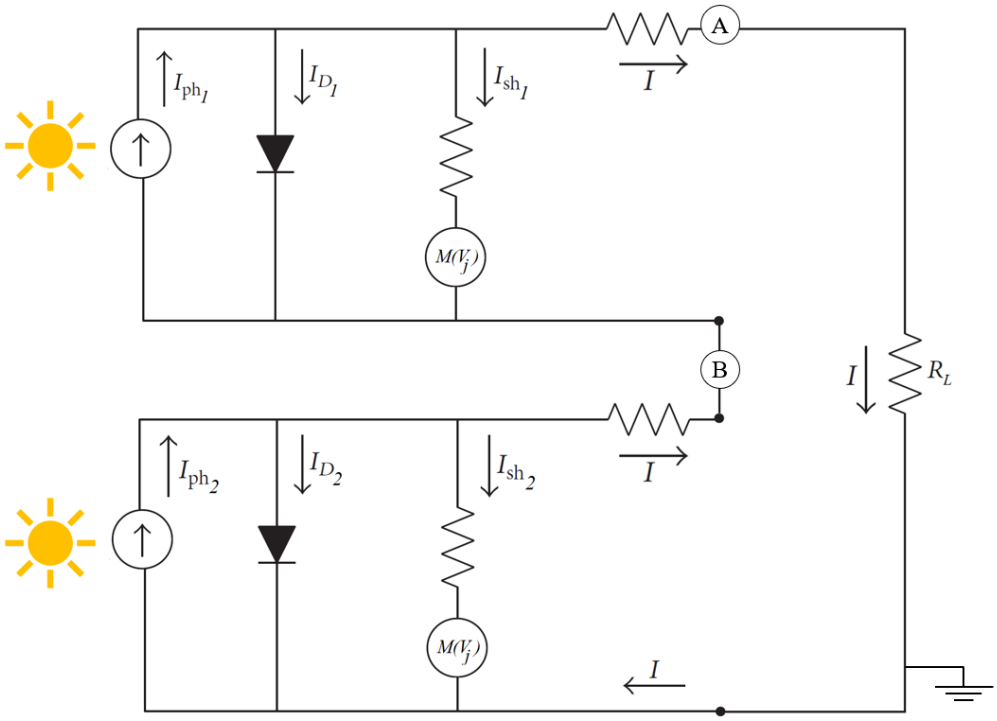

Figure 3.12: Two cells connected in series, exposed at the same irradiation, both connected in parallel to a resistive load.

It can be seen, in Fig. 3.9, that the avalanche current is severely more detrimental to the shaded solar cell than the leakage current. According to Lim, Min, Jung, Jae Ahn and Hyung Ahn [54], the reverse characteristic of mono-Si solar cell and multi-Si solar cell is different. Their reverse characteristic is shown in Fig. 3.14. It is clear that c-Si solar cells must be under high reverse bias to generate avalanche current compared to multi-Si solar cells. Hence, when mono-Si and multi-Si PV modules are manufactured with the same amount of cells and bypass diodes, multi-Si PV modules are more prone to develop hot-spot than mono-Si PV modules.

Independently of the type of the cell (mono-Si or multi-Si), the diode current and the leakage (shunt) current can be detrimental without the avalanche effect. In the last decade, Breitenstein, Rakotoniaina, Al Rifai and Werner [55] have been investigating '*shunts*' in crystalline silicon solar cells by means of lock-in thermography (LIT)[1]. They indicate that in the traditional interpretation of I-V characteristic of solar cells all non-linear (or diode-like) currents are attributed to the cell, and only linear (ohmic) currents paths are attributed to shunts. However, they discovered by means of LIT that not only *ohmic shunts* exist but also *diode-like shunts*. To understand the origin of linear and non-linear shunts, it is necessary to use a more detailed equivalent circuit than the one-diode model.

[1]Lock-in thermography means that the heat in an extended sample is generated periodically and the lock-in correlation process is applied to the temperature signal of each pixel of an image of the surface of the sample under investigation [56]

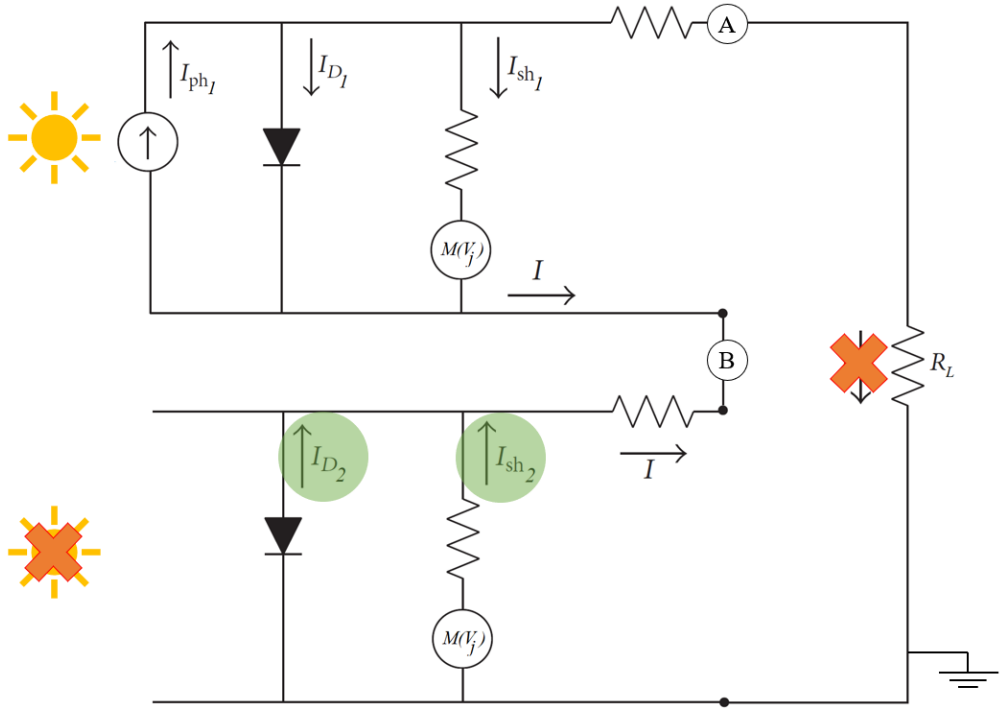

Figure 3.13: Two cells connected in series, one exposed to light and the other totally shaded, both connected in parallel to a resistive load.

The one-diode model is a simplification of the classical two-diode model. The diode current of the one-diode model is explained in more detail with two diodes in the two-diode model. Therefore, in the latter model, the dark current flows through the first diode, second diode and shunt resistance. The current flowing trough the first diode is the so-called *diffusion current*, while the *recombination current* flows trough the second diode. The current trough the shunt resistance is also called leakage or shunt current. According to Izadian [51] and Breitenstein [57], the diffusion current is due to recombination in the base and the emitter (including their surfaces) while the recombination current is due to recombination in the depletion region (or SCR).

Experts in the field of shunts use the term 'shunt' for any position in solar cell showing a dark-current contribution additional to the diffusion current under forward or reverse bias [56]. This means that a site within the cell that exclusively increase the diffusion current is not considered a shunt. In contrast, a site that increase the leakage or the recombination current it is.

According to Breitenstein et al. [58], ohmic shunts are due to incomplete edge insulation, cracks, *Al* contamination of the emitter, and/or material-induced defects. Somasundaran and Gupta [59] explain that ohmic shunts increase the leakage current. Therefore, linear shunts can be detected at reverse bias. Since the leakage current at reverse bias should be small, high currents indicate the presence of ohmic shunts. In the other hand, Breitenstein, Warta and Lagenkamp [56] and Breitenstein et al. [55] explain that non-linear shunts are due to localized sites with high recombination rate, which increase the recombination current. Since recombination current dominates the diffusion current in high forward bias, the diode-like shunts can be observed at high forward bias (beyond 0.6 V).

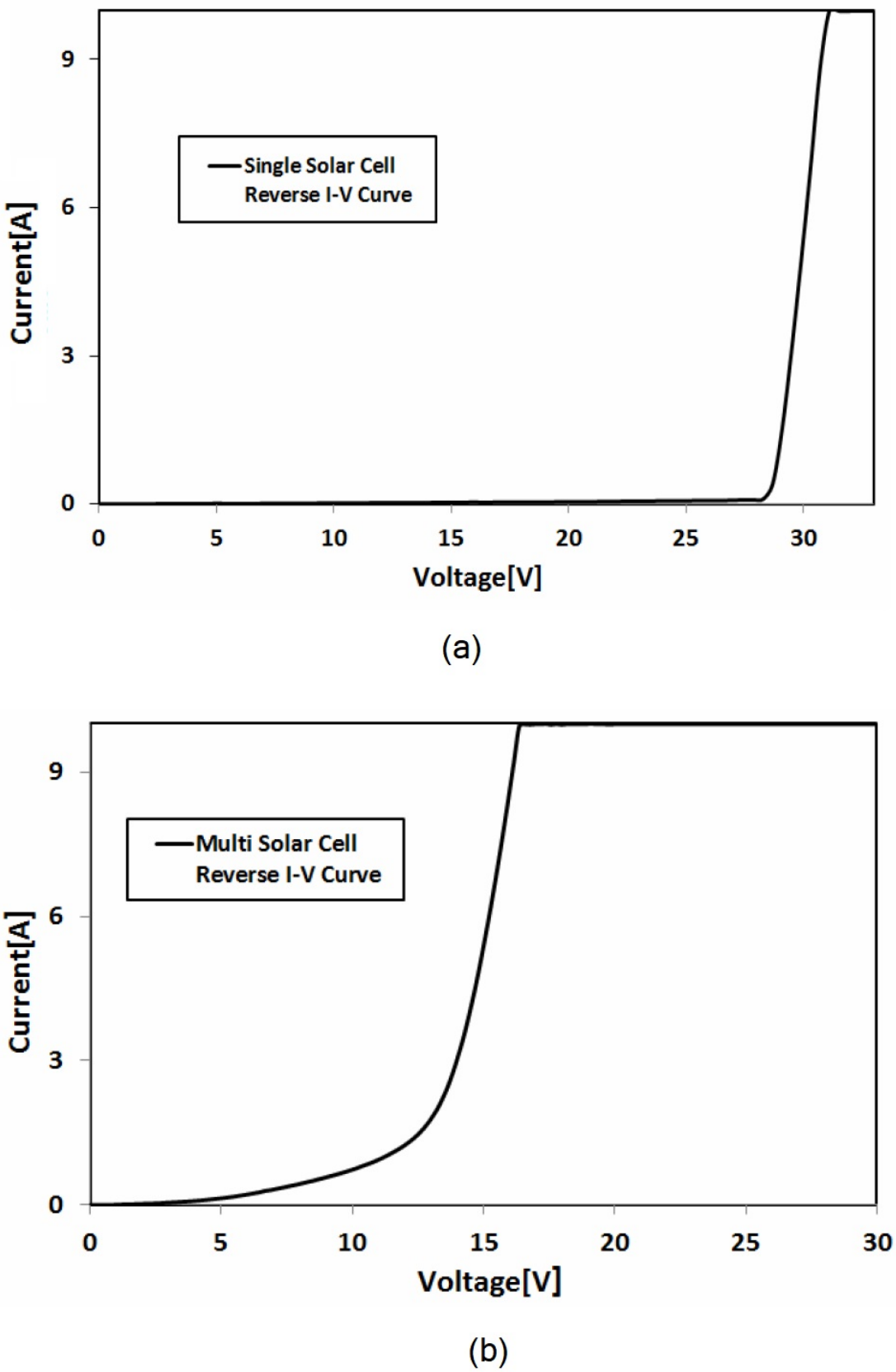

Figure 3.14: Reverse I-V curve of (a) crystalline silicon solar cell and (b) multi crystalline solar cell [54].

According to Breitenstein et al. [55], nine types of shunts have been found for mono-Si and multi-Si solar cells. Six of them are process-induced while the other three are material-induced. They state that the most important process-induced shunts are "residues of the emitter at the edge of the cell, cracks, recombination sites at the cell edge, Schottky-types below grid-lines, scratches, and aluminum particles at the surface". They also indicate that material-induced defects are strong recombination sites, inclusions of grown-in macroscopic Si_3N_4 and inversion layers caused by microscopic SiC precipitates on grain boundaries.

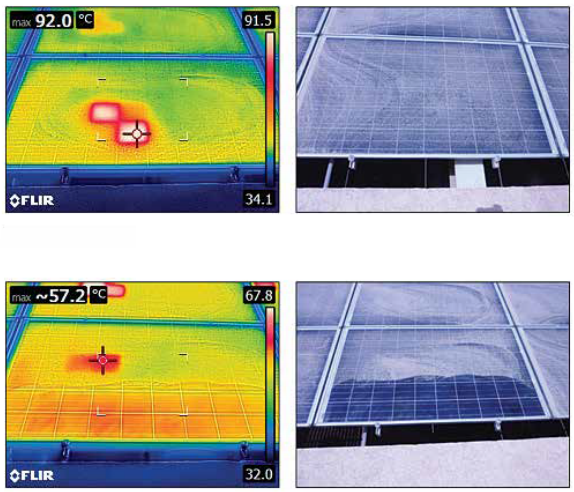

Figure 3.15: Thermal-image of a soiled PV module before (above) and after (below) cleaning the glass [60].

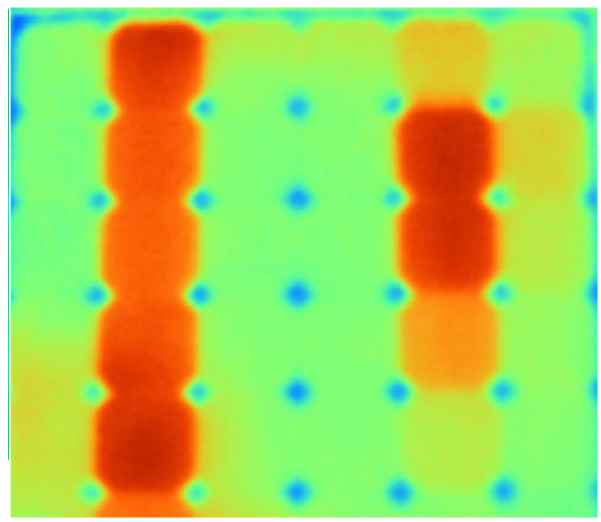

Figure 3.16: Thermal-image showing hot cells on an entire string [61].

hot-spots can be easily seen by thermal-images using regular thermography. Therefore, an IR-camera is suitable to investigate the thermal irradiation of solar panels operating under sunlight conditions. Fig. 3.15 and Fig. 3.16 shows two examples of hot cells. In the case of Fig. 3.15, the thermal and visual-image of a soiled (shaded) PV module before and after cleaning part of the glass is shown. It can be seen that the hot cell appearing when the module is totally soiled (Fig. 3.15 above) disappears when the string is cleaned (Fig. 3.15 below). This means there is a mismatch between this cell and the rest of the string at low voltage, which are triggered at high soiling (shading). In the other hand, Fig. 3.16 shows several cells operating at high temperatures in two strings.

To make a qualitative assessment of thermal abnormalities in PV modules, it is possible to search typical thermal patterns that PV modules presents. These typical patterns are the result of extensive studies in the past decades. Fig. 3.17 and Fig. 3.18 shows two examples of typical abnormalities of strings within PV modules. The first is a shorted string while the second is an open string. Since the shorted string can release the generated energy, the different temperatures of the cells are due to current mismatch. In contrast, an open-circuit string cannot release the generated energy and heat up homogeneously. Appendix G contain a matrix with typical thermal abnormalities of c-Si PV modules.

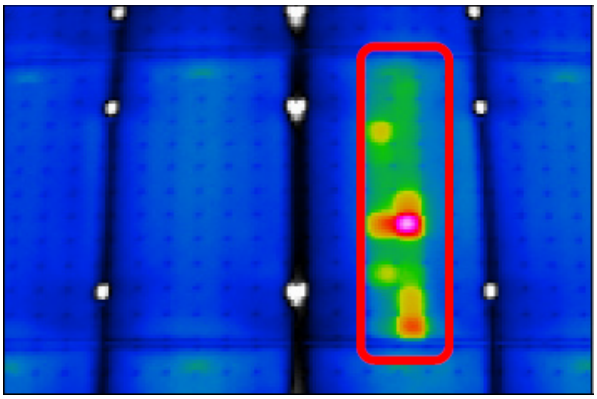

Figure 3.17: Shorted string at the middle [62].

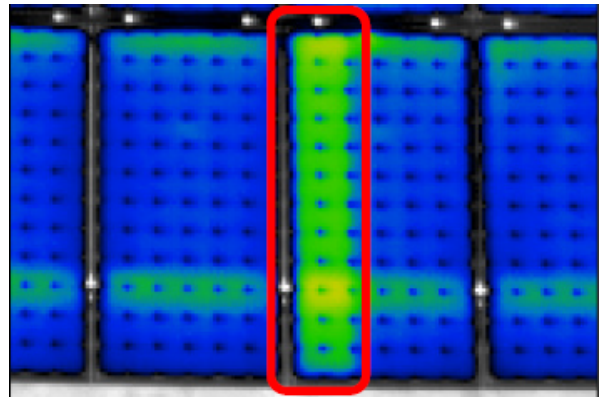

Figure 3.18: Open string at the left [62].

3.2.2 Metallization

Solder joint failure/fatigue

From section 2.2.2 it can be seen that in the solder bond there are several layers of different materials interacting with each other, whether it is a bond between two ribbon strips or a bond between a ribbon strip and the silver busbar of the solar cell. Among these different layers, several interfaces that can undergo into failure due to different reasons can be found.

Jeong, Park and Han [63] studied the solder interconnection failure of a 25-years-old c-Si PV module with 23% of efficiency. Fig. 3.19 shows their most important findings, where (a) shows the interfaces that are relevant. At the upper ribbon wire, they found cracks between ribbon wire solder and Ag paste (b). At the bottom ribbon wire, they found solder/solder cracks (c) and solder-Ag paste cracks (d). Table 3.2 summarizes the causes for each failure mode that the joint underwent in their study.

Table 3.2: Failure modes and its causes [63].

Failure mode	**Causes**
Crack and void between ribbon wire and Ag paste	Thermal fatigue, over soldering, thermal shock by current.
Corrosion between ribbon wire and Ag paste	Moisture
Ribbon wire delamination	Thermal fatigue, weak soldering
Ribbon wire burnout	Over-current

Present literature concerning joint bond fatigue agrees with CTE mismatch being the most typical cause of failure. According to Yedidi [30], solder bond fatigue is due to thermal expansion and contraction, poor quality of solder bond process, flexing due to wind loading

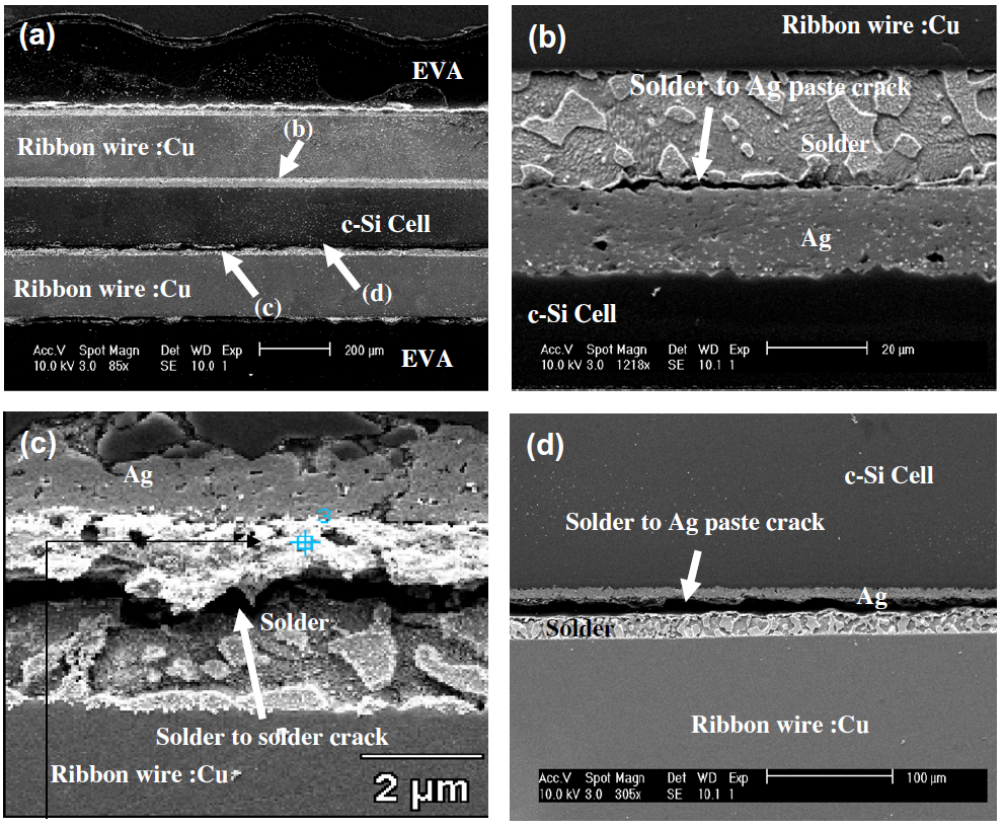

Figure 3.19: (a) X-section view of test module, (b) Top ribbon wire solder interconnection: Solder to Ag crack, (c) Bottom ribbon wire solder interconnection: Solder to solder crack and (d) Bottom ribbon wire solder interconnection: Solder to Ag crack [63].

and vibration due to packing or transportation. Köntges et al. [64] explained that high intense deformation of the solder mechanically weakens the cell interconnect ribbon. They also described that narrow distance between cells promotes cell interconnect ribbon failure and hot-spot by partial cell shading during long-term operation also weakens the solder. Furthermore, Kraemer, Seib, Peter and Wiese [65] explained that stress gradients appear along the silicon thickness and the most biggest gradients can be found at the edge of the front side busbar and at the edge of the outermost back contact area (where cracks are often found).

Thermal and mechanical stress are not the only reasons for joint solder separation. Itoh et al. [66] explained that the interconnection could be separated due to silver or copper leaching because metals are easily dissolved into solder. They observed Ag leaching "forms Ag_3Sn compound with rigid and brittle character".

The solder can also melt or undergo corrosion. Kuitche, TamizhMani and Pan [67] studied field inspection data of PV modules deployed in Arizona. They found that cyclic temperature stresses or vibration, thermal and mechanical stress and corrosion can lead to solder into melting. This melting can create an open-circuit or increase the series resistance of the metallization. In the first case the open-circuit can develop into a DC arc on a sunny day (see Fig. 3.20) and in the second case the high resistance can dissipate too much energy creating a hot-spot (see Fig. 3.21).

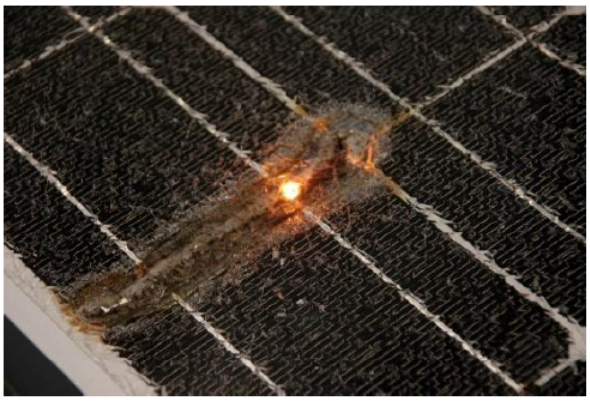

Figure 3.20: DC arcing at the cell interconnect ribbons [32].

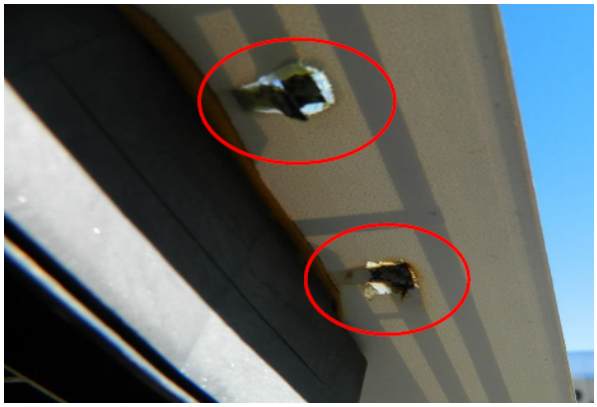

Figure 3.21: String interconnect ribbon breakage and severe hot-spot [31].

Kuitche et al. [67] also found that high levels of moisture, and temperature in combination with humidity and cyclic temperature can lead to solder joint discoloration and/or corrosion as shown in Fig. 3.22 and Fig. 3.23. Additionally, Schneller et al. [23] and Köntges et al. [2] indicated that acetic acid formation (not desirable product from EVA) can act as a catalyst in the corrosion of metallization.

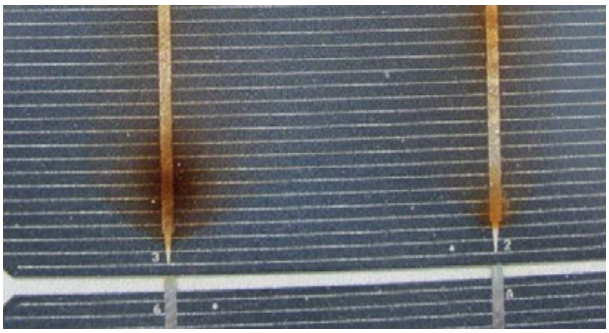

Figure 3.22: Discolored ribbon onto the cell's busbars [68].

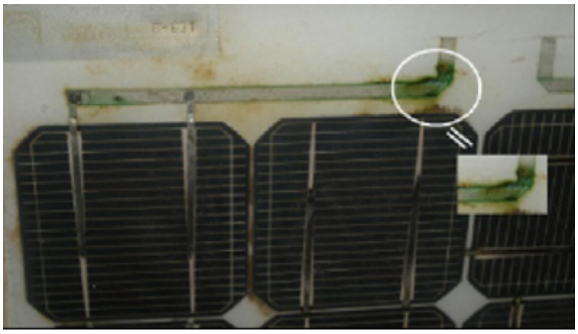

Figure 3.23: Corrosion of metallic contact [69].

3.2.3 EVA encapsulant

3.2.3.1 Discoloration (browning or yellowing)

Discoloration of EVA is a failure mode that can be observed with the naked eye. PV modules show yellowish or brownish discoloration over their service time due to environmental conditions stresses. According to Köntges et al. [2], discoloration has a direct impact in the decrease of shot-circuited current. Fig. 3.24 and Fig. 3.25 show two cases of heavy discoloration (brown color) of c-Si PV modules that are not related.

The literature for the discoloration of EVA is rich and several studies have been carried out since 1990. There are several causes that leads to discoloration of EVA. However, according

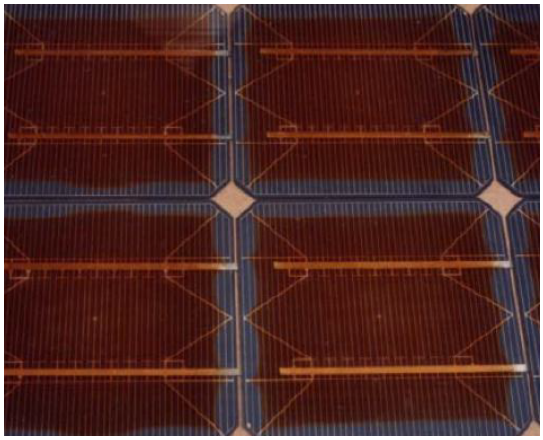

Figure 3.24: Browning (discoloration) EVA over solar cells [70].

Figure 3.25: Browning (discoloration) EVA of an entire PV module with pattern [17].

to Kuitche et al. [27], no matter what causes the discoloration of the encapsulant, the mechanism involves photo-thermal degradation reactions and thermal degradation reactions. This means that the main factor of discoloration is heat but photo-thermal degradation is more aggressive than thermal degradation.

Pern and Czanderna [71] explained that high temperatures degrade the UV absorber and the EVA gets more cross-linked (thermal degradation). As a result, EVA absorbs more UV-light than expected. According to them, UV-light absorption leads to the formation of chromophores and acetic acid. Additionally, the degradation of the UV-absorber is gradually worsened by photo-oxidation.

Just the heat is capable of discoloring EVA, but it will take too many years to turn the polymer into yellow or brown. Acetic acid catalyzes EVA degradation in the presence of heat and the rate of discoloration is heavily increased. According to Pern and Czanderna [71], the presence of the UV-absorber and the antioxidants reduces the rate of acetic acid. However, the acid can deactivate antioxidants and considering the UV-absorber thermal degradation the situation gets worse. In the other hand, chromophores are UV-excitable and they can increase the amount of UV-absorption as explained in a later study of Czaderna and Pern [72].

In a further study, Pern [73] showed that the UV-absorber concentration in a UV-exposed PV module decreases from the edges towards the centre of the solar cells leading to discoloration patterns such as the ones in Fig. 3.24 and Fig. 3.25. However, Köntges et al. [2] explained that the diffusion of oxygen leads to an in-homogeneous concentration of UV-absorber. Therefore, Köntges assumed that oxygen diffusion can help to preserve the UV-absorber concentration in the presence of Hindered Amine Light Stabilizers (HALS). The schematic shown in Fig. 3.26 explain the assumptions of Köntges.

The first three blocks in Fig. 3.26 show that residual peroxides (and other products) from partially cured EVA could further react with UV-light during the service lifetime of the PV module. This is just another mechanism to generate chromophores. Fourth and fifth blocks to the right indicate that if oxygen does not diffuse (typical for glass/glass modules), HALS

and UV-absorber are photo-depleted and chromophores absorb a lot of radiation increasing the rate of yellowing. In contrast the block at the left indicates that if oxygen diffuses, HALS protects the UV-absorber and yellowing can only be achieved by photo-bleaching (expected degradation mechanism for service lifetime of a PV module).

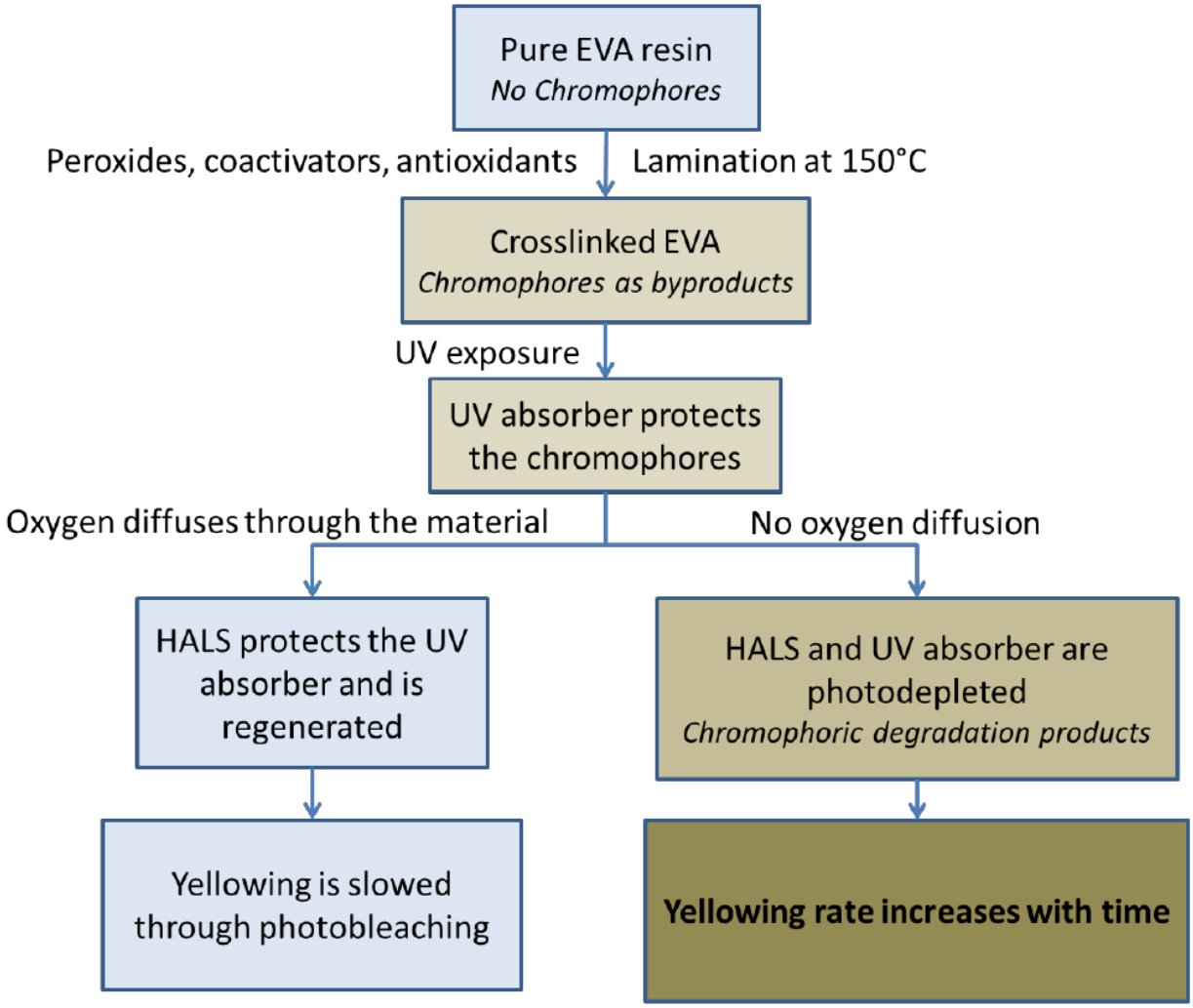

Figure 3.26: Schematic diagram of degradation pathways of the yellowing process in an EVA-encapsulated PV module [2].

3.2.3.2 Delamination

Here, delamination is referred as the loss of adhesion between two different materials. This means that delamination can only occur at interfaces. Moreover, the important interfaces are EVA/glass, EVA/cell and EVA/backsheet. According to Shioda [74], delamination usually occurs in the vicinity of interconnections on cells (see Fig. 3.27) and the outer portions in a plane of the PV module. Other examples of EVA delamination are shown in Fig. 3.28 and Fig. 3.29.

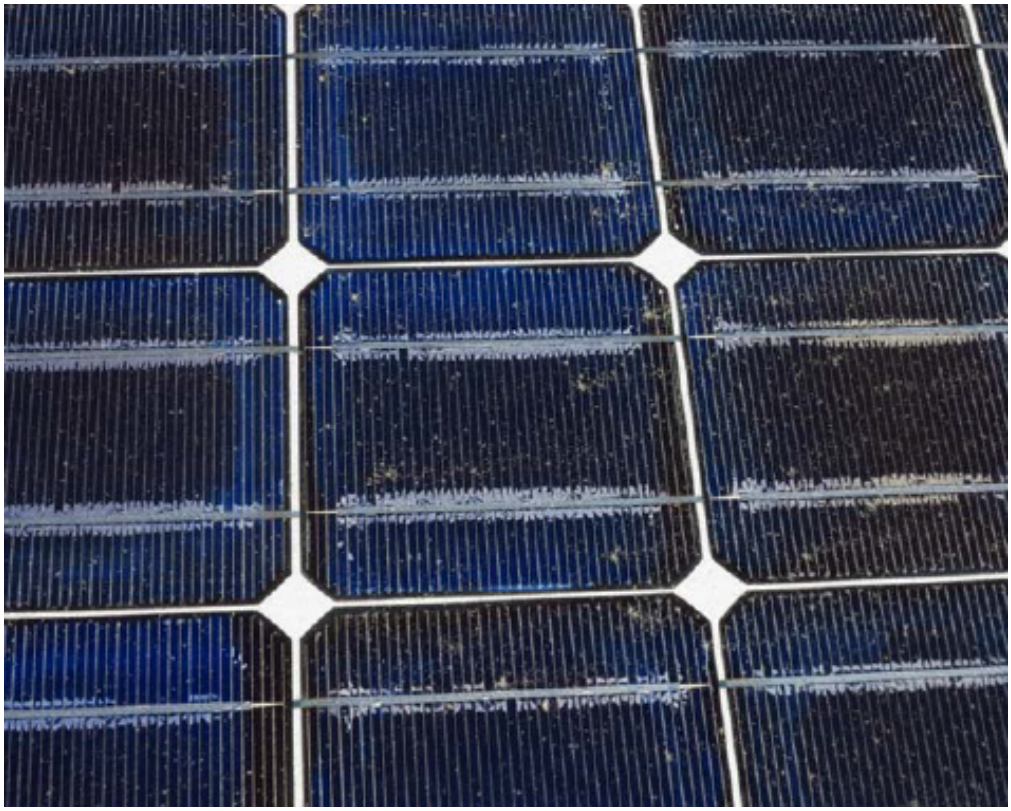

Figure 3.27: Delamination of EVA near the interconnections on cells [75].

Novoa, Miller and Dauskardt [76] explained that "encapsulation debonding occurs when the strain energy release rate, $G\ Jm^{-2}$, or debond driving force, is equal to the critical debond energy (adhesion) at the encapsulation interface, G_c". However, in the presence of chemical species and/or light (active environments) debonding can occur even if $G < G_c$ because the environment affects the kinetic processes of the EVA.

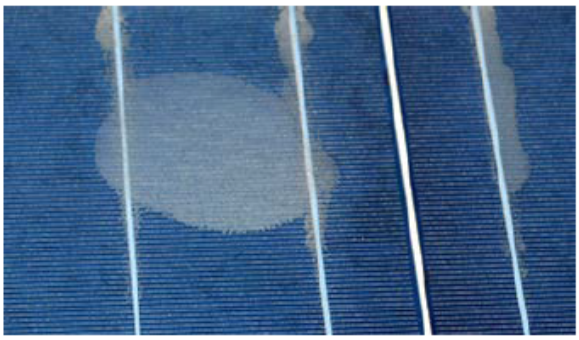

Figure 3.28: Example of EVA delamination of a PV module operating in warm and humid climate [39].

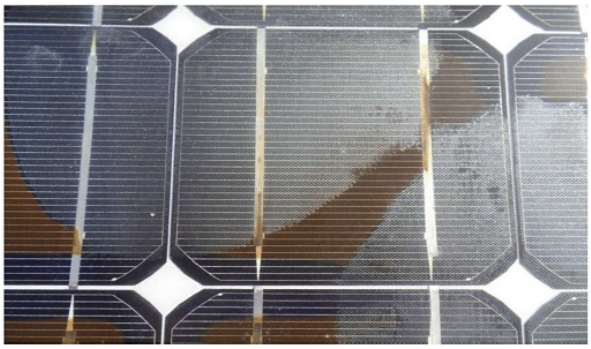

Figure 3.29: Example of excessive delamination over the surface's cell [77].

In the case of passive environments, Köntges et al. [64] explained that delamination is more likely to happen at EVA/cell interface than EVA/glass interface because initially the adhesion strength is more limited at the EVA/cell interface. Köntges also indicated that excess of EVA (due to uncontrolled lamination) could cause significant tensile stress at the

edges of the module. Additionally, he explained that glass is not perfectly flat and the texture can also add mechanical stress leading to delamination.

In the case of active environments, factors such as temperature (or heat), radiation, moisture and chemical reactions are the most relevant for EVA delamination. In other study, Köntges et al. [2] described how these factors affect EVA. According to Köntges, the decomposition of UV absorbers (due to UV-light) forms benzoic acid which catalyses and accelerates the debonding of EVA/glass interface. Furthermore, Köntges et al. [2] and Novoa et al. [76] explained that the adhesive energy G_c of EVA/glass interface decays with the temperature and also with the ambient moisture (because EVA is permeable to vapour diffusion). Fig. 3.30 shows how much the debond energy G_c of a module decreased (97%) in 10 years of field exposure.

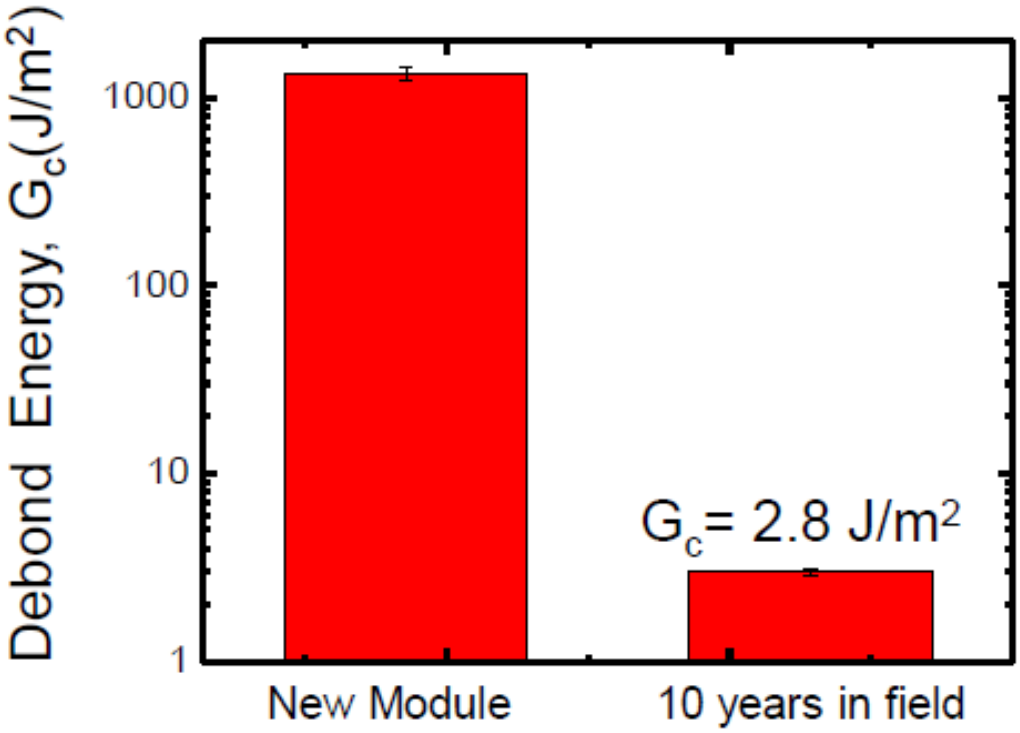

Figure 3.30: Debond energy G_c comparison between a new module and a 10-years-aged module [78].

Relative to chemical reactions as other factor of active environment, Shioda [74] observed that the component $TiOx$, which is deposited as an AR coating on the surface's cell, led to chemical adhesion weakening that induce delamination. Fig. 3.31 shows an example of fracture between EVA and $TiOx$ by means of SEM (scanning electron microscope). In the other hand, Dhere and Pandit [79] observed the impurity concentration of some species in acceleration-tested modules, which are modules tested in chambers with accelerated climatic conditions. They found that carbon concentration decreased and phosphorous and sodium concentrations increased at the surface's cell. According to them, carbon concentration has direct correlation with adhesional strength whereas phosphorous and sodium have inverse correlation with adhesional strength. Finally, they mentioned that phosphorous comes from n-type doped Si layer of the cell and sodium arose from soda-lime glass.

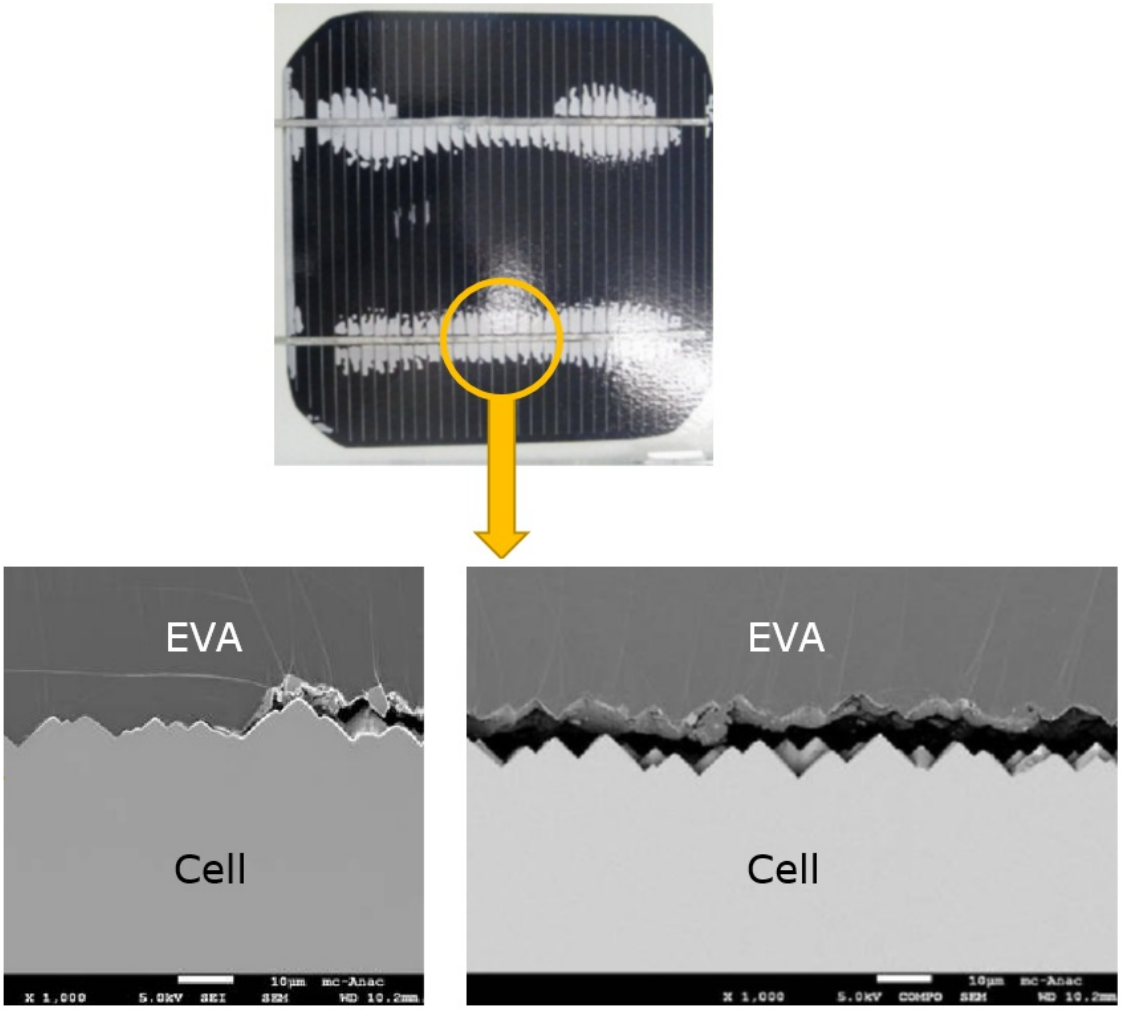

Figure 3.31: Cross-sectional view of EVA/cell interface by SEM (scanning electron microscope) [74].

3.2.4 Polymeric backsheet

3.2.4.1 Delamination (interlayer adhesion)

In the previous section (3.2.3) delamination of various interfaces was reviewed. All those interfaces considered EVA-encapsulant with its adjacent layers (glass, cell and backsheet). In this section, a review of the loss of adhesion between the layers composing the backsheet will be given. Remember that a backsheet is composed of a inner-, core- and outer-layer and those three layers are glued by other adhesive layers. Delamination means the loss of adhesion such as in the examples shown in Fig. 3.32 and Fig. 3.33. Cracks, bubbles or melting in the backsheet are not considered as delamination.

Oreski and Wallner [81] explained that multilayer backsheets are expected to age especially "at the surface, in the bulk of a layer or within the interfaces". Novoa, Miller and Dauskardt [82] explained that interlayer debonding "occurs when the debong-driving force 'G' Jm^{-2}, which is a function of the applied mechanical stress, is equal to the critical debond

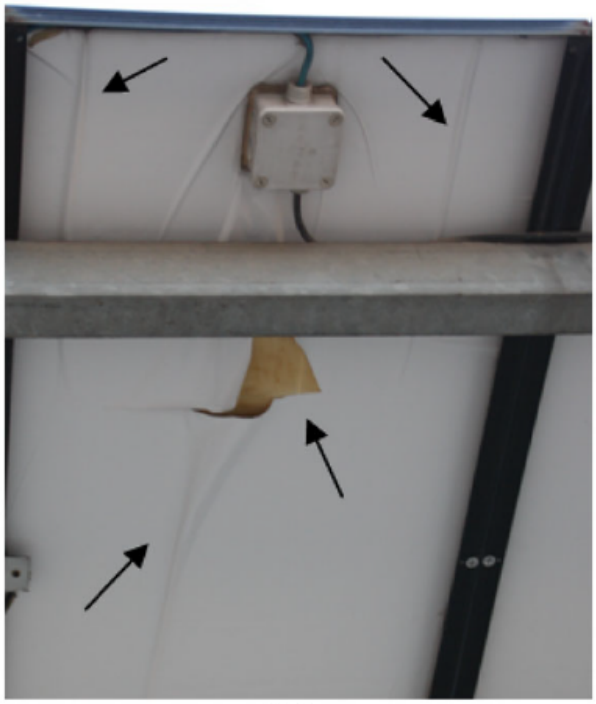

Figure 3.32: Backsheet delamination at the outer PET/PVF interface (after 17 years of operation) [80].

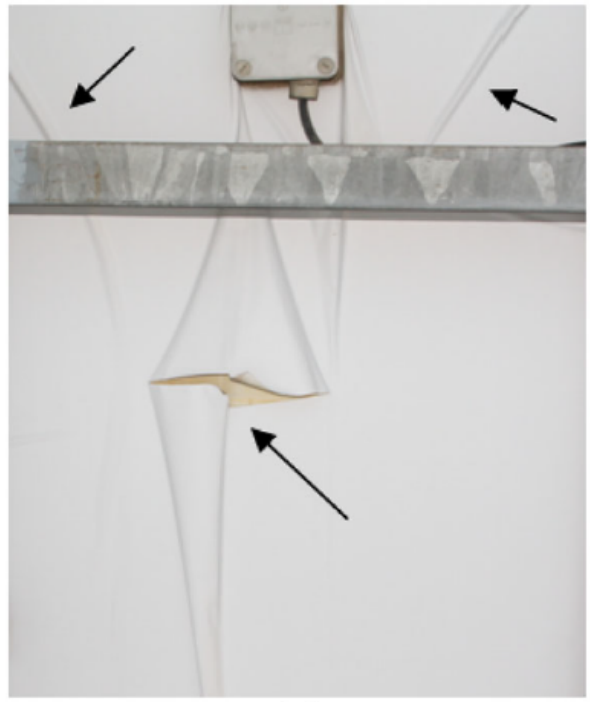

Figure 3.33: Another module subjected to the same conditions as module in Fig. 3.32 [80].

energy of the backsheet, G_c". They studied a backsheet consisting of PVF/PET/EVA. According to their results, the value G_c was higher for all the unaged specimen. Specifically, they observed debonding between PVF/PET interface in all the samples as temperature or humidity increase.

Lin, Krommenhoek, Watson and Gu [83] studied a backsheet comprising PET as outer and core layers with three EVA layers having different VA content, along with two inner adhesive layers between PET/PET interface and PET/EVA interface (see Fig. 3.34). They exposed the backsheet to UV radiation at 85°C, 5% RH (dry environment) and at 85°C, 60% RH (humid environment). According to their results, dry conditions did not show delamination or degradation. In contrast, inner adhesive layers degraded due to humid conditions (moisture) until PET/PET layers experienced complete delamination after 3000 h.

Kim et al. [84] also studied acceleration-tested modules. They observed delamination between PVF or PVDF and PET. According to them, the decrease in the mechanical strength is due to thermal and hydrolytic degradation of the core PET. They suggested that tensile strength is proportional to the molecular weight while random chain scission causes loss of molecular weight. They also found that hydrolysis resistant PET is more endurable than regular PET which is expected because Oreski and Wallner [85] found that PVDF/SiO_x-PET interface present higher initial value of adhesion than PVDF/PET interface.

Interlayer debonding failure not only depends on temperature and humidity but also UV light. E. Wang, Yang, Yen, Chi and C. Wang [86] studied the debonding mechanism on c-Si PV modules based on TPT and TPE backsheets. In their study, they observed that the

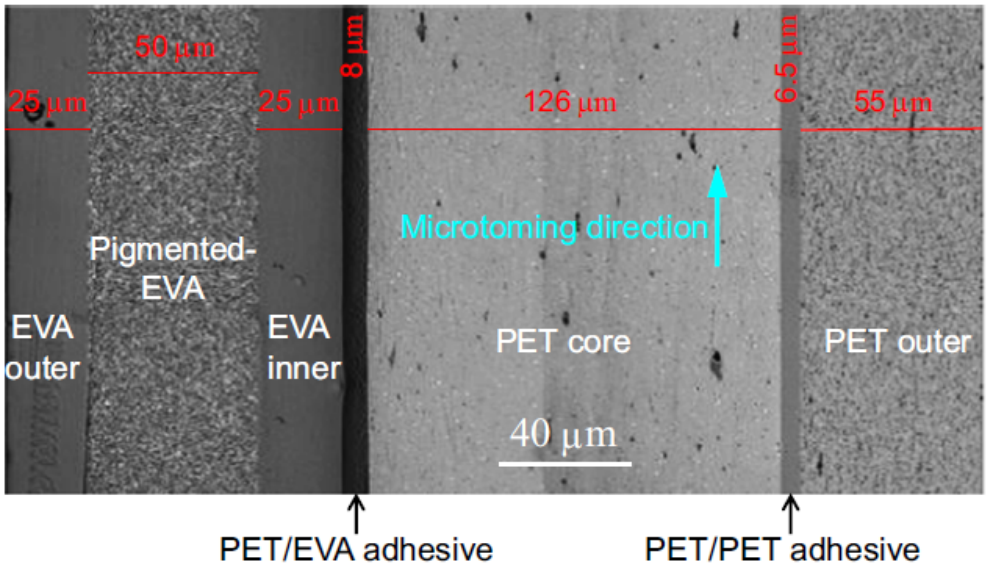

Figure 3.34: Cross-sectional view of a healthy PPE backsheet by LSCM (Laser Scanning Confocal Microscopy) [83].

cause of loss of adhesion due to UV light exposure was related to energy light being much larger than polymer bond dissociation.

3.2.4.2 Bubbles

Bubbles are the result of the loss of adhesion of the EVA/backsheet interface but in a specific and confined area that contain air or gases. Fig. 3.35 shows the back side of a module having several small bubbles while Fig. 3.36 shows a module with a big bubble. Bubbles are not only an aesthetic problem. They reduce the thermal conductivity of the module. Therefore, they can cause hot spots.

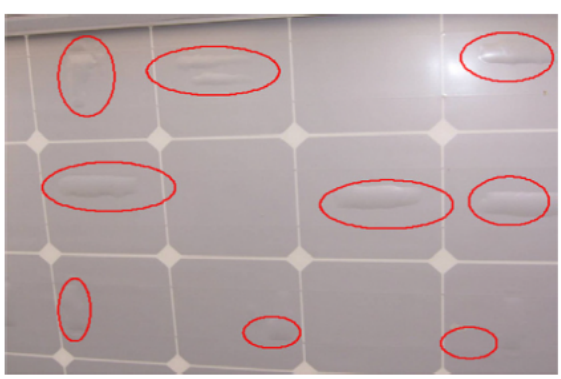

Figure 3.35: Bubbles on the back side of a PV module [87].

Figure 3.36: 5-year PVDF-Backsheet shows bubbling issue at seashore area (Subtropical & Seashore) [88].

Köntges et al. [2] observed bubbles at Sanyo modules fielded in Tucson. They suggested that bubbles are created because CO_2 gas, generated as a byproduct of cross-linking reactions,

cannot escape the backsheet due to a vapor barrier (aluminum foil). In other study of Köntges et al. [64], they suggested that bubbles can be generated because of the presence of flux residues (soldering liquid) or the vaporization of water within EVA-encapsulant.

3.2.4.3 Cracks and embrittlement

Cracks and embrittlement are closely related to delamination. A material is brittle when it breaks easily under stress. For example, the insulation of cables in a PV plant can brittle due to longer UV exposure. Therefore, a brittle material can also break. Backsheets under certain conditions can first brittle, then crack and even delaminate. Fig. 3.37 shows an isolated crack on a backsheet of a fielded module while Fig. 3.38 shows a specific pattern of cracks along the tabbing ribbon. A brittle backsheet is not easy to visualize because is a change in the texture. Therefore, is easy to detect by touching the material.

Figure 3.37: Isolated crack on the back side of a fielded module [39].

Figure 3.38: PET-based backsheet fielded for 4 years showing cracks along the tabbing ribbon on the back side [89].

Oreski and Wallner [85] observed significant embrittlement due to DH test in PET- and PVF-based backsheets. E. Wang et al. [86] did not detect embrittlement until 2000 h of DH test for PET-based backsheet. Lin et al. [83], which studied the backsheet in Fig. 3.34, found that the PET outer layer of the backsheet experienced cracks/holes after aging in humid and dry conditions. However, the propagation of the cracks were more severe under humid conditions. According to them, the stress intensity factor for PET under humid conditions is one order of magnitude greater than in dry conditions.

Gambogi et al. [90], explained that PET-based backsheets that undergone hydrolysis, thermal, and/or UV degradation are expected to crack. According to their results, aged backsheet loss the mechanical properties (tensile and elongation) decreasing the molecular weight leading to cracks. Fig. 3.39 shows four PET-based backsheets severely damaged (cracked) after 360 h of front UV exposure to study the inner layer.

Finally, UV exposure is not the only factor that triggers backsheet degradation. Illya et al. [91] concluded that either water vapor or salt mist causes embrittlement in their study of traditional backsheet degradation in salty environments. An increase of embrittlement

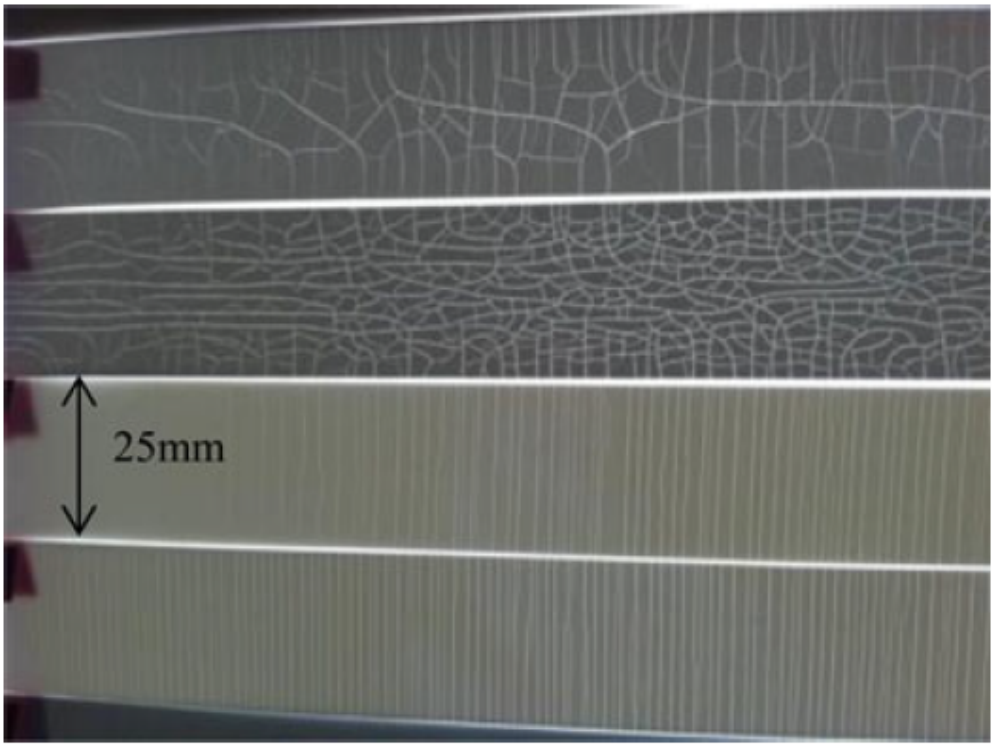

Figure 3.39: Four PET-based backsheets with severe inner layer damage due to UV exposure [90].

was related to a drop in the elongation or molecular weight of the polymer by Blieske and Stollwerck [19]. They observed a fast decrease of strain at break for a $SiOx$-PET-based backsheet after 2000 h of DH test exposure.

3.2.4.4 Discoloration (browning or yellowing)

Discoloration (yellowing or browning) can happen to any polymer not only to EVA-encapsulant but also to the backsheet. Fig. 3.40 shows various examples of PV modules with discolored backsheets. Since the backsheet is not in the optical path of the light, its discoloration will not directly impact the module performance. However, discolored regions of the backsheet leads to higher absorption of irradiation which results in higher operating temperatures that accelerate the degradation of the module.

It is important to understand that the three layers of a backsheet are not exposed to the same conditions in the field. Since the glass and the EVA-encapsulant absorb light in the range of 300 to 360 nm [90] UV-A radiation is not strong over the inner layer of the backsheet. Additionally, the reflected radiation from the ground that impact the outer layer of the backsheet usually presents higher power in the UV-A range than UV-B range [90].

Gambogi et al. [90] analyzed the change in color of PET- and PVF-based backsheets under accelerated UV conditions and compared the results with fielded-module data. Several conclusions can be obtained from these two different sources of information. Fielded modules

Figure 3.40: Typical backsheet yellowing after short period of field installation [92].

showed that PET discoloration is more strong than PVF, meanwhile acceleration-tested modules suggested that UV exposure shows better agreement with fielded-module data than DH-acceleration-tested data. Therefore, Gambogi suspected that yellowing is related to photo-degradation and not to hydrolysis damage. Fig. 3.41 shows a fielded module showing severe backsheet yellowing.

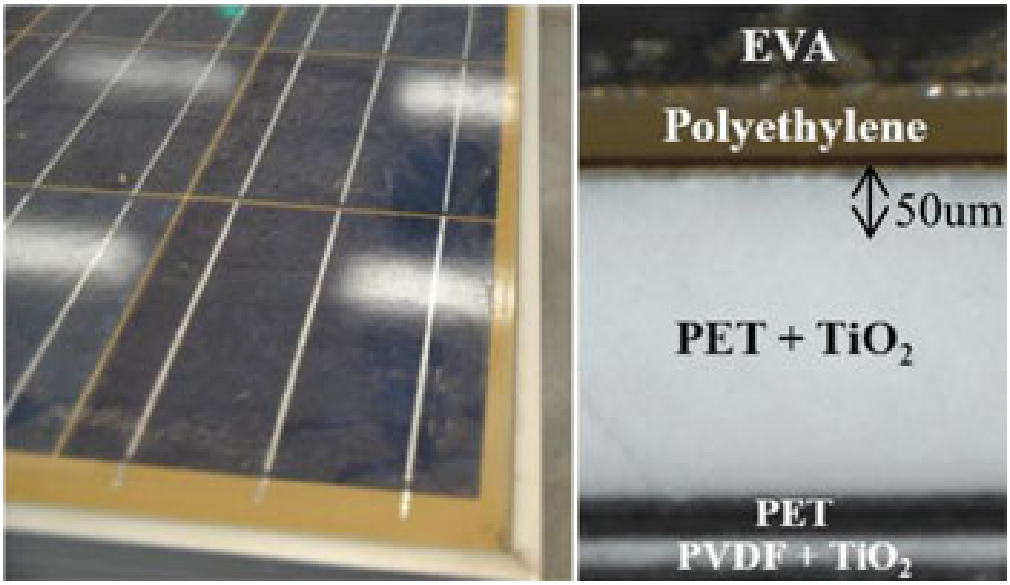

Figure 3.41: Module with discolored backsheet studied by Gambogi et al. [90].

Liu, Jiang and Yang [92] studied the degradation mechanisms of UV-aged (up to 3000 h) commercial PV backsheets (comprised of EVA and fluoropolymers). According to them,

the yellowing behavior of the backsheet is caused by the formation of chromophores due to polymer degradation. Chromophores are macro-molecular chains that absorb specific frequencies of light resulting in pigmentation of the molecules (see section 3.2.3.1 for more information about chromophores). The results of their study showed that higher UV dosage leads to more severe chemical degradation, which causes larger shift in color.

3.2.5 Soda-lime front glass

3.2.5.1 Cracking, shattering or chipping

Cracked glass is not directly detrimental to PV modules. Fig. 3.42 shows a broken module which operated for 5 years without noticeable power degradation. The problem is that when glass is broken, further failure mechanisms activate. For example EVA-encapsulant can delaminate or discolor or the metallization can corrode, etc.

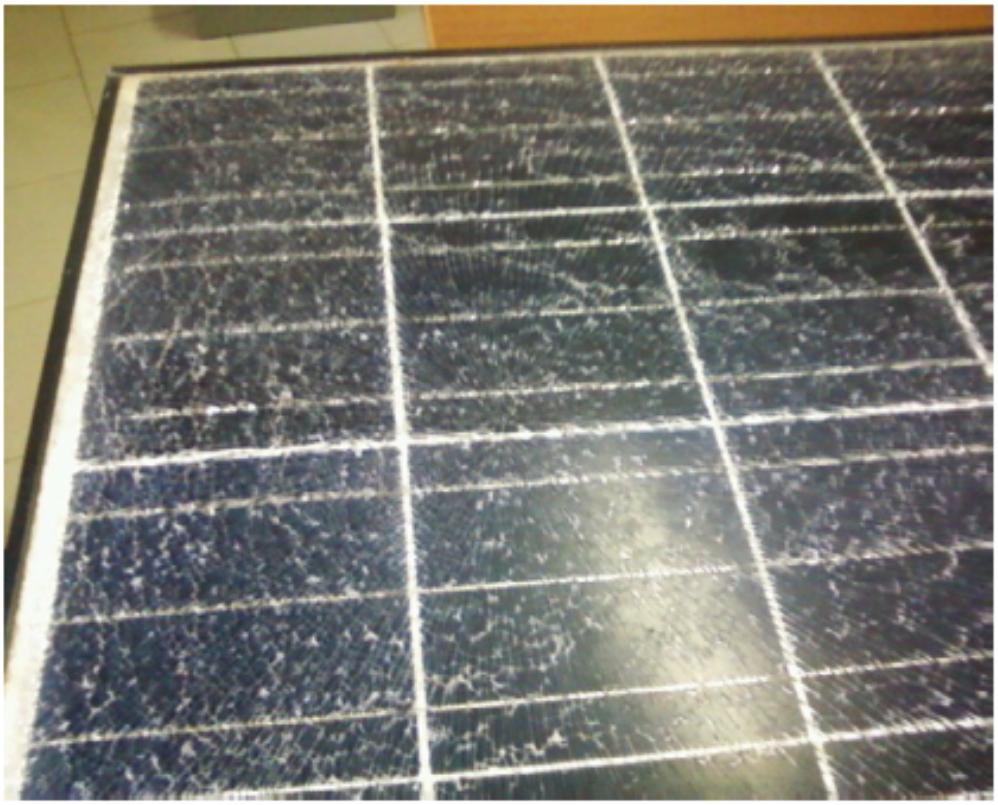

Figure 3.42: Broken PV module operating for 5 years without noticeable power loss [87].

It is not surprising that glass breaks due to improper handling or by hard object impacts, but these are not the only reasons. Crystalline silicon solar modules qualification tests within IEC 61215 includes an impact test for hail and large loads. However, according to Schneller et al. [23], glass may still break in extreme weather conditions or due to thermo-mechanical forces. Schneider [93] explained that glass can break not only due to environmental conditions, but also due to chemical contamination within the materials or hot-spots. The pattern

of the broken glass can indicate if the failure was due to external forces or internal problems. Fig. 3.43 shows a glass cracked by an external impact while Fig. 3.44 suggests other causes.

Barry [94] observed that glass breaks when an applied load exceeds the strength of the glass. Furthermore, he specified different causes for glass breakage such as: tensile stress (bending, expansion or thermal load), incorrect clamped edges (bending stress) and spontaneous breakage (without any applied load). Additionally, he explained that glass's AR coating (to reduce light reflection) can appear transparent, but it can absorb infrared light and increase the stress within the glass. Once the glass is broken, according to Webb and Hamilton [95], moisture can induce crack growing.

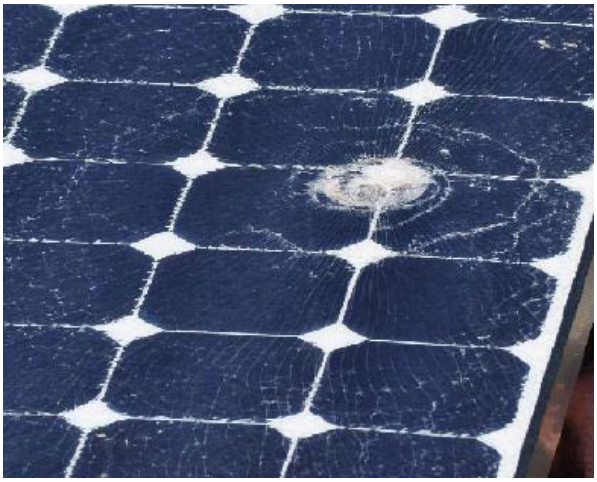

Figure 3.43: Bullet hole on PV glass [96].

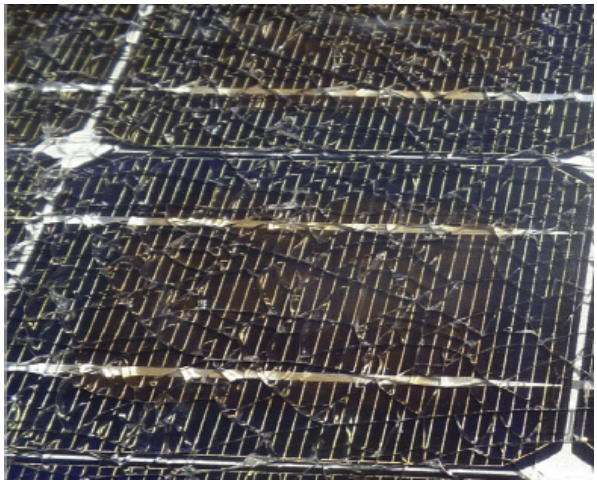

Figure 3.44: Glass breakage of all surface module [77].

Cording [97] described the glass as an object that is very strong in compression, but weak in tension. He explained that when glass breaks, it is due to tensile failure. Furthermore, glass cannot be deformed like steel and if a small force on the glass exceeds a certain value, the glass will brittle. Cording described several causes for glass breakage such as: laminating stress, surface damage, thermal stress, and mechanical forces like framing or mounting stress, wind, snow and hail.

3.2.5.2 Abrasion or soiling

Dust or soiling particles composition can vary from region to region. The dust in the middle of a desert is different from the dust in the middle of a city or near an industrial zone. However, no matter what the dust is made of, Kazmerski et al. [98] defined dust "as any particulate matter less than 500 μm in diameter".

Ferrara and Philipp [99] described the abrasion mechanism induced by the combination of sand and wind which damage the surface of the glass resulting in frosting of the glass and/or damage of the AR coating of the glass. Depending on the composition of the dust, it is possible that dust combined with wet and dry cycles create a concrete layer of sand that can be glued to the glass surface. This mechanism is also called soiling. Sánchez-Friera,

Piliougine, Peláez, Carretero and Sidrach de Cardona [100] explained soiling as an irreversible process where the PV module darkened at its lower edge. They explained that this is caused by deposition of airborne particles, sedimentation of rainwater deposits and leaching or ion exchange between alkalis in the glass and hydrogen ions in the water. Fig. 3.45 shows a solar panel with accumulated sand on its surface.

Figure 3.45: UDTS 50 PV panel with sand dust accumulation in Research Unit in Renewable Energies in Saharan Medium [77].

Kazmerski et al. [98] investigated the most fundamental mechanisms of adhesion of dust on module surface for different dust compositions. According to their study, dust particles glued on module's surface from modules installed in Middle East, North Africa and India are mainly composed by silicon oxide while from modules installed in Europe, South/North America and Asia are composed by soil and fuel components and other organic and mineral matter. According to their experiments, a strong bonding between the dust and the glass exists "due to surface organic/mineral concentrations that chemically bind the dust particle to the surface under the influence of water and likely UV light". Finally, Kazmerski mentioned that dust particles with fuel components (hydrocarbon source) interact with water (moisture) in analogous ways.

Said and Walwil [101] also investigated the particle adhesion forces of dust on glass surface.

They concluded that these forces depend on the area of contact between dust particle and glass surface. Thus, for flat surfaces the adhesion forces increase if the particle size increases. Furthermore, coarse dust particles have less adhesion than smooth ones because the contact area between particle and surface is less for the first particle. Finally, Said and Walwil suggested that humidity enhances the bonding of the dust "due to formation of water capillary bridge between dust particles on glass surface".

Fig. 3.46 shows an example of severe soiling for PV modules operating in desert conditions. It can be seen that the ambient dust concentration is high and the adhesion effect is present in most of the PV modules. Cleaning, in severe dust concentration cases, may require weekly frequency to keep soiling loss below 2%. Fig. 3.47 shows manual cleaning for a power plant in the middle of the desert. This system of keeping soiling losses at low percentages can cost a lot of money and man's hours.

Figure 3.46: Severe soiling on PV module's surface in desert conditions [2].

Figure 3.47: Manual cleaning of a PV array [2].

3.2.5.3 Corrosion or weathering

PV modules installed near sea shores or in very salty environments that are also exposed to wind and water can become covered by a white salty layer that can be worse than soiling. This can also happen to modules installed near industrial areas which are exposed to several types of gases such as O_3, NH_3, SO_2, H_2S, Cl_2, etc. According to Ferrara and Philipp [99], these gases alone or in combination with humidity (rain, fog, dew, etc.) can cause corrosion

for being acids (HNO_3, H_2SO_4, etc.). Fig. 3.48 shows white stain made of salt on the edge of a CIGS module while Fig. 3.49 shows a module with a severe layer of salts on the whole surface.

Figure 3.48: White deposits (salts) at the edges of the CIGS Module [102].

Figure 3.49: PV module with hard water marks. Photo obtained from `https://www.solarglassshield.com`.

Another type of corrosion is related exclusively to water. According to Cording [97], the mixture of silica and soda from glass is water soluble. Leed and Pantano [103] mentioned that glasses have a wide range of surface absorption sites. According to them, "these sites are places where the surface electrostatic field is strong enough to exert a significant attractive force on polar molecules such as water". Furthermore, they mentioned that chemical absorption occurs at these sites following hydration, corrosion and glass's fatigue. Finally, they explained that when sodium is added to silica, the number of coordination defects is greatly reduced.

Barry [94] shortly describe the effect of water on soda-lime glass. He explained that water leach sodium making an alkali solution which attacks the silicate structure. Finally, Cording [97] explained in detail the chemical reactions between water and glass. He described that sodium dissolved into trapped water causing the pH of the water to become very alkaline. The alkaline solution attacks the silica, consequently sodium dissolves and maintain the alkalinity. This endless cycle degraded the surface appearance known as "stain".

3.2.6 Aluminum frame

3.2.6.1 Corrosion or weathering

Here, corrosion is defined from a chemical point of view, such as oxidation. Fig. 3.50 is a very good example of oxidation where all the frames of a group of modules (installed on a roof) are rusty.

Electricity is generated due to electric potential difference between two electrodes. Metals and alloys have different electrode potentials. Therefore, when two dissimilar metals are in

contact one acts as a cathode and the other as anode. The potential difference between the metals is the driving force for ion migration in the presence of an electrolyte such as water. In this situation, the anode releases electrons to the cathode leading to corrosion at the metal being the anode. This process is known as *Galvanic corrosion*.

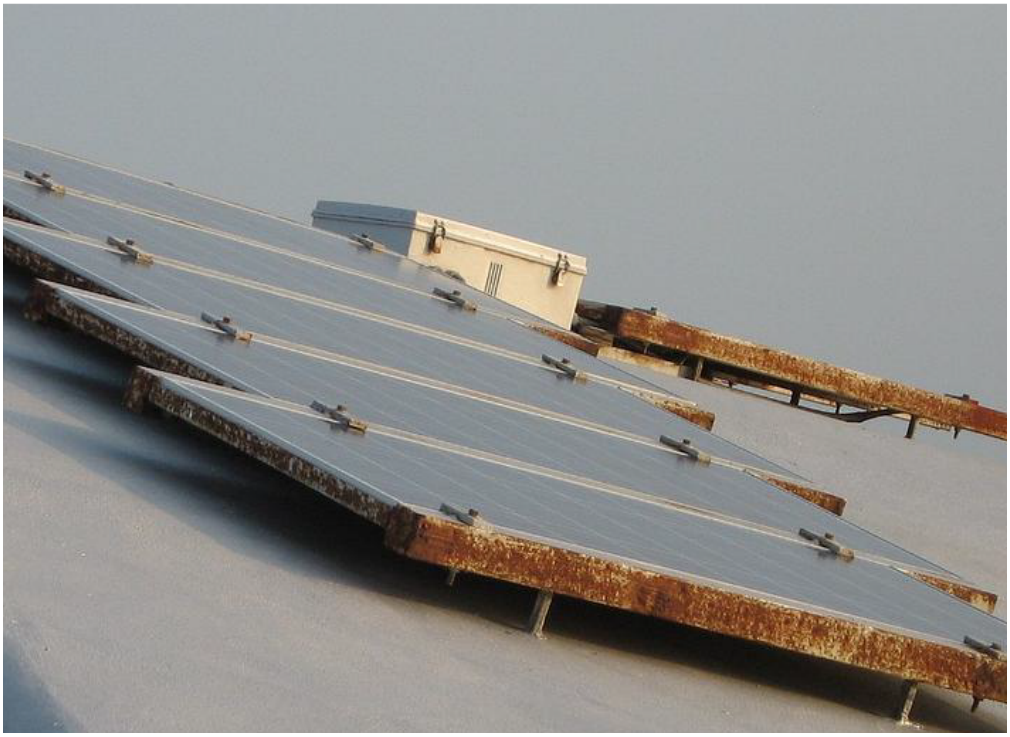

Figure 3.50: PV modules installed on a roof with rusty frames [93].

Schneider [93] described that corrosion in the frame can be caused due to bad installation leading to leakage current that flows through the frame or mounting screws corrosion. He also stated that weather (salt, acid rain or pollution) can induce corrosion of the frame. Ferrara and Philipp [99] explained that all metals can show defects (aluminum alloys, stainless steel, cooper, soldering agents, etc.) and "the corrosion of these metals can be caused by atmospheric humidity alone or in combination with gases". They also mentioned that the corrosion reaction will be accelerated by higher temperatures.

Grounding of PV modules are made through the frame and depending on the approach different metals and alloys can be used. E. Wang, Yen, C. Wang, Ji and Zgonena investigated the long-term effectiveness of different PV grounding devices under harsh environmental laboratory testing conditions. They observed frame's surface corrosion and white powder made of metal oxides after salt mist aging (see Fig. 3.51 and Fig. 3.52). In some cases, they observed that the tin was removed from the lug connectors leaving the inner copper exposed. The copper and the aluminum create a galvanic environment accelerating the corrosion. Additionally, they experienced other forms of corrosion mechanisms such as *Crevice corrosion*[2] and *Pitting corrosion*[3]

[2] https://en.wikipedia.org/wiki/Crevice_corrosion
[3] https://en.wikipedia.org/wiki/Pitting_corrosion

Figure 3.51: Build-up of white oxidation on the aluminum frame (screw sample) [104].

Figure 3.52: Build-up of white oxidation on the aluminum frame (lug sample) [104].

3.2.6.2 Distortion, bending and detachment

Distorted, bent or detached aluminum frames do not directly impact the power output of PV modules. Nevertheless, degraded frames can eventually allow water, moisture or humidity to penetrate the module leading to other failures. Also, they can jeopardize the stability and security of the structure. On the other hand, mechanical load testing of PV modules focuses attention on cell's crack development and also glass breakage but does not paid attention to frame distortions. In this context, information related to failure mechanisms of distorted, bent and detached frame is scarce. Fig. 3.53 and Fig. 3.54 are two examples of bent frame where the first one is due to snow load.

Figure 3.53: PV module frame damage because of snow load [105].

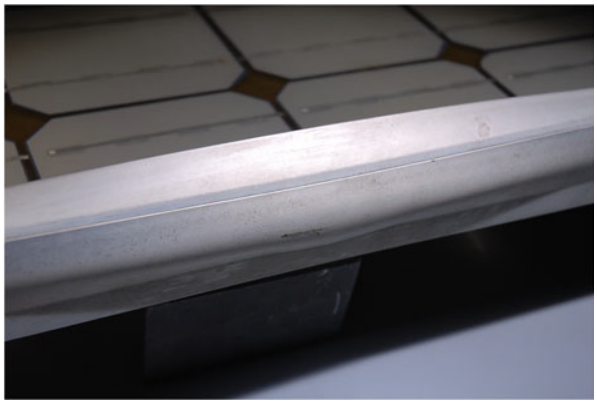

Figure 3.54: PV module with bent aluminum frame [106].

Although there is little information about frame failure modes, some authors have briefly studied the subject. Rajput, Tiwari, Sastry, Bora and Sharma [107] implied that module's frame distortion may be due to thermal cycling and fatigue of the metallic frame. According to Ferrara and Philipp [99], distortion can be caused by mechanical loads from snow or strong wind that can result in a total collapse of the PV module. Munoz, García, Vela and Chenlo [108] defined the detachment of the frame as the separation of the frame from the rest of

the module. They explained that the main cause for detachment is a defect on the adhesive tape. Furthermore, they explained that detachment can occur due to excessive weight (wrong installation) or snow/ice accumulation on the module. Fig. 3.55 shows a detached frame.

Figure 3.55: Detachment of the frame [108].

3.2.7 Junction box and bypass diodes

3.2.7.1 Detachment

The detachment of the junction box from the back of the backsheet material is due to a failure in the sealing adhesive or the degradation of the backsheet. If the junction box detaches from the back side of the module then there is a risk of moisture ingress with subsequent corrosion. Fig. 3.56 shows a completely detached junction box while Fig. 3.57 shows a poorly glued junction box that could easily separate from the backsheet.

Figure 3.56: Detached junction box from the back side of a PV module [69].

Figure 3.57: Poorly bonded junction box [64].

According to Miller and Wohlgemuth [109], the detachment of the box can result from the degradation of the backsheet such as delamination or hydrolysis. Furthermore, Wohlgemuth, Cunningham, Nguyen, Kelly and Amin [110] and Köntges et al. [64] observed that some adhesive materials are good only for short term. Additionally, Ferrara and Philipp [99] suggested that UV radiation, heat and humidity can lead to adhesive degradation.

Related to differences between polyethylene (PE) and polyurethane (PUR) foam tapes and acrylic foam tape, the last foam tape is more robust. According to FABRICO™, the compressive and cohesive strengths of PE and PUR foam tapes are poor. Therefore, foams can tear. They also mentioned that elongation and maximum static load are low. Therefore, repeated expansion and contraction with other materials due to temperature cycles will degrade the foams. In contrast, they mentioned that acrylic foams can stretch and retract without debonding. Acrylic foams can also resist high wind forces and unlike PE foam tapes, they withstand extreme temperatures.

3.2.7.2 hot-spots and arcing

In general, hot-spots and arcs can lead to fire, therefore to a catastrophic failure. Hot-spots cannot be seen by the naked eye but with thermal camera while arcs can be seen when they happen. Once the arc is extinguished, they leave behind burn marks. Fig. 3.58 shows several hot-spots on a PV module but it is clear that one of them is the junction box (black circle). The junction box shown in Fig. 3.59 is evidently burned and the most probable cause is an arc.

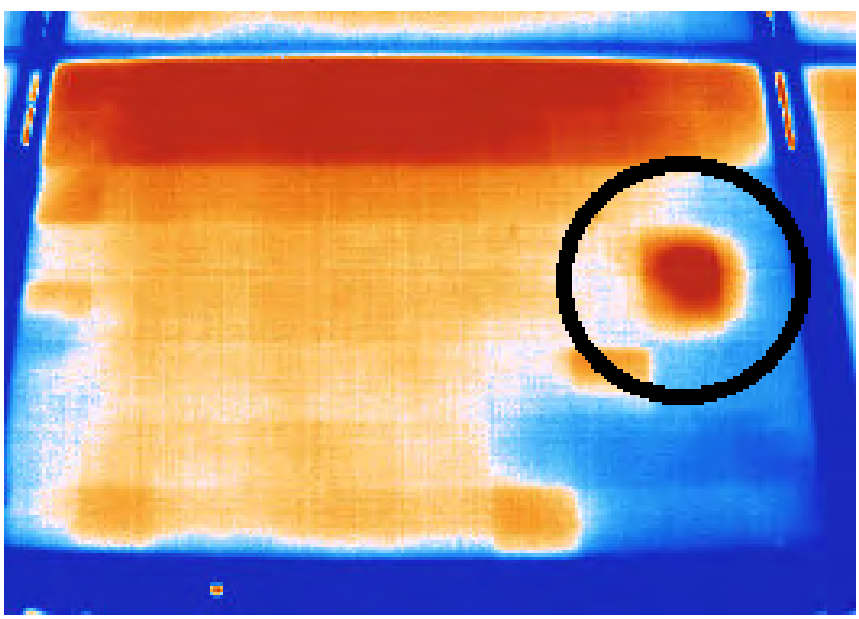

Figure 3.58: Thermal-image of a PV module with several hot cells [111].

Schneller et al. [23] explained that series or parallel arcs are possible within a junction box. Series arcs occur when an open-circuit exists in a single conductor while parallel arcs occur

Figure 3.59: Burn mark on a junction box [96].

between two different conductors at different potentials. According to Colli [112], aged or damaged contacts could lead to arcs. Colli explained that poor or intermittent contacts can be caused by corrosion (due to climatic conditions). Additionally, Itoh et al. [66] described that poor contact or solder joint fatigue can be induced by repeated heat cycles while Köntges et al. [64] explained that they can be induced by low soldering temperature or chemical residuals from the soldering process. Several authors state that screwed or fitted contacts are less reliable than soldered connections. Fig. 3.60 shows a wire that is not properly connected because is in contact with the bypass diode and Fig. 3.61 shows a contact operating at higher temperature.

Figure 3.60: Poor wiring within the junction box [64].

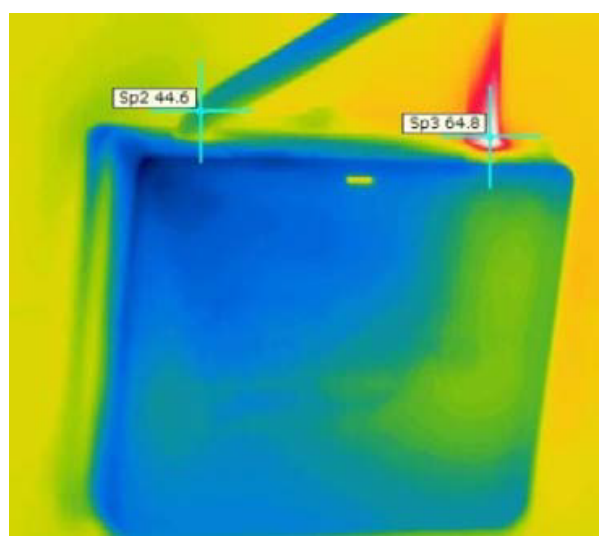

Figure 3.61: Junction box contacts with a temperature difference of 20°C [96].

Bypass diodes can lead either to arcs or to hot-spots. These diodes can fail due to different

reasons. According to Schneller et al. [23], the bypass diode is the only component within the PV module that is sensitive to ESD. This means that they can fail if a lightning strikes the PV module. Another reason why bypass diodes fail is that semiconductors, such as those used

Figure 3.62: Damage diodes within a junction box [61].

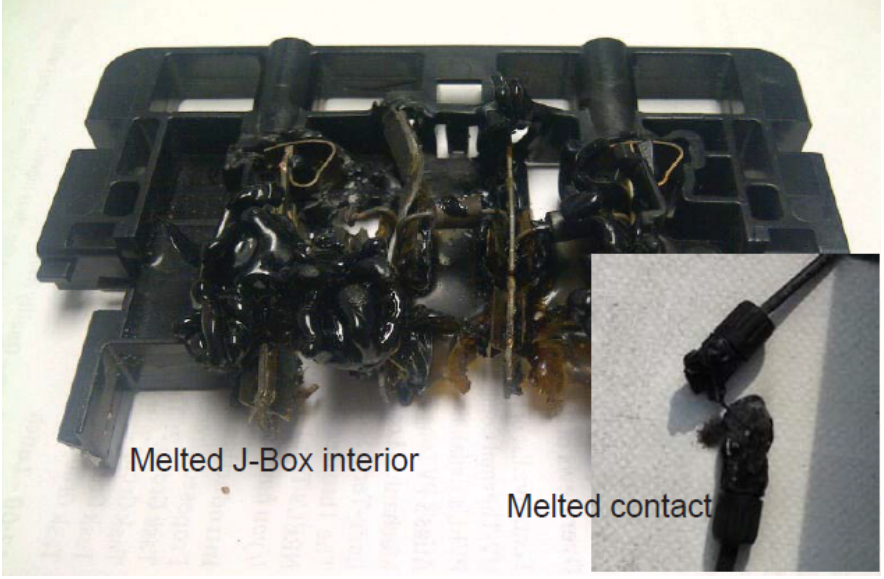

Figure 3.63: Junction box and wiring failures from overheating within 2-3 years in the field [113].

to make these diodes, experience thermal runaway. Schneller et al. explained that this effect occurs when an excessive current flows through the device increasing its temperature resulting in higher current flow until thermal damage. Bypass diodes in the field experience

this behavior when returning to reverse bias from high temperature forward bias operation. Finally, bypass diodes that continuously operate in forward condition lead to excessive heating elevating the junction box temperature. Fig. 3.62 shows burned diodes within a junction box while Fig. 3.63 shows an overheated fielded junction box.

3.2.8 PV module in general

Potential induce degradation

Currently the degradation mechanisms of PV modules that undergo PID are only under understood for conventional *p*-type c-*S*i modules, but is not fully understood for other technologies. The reliability of PV modules is getting attention from researchers, manufacturers, bankers and investors and PID is gaining importance in the last decade. Several improvements have been done in PID's research, but a lot of questions remains without answers.

PV systems connect modules in series to increase the total voltage of the whole array, this way the system increase its ability to deliver power without increasing losses due to heat dissipation of the current flowing. At the same time, frames are grounded for safety reasons. High voltage and grounded frames leads to a potential difference between the frame and the solar cells within each PV module. Depending on the position of the module within the array, this potential difference is unique for each module. Fig. 3.64 shows an scheme of 5 modules connected in series with the frame grounded. The potential difference between the cell and the frame in the middle is zero and increases in magnitude towards both ends of the string.

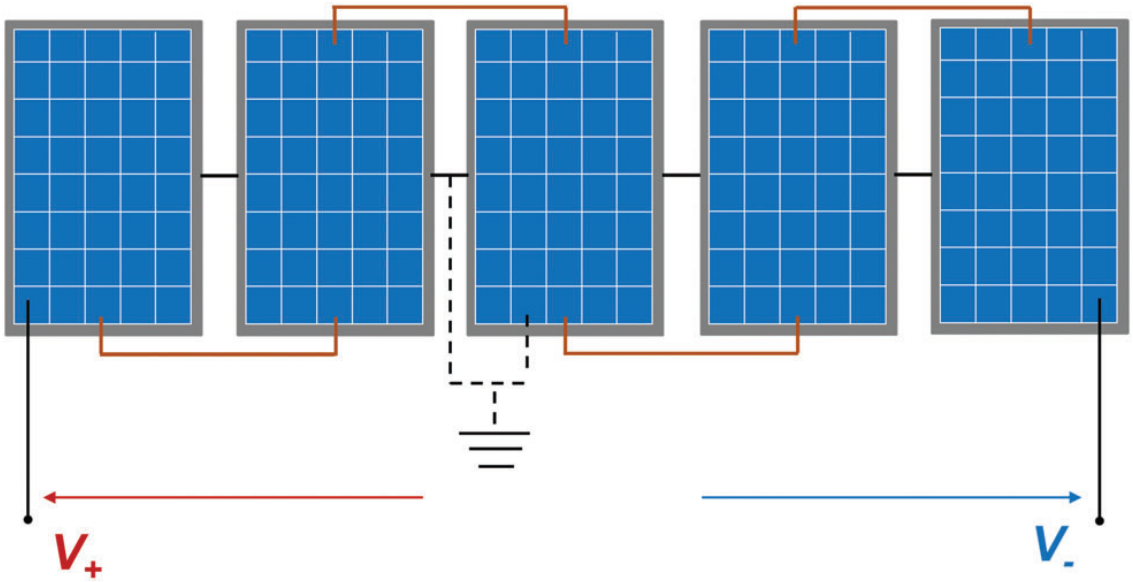

Figure 3.64: A simplified schematic diagram of a PV system with a floating potential, modules are connected in series and frames are grounded [114].

The potential difference between the cell and the frame induce leakage currents to flow from the frame to the solar cell or vice versa, it depends on the modules position within the

array. This results in PID, which is influenced by several factors such as the properties of the solar cell's AR coating, encapsulation materials, construction of the module (e.g. frame or frame-less) and system topology [114]. Furthermore, even for identical modules different extents of PID can be induced. The extent will depend on environmental (temperature, humidity, condensation, etc.), grounding conditions of the glass surface (wet or dry), and exposure to light. According to Luo et al. [114], the amount of soiling over the surface can influence in the PID susceptibility of the module.

Luo et al. [114] indicate that in standard c-Si PV modules leakage currents can flow from the module frame to the solar cells along several different pathways, which are shown in Fig. 3.65. According to Fig. 3.65, the possible paths are:

1. along the surface of the front glass, and through the bulk of the glass and encapsulant;
2. through the bulk of the front glass and encapsulant;
3. along the interface between the front glass and the encapsulant, and through the bulk of the encapsulant;
4. through the bulk of the encapsulant (laterally);
5. along the interface between the encapsulant and the backsheet, and through the bulk of the encapsulant;
6. along the surface of the backsheet, and through the bulk of the backsheet and encapsulant.

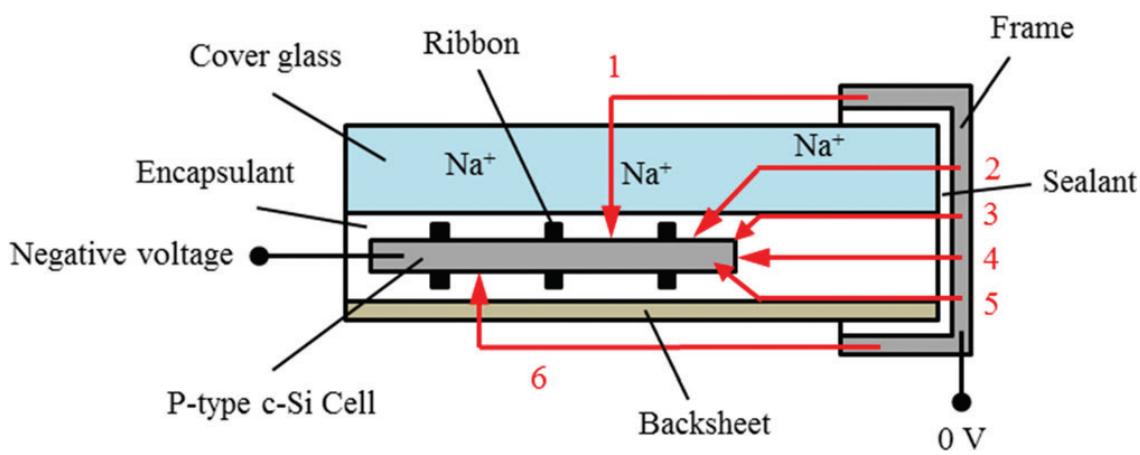

Figure 3.65: Cross section of a conventional c-Si PV module constructed with a glass-encapsulant-cell-encapsulant-backsheet package and modelling of the possible leakage current pathways [114].

The flowing of the current, shown in Fig. 3.65, is shown in a conventional way. This means that if the solar cells are positively biased relative to the frame, then the direction of the current flowing will be reversed. Among the 6 possible paths that the leakage current can flow, path 1 is most detrimental under outdoor conditions due to the increase in the conductivity of the glass due to rain and humidity [114]. In contrast, path 6 is often neglected because

due to the excellent electrical resistance of the backsheet and the Al BSF of the solar cells [114].

It is known that the most common type of PID for the conventional p-type c-Si module is PID-shunting (PID-s). Several studies have shown that under negatively-biased conditions, sodium ions (Na^+) drift through the SiN_x AR coating towards the interface between the Si cell and the AR coating and penetrates into the $n^+ - p$ junction. According to [114], this penetration results in significant ohmic and non-ohmic shunting degrading the voltage and the FF of the module. Since at low levels of irradiance the dark current is dominant over the photo-current, PID-s is more detrimental at low light. Accumulation of sodium ions are confirmed to be strongly correlated with shunted regions of PID-affected modules. The migrations of these ions seems have several sources, soda-lime glass contain sodium and its bulk resistivity is facilitated by Na ion migration. However, at cell level (without glass) Na migration is also observed by Naumann et al. [115]. Hence, another possibility is Na source is the sodium contamination of the SiN_x layer of the cell. Of course, both contributions are possible independently.

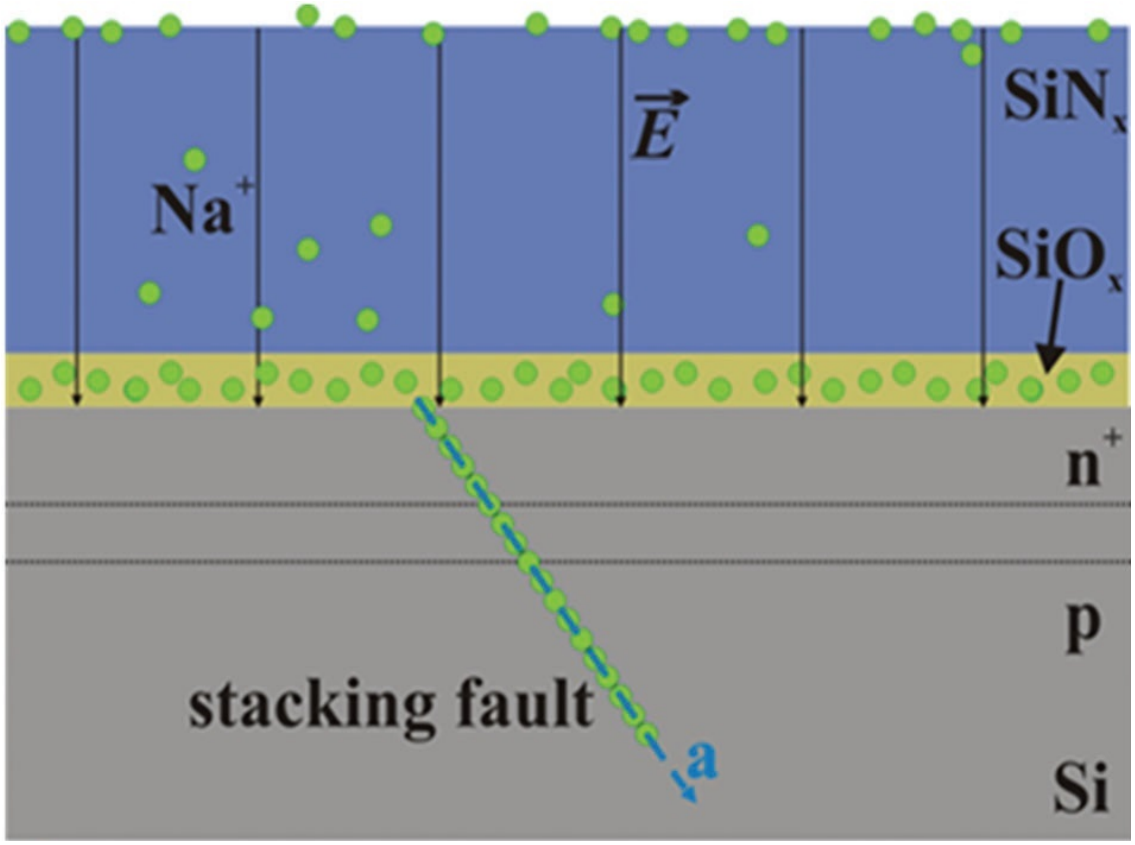

Figure 3.66: Schematic drawing of a solar cell cross section and transport of Na^+ (green dots) through the SiN_x layer and subsequent diffusion into the stacking faults. Image adapted from [114].

Other investigations related to PID of conventional p-type c-Si PV modules, indicated that the stacking faults (defects) in Si were contaminated by Na [116, 117, 118]. The stacking faults extent from the SiN_x/Si interface across the p-n^+ junction into the p-doped Si base material by several micrometers. As PID progresses, Na^+ drift towards the SiN_x/Si

interface and accumulate in the SiO_x interlayer (native oxide layer). Then, Na^+ diffuse into the stacking faults from the SiO_x interlayer and is neutralized by free electrons in the n^+ emitter allowing more Na^+ to follow (see Fig. 3.66).

As stated above, the root causes for PID are different for different type of modules technology. Degradation process related to a degradation of the front side passivation layer (PID-p) is observed by Naumann et al. [119] in IBC cells from SunPower with SiO_2 for surface passivation. According to Swanson et al. [120], when an n-type c-Si IBC cell is subjected at high positive voltage, leakage current flow from the cell through the encapsulant and the glass to the grounded frame. They indicate that this results in negative charges accumulated on the surface of the SiN_x AR coating of the cell (see Fig. 3.67, which are trapped within the AR coating due to the high resistivity of SiO_2 and /or SiN_x film. Hence, positive holes are more attracted to the front surface of the cell, where they recombine with electrons, than to the back contacts. According to Swanson [120], this results in an increase of surface recombination and reduce the current and the voltage.

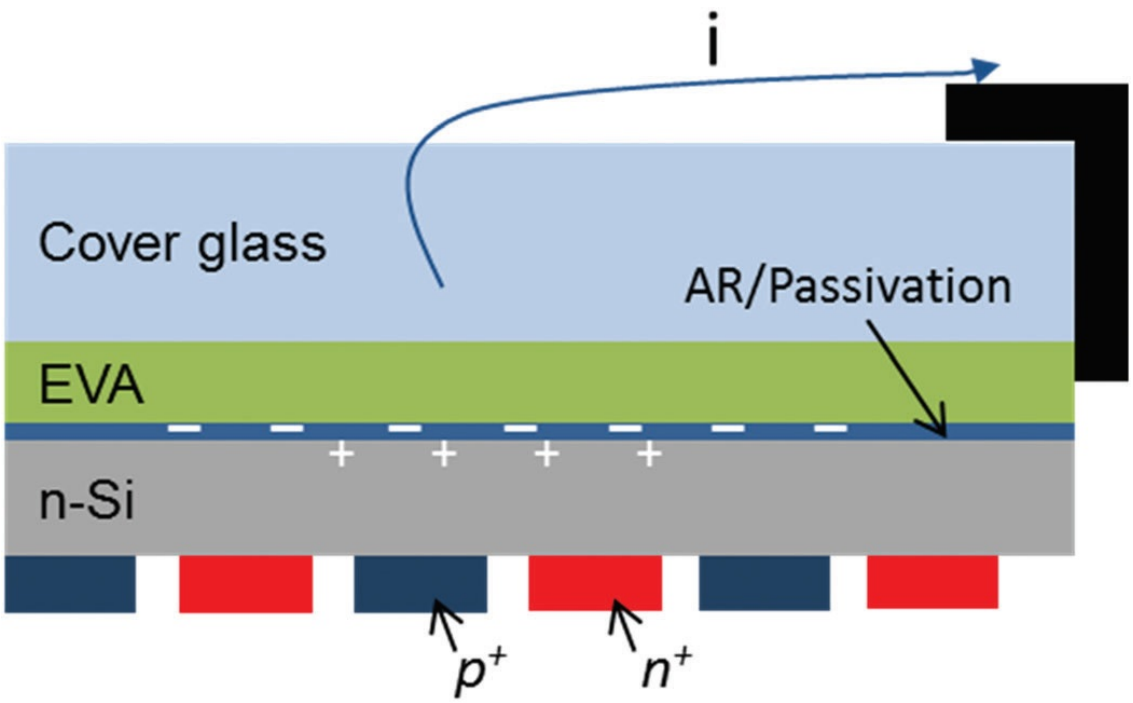

Figure 3.67: A schematic diagram illustrating the surface polarization passivation effect in SunPower's n-type IBC c-Si cells. Current "i" represents the leakage current. The frame is grounded. Image from [114].

Finally, Swanson et al. [120] indicated that the PID-p is reversible, and can be avoided by operating modules at negative voltages with respect to ground for n-type front surfaces (and positive voltages for p-type front surfaces). Also, Luo et al. [114] indicates that PID-s is associated with a reduction of the shunt resistance of conventional $p-$-type c-Si modules, while Naumann et al. [119] explain that shunting does not occurs in PID-p even though it was expected due to rear side p-n junction of the IBC cell.

Chapter 4

Field Inspection Methods for Fielded PV Modules

Standard series for solar cells, modules and systems prepare recommendations for the manufacture processes and materials, quality control (QA), test requirements, performance, safety issues, etc.; regarding to solar cells, modules and systems. One of the most important technical committee for solar energy standardization is the IEC Technical Committee TC82 established in 1981. The aim of TC82 is to prepare international standards for photovoltaic systems and all the elements within the system. The subcommittees or working groups within the IEC TC82 are: WG 1 - Glossary; WG 2 - Modules, non-concentrating; WG 3 - Systems; WG 6 - Balance-of-system components; WG 7 - Concentrator modules and WG 8 - Photovoltaic cells.

Apart from IEC, there are four important technical committees. The ISO Technical Committee TC180 that prepares international standards for the development, testing, installation and servicing of equipment and systems related to solar energy. The working groups within ISO TC180 are: WG 1 - Nomenclature and WG 3 - Collector Components and Materials. The ASTM Committee E44 on Solar, Geothermal and Other Alternative Energy Sources; which is composed by several working groups. Within ASTM Committee E44, the WG 9 - Photovoltaic Electric Power Conversion addresses PV topics. The IEEE SCC21 Standards Coordinating Committee on Fuel Cells, Photovoltaics, Dispersed Generation, and Energy Storage and finally the SEMI (Semiconductor Equipment and Materials International).

Another important entity is NREL. The National Renewable Energy Laboratory of the United States is the only federal laboratory dedicated to the research, development, commercialization, and deployment of renewable energy and energy efficiency technologies. NREL also performs research on PV under the National Center for Photovoltaics. This laboratory has several facilities for PV research, development, testing and deployment. Their work on PV has high international impact. Therefore, NREL work will be considered in this review.

The last, but not least, is IEA. The International Energy Agency has a Photovoltaic Power Systems Programme (PVPS) that is one of the collaborative R&D Agreements established within the agency and, since its establishment in 1993, the PVPS participants have been

conducting a variety of joint projects in the application of photovoltaic conversion of solar energy into electricity. Currently there are 31 members within IEA PVPS and one of them is Chile. Therefore, IEA PVPS research and development will be considered in this review.

The following literature review is based on guidelines and standards from all these technical committees with the addition of NREL and IEA PVPS.

4.1 Visual Inspection

The international standard IEC 61215 (ed. 2016) lays down requirements for the design qualification suitable for long-term operation in general open-air climates. The objective of the test sequences [53], described within IEC 61215 series, is to determine the electrical and thermal characteristics of the module and to show, as far as possible, that the module is capable of withstanding prolonged exposure in climates described in the scope. Within IEC 61215, the visual inspection method is not intended to be used with fielded modules. In contrast, the procedures are focused in determining visual failures of new modules subjected to a series of laboratory tests such as outdoor exposure test, hot-spot endurance test, UV preconditioning, thermal cycling (TC) test, humidity freeze (HF) test, damp heat (DH) test, etc. Hence, the list of typical failures according to IEC 61215 is quite poor and not very detailed to investigate failures of degraded modules in the field.

ASTM has an active standard, ASTM E1799 (ed. 2012), named Standard Practice for Visual Inspections of Photovoltaic Modules. This standard covers procedures and criteria for visual inspections of photovoltaic modules. Within ASTM E1799, like IEC 61215, the visual inspection is performed before and after modules have been subjected to laboratory stress tests. Also, ASTM E1799 does not establish pass or fail levels. Like IEC 61215, ASTM E1799 has a reduced list of visual failures due to its scope.

Packard, Wohlgemuth and Kurtz [17] did an amazing work developing a tool for the evaluation of visually observable defects in fielded PV modules. In their work, they tried to adhere to IEC/UL (International Electrotechnical Committee/ Underwriters Laboratories Inc.) standard terminology and balance the collection of sufficient detail for failure mode evaluation against desires to minimize recording time per module.

The IEC is currently developing a new standard, IEC 62257-10 (ed. 2017), that for now is a Publicly Available Specification or a published draft. IEC PAS 62257-10 [121] is designed to be used as a guide to visually inspect front-contact mc-Si and c-Si solar PV modules for major defects. This standard presents its own checklist for major failures (specifying one checklist for new modules and other for used modules), but the components are inspected following the procedure developed by Packard et al. [17].

4.1.1 IEC 61215-1

IEC 61215 standard presents the requirements for the design qualification and type of approval of terrestrial photovoltaic modules suitable for long-term operation in general open-air

climates, as defined in IEC 60721-2-1. IEC 61215 applies for crystalline silicon and thin-film modules. Concentrator modules are not within the scope. The objective of the test sequence is to determine the electrical and thermal characteristics of the module and to to show, within the reasonable constrains of cost and time, that the module is capable of withstanding prolonged exposure in the climates described in the scope.

The sampling subjected to study corresponds to ten PV modules that are subjected to the test sequence flow shown in Fig. 4.1. Modules are divided into the groups according to the test sequence, which are group A (3 modules), group B (1 module) and group C-E (2 modules each). The test sequence must be carried out in the order specified. The MQT (Module Quality Test) designations in the boxes of Fig. 4.1 refer to the corresponding test definitions in IEC 61215-2.

According to IEC 61215-1, a PV module pass the qualification tests when it meets all the following criteria [122].

1. Verification of rated label values (Gate No. 1)

   (a) The measured maximum STC power ($P_{max}(lab)$) of each module in the stabilized state shall be equal or higher than the maximum rated nameplate power ($P_{max}(NP)$) of each module without tolerance. Must be noted that $P_{max}(lab)$ must consider the uncertainty of the laboratory's measurement and $P_{max}(NP)$ must consider the manufacturer's rated lower production tolerance for P_{max}.

   (b) The measured maximum open-circuit voltage ($V_{oc}(lab)$) of each module in the stabilized state shall be equal or less than the maximum rated nameplate open-circuit voltage ($V_{oc}(NP)$) of each module without tolerances. Must be noted that $V_{oc}(lab)$ must consider the uncertainty of the laboratory's measurement and $V_{oc}(NP)$ must consider the manufacturer's rated upper production tolerance for V_{oc}.

   (c) The measured maximum short-circuit current ($I_{sc}(lab)$) of each module in the stabilized state shall be equal or less than the maximum rated nameplate short-circuit current ($I_{sc}(NP)$) of each module without tolerances. Must be noted that $I_{sc}(lab)$ must consider the uncertainty of the laboratory's measurement and $I_{sc}(NP)$ must consider the manufacturer's rated upper production tolerance for I_{sc}.

2. Verification of maximum power degradation during type approval testing (Gate No. 2)

   (a) at the end of each test sequence or for sequence B after bypass diode test, the maximum power output drop of each module ($P_{max}(lab_{GateNo.2})$) shall be less than 5% of the module's initial measured output power ($P_{max}(lab_{GateNo.1})$). Must be noted that $P_{max}(lab_{GateNo.1})$ must consider the reproducibility. The reproducibility shall be less than the one stated for silicon crystalline technology within IEC 61215-1.

3. Electrical circuitry

   (a) Samples are note permitted to exhibit an open-circuit during the tests.

4. Visual defects

   (a) There is no visual evidence of mayor defect, as defined in the major visual defect list below.

5. Electrical safety

   (a) The insulation test (MQT 03) requirements are met after the tests.

   (b) The wet leakage current test (MQT 15) requirements are met at the beginning and the end of each sequence.

   (c) Specific requirements of the individual tests are met.

The major visual defects, which IEC 61215-1 considers, are defects that may cause a risk of reliability loss, including power output. The observations that are considered to be major visual defects are [122]:

- Broken, cracked, or torn external surfaces.
- Bent or misaligned external surfaces, including superstrates, substrates, frames and junction boxes to the extent that the operation of the PV module would be impaired.
- Bubbles or delaminations forming a continuous path between electric circuit and the edge of the module.
- If the mechanical integrity depends on lamination or other means of adhesion, the sum of the area of all bubbles shall not exceed 1% of the total module area.
- Evidence of any molten or burned encapsulant, backsheet, front-sheet, diode or active PV component.
- Loss of mechanical integrity to the extent that the installation and operation of the module would be impaired.
- Cracked/broken cells which can remove more than 10% of the cell's photovoltaic active area from the electrical circuit of the PV module.
- Voids in, or visible corrosion of any of the layers of the active (live) circuitry of the module extending over more than 10% of any cell.
- Broken interconnections, joints or terminals.
- Any short-circuited live parts or exposed live electrical parts.
- Module markings (label) are no longer attached or the information is unreadable.

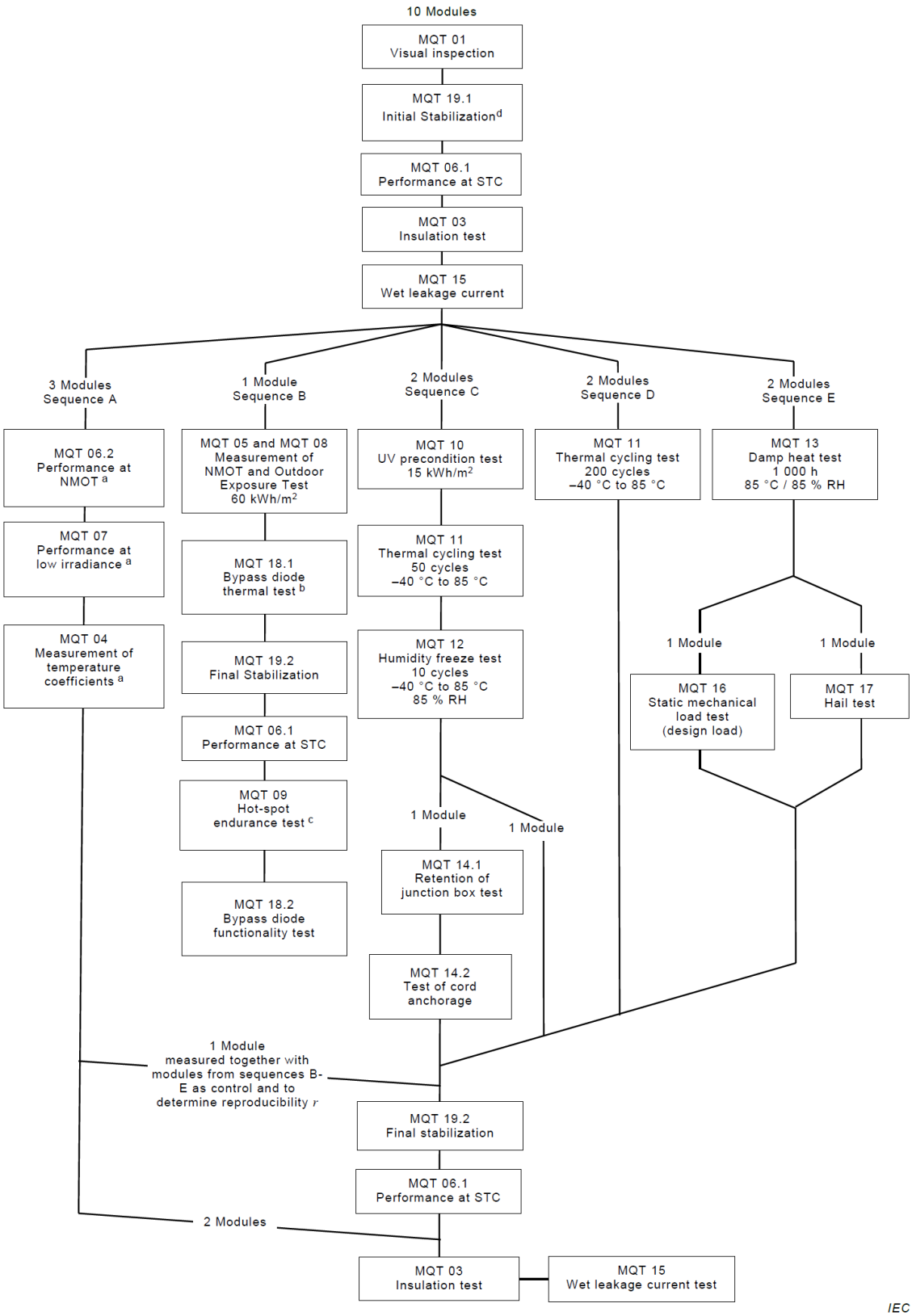

Figure 4.1: Qualification test sequence flow within IEC 61215-1. MQT corresponds to Module Quality Test [122].

4.1.2 ASTM E1799

ASTM E1799 [123], published in 2012, covers procedures and criteria for visual inspections of PV modules. The inspection of the modules is performed before and after the modules have been subjected to environmental, electrical, or mechanical stress testing. The use of this standard is to provide a recognized procedure for performing visual inspections and to specify effects that should be reported. Since the effects can be subjective, the determination of pass/fail criteria for a module is under the judgment of the user of this practice.

The procedure for visual inspection according to ASTM E1799 [123] is as follows:

The *Pre-Test Inspection*, as its name states, corresponds to the visual inspection of the module prior any stress test. The inspection in this stage consists in the determination of the presence or the absence of the anomalies presented in the list below.

- Shipping damage,
- Poor workmanship,
- Defects in mounting brackets or structures,
- Cracking, shrinkage, distortion, or tacky surfaces of polymeric materials,
- Failure of adhesive bonding,
- Bubbles or delamination of encapsulant materials,
- Presence of foreign material,
- Corrosion of fasteners, mechanical members, or electrical circuit elements,
- Voids in or corrosion of any thin-film photovoltaic layers,
- Discoloration of superstrate encapsulating materials,
- Discoloration of active photovoltaic elements,
- Broken, cracked, etched, scratched, wrinkled, or torn external surfaces,
- Broken or cracked active photovoltaic elements,
- Broken, cracked, or faulty electrical interconnections,
- Cracked or damaged structural elements,
- A photovoltaic cell touching another cell or the module frame,
- Electrical terminals not bonded to the module or the module junction box,
- Missing, peeling, or damaged metal layers on cell surfaces, and

- Any additional anomalies or defects specified by the user of this practice that are evident.

Once the anomalies are determined within the module, the standard does not specify any procedure for the documentation. ASTM E1799 [123] states that "the records may be any combination of descriptions, diagrams, or images of any anomalies or defects noticed during the inspection". Although, the standard specifies that the location of the defect must be unambiguously documented.

The *Post-Test Inspection* repeats the visual examination made in the pre-test inspection after modules underwent stress testing. The examination must be done in the same conditions as in the pre-test examination. The recording of anomalies in this case consider only new information or changes in comparison with the pre-test information.

Finally, ASTM E1799 [123] indicates that the user must do the comparison between pre- and post-test inspections to determine the visible effects of the stress testing on the test samples. According to the standard, the report shall at least include: (1) any anomalies/defects that were found in addition to the list above, (2) results of both visual inspections and (3) determination of the visible effects of the stress testing.

4.1.3 IEC PAS 62257-10

IEC PAS 62257-10 clarifies, at the beginning, the terminology that is used within their draft. The clarification, shown in Fig. 4.2, is made for the front and the back of a PV module and is also detailed for the front of a single c-Si solar cell. When the cell interconnect ribbon is perfectly aligned with the busbar, the busbar cannot be seen because is completely covered by the ribbon.

This draft also provides a comparative rating of the severity of the defects. The scale range of severity is from 1 (green) to 5 (red) while there is also a symbol that indicates the presence of a safety risk. Fig. 4.3 shows an example of a failure with a severity of 4 that induce a safety risk.

Table 4.1 explains the meaning of each severity number and the safety risk symbol. It is important to understand that the symbol "S" is separated from the quantitative scale. This symbol just enunciates if a defect presents a safety risk or not, while the quantitative scale indicates the severity of the defect.

Fig. 4.4 and Fig. 4.5 show real examples for specific defects that presents a safety risk. The missing label has a severity of 1 while the burn mark at the backsheet has a severity of 5.

This document includes recommendations on an inspection procedure and accept/reject criteria. In general and briefly, the document indicates the following inspection procedure:

1. Identify and differentiate the different product types/sizes to be inspected.

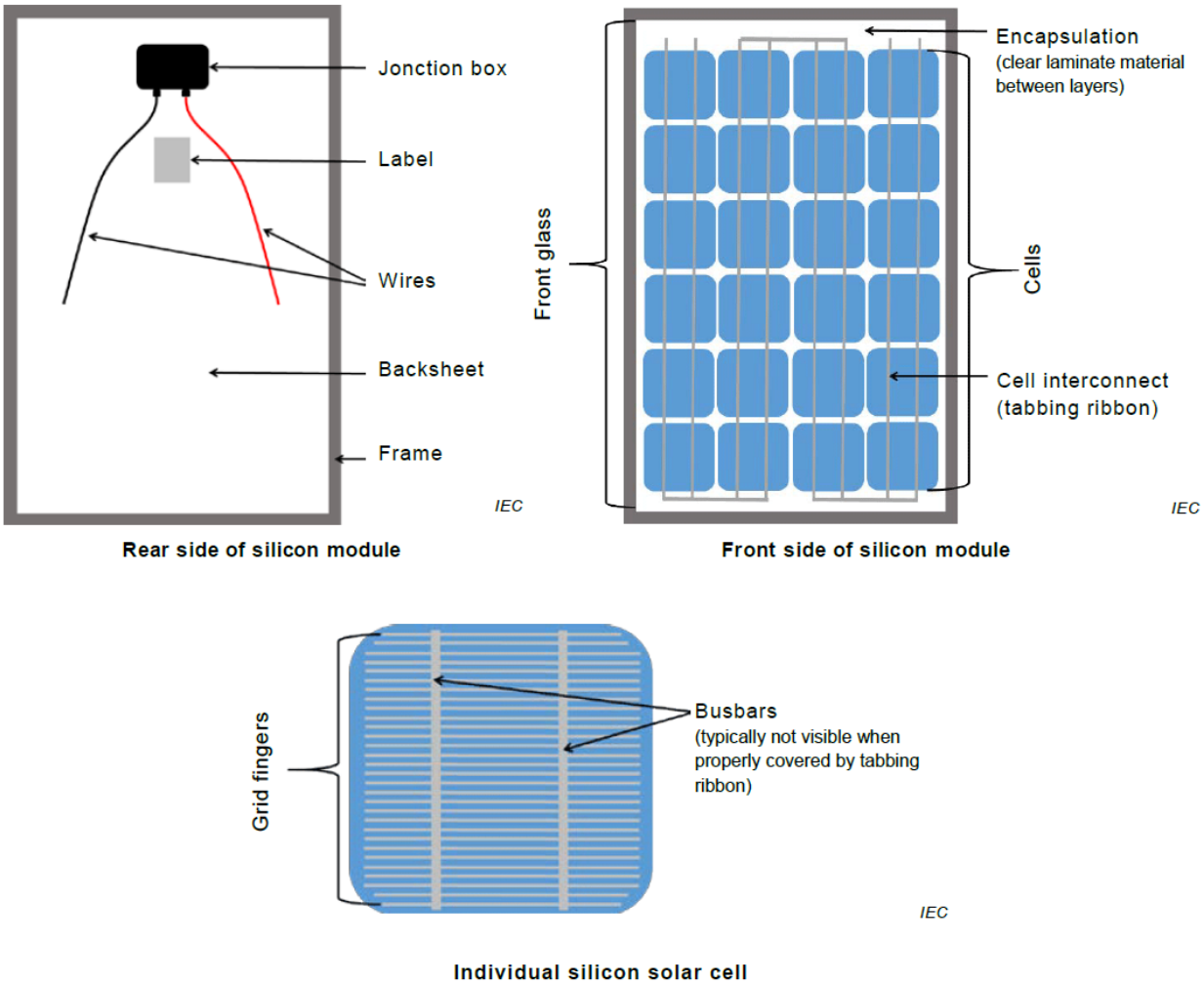

Figure 4.2: Clarification of terminology used within IEC 62557-10 [121].

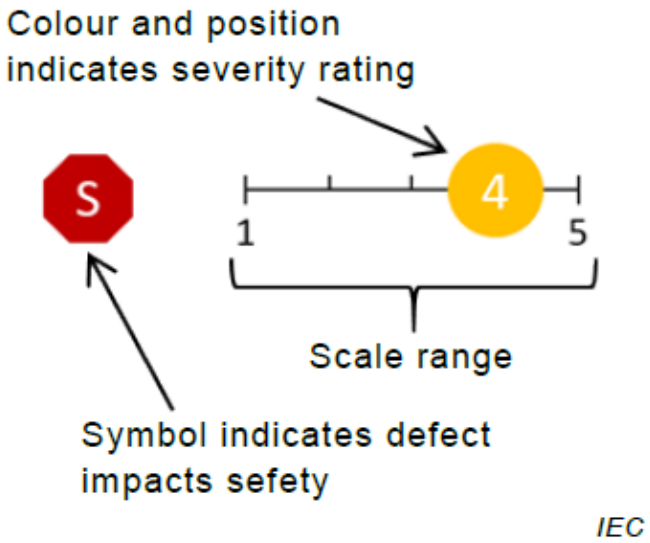

Figure 4.3: Severity rating for defects used within IEC 62557-10 [121].

2. Select a minimum of 8 samples of each size/type randomly for inspection (see IEC 61215)

3. The inspector should complete one checklist per sample, proceeding through the list of defects in the order in which they are presented.

   (a) For each defect complete the checklist with an indication of defect presence, severity and whether or not the defect presents a potential safety risk.

   (b) If needed take photos of the defects, with overview photos of the front, back and label of the module.

   (c) For used samples, both "new" and "used" checklists should be completed in this order.

   (d) Once the inspection checklist is complete the inspector can determine if the module is acceptable using the accept/reject criteria.

Table 4.1: Symbology of the severity scale range and defects safety risk used within IEC 62557-10 [121]

Key	**Explanation**
S	Symbol indicating a safety risk, separate from quantitative scale
1	The defect is an indicator of poor quality with no direct effect on performance or reliability
2	The defect has a minor impact on performance and/or reliability
3	The defect has a moderate impact on performance and/or reliability
4	The defect has a high impact on performance and/or reliability
5	The defect is indicative of a major quality issue, a critical failure, or counterfeit panel

The recommended accept/reject criteria within IEC 62257-10, which can be modified depending on the application and the end user, is briefly described in the following paragraph.

A PV module sample will be considered to be rejected due to its observable quality defects if any of the following conditions are met:

1. If any single observed defect has been evaluated as a severity of 5.

2. If any single observed defect has been evaluated to pose a safety risk.

3. If any combination of observed defects that have a summed severity score greater than or equal 5 (this number can be changed at the discretion of the end user)

4. If any module that is expected to be new shows any of the used module defects.

Annex A within IEC 62257-10 contains two checklists (for new and used modules), which includes the following defects:

1. Checklist for new modules:

   (a) Label: missing, poorly attached, information is missing, incorrect spelling

   (b) Backsheet: delamination

   (c) Junction box: faulty electrical connection, cracks/breaks/gaps in housing, sealant failure, electrical polarity nor indicated

   (d) Wiring: wire(s) missing or poorly attached, too short and/or too thin

   (e) Frame: damaged, adhesive/sealant failure

   (f) Front glass: cracking, scratches

   (g) Encapsulation: delamination

   (h) Cells: fake, dummy pieces disguising missing material, cracks, partially covered, scratches, differently sized, edge chips, all cells very shiny

   (i) Cell metallization: fingers not connected to busbar, not the same pattern on all cells, fingers off of the edge of the corner of the cells

   (j) Cell interconnection: interconnection is discontinuous, cells connected in parallel (counterfeit), poorly aligned and/or soldered, cells connected in parallel (real cells)

2. Checklist for used modules:

   (a) Label: see new module checklist

   (b) Backsheet: burn marks, discoloration (in addition to new module checklist)

   (c) Junction box: see new module checklist

   (d) Wiring: cracks or exposed metal (in addition to new module checklist)

   (e) Frame: see new module checklist

   (f) Front glass: see new module checklist

   (g) Encapsulation: discoloration (in addition to new module checklist)

   (h) Cells: snail trails, shiny locally/inconsistent color (in addition to new module

checklist)

(i) Cell metallization: see new module checklist

(j) Cell interconnection: see new module checklist

Annex B and C within IEC 62257-10 contain a catalogue of defects for new and used modules respectively. Fig. 4.4 and Fig. 4.5 show an example for a defect within the Annex B and Annex C respectively.

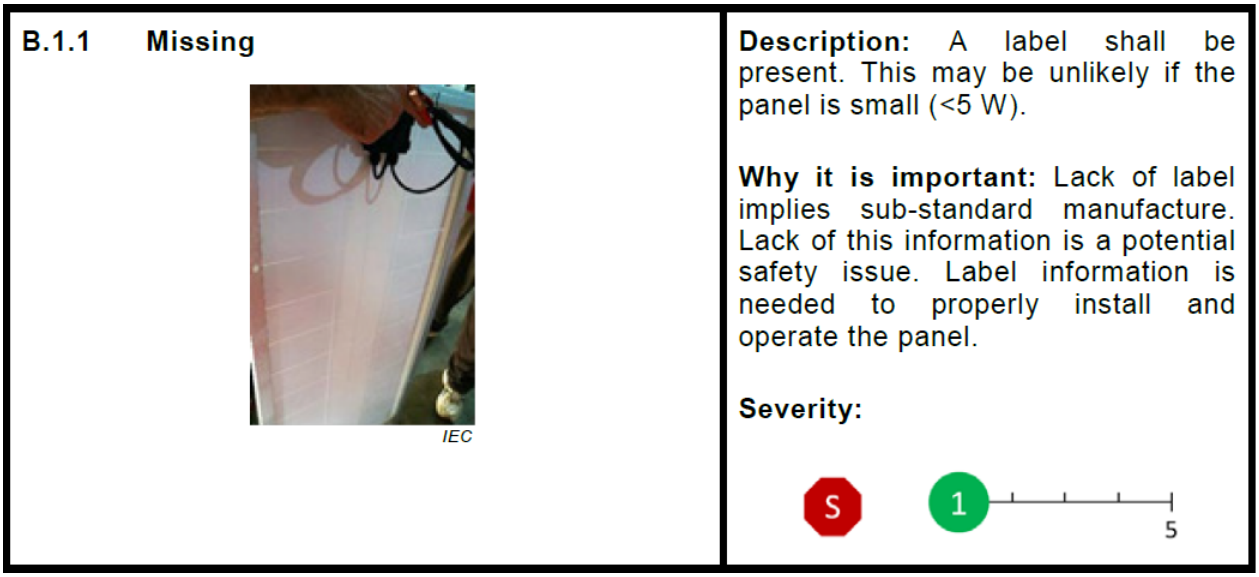

Figure 4.4: Defect for a new module within Annex B from IEC 62557-10 [121].

Figure 4.5: Defect for a used module within Annex C from IEC 62557-10 [121].

4.1.4 NREL visual inspection data collection tool

Packard et al. [17] designed a visual inspection data collection tool for the evaluation of fielded PV modules, to describe the condition of PV modules with regard to field performance. Their objective was to regularize the collection of the data to minimize time while collecting sufficient information from the PV modules. The tool is composed of 14 sections included in their appendix A1 [17]. Sections 1-2 collect information about field site, system configuration, and module identification. Sections 3-13 focus on individual components, starting from the back and ending at the front of the module. The final section, which is 14, focuses on electronic records.

Appendix A2 [17] contains a presentation with photographic examples of real defects as a complement. This presentation provides example photographs for training purposes for the cataloging of module condition by visual inspection. Fig. 4.6 shows an example of a photograph within the presentation. Within Fig. 4.6, a failure of the adhesive of the junction box is shown. The slide explains how the failure must be classified. Additionally, another example is shown in Fig. 4.7 that explains how must be classified a failure of the sealant of a frame-less PV module. The presentation contains at least one example for each section (from 1 to 14) of the visual inspection form.

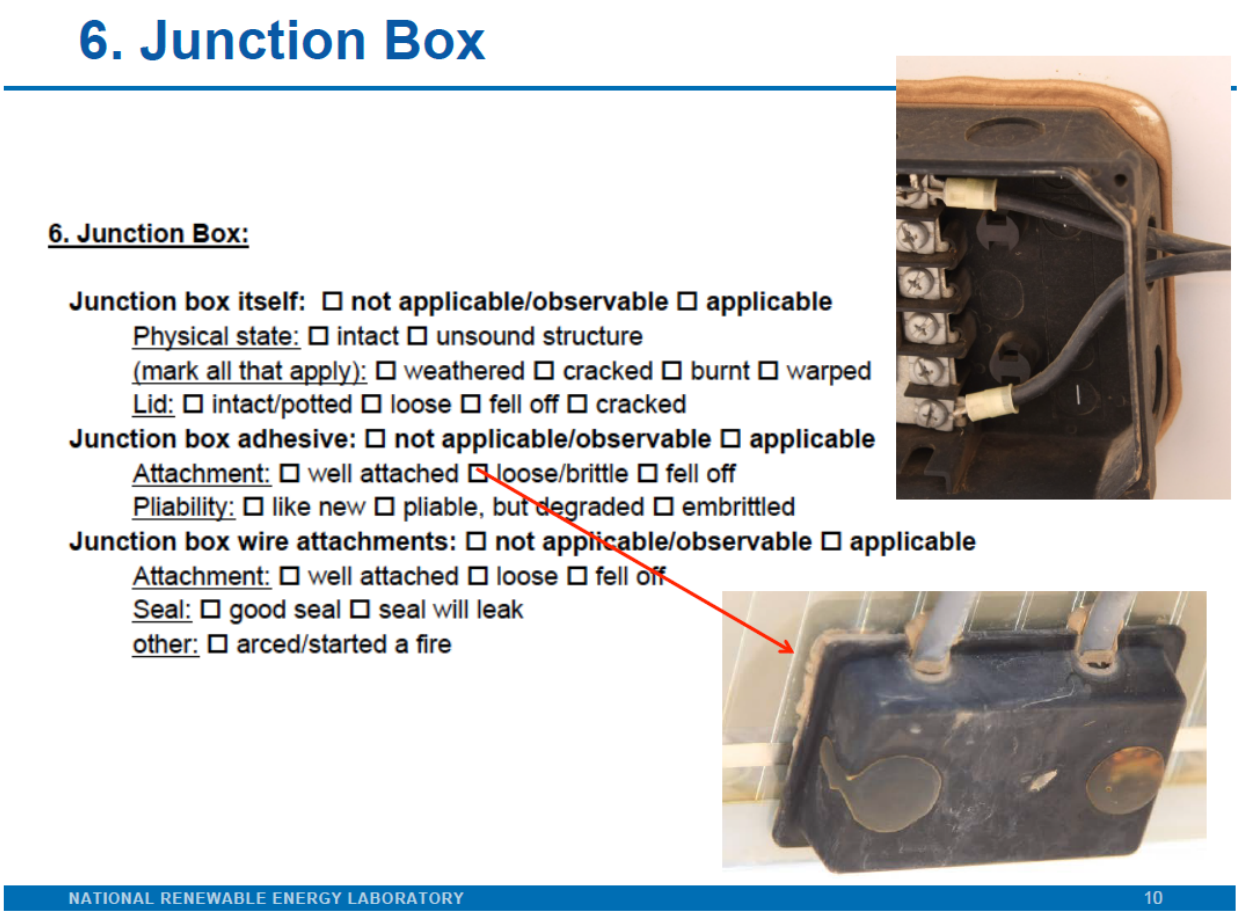

Figure 4.6: Junction box adhesive loose/brittle [17].

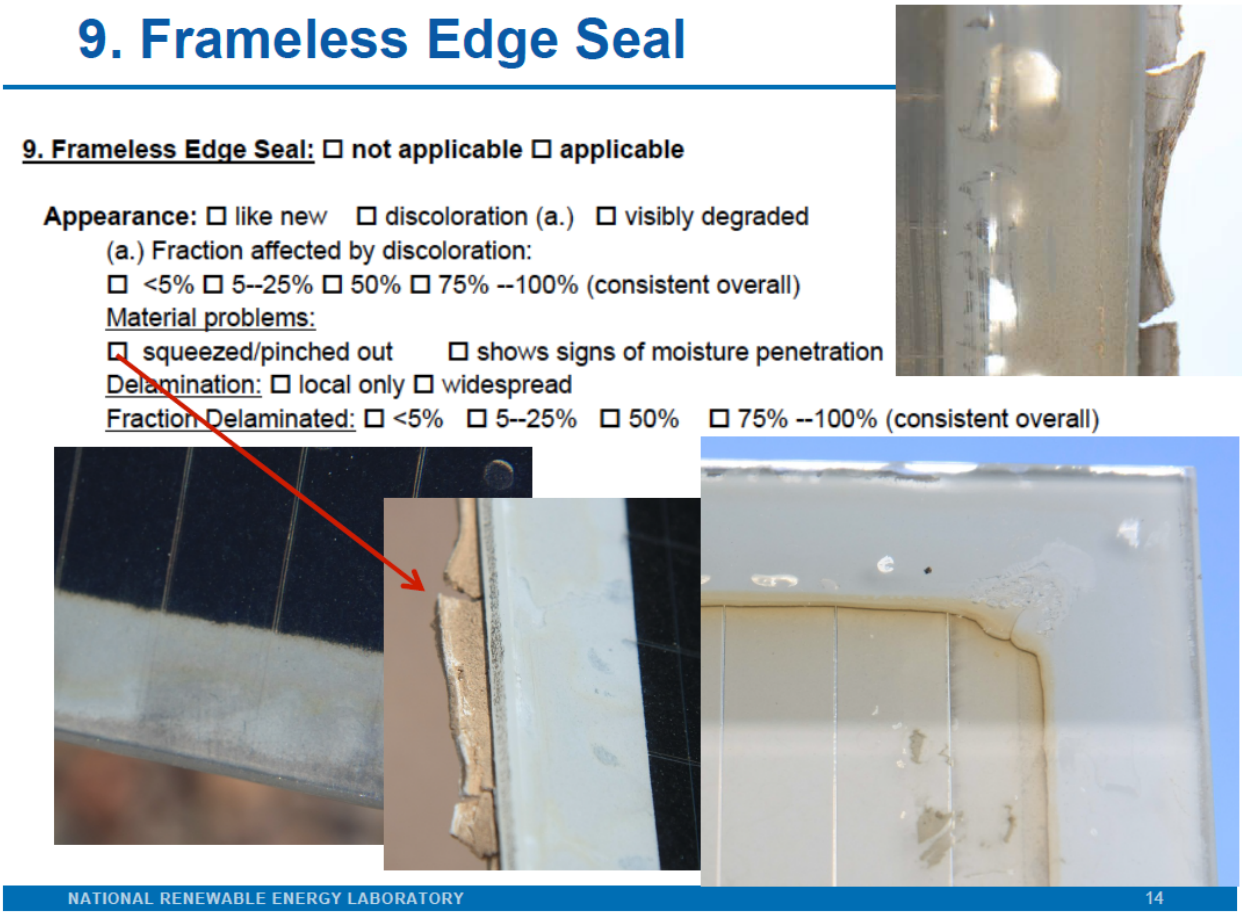

Figure 4.7: Frameless edge seal squeezed/pinched out [17].

Within the visual inspection data tool, detailed instructions are given for each part to reduce ambiguity and variation in the survey responses. If a new type of defect is found that cannot be classified according to the tool, a section with "Other" (at the end of the collection tool) is available for the recording of this new observation. According to Packard et al. [17], the visual collection tool within the appendix A1 takes approximately 8 minutes to be conducted by a pair of two experienced inspectors. It is often necessary to inspect a large number of PV modules in a short time, which does not need such amount of detail. For this cases, Packard et al. [17] developed a short version of the visual collection tool that is provided in their appendix A3.

The short version of the visual inspection tool follows the same structure and format as the long version, while removing damage location and quantification of damage extent. Fig. 4.8 shows an example of the section 4, which collects defects and anomalies of the backsheet, of the long version. It can be seen in Fig. 4.9 that the short version collects considerably less information. The long version considers the number of times that one defect is present in the sample and/or the percentage of the extension of the defect over the whole surface of the sample. The short version does not consider such details.

According to Packard et al. [17], electronic records are not necessary. However, if electronic records are taken, they recommend the use of an I-V tracer and a thermal camera.

4. Backsheet: ☐ **not applicable** ☐ **applicable**

Appearance: ☐ like new ☐ minor discoloration ☐ major discoloration
Texture: ☐ like new ☐ wavy (not delaminated) ☐ wavy (delaminated) ☐ dented
Material quality --chalking: ☐ none ☐ slight ☐ substantial
Damage: ☐ no damage ☐ small, localized ☐ extensive

Damage Type (mark all that apply):
☐ burn marks (a.) ☐ bubbles (b.) ☐ delamination (c.) ☐ cracks/scratches (d.)

(a.)Burn marks (#):☐ 1 ☐ 2 ☐ 3 ☐ 4--10 ☐ >10
Fraction of area burned:
☐ <5% ☐ 5--25% ☐ 50% ☐ 75% --100% (consistent overall)
(b.) Bubbles(#): ☐ 1 ☐ 2 ☐ 3 ☐ 4--10 ☐ >10
Average bubble dimension: ☐ <5mm ☐ 5--30mm ☐ >30mm
Fraction of area with bubbles > 5 mm:
☐ <5% ☐ 5--25% ☐ 50% ☐ 75% --100% (consistent overall)
(c.) Fraction of area delaminated:
☐ <5% ☐ 5--25% ☐ 50% ☐ 75% --100% (consistent overall)
Fraction of delamination that exposes circuit or cell(s)
☐ <5% ☐ 5--25% ☐ 50% ☐ 75% --100% (consistent overall)
(d.) Cracks/scratches (#): ☐ 1 ☐ 2 ☐ 3 ☐ 4--10 ☐ >10
Cracks/scratches location: ☐ random/no pattern ☐ over cells ☐ between cells
Fraction of area affected by cracks/scratches (approx.):
☐ <5% ☐ 5--25% ☐ 50% ☐ 75% --100% (consistent overall)
Fraction of cracks/scratches that expose circuit (approx.):
☐ 0% ☐ 25% ☐ 50% ☐ 75% ☐ 100%

Figure 4.8: Section 4 of the long form of the visual inspection tool within NREL appendix A1 [17].

4. Backsheet: ☐ **not applicable** ☐ **applicable**

Appearance: ☐ like new ☐ minor discoloration ☐ major discoloration
Texture: ☐ like new ☐ wavy (not delaminated) ☐ wavy (delaminated) ☐ dented
Material quality --chalking: ☐ none ☐ slight ☐ substantial
Damage: ☐ no damage ☐ small, localized ☐ extensive

Damage Type (mark all that apply):
☐ burn marks ☐ bubbles ☐ delamination ☐ cracks/scratches

Figure 4.9: Section 4 of the short form of the visual inspection tool within NREL appendix A3 [17].

4.2 I-V Curve Measurements

Two (international) standards exist that explain how to correctly obtain the current-voltage (I-V) characteristic of a PV module. IEC 60904-1 describes the procedures to obtain the curve under natural or simulated sunlight source, which are applicable to a single solar cell, a string of solar cells or an entire PV module. Within the standard, requirements for the measurement are explained. Additionally, IEC 60904-1 specifies the apparatus required for the measurements for both light sources (natural or simulated).

The other standard, ASTM E1036, contains more information and instructions than IEC 60904-1. ASTM E1036 makes a summary of the test methods used to measure the performance of the PV module (or array). The standard also specifies the apparatus required, procedures to obtain the data, calculation to the correction of the data points and minimum mandatory reporting requirements.

The next sections covers the review of both previously mentioned standards.

4.2.1 IEC 60904-1

IEC 60904-1 [124] describes the procedures to measure the I-V curve of PV modules under natural or simulated sunlight. Multijunction PV modules and concentrator PV modules are not in the scope, but they can be considered under certain circumstances. The purpose of this standard is to minimizing measurement uncertainty.

4.2.1.1 Equipment list (with specifications)

According to IEC 60904-1 [124], the necessary equipment to perform the I-V curve measurements in natural sunlight are the following:

a. *PV Reference Device or Pyranometer* —A PV reference devices (e.g. reference cell) or a pyranometer. PV reference devices must be calibrated in conformance with IEC 60904-2 [125] and its spectral response shall be matched with the spectral response of the test PV module. If a spectral mismatch exists, a correction of the spectral mismatch must be performed in conformance with IEC 60904-7 [126]. According to IEC 60904-10 [127], the short-circuit current of the PV reference device must be linear over the irradiance range of interest.

b. *Temperature Measurement Device A* —A device to measure the temperature of the PV reference device. This device must have an accuracy of ±1°C with repeat-ability of ±0.5°C. If the reference devices is a pyranometer, its temperature measurement is not required.

c. *Temperature Measurement Device B* —A device to measure the temperature of the test PV module. This device shall determine the temperature of the test PV module using

the Equivalent Cell Temperature (ECT) method in conformance with IEC 60904-5 and must have an accuracy of ±1°C with repeat-ability of ±0.5°C.

d. *Two-axis Tracking System* —The tracking system must be capable of tracking the sun with an accuracy of ±5°.

e. *Spectroradiometer* —This device is used to measure the spectral irradiance of the sunlight. It must be capable of measuring the spectrum in the range of the spectral response of the test PV module and the reference cell.

f. *Voltage and Current Measurement Devices* —Voltage and current of the test PV module must be measured using independent leads from the terminals of the test PV module. Therefore, 4-wire connections should be used. The accuracy of the open-circuit voltage and short-circuit current shall be ±0.2%.

g. *Variable Bias* —The short-circuit current, which is measured at zero voltage, shall be measured using a variable bias (preferably electronic) to offset the voltage drop across the external series resistance of the test PV module.

4.2.1.2 Inspection procedure

With regard to the procedure to use these measurement devices, IEC 60904-1 [124] states the following instructions:

1. Mount the reference device near and co-planar (±2°) with the test module on the two-axis tracker. Both shall be normal to the direct solar beam with ±5°. Connect the voltage, current and temperature measurement devices.

2. If the test module and the reference device are equipped with temperature control, set the control to the desired value. If not, there are three methods to do the same:

   (a) shade the test module and the reference device from the sun and wind until their temperature is uniform within ±2°C of the ambient temperature, or

   (b) wait until the test module achieves thermal equilibrium, or

   (c) pre-condition the test module to a point below the target temperature and let it reach thermal equilibrium.

3. Record the *I-V* curve and temperature of the test module in concordance with the recording of the output and temperature (if necessary) of the reference device. The measurements can be done immediately after removing the shade.

   (a) To measure the short-circuit current, offset the voltage drop across the test module at zero voltage with the variable bias. Alternatively, the short-circuit current may be extrapolated from the *I-V* curve. The extrapolation shall be performed using a voltage that is not higher than 3% of the test module open-circuit voltage and

can be performed only if the relationship between the current and voltage is lineal.

(b) Ensure that the test module and the reference device temperature are stable within ±1°C and that the measured irradiance (using the reference device) remains constant within 1% during the recording period.

4. If a pyranometer is used, perform a simultaneous measurement of the spectral irradiance using the spectroradiometer.

4.2.1.3 Calculations and corrections

IEC 60904-1 [124] indicates the following calculations and corrections after the measurements:

a. Calculation of the effective irradiance for the test module under the AM1.5 spectrum (described in IEC 60904-3 [128]) using the test module spectral response (see IEC 60904-7 [126]).

b. Correct the measured I-V curve to the desired irradiance and temperature conditions in concordance with IEC 60891 [129] (for linear devices).

4.2.1.4 Test report

According to IEC 60904-1 [124], the test report with the performance characteristics and test results shall be in accordance with ISO 17025 [130].

4.2.2 ASTM E1036

ASTM E1036 [131] explains the test methods for "Electrical Performance of Nonconcentrator Terrestrial Photovoltaic Modules and Arrays Using Reference Cells". The electrical performance of a PV device is derived from its I-V curve. The minimum electrical characteristics that are needed to obtain the performance are: short-circuit current, open-circuit voltage, maximum power, and voltage at maximum power.

The test methods are intended to obtain the electrical performance of the PV device (modules or arrays) under natural or simulated sunlight. The scope of this standard consider only nonconcentrator PV modules or arrays that do not contain series-connected PV multijunction devices.

4.2.2.1 Equipment list (with specifications)

To be able to go through the methods, the apparatus that ASTM E1036 indicates as necessary are:

a. *Photovoltaic Reference Cell* —A calibrated reference cell to determine the total irradiance during electrical performance measurement. The spectral mismatch parameter (determined by ASTM E973 [132]) between the reference cell and the test module must be equal or less than 1.00 ± 0.05. ASTM E1040 [133] recommends physical characteristics of reference cells.

b. *Test Fixture* —The test module must be mounted in a test fixture that facilitates temperature measurement and four-wire current-voltage measurements. Arrays installed in the field must be tested as installed.

c. *Kelvin Probe* —An arraignment of contacts for the test module. One pair in parallel to measure the voltage across the test module and the other pair in series to measure the current flowing through the test module (see ASTM E948 [134]).

d. *Light Source* —The light source shall be either natural sunlight or a solar simulator (class A, B or C simulation as specified in ASTM E927 [135]).

e. *Temperature Measurement Equipment* —Equipment to measure the temperature of the test module and the reference cell (or reference module). The equipment shall have a resolution of 1°C and a total error of less than ±1°C of reading. Multiple sensors shall be attached to the test module and the averaged must be used to obtain the test module temperature.

f. *Variable Load* —The test module must be tested at different points along its I-V curve. Therefore, an electronic load is needed. The load should be capable of operating within 1% of V_{oc} and 1% of I_{sc} of the test module and should allow the test module output power to be varied in increments as small as 0.2% of the test module maximum power.

g. *Current Measurement Equipment* —Equipment to measure the current through the test module and the short-circuit current of the reference cell (or reference module). The resolution of the equipment shall be at least 0.05% of the maximum current encountered, and shall have a total error of less than 0.2% of the maximum current encountered.

h. *Voltage Measurement Equipment* —Equipment to measure the voltage across the test module. The resolution of the equipment shall be at least 0.05% of the maximum voltage encountered, and shall have a total error of less than 0.2% of the maximum voltage encountered.

In relation to the reference cell, the device can be calibrated under any distribution of irradiance, such as direct normal or global spectrum. The reference cell therefore determines to which spectrum the test module performance is referred. Hence, it is a requirement that the spectral response of the reference cell must be close to the spectral response of the test module. Also, the spectral distribution of the light source and the spectral response of the reference cell must be known. The difference between both spectral distributions must be accounted by the correction of the calibration constant of the reference cell using the spectral mismatch parameter (defined in point 1 within the apparatus list).

About the test measurements, they can be made in any conditions. Once they are taken,

the measurement data can be numerically translated to standard conditions (STC), to nominal operating conditions (NOC), or to any conditions required from the user. STC and NOC are shown in Table 4.2. The performance at the reporting conditions (RC) shown in Table 4.2 are obtained in two different ways depending on a requirement. If the test conditions are such that the device temperature is within ±2°C of the RC temperature and the total irradiance is within ±5% of the RC irradiance, the numerical translation consists of a correction of the measured device current based on the total irradiance during the I-V measurement. If the requirement is not met, according to ASTM E1036, performance at RC is obtained from four separate I-V measurements at temperature and irradiance conditions that bracket the desired RC using a bilinear interpolation method.

Table 4.2: Reporting conditions [131]. NOCT corresponds to nominal operating cell temperature.

Reporting Conditions	**Total Irradiance** Wm^{-2}	**Spectral Irradiance**	**Device Temperature** °C
Standard reporting conditions	1000	ASTM G173 STD Spectra	25
Nominal operating conditions	800	...	NOCT

4.2.2.2 Inspection procedure

Regarding to procedures to obtain the performance of the test module, ASTM E1036 explains two techniques. The *Momentary Illumination Technique* (MIT) is valid when the source light is a pulsed solar simulator, shuttered continuous solar simulator, or shuttered sunlight while *Continuous Illumination Technique* (CIT) is valid for testing in continuous solar simulators or natural sunlight. According to ASTM E1036 [131], the procedures for CIT are the following:

1. Determine the spectral mismatch parameter, M, using ASTM E973 [132].

2. Mount the reference cell and the module test in the test fixture co-planar within ±2°, and normal to the illumination source within ±10°. If the test module cannot be aligned within ±10°, the solar angle of incidence, the test module orientation and its tilt angle must be reported with the data.

3. Connect the four-wire Kelvin probe to the test module output terminals.

4. Expose the test module to the illumination source for a period of time sufficient for the module to achieve thermal equilibrium.

5. The total irradiance may be determined prior to the performance measurement if the temporal instability of the light source is less than 0.1% (as defined in ASTM E927 [135]). For this case, measure the short-circuit current of the reference cell, I_r.

6. Obtain the average temperature, T_c, of a cell in the module. One method is to use the temperature measurement equipment specifies in the apparatus list above. Another method can be use for outdoor testing, if the NOCT correction factors are known. For this method, the ambient air temperature and the wind speed must be measured.

7. Measure the reference cell temperature, T_r.

8. Measure the I-V curve of the test module by changing the value of the electronic load. At each point of the I-V curve, measure the test module voltage, test module current and I_r. If the temporal instability of the light source is less than 0.1% (as defined in ASTM E927 [135]), it is not necessary to measure I_r at each point.

9. Once the I-V curve is obtained, verify that the change in temperature during the test is less than 2°C.

10. If the test conditions are such that the device temperature is not within ±2°C of the RC temperature or the total irradiance is not within ±5% of the RC irradiance, repeat three times all previous steps to obtain a total of four I-V curves for the bilinear interpolation method.

4.2.2.3 Calculations and corrections

Before reporting the data, a few values must be corrected and other must be calculated. ASTM E1036 [131] mentions the following corrections and calculations:

1. Adjustment of the reference cell calibration constant.

2. Calculation of the total irradiance during the performance measurement(s).

3. If the test conditions are such that the device temperature is within ±2°C of the RC temperature and the total irradiance is within ±5% of the RC irradiance, correction of the current at each point of the I-V curve for irradiance must be made. If the provision is not met, the bilinear interpolation method must be used to calculate the I-V curve at RC using the four I-V curves obtained in the procedure.

4. Determination of the short-circuit current, I_{sc}, from the I-V curve. If an I-V data pair exists where V is 0.0 ± 0.005 V_{oc}, I from this pair can be considered to be I_{sc}. If such point does not exists, the short-circuit current must be calculated from several I-V data pairs where V is closest to zero using linear interpolation or extrapolation.

5. Determination of the open-circuit voltage, V_{oc}, from the I-V curve. If an I-V data pair exists where I is 0.0 ± 0.001 I_{sc}, V from this pair can be considered to be V_{oc}. If such point does not exists, the open-circuit voltage must be calculated from several I-V data pairs where I is closest to zero using linear interpolation or extrapolation.

6. If the test conditions are such that the device temperature is not within ±2°C of the RC temperature or the total irradiance is not within ±5% of the RC irradiance, use

the bilinear interpolation method to calculate the I-V curve.

7. Formation of the PV curve by multiplying V_o (voltage at RC) by I_o (current at RC).

8. Determination of the maximum power point P_m, and the corresponding V_{mp}, in the PV curve. The procedure for this, specially for modules with FF (Fill Factor) greater than 80%, considers the execution of a fourth-order polynomial least-squares fit to the PV curve.

9. Calculation of the FF of the PV module.

4.2.2.4 Test report

Finally, ASTM E1036 [131] describes the minimum mandatory reporting requirements that are grouped into four different sections. The sections are *Test Module or Array Description*, *Reference Cell (or Module) description*, *Test Conditions* and *Test Results*.

4.3 Thermal Imaging

4.3.1 Basic principles of radiometry

The definition of radiometry, in the field of physics, corresponds to a set of techniques to detect and measure electromagnetic waves and its magnitudes. These techniques are based on Planck's law and Stefan-Boltzmann's law, which in turn are based on the behavior of a black body. First, it is important to understand the basics of radiometry and then to get an idea of the optic properties of matter. Knowledge of radiometry will give insights about how electromagnetic radiation behaves and how can it be measured while optic properties of matter will give a perception of what are the important parameters that must be considered when taking a measurement.

Radiometry describes energy transfer when the heat exchange to reach thermodynamic equilibrium cannot be transferred by conduction or convection, just radiation. When two objects in the middle of the vacuum are at different temperatures and they do not touch one another, the hottest object transfers energy to the coolest object via radiation until they are at the same temperature. The electromagnetic spectrum, shown in Fig. 4.10, indicates the range of wavelengths for each type of electromagnetic waves. Specifically for thermographic studies, the important types of waves are ultraviolet (UV, 100 nm - 400 nm), visible (VIS, 400 nm - 800 nm) and infrared (IR, 800 nm - 10^6 nm). The thermal radiation wavelength is from 100 nm to 10^5 nm while most of the solar radiation wavelength is from 300 nm to 3000 nm.

All matter emits radiation except when it is at 0 K (or -273.15°C). The *radiance* of the emitting surface is the power of the electromagnetic waves that the surface emits in a

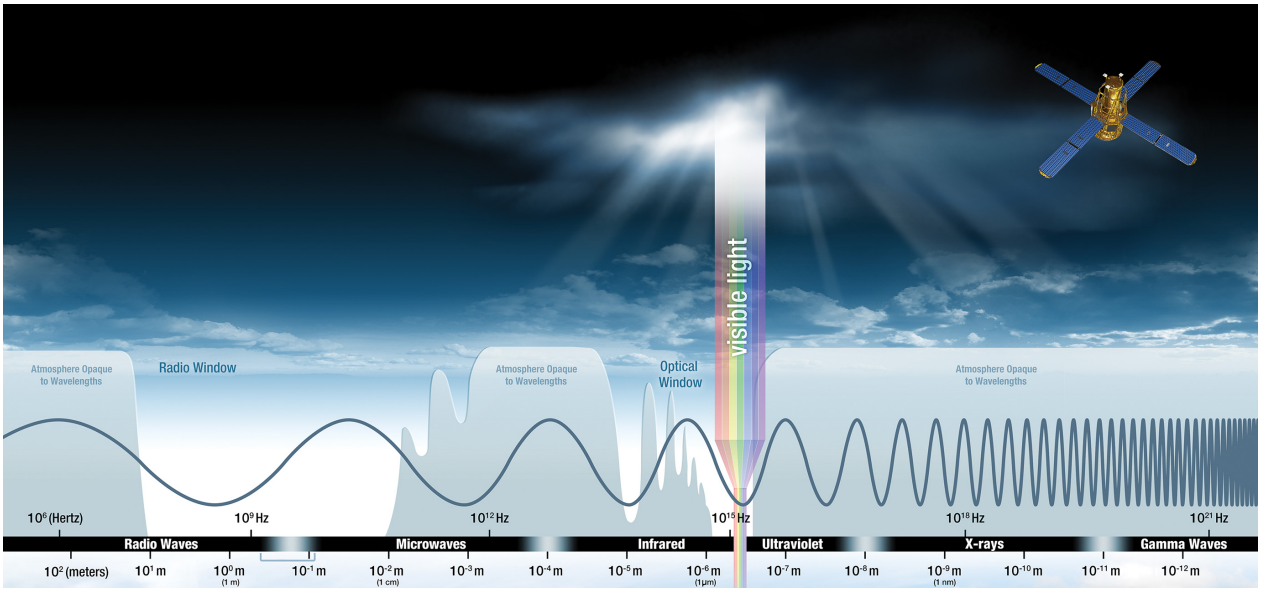

Figure 4.10: A scheme of the electromagnetic spectrum with indication of frequencies and wavelengths. Image obtained from `https://science.nasa.gov`.

determined direction per solid angle and apparent emitter's surface. Hence, the radiance units are $Wm^{-2}sr^{-1}$. *Irradiance* is the same power that impacts a surface in a determined direction per solid angle and apparent receptor's surface. Radiance and irradiance have the same units because they are considering the same power density, but the reference system of radiance is the emitter and of irradiance is the receptor.

A black body is an ideal object (just theoretical, not real) that absorbs all incident radiation from any direction and at any wavelength. The emission of a black body depends on the wavelength and its temperature, but does not depend on direction. This means that a black body is a diffuse emitter. Fig. 4.11 shows the spectral radiant emittance of a black body. It can be seen that at higher temperatures the peak of spectral radiance occurs at lower wavelengths. Several can be done by this phenomenon. Humans can only see in the visible range, therefore the emission of radiation of surfaces at low temperature can be seen with cameras in the correct spectral range. Metals heated by a blacksmith display a red color at high temperatures. If the temperature of the metal continues to increase, the metal will display a brighter color because the sum of the visible spectra is white.

According to *Planck's law*, the spectral radiance distribution, $E_{b\lambda}$ (in $Wm^{-2}nm^{-1}$), emitted by a black body depends on the wavelength, surface temperature, speed of light and refractive index of the medium. The total radiance, E_b (in Wm^{-2}), of a black body corresponds to the integration of the spectral radiance distribution for all the wavelengths. The total radiance is directly proportional to the Stefan-Boltzmann constant σ (5.67×10^{-8} $Wm^{-2}K^{-4}$) and to the fourth power of its surface's temperature. This last relationship is known as *Stefan-Boltzmann law*.

It is known that at a given temperature, no surface can emit more energy than a black body. The *emissivity*, ε, is a surface property that indicates this limitation of energy emission of a real object in comparison to a black body. The emissivity can be different for each

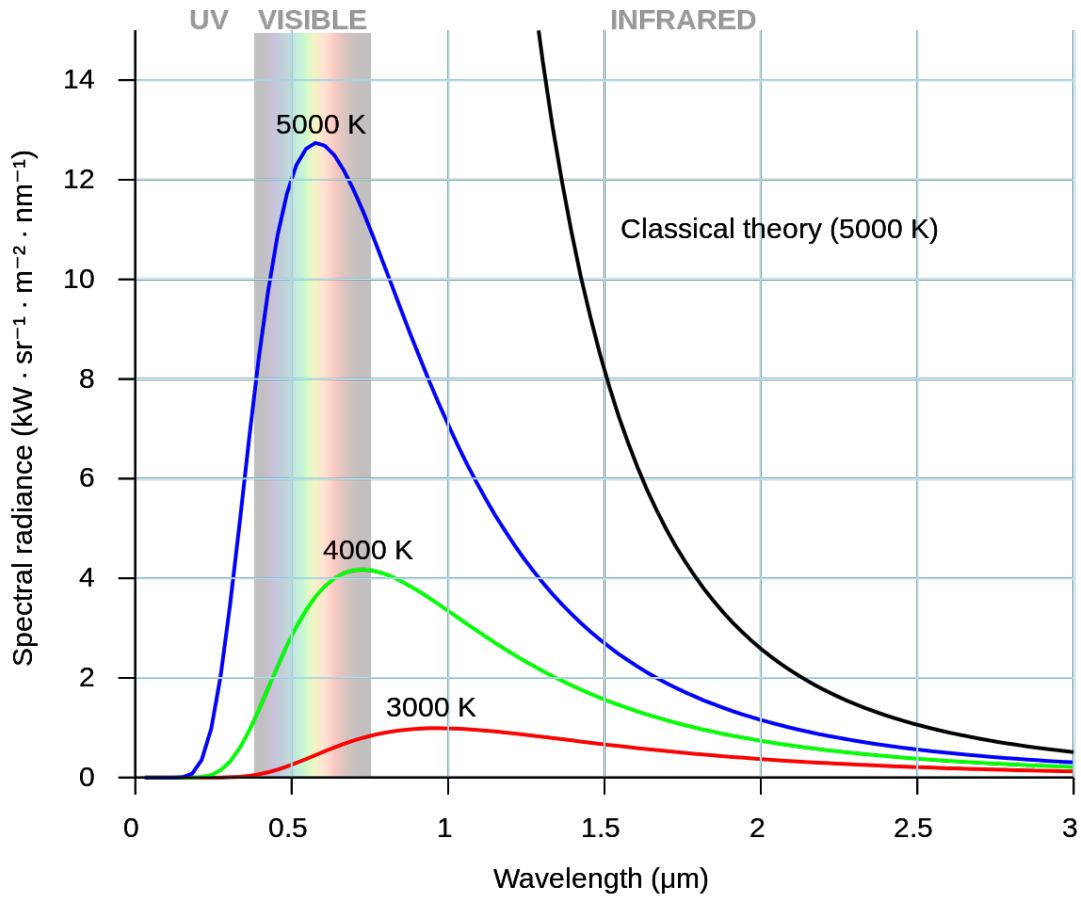

Figure 4.11: Spectral radiant emittance of a black body at different temperatures. Image obtained from `https://en.wikipedia.org/wiki/Black-body_radiation`.

wavelength and depends on factors such as temperature, surface conditions (e.g. clean, dirty, polished, new, old, etc.) and emission angle. Since the emissivity is defined as the ratio of the emitted radiation of a surface to the emitted radiation of a black body at the same temperature, the emissivity of a black body is 1 and the emissivity of real objects is between 0 and 1 (excluding the extremes).

Regarding to optical properties of matter, the radiation that impacts a surface can be reflected, transmitted and/or absorbed. Due to the radiative transport equation; which states that the sum of the reflected, absorbed and transmitted radiation is equal to the incident radiation; the sum of the reflection, absorption and transmission coefficients is 1. *Kirchhoff law* states that at a given temperature and in local thermodynamic equilibrium, the emissivity of an object is equal to its absorptivity. Hence, a real object in thermodynamic equilibrium cannot absorb all the incident radiation because its emission coefficient is less than 1. Furthermore, the transmission coefficient of opaque objects can be approximated to zero. Therefore, the reflection coefficient of an opaque object in local thermodynamic equilibrium can be known if the emissivity of its surface is known.

As mentioned before, real objects do not behave like ideal black bodies. The radiance that they emit at a given wavelength is a fraction of the emission of a black body. Sometimes it can be assumed that the emissivity and absorptivity of a surface are independent from the

wavelength in a specific spectral range. This is known as *gray body* approximation. This concept can result in very precise values for uniform surfaces.

4.3.2 IEC TS 62446-3

The thermographic (infrared) inspection, within IEC 62446-3 [62], is centered in PV modules and plants in operation. This means that not only PV modules are considered in the inspection, but also BOS components such as cables, contacts, fuses, switches, inverters, and batteries. This technical standard includes the requirements for the equipment, ambient conditions, inspection procedure and personnel qualification. The inspection is based on passive techniques under natural sunlight operation (simulated sunlight is out of the scope). Within the standard, two different levels of inspection are given. The simplified inspection requires low qualifications for personnel where the main purpose is to verify that PV modules and BOS components are working properly. Therefore, a simplified inspection can give information about which PV modules or BOS components must be further inspected in detail. The detailed inspection requires deeper understanding. Hence, the personnel requires higher degree of expertise. This inspection is used to analyze abnormal PV modules and/or BOS components in detail and can be done as periodical inspection or for trouble-shooting.

4.3.2.1 Equipment list (with specifications)

According to IEC 62446-3 [62], the necessary equipment for the thermographic inspection is shown in the following list:

a. *Infrared (IR) Camera* —IR-cameras can be MWIR (mid-wavelength) or LWIR (long-wavelength). LWIR-cameras operate in the spectral range of 8 μm to 14 μm while MWIR-cameras operate in the range of 2 μm to 5 μm. Due to the spectral range, MWIR-cameras shall be used only for BOS components. The geometric resolution of the camera is also important. For PV modules, one pixel must contain as maximum 3 cm length of edge. This can be translated to 5 $\times$ 5 pixels per cell (considering a cell edge of 6 inches). For electrical connections, the geometrical resolution shall match the smallest object area (for high-quality images is defined as 3 $\times$ 3 pixels). IR-cameras with resolution higher or equal to 320 $\times$ 240 pixels are recommended.

b. *Photo Camera* —Apart from the IR-camera, a photo-camera is recommended. Visual documentation is only necessary when the corresponding thermal-image shows abnormalities. The resolution of the visual-image must be higher than the thermal-image and shall have a similar FOV (Field Of View) to capture details. In many cases the photo-camera is integrated within the IR-camera, but these integrated photo-cameras normally do not meet the minimum requirements of resolution. For IR-cameras of 640 $\times$ 480 pixels a separate photo-camera of at least 9 megapixels is recommended.

c. *Irradiance Sensor* —A crystalline silicon reference cell or a pyranometer calibrated with an accuracy of $\pm 5\%$.

d. *Temperature Sensor* —A temperature sensor shielded from the direct light and wind calibrated with an accuracy of ±5%.

e. *Anemometer or Bft-scale*[1] *Chart* —For an estimation of the wind speed.

f. *Second Photo Camera* —For an estimation of cloud coverage and degree of soiling.

g. *DC (clamp) Ampere Meter* —An ampere-meter is necessary for the measurement of the current of PV modules. It must be calibrated with an accuracy of ±2%.

Table 4.3 contains a more detail information about the minimum requirements for the IR-cameras.

Table 4.3: Minimum requirements for IR-cameras according to IEC 62446-3 [62].

Feature	**Minimum requirements**
Spectral response	2 μm to 5 μm (mid wavelength) or 8 μm to 14 μm (long wavelength)
Temperature-sensitivity and calibration range (object temperature range)	-20°C to +120°C
Operating ambient air temperature range	-10°C to +40°C
Thermal sensitivity	NETD[2] $\leq$ 0.1 K at 30°C
Geometric resolution	- For PV module: max. 3 cm of the module edge per pixel. - For Electrical connections the geometrical resolution (real measurement spot) hast o match the smallest object area to be verified.
Absolute error measurement	$\leq \pm 2\ K$
Adjustable parameters	Emissivity (ε), reflected temperature (T_{refl})
Adjustable functions	Focus, temperature level and span
Measurement functions	Measuring spot, measuring area with average and maximum temperature

[1]Beaufort (scale) —is a scale that quantifies wind speed by phenomenological criteria.

[2]Noise Equivalent Temperature Difference —is the smallest temperature difference (in mK) detectable by an IR-camera.

4.3.2.2 Inspection procedure

Regarding to the procedure for the outdoor inspection, IEC 62446-3 [62] describe the following steps:

1. The plant shall be in operation before the inspection begins. Moreover, the PV modules that will be inspected must be under thermal equilibrium (thermal steady state condition). Soiling must be low (less than 10% operating I_{mpp} loss) and homogeneous to avoid localized thermal effects. However, it would be desired to conduct the inspection without cleaning.

2. Prior the thermographic inspection, it is recommended to do a visual inspection to determine if the previous step is met.

3. If the operating conditions of the PV module or plant changes, a waiting time of at least 15 minutes is recommended to regain the steady state condition. Changes in the operating condition can be due to environmental changes. The minimum requirements for inspection conditions are given in Table 4.4.

Table 4.4: Minimum requirements for inspection conditions according to IEC 62446-3 [62].

Parameter	**Limits**
Irradiance	- Minimum 600 Wm^{-2} in the plane of the PV module. - Measured operating current shall be a minimum of 30% of rated system current within the inspected current path.
Wind speed	Maximum 4 Bft or 28 km/h
Cloud coverage	Maximum 2 okta of sky covered by cumulus clouds
Soiling	No or low. Cleaning recommend.

4. The adjustment of the IR-camera must be verified prior thermal inspection. Most important parameters are: geometrical resolution, angle of view and emissivity.

   (a) The distance between the inspected PV module and the IR-camera shall fulfill the geometrical resolution according to Table 4.3. Part 1 of Annex A from IEC 62446-3 [62] gives two examples. One that met the geometrical resolution requirements and one that does not.

   (b) The angle between the IR- camera and the surface of the inspected PV module must be as perpendicular as possible (greater than 30°). Reflection from objects

(including the measuring personnel and the IR-camera) in the vicinity of the inspected PV module should be avoided. Part 2 of Annex A from IEC 62446-3 [62] gives an example for the correct angle of the camera.

(c) The emissivity of the camera must be adjusted according to the surface conditions of the PV module. This must be done by a qualified thermographer. The emissivity depends on many factors: material of the inspected object, the surface of the object (including soiling, bird drops, etc.) and third angle of view.

5. Together with the thermal-image, a visual-image should be also taken. When a thermal abnormality is found the visual-image is mandatory. Moreover, the exact position of all the findings must be documented, including the operating conditions (with the local DC load) and the environmental conditions.

6. The measuring personnel can examine the PV module or PV plant in detail or in a simplified procedure. Annex B from IEC 62446-3 [62] specifies the personnel requirements for both inspection levels. In the simplified inspection, measuring personnel can not do conclusions about module quality. Absolute temperatures are not determined. Therefore, thermal patterns are used to evaluate the abnormalities. Annex C from IEC 62446-3 [62] includes a matrix with thermal abnormalities patterns/examples. In contrast, the detailed inspection may include thermal patterns or abnormalities that are not present in the matrix in Annex C from IEC 62446-3 [62].

7. Fast carriers for IR-cameras (e.g. aerial drones) are classified as simplified inspection procedure in order to find PV sub arrays/strings/modules with noticeable problems. In this cases, the moving speed of the camera shall be chosen with respect to time constant of the camera's IR-detector to avoid smearing effects. For common IR camera bolometer detectors, smearing effects can appear at a moving speed of 3 m/s.

4.3.2.3 Evaluation

Regarding to the evaluation of the data obtained with the inspection; this standard indicates which measurements and observations are important for evaluation, introduces several techniques to evaluate thermal-images, gives a classification of thermal abnormalities and guidance for the projection of the temperature differences to nominal irradiance.

For a proper evaluation of the thermal-images it is important to take into account maximum temperatures, temperature differences and profiles, amount and movement of clouds, wind speed and direction, previous mechanical stress from installation history log-file, soiling, visual inspection, irradiance and/or DC load of the system. Information regarding previous thermal inspection is also important for the evaluation. Regarding to evaluation techniques, it is not mandatory to follow up the ones within the standard.

Simplified evaluation

Evaluation for simplified inspection classifies the thermal abnormalities according to the classes (CoA) within Table 4.5. Class 1 considers no abnormalities, class 2 considers thermal

abnormalities that do not cause relevant safety problems and class 3 considers abnormalities that drives immediate actions due to safety issues. Once the class of the abnormality is determined, the evaluation of the thermal pattern is studied according to Annex C from IEC 62446-3 [62].

Figure 4.12 shows an example of three thermal patterns within Annex C from IEC 62446-3 [62]. The first pattern is related to strings while the other two are related to PV modules. The category (in the second column) indicates the problem/abnormality and the technology of the module under inspection while the third column indicates the CoA. The fourth column gives a range of temperature (in K) for the temperature difference to normal operating device (ΔT_2). Measurements of temperature are not mandatory for a simplified evaluation but can supplement thermal pattern for checking. For further explanation of ΔT_2 see section 4.3.2.3. The last column in Fig. 4.12 indicates if the abnormality is assessable by thermal pattern only or also by visual-image, classifies the abnormality as extended area or point, makes recommendation to found the source of the abnormality (not always) and gives an explanation of the abnormality. The entire Annex C contains 12 examples of thermal pattern abnormalities.

Table 4.5: Allocation in classes of abnormalities according to IEC 62446-3 [62].

Class of Abnormality (CoA)	**Recommendation for actions**
1 (no abnormalities - OK)	No imminent action.
2 (thermal abnormality - tA)	Checking the cause and, if necessary, rectification in a reasonable period.
3 (safety relevant thermal abnormality - dtA)	Prompt interruption of operation, checking the cause and rectifications in a reasonable period.

Detailed evaluation

Regarding to the detailed evaluation, Annex D from IEC 62446-3 [62] gives a method for the comparison of the temperatures of the abnormalities using polygon measurement areas or spot. The temperature for extended areas corresponds to arithmetic mean temperatures while for spots corresponds to the spot-maximum temperature. Temperature comparison ΔT can be calculated between point abnormalities and/or mean values of extended areas. Annex D gives two examples of temperature comparison, one using arithmetic mean value and the other using arithmetic mean value with spot value. Both by polygon measurement method. According to IEC 62446-3 [62], for long term comparison (e.g. between two inspections), the temperature difference ΔT of both inspections shall be normalized to 1000 Wm^{-2}.

The temperature difference ΔT_{nom}, which is given by $\Delta T_{nom} = f \cdot \Delta T$, is the temperature difference between functioning and non-functioning components under identical irradiance condition extrapolated to nominal conditions (1000 Wm^{-2}). The calculation of the extrapolation is given within the standard and considers the temperature difference between func-

Example 1 – 3: Strings and modules	Category	CoA	Temperature difference to normal operating device at 1 000 W/m^2 (ΔT_2)	Thermal pattern, definition and additional information of abnormality
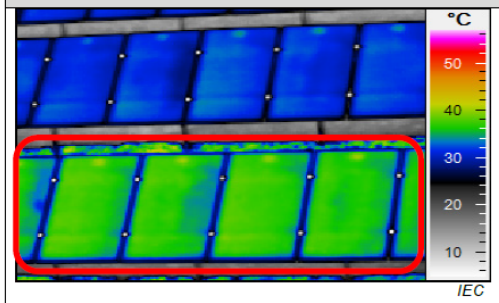	**Modules in open circuit** **(crystalline Si and thin film)**	2	2 K to 7 K (at 15 % module- efficiency typically 4 K to 6 K)	Assessable by thermal pattern and classified as a extended area abnormality. The module surface is homogeneously heated. ΔT of the junction box is similar to operational state. Recommended: check module, state of operation of inverter, and condition of cabling, connectors, and fuses.
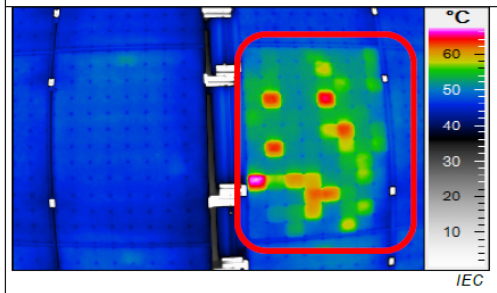	**Module in short circuit** **(crystalline Si)**	2	Averaged 2 K to 7 K over module surface (at 15 % module- efficiency typically 4 K to 6 K)	Assessable by thermal pattern, visual image and classified as a extended area abnormality. Similar pattern as with broken front glass (check isolation resistance), PID, cell defects and mismatch. Recommended: check module and cabling.
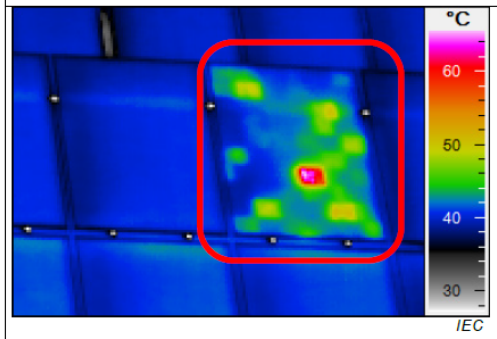	**Crystalline Si module with broken front glass** **(crystalline Si)**	3	Averaged 0 K – 7 K over module surface (at 15 % module- efficiency typically 0 K – 6 K)	Assessable by thermal pattern and visual image. Beware of high voltage as isolation resistance is lost. Similar pattern as modules in short circuit, with PID, cell defects and mismatch. Sometimes just single broken cells are heated. In the first weeks after the breakage, a module with broken glass can show almost normal thermal behaviour.

Figure 4.12: Example of the matrix for thermal abnormalities of PV modules within Annex C from IEC 62446-3 [62].

tioning and non-functioning components under operating conditions (ΔT), the irradiance or the load (DC current) at operating and nominal conditions, and an exponential factor that take into account the shape and the form of the abnormalities (point or extended area). The exponential factor in combination with the irradiance/load terms is known as *correction factor* (f). The values of the correction factor for point and extended area abnormalities of PV modules and BOS components can be found in Fig. 4.13.

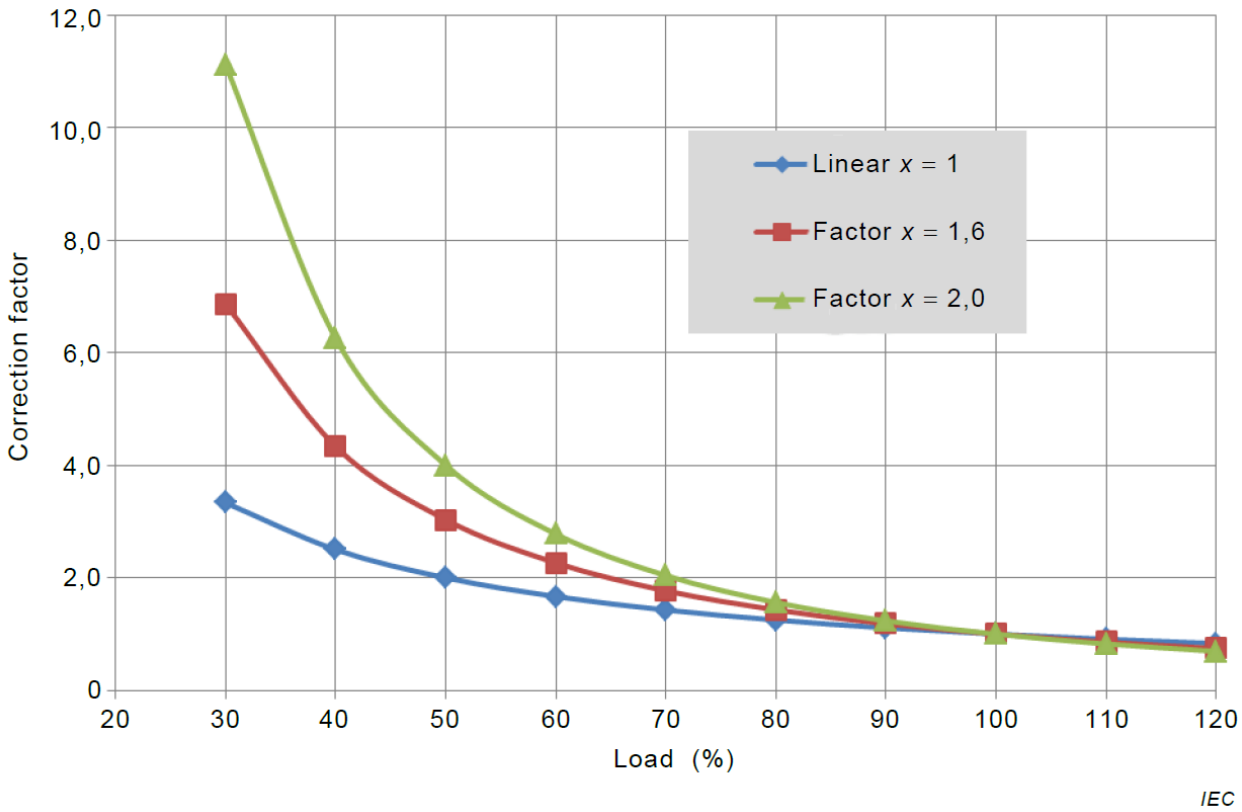

Figure 4.13: Graphic representation of the correction factor for temperature differences to nominal irradiance/load conditions as a function of the relative irradiance/load [62].

4.3.2.4 Inspection report

The inspection report is divided into 12 parts, which are: information about personnel, camera, day and time, location, inspection scope, environmental conditions, soiling, inspection procedure, founded abnormalities, recommendations for next inspection, recommended actions and summary of the results. Apart from this 12 parts, more information must be added to the report for thermal abnormalities within a PV module. When a PV module presents one or more thermal abnormality, the thermographic image shall show the entire PV module while pointing out the position of the junction box and the lower edge within the installation. For every thermal-image the report adds 8 new parts of information, which are: information about description of the object; name, date and time of the image; camera system, serial number and lens; emissivity and reflected temperature; and location of PV module within the PV plant. Also an extra thermal-image with sufficient resolution for visual details (in case

of immediate action is required), temperature difference of the abnormality in comparison with a regular spot (in the case of detailed inspection) and the last part consider conclusions and recommendations for further actions.

4.3.3 IEA PVPS Review on IR Imaging for PV Field Applications

IEA PVPS is finishing a draft related to IR and EL (electroluminescence) imaging for field applications [136]. The review is strongly focused in environmental and device requirements in one hand and interpretation of abnormalities in the other hand. The aim of the review is to provide guidance and recommendation in the use of IR and EL imaging techniques to assess PV modules in the field (under natural sunlight).

4.3.3.1 Camera requirements

IR-cameras can be fabricated with cooled or uncooled detectors. Cooled sensors are not commonly used in PV applications due to the cost and complexity of the cooling system. Uncooled cameras can work at ambient temperatures and the most common sensor architecture is the micro-bolometer[3]. According to IEA PVPS [136], there are several types of uncooled cameras in the market. Table 4.7 shows the most important characteristics of IR-cameras that are commonly used for PV applications. It can be seen that typical detector resolution (in pixels) for IR-cameras are 160×120 and 320×240 while the visual-image resolution is always higher than the detector being 320×240 and 640×480 respectively. The spectral range is the same for all the cameras because the application is the same (PV field application). Finally, the thermal sensitivity, excluding the high quality Infratec camera, varies from 50 mK to 80 mK.

IEA PVPS distinguished four classes of IR-cameras, which are lower, medium, professional and professional upper classes. The main differences among these classes are shown in Table 4.6. The information within Table 4.6 is not only for class comparison but also the general requirements for IR-cameras depending on their class. What is not a requirement is the temperature range because is not necessary to reach 2000°C for PV field applications. The other general requirements within Table 4.6 are briefly explained in the list below.

- The *detector resolution* of the camera defines the amount of pixels (data acquisition points) to create a visual-image from the thermal characteristics of the inspected surface. Cameras with higher detector resolution are more expensive but also more accurate. They can identify smaller image details or the same details at further distances.

- The *Thermal sensitivity (or NETD)*, which was briefly defined in the previous section, is basically noise. The noise is a variation of signal in the sensor that is not due to objects in the FOV, which limits the ability of the camera to measure small temperatures. Therefore, small NETD are better because variation temperatures smaller than the noise can not be perceived.

[3] `http://www.flirmedia.com/MMC/CVS/Appl_Stories/AS_0015_EN.pdf` (page 3).

- The *accuracy* indicates the error for the internal technical processes and calculations performed by the camera to identify the temperature value associated with each pixel of the thermal-image.

- The *focus* can be fixed, manual or automatic. This is needed to take sharped images.

- The *digital camera* resolution corresponds to the resolution of a regular camera for visual-images.

- The *adjustable emissivity* indicates that the emissivity can be manually changed for better readings.

- The *interchangeable lens* indicates if the lens are interchangeable. For example, wide angle or telephoto lens are interchangeable lens.

Table 4.6: General requirements for IR-cameras according to IEA PVPS [136].

Camera parameter	**Lower class**	**Medium class**	**Professional class**	**Professional upper class**
Calibration certificate	Yes	Yes	Yes	Yes
Temperature range	-20°C to +250°C	-20°C to +650°C	-20°C to +1200°C	-40°C to +2000°C
Resolution (Super resolution)	160×120	320×240	320×240 (640×480)	640×480 (1280×960)
Thermal sensitivity	$<0.1\ K$	$<0.05\ K$	$<0.04\ K$	$<0.002\ K$
Accuracy	±2°C	±2°C	±2°C	±1°C
Focus	Fix	Manual	Manual & Auto	Manual & Auto
Digital camera	-	2 Megapixels	3 Megapixels	5 Megapixels
Adjustable emissivity	0.01 - 1.00	0.01 - 1.00	0.01 - 1.00	0.01 - 1.00
Voice recording	-	Yes (short)	Yes	Yes
Interchangeable lens	-	Yes	Yes	Yes
GPS recording	-	-	Yes	Yes
External wireless sensor function	-	-	Yes	Yes

Table 4.7: IR-cameras commonly used in PV applications according to IEA PVPS [136].

Manufacturer (model)	**Detector resolution (pixels)**	**Image display (pixels)**	**Spectral range (μm)**	**Thermal sensitivity (mK)**	**Accuracy % of reading**	**Battery**	**Weight (kg)**	**Focus mode**	**Warranty (years)**
Testo (875i-2DLX)	160×120	320×240	8.0 to 14	50	2	4 hours+	0.900	Manual	2
Flir (E6)	160×120	320×240	NA	60	2	4 hours	0.575	Auto	10
Satir (GN)	160×120	640×480	8.0 to 14	80	2	NA	0.500	Manual	NA
Fluke (TiS45)	160×120	320×240	7.5 to 14	50	2	4 hours+	0.720	Manual	2
Trotec (V Series)	160×120	640×480	8.0 to 14	80	2	2-3 hours	0.500	Manual	NA
Testo (882)	320×240	320×240	8.0 to 14	50	2	4 hours+	0.900	Manual & Motor	2
Flir (E8)	320×240	320×240	NA	60	2	4 hours	0.575	Auto	10
Fluke (Ti450)	320×240	640×480	7.5 to 14	50	2	3-4 hours	1.040	Manual & Auto	2
Satir (Hotfind)	384×288	640×480	8.0 to 14	50	2	NA	0.600	Manual & Motor	NA
Trotec (LV Series)	384×288	640×480	7.5 to 14	50	2	2-3 hours	0.650	Manual	NA
Infratec (Variocam HD 900)	1024×768 @30 Hz	1280×800	7.5 to 14	20	1	2-3 hours	1.600	Manual & Auto	2

4.3.3.2 Environmental conditions

Environmental conditions affect the output power of PV modules. Voltage is very sensitive to temperature changes while the current is very sensitive to irradiance changes. According to IEA PVPS [136], a typical PV module takes 5 to 15 minutes to thermally stabilize for new environmental conditions. Therefore, before taking a thermal picture, it is recommended to wait at least 15 minutes if there are clouds moving (change in irradiance) above the inspected module, or the wind speed increase (surface temperature changes), or there is any change in the environmental conditions.

Objects that are in the neighborhood of the inspected PV module must be taken into account. Reflections from buildings, trees, or anything that is near the PV module must be avoided. Since there are some objects that can not be moved, the personnel doing the inspection can change the position or the angle of the camera to avoid reflections.

Another important requirement to take a high quality thermal-image is the minimum irradiance. Inactive parts (abnormalities) in a PV module emits more infrared radiation than active parts. This means that inactive parts are hotter than active parts. This happens because the inactive parts continue to generate electron-hole pairs (via photoelectric effect) due to the sunlight, but those damage parts can not convert the power into DC current. Therefore, the energy remains as heat. According to IEA PVPS [136], the temperature difference between active and inactive parts is slight and often proportional to the irradiance. Therefore, some thermal abnormalities can only be seen at high irradiance.

According IEA PVPS [136], it is recommended that weather conditions lead to a temperature difference ΔT of at least 2.5 K. They indicate that the temperature difference between active and inactive parts can be estimated as:

$$\Delta T = (G_T/G_{NOCT}) \cdot (T_{NOCT} - T_{a;NOCT}) \cdot \eta_{mod} \tag{4.1}$$

where G_T is the global irradiation intensity on the module plane (in Wm^{-2}), G_{NOCT} is the global irradiation intensity on the module plane (800 Wm^{-2}) used to measure the nominal operating cell temperature T_{NOCT} at ambient temperature $T_{a;NOCT}$ (20°C) and η_{mod} is the module efficiency. IEA PVPS [136] states that T_{NOCT} is typically given for free standing PV module and must be corrected for mounted PV modules. According to them, for rack and direct mount the corrections are $T_{NOCT} = NOCT + 3$°C and $T_{NOCT} = NOCT + 18$°C respectively.

The module efficiency at standard conditions η_{STC} can be corrected to another module temperature T_{mod} using the power temperature coefficient C_T as:

$$\eta_{mod} = (1 - (T_{mod} - 25°\text{C}) \cdot C_T) \cdot \eta_{STC} \tag{4.2}$$

According to IEA PVPS [136], the easiest equation to calculate T_{mod} for practical use (rough estimation) is:

$$T_{mod} = T_a + (G_T/G_{NOCT}) \cdot (T_{NOCT} - T_{a;NOCT}) \cdot (1 - \eta_{mod}) - f(\nu_{wind}) \tag{4.3}$$

where T_a is the ambient temperature and f is a function of the wind speed ν_{wind}. Together equation 4.2 and equation 4.3 are implicit equations that can be easily solved by data calculation sheet.

As a conclusion, IEA PVPS [136] determined that for most practical cases an irradiance of 600 Wm^{-2} is enough to detect abnormalities due to inactive parts in a PV module.

4.3.3.3 Inspection procedure

The procedure that IEA PVPS [136] established for taking thermal-images is very simple. It is divided into two parts: preparation before inspection and the inspection on-site. The steps within each part is explained below.

1. Preparation for inspection:
   (a) Gathering technical information: PV modules type and specifications, plan view of installation, PV arrays and string arrangement, etc.
   (b) Follow-up and confirm suitable experimental and environmental conditions.
   (c) Checklist for all the equipment.
2. On-site inspection:
   (a) Define measurement positions.
   (b) Optimize IR-camera configuration.
   (c) Targeted PV modules/strings may need additional tests, such as I-V curve measurements and visual inspection. If possible, diagnose and/or repair on-site.

According to IEA PVPS [136], the most important factor for any thermographic inspection is the maximum distance between the camera lens and the surface of the inspected object. In compliance with IEC 60904-3 standard, IEA PVPS recommend a distance-to-target (d_{max}) limit where the thermal-image of a single cell from an inspected PV module contain 5×5 pixels. To calculate the maximum distance; the FOV, IFOV (instantaneous FOV), MFOV (measurement FOV) and physical dimensions of the surface of the inspected objects are necessary.

As an example, the *open field of view calculator* of InfraTec [137] is used to determined the maximum distance-to-target in compliance with the recommendation above. To compliance with the recommendation of 5×5 pixels per cell, the pixel size (i.e. the IFOV) shall not be more than $160/5 = 32$ mm (for a standard solar cell size of 160×160 mm^2). Fig. 4.14 shows that for an IR-camera of 160×120 pixels of resolution with a standard lens of 11 mm, the

limit of the distance-to-target is 14.1 m. This means that the personnel doing the inspection can not take a thermal-image from a distance higher than 14.1 m from the inspected object.

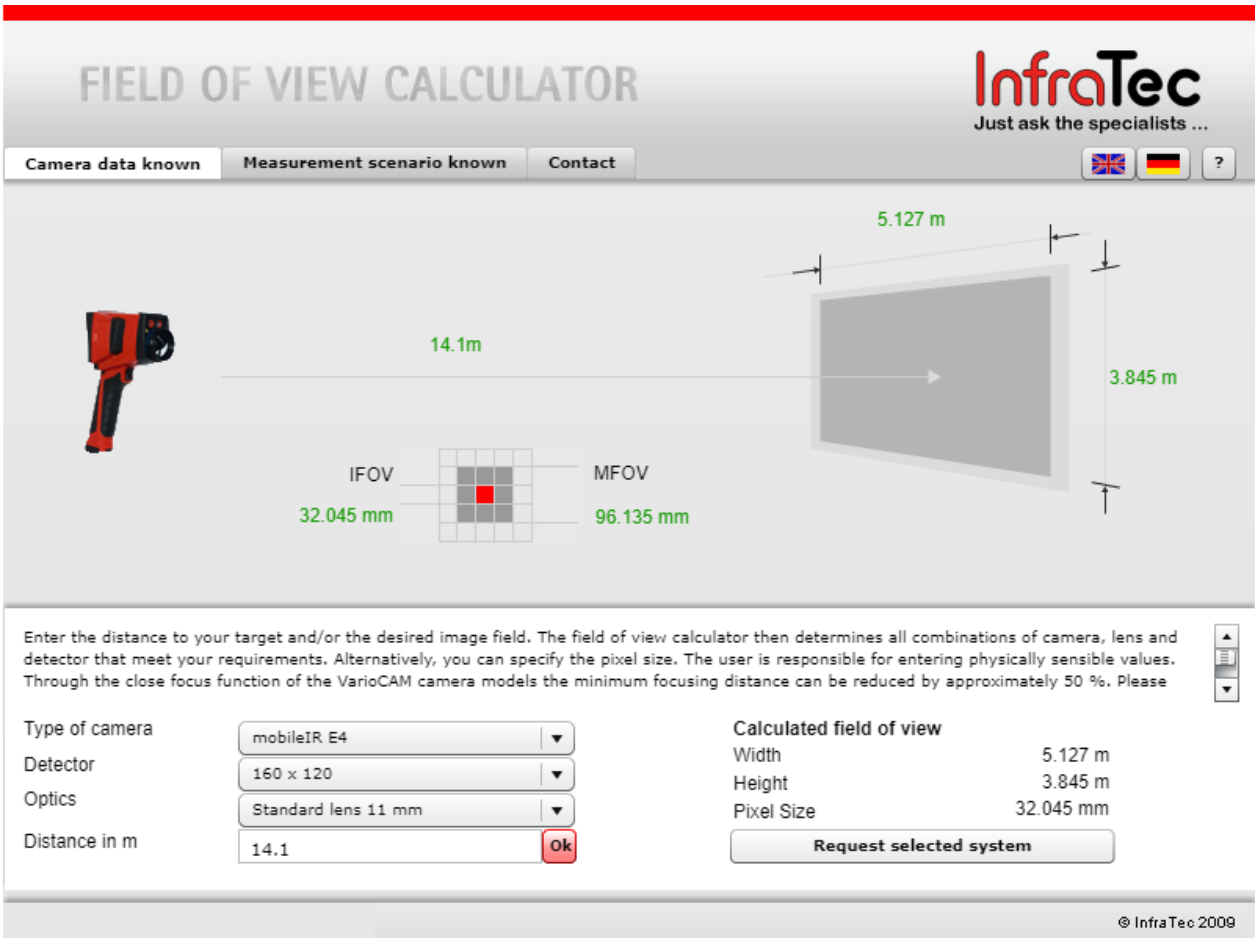

Figure 4.14: Example of the calculation of distance-to-target limit, in compliance with 5×5 per cell, for a thermal camera of 160×120 pixels of resolution with a standard lens of 11 mm [137].

4.3.3.4 Evaluation

The guidelines for evaluation of PV modules made by IEA PVPS [136] start with the explanation of patterns with abnormalities of PV modules, followed by an explanation of PID (potential induce degradation) analysis, and finally with recommendations for analysis and further actions. IEA PVPS indicates that the main thermal patterns for PV modules are hot-spots (due to breakage of front glass, external shading and internal problems) and heated bypass diodes. They describe patterns for breakage of front glass, for hot-spot (due to internal problems and external shading), for heated bypass diodes, and others (miscellaneous). Fig. 4.15 shows an example of a thermal pattern for a breakage front glass with a brief explanation of the possible causes.

Regarding to the explanation of PID analysis, IEA PVPS [136] indicates that IR thermography imaging can get an estimation of the degree of PID-s (PID by shunts). This estimation

2.3.1.1 Breakage of PV module front glazing

Figure 2-6 through Figure 2-9 show breakages of the front glass, caused by heavy impacts such as hail or other extreme mechanical stress onto the module frame, causing the front glass of the PV module to be damaged. The damage of the front glass often creates broken hot cells in the damaged PV module.

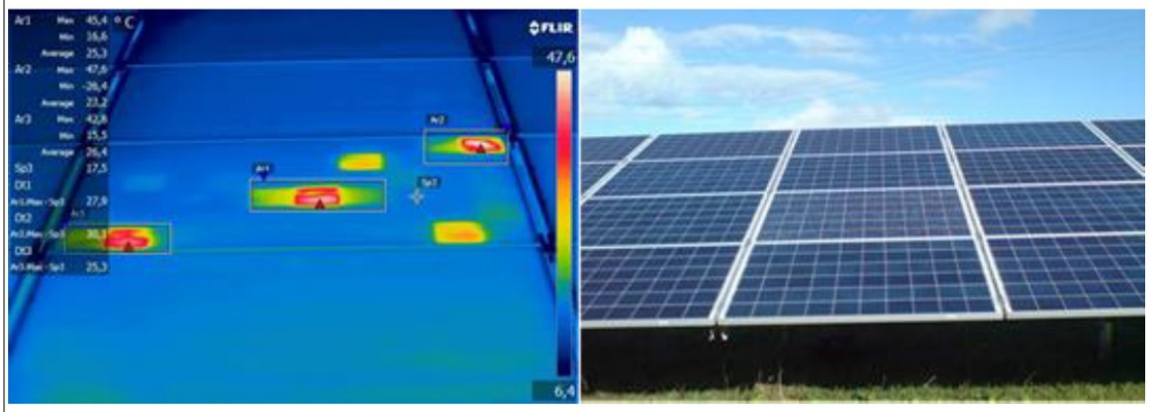

Figure 2-6: Breakage of front glass.

Figure 4.15: Example of a thermal pattern for a PV module according to IEA PVPS [136].

is based on the combination of the pattern shown by the thermal-image and the position of the PV module within the array in relation to the negative pole of the array. According to IEA PVPS, PID can be found with 2 methods. The main field method is IR imaging under clear sky conditions during normal operation and the second method is IR imaging during the night while an external current is applied to the inspected module (analogous to EL imaging).

About the recommendations for analysis, IEA PVPS [136] indicates that the personnel must have knowledge of thermal imaging techniques as well as of PV modules behavior and design. Also, they state that the camera's software can be used for quick analysis or for a small amount of PV modules. In the case of inspecting a large number of PV modules, the use of the software for PC is recommended. According to them, the sufficient features for image analysis are: altering of emissivity and reflected temperature, altering the color scale (by type, level and span) and setting (spot, linear and area) measuring fields.

Within the recommendations for analysis, IEA PVPS [136] also indicates analysis procedure. The procedure is divided into three parts. First, thermal-images must be sorted to match the location of the inspected PV modules. Secondly, thermal-images must be qualitatively analyzed by thermal patterns searching. Finally, the third parts depend on the issues in the second part. If an abnormality cannot be evaluated with the help of thermal patterns, then it must be quantitatively evaluated. For this, the temperature measuring functions of the software should be used (spot and/or polygon measuring fields). Must be noted that the qualitative analysis has a quantitative aspect. In the qualitative analysis, the span of the color scale should be linearly altered with the efficiency of the inspected PV module and the irradiance. For most cases, according to IEA PVPS, the temperature difference (span) shall be around 20-30 K for a module efficiency of 15% at 1000 Wm^{-2}.

4.4 Electroluminescence Imaging

4.4.1 Basic principles of Electroluminescence

Solar cells generate a current when they are exposed to solar radiation. They can also do the opposite, which is emit radiation when they are fed with current. This last phenomenon is known as electroluminescence (EL) process. Since solar cells are essentially diodes, the injected current causes radiative recombination of carriers which in turn causes light emission. Fig. 4.16 shows the circuit and band diagram of a diode (or a p-n junction) under forward bias. When the diode is forward biased, the holes from the p-region are pushed into the n-region facilitating the recombination process. The same happen to the electrons in the n-region, but in the opposite direction. The recombination of an electron with a hole release a photon that has an energy similar to the band-gap of the diode's semiconductor. Hence, the probability of the photon being absorbed by the material is low and the photon exits the material as radiation.

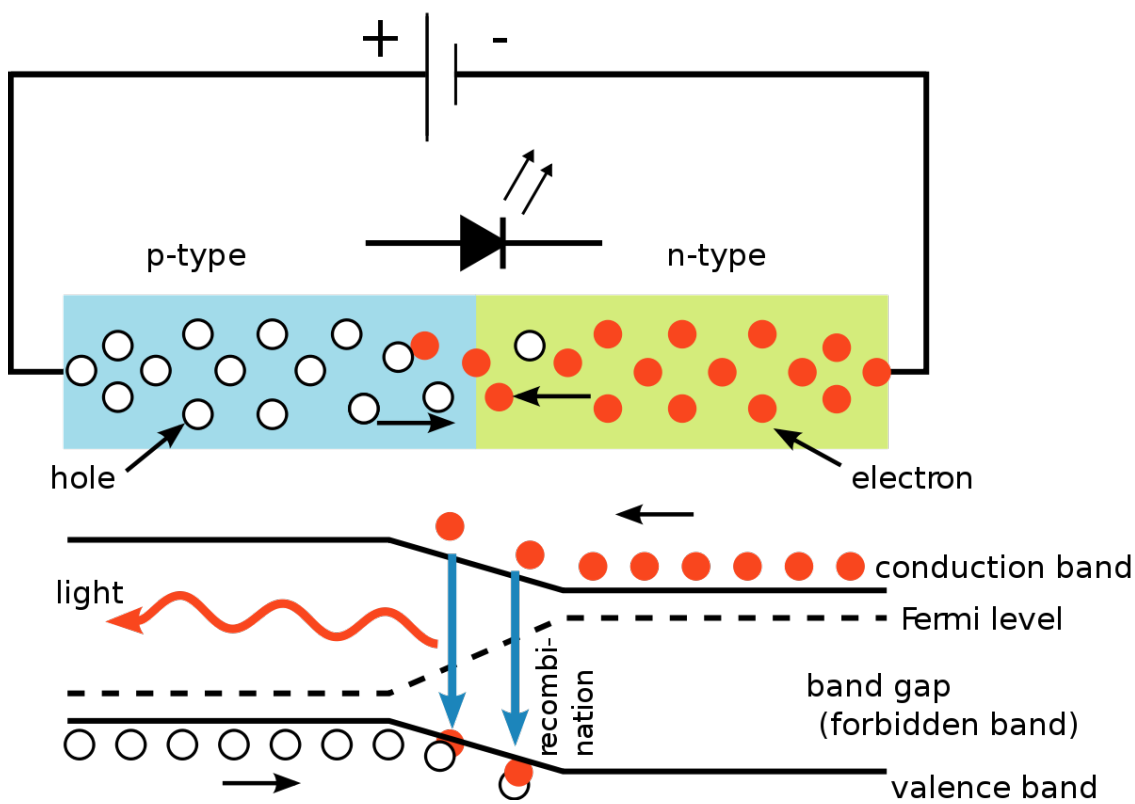

Figure 4.16: Circuit and band diagram of a light emitting diode under forward bias. Image obtained from `https://en.wikipedia.org/wiki/Band_diagram/`.

The process described in the paragraph above is referring to radiative recombination, but within a solar cell exist three types of recombination processes. The processes are known as radiative, Auger and Shockley-Read-Hall (SRH) recombination. It is important to understand the different types of recombination processes because not all of them involve the release of a photon. Honsberg and Bowden [138] explain the three types of recombination

briefly, but precisely.

According to them, the SRH recombination process occurs mainly in materials that are not pure, which have a lot of defects. The process of the recombination is divided in two steps. First an electron (or hole) is trapped within an energy state within the forbidden band due to a defect of the lattice. Secondly, a hole (or an electron) moves to the same energy state before the electron is thermally re-emitted to the conduction band, then it recombines. The recombination releases a phonon, which means that the energy is transferred to the lattice as vibration. Depending on the amount of defects and their corresponding energy states within the forbidden band, the rate of recombination can be low or high.

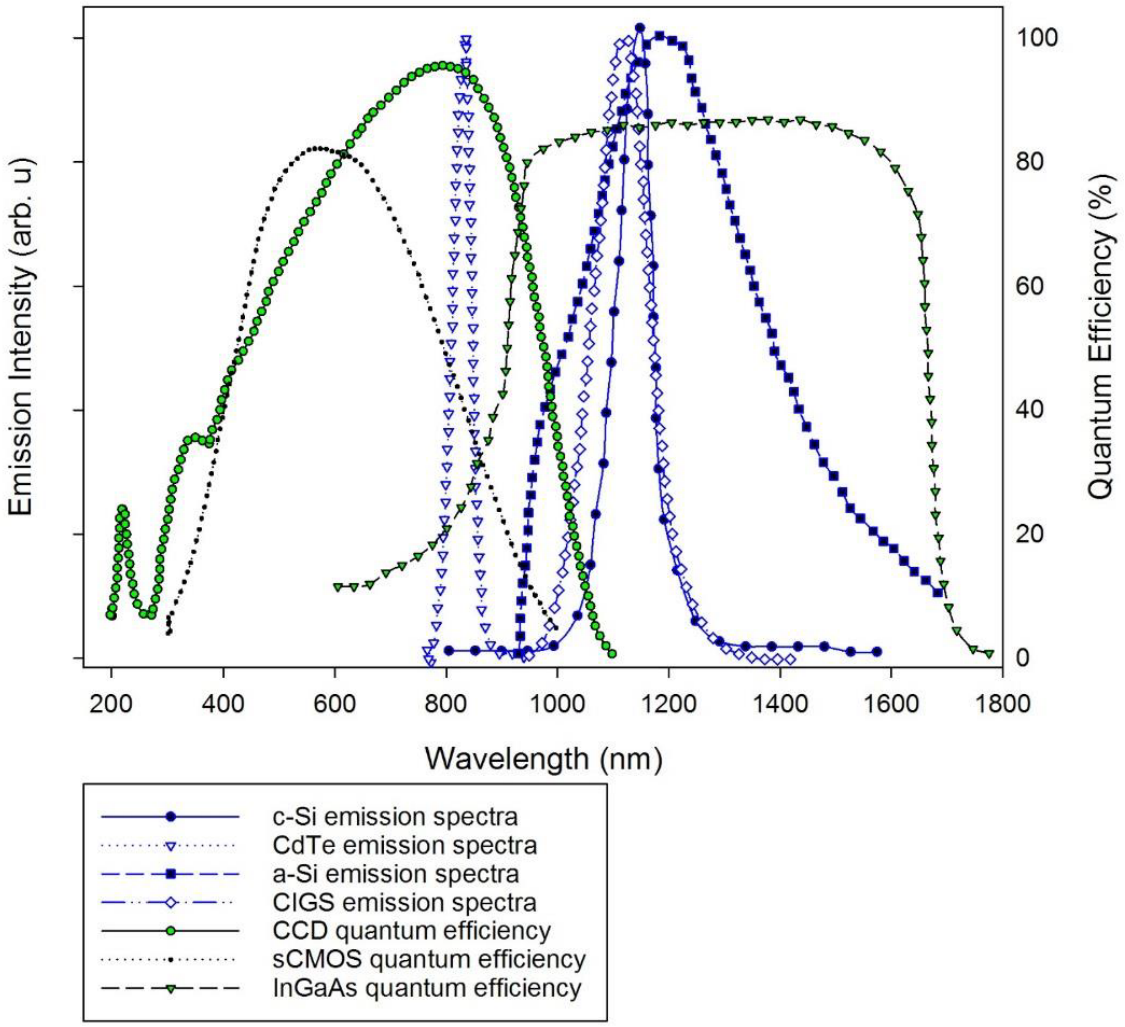

Figure 4.17: Emission spectra of different solar cell technologies and the quantum efficiency of silicon CCD, CMOS and InGaAs CMOS sensors [136].

Regarding to Auger recombination, Honsberg and Bowden [138] explain that a third particle is involved in this process. When an electron recombines with a hole (or vice versa) the energy is transferred to another electron within the conduction band. When the electron is thermalized, it goes back down to the conduction band edge. This type of recombination is predominant when there are high amount of carriers due to high doping of the semiconductor material or high levels of injection due to high radiation.

Specifically for silicon solar cells, which have indirect band-gap, the recombination is mainly due to defects in the lattice or Auger recombination [138]. Hence, the recombination that produce radiative emission, which is band-to-band recombination, is low for silicon cells. Although the radiative emission is low, a peak can be identify at 1150 nm and it can be measured by sensitive sensors in that range. Fig. 4.17 shows the emission spectra range of several solar cell technologies and the quantum efficiency of different EL-camera's sensors. It can be seen that CIGS and c-Si technologies are within the range of 1000 to 1300 nm. Meanwhile, CdTe has an emission spectra between 750 and 850 nm being the narrowest spectra range. The widest corresponds to a-Si technology with a range between 900 and 1700 nm. For most technologies, the emission peak is near 1100 nm but for CdTe.

Regarding to the quantum efficiency of EL-camera's sensors, the spectral response of silicon charge-coupled-devices (Si CCD) is not very sensitive in the range of c-Si, a-Si and CIGS solar cells but CdTe. The same happens with the spectral response of silicon complementary metal oxide semiconductor (Si CMOS). However, the spectral response of InGaAs CMOS is sensitive in the long wavelength part of the spectrum. When only the sensitiveness of the spectral response of materials is considered for choosing an EL-camera's sensor for c-Si solar cells, then InGaAs CMOS will always be the first choice. However, there are other factors that must be taken into account, for example the ratio between sensitiveness and cost.

4.4.2 IEA PVPS Review on EL-Imaging for PV Field Applications

EL imaging has become a very popular technique for the inspection of PV modules for minority carrier lifetime, micro cracks, shunts, and voltage differences [136]. Currently, there are not international standards for the quantitative interpretation of EL-images. IEC is developing a technical specification of EL-imaging techniques for PV modules (IEC 60904-13) that is not publicly available yet. This technical specification gives guidance about the procedure of EL imaging, the post-processing of the EL-images and their interpretation from a qualitative and quantitative point of view.

Based on the guidelines from IEA PVPS [136], one of the most important parts for EL-imaging is the selection of a camera and of course the requirements for taking images. According to them, camera detectors that are mostly use for EL-cameras are CCD or CMOS detectors. They mention that the most important parameters for the camera selection are: number of pixels, noise, quantum efficiency at the wavelength of interest, and dynamic range. Regarding to the procedure, it is highly recommended to use tripods or other structures fixed to the PV module's frame so the camera is steady and as perpendicular as possible to the surface. Finally, the quality of the images improve when they are taken under dark environments.

In the following sections, all mentioned above will be explain in more detail.

4.4.2.1 Camera requirements

Nowadays, there are several options available in the market that are suitable for

EL-measurements. According to IEA PVPS [136], MILC (mirror-less interchangeable lens camera) and modified DSLR (digital single-lens reflex camera) cameras have a broad range of specifications that can be suitable for EL-imaging. The cameras can have two styles, the line-scan style consisting of a 1D line of pixels or an area style consisting of 2D array. Cameras with the second style are capable of taking a single image for an entire cell or PV module.

Within the camera, the most important part is the sensor. The most common sensors for EL-imaging are CCD and CMOS, which can be found in a variety of types due to the optimization of resolution, sensitivity, spectral response and cost. Silicon CCD sensors are very common due to their low cost and high resolution, but they have low sensitivity beyond 1000 nm. Although InGaAs CMOS sensors have lower resolution and are more expensive, their advantage is the higher sensitivity (see Fig. 4.17) for c-Si spectrum range.

Once the type of the sensor is chosen, other specifications such as spectral band, sensitivity and resolution is determined by the type of sensor. Table 4.9 shows a representative, but not exhaustive, list of EL-cameras currently available in the market. According to IEA PVPS [136], there are a broad range of different EL-cameras and styles. They categorized this broad range into three classes: lower, medium and professional class. The requirements for each class is shown in Table 4.8.

Table 4.8: General requirements for EL-cameras according to IEA PVPS [136].

Camera parameter	**Lower class**	**Medium class**	**Professional class**
Type of sensor	CCD	CMOS/CCD	CMOS/CCD
Resolution			
(CCD)	<1 megapixel	1-5 megapixel	>5 megapixel
(CMOS)		320×256	640×512
Sensitivity			
(dynamic range)	2500:1	5000:1	10000:1
(exposure time)	>10 s	1-10 s	<1 s
Spectral band	Si (0.3-1.1)	Si (0.3-1.1)	Si (0.3-1.1)
		InGaAs (0.7-2.6)	InGaAs (0.7-2.6)

- The *type of sensor* —can be CCD or CMOS. CCD sensors are commonly made of silicon material while CMOS sensors are made from silicon or InGaAs materials. As stated in previous paragraph, the material will define the spectral response of the

sensors. Therefore, the material also define the quantum efficiency (spectral band). The spectral band for silicon is 0.3-1.1 μm while for InGaAs (in the long range) is 0.7-2.6 μm. The type of sensor must be chosen based on the technology of the PV module that will be under inspection (c-Si, a-Si, CIGS, CdTe, etc.).

- The *resolution or number of pixels* —allow images to be taken far or near to the inspected PV module. Higher resolutions allow to take one image of several PV modules at once without losing quality or enable the possibility of more detail when the image is taken at near distance from one PV module. Higher resolutions are always better.

- The *sensitivity* —is directly related to quantum efficiency and spectral response. For an specific type of sensor certain wavelengths are considered signals and others are just noises. The signal-to-noise ratio can be improved by increasing the quantum efficiency of the sensor (spectral band) and/or reducing the sources of noise (cooling). The improvement of this ratio means better sensitivity.

- The *spectral band* —indicates the range where the camera's sensor is sensitive. The quantum efficiency can be further improved by applying additional coating to lenses or more lenses.

- The *type of cooling* —is very important when it comes to improve the signal-to-noise ratio. Longer exposures times (more than 10 s) require deep-cooling while exposures times such as 1 s or less reduce the demand of cooling. It is important to maintain the lowest noise possible for higher quality images.

Multiple settings for EL-imaging can be configured within an EL-camera. According to IEA PVPS [136], typical camera features are the focus, aperture, zoom, ISO, exposure time, and storage file depth. For lower time of exposure, the lens aperture value must be low. This means that the lens is fully open and a lot of light pass through the lens. When the camera is not steady and perpendicular to the PV module's surface, the EL-images tend to be blurry. This means that the aperture value must be increased to increase the depth of field and sharpness of the images. This must take into account that higher aperture values required deep-cooling systems because the exposure time also increases.

In order to centre the depth of field, the focus of the camera should be at a distance that averages the minimum and maximum distance of the camera from the inspected PV module. For example, when the camera is focused on the first row of modules of an array, then the image will be very blurry for the subsequent rows that appears within the image. In the other hand, ISO determines how sensitive the camera is to incoming light. To improve the time required to focus, it is best to decrease the exposure time with a very high ISO. It is not recommended to use an ISO higher than 400 because very high ISO dramatically increase image noise.

Regarding to bit storage resolution, it is recommendable to store images with a format of more than 8 bit per color channel. According to IEA PVPS [136], the main benefit is that brightness corrections can be done without decreasing the quality in the post processing of the image.

Table 4.9: List of EL-cameras available in the market that are suitable for EL-imaging of PV modules according to IEA PVPS [136].

Manufacturer	**Model**	**Camera type**	**Sensor type**	**Resolution**	**Type of cooling**	**Size** (mm)	**Weight** (kg)
Andor	DU491A	Linescan	InGaAs CMOS	1021	Thermoelectric	$155 \times 101 \times 100$	2
Hamamatsu	C10633-13	Area	InGaAs CMOS	320×256	None	$50 \times 50 \times 50$	0.23
Hamamatsu	C12741-11	Area	InGaAs CMOS	640×512	Thermoelectric w/forced water	$189 \times 108 \times 110$	3.4
NPC group	EPTiF	Area	InGaAs CMOS	320×256			
UTS Aerospace systems - Sensors Unlimited	320KTS	Area	InGaAs CMOS	320×256	Room temperature	$65 \times 56 \times 53$	0.27
UTS Aerospace systems - Sensors Unlimited	GA1280JS	Area	InGaAs CMOS	1280×1024	Room temperature	$42 \times 41 \times 41$	0.235
UTS Aerospace systems - Sensors Unlimited	1024-LDM	Linescan	InGaAs CMOS	1024	Room temperature	$76 \times 74 \times 61$	0.45
Xenics	Bobcat-320-Gated	Area	InGaAs CMOS	320×256	Thermoelectric	$72 \times 55 \times 55$	0.285
Andor	Clara Interline CCD Series	Area	Si CCD	1392×1040	Thermoelectric	$127 \times 112 \times 96$	2.2
Andor	PV Inspector	Area	Si CCD	1024×1024	Thermoelectric	$208 \times 105 \times 64$	2.2
Camels	MT-EL-H1709M	Area	Si CCD	1392×1040	Thermoelectric w/forced air	$730 \times 465 \times 465$	150

Manufacturer	**Model**	**Camera type**	**Sensor type**	**Resolution**	**Type of cooling**	**Size** (mm)	**Weight** (kg)
Camels	MT-EL-H1708M	Area	Si CCD	1392×1040	Thermoelectric w/forced air	Custom	
Camels	MT-EL-H1708I	Area	Si CCD	1392×1040	Thermoelectric w/forced air	$130 \times 125 \times 55$	
Camels	MT-EL-H1709I	Area	Si CCD	1392×1040	Thermoelectric w/forced air	$130 \times 125 \times 55$	
Chinup technology	EL-MT01M	Area	Si CCD	1640×1130			
Greateyes	LumiSolarCell	Area	Si CCD	2048×2048		$1120 \times 715 \times 600$	60
Greateyes	LumiSolarProfessional Inline	Area	Si CCD			$2200 \times 2200 \times 1400$	
Greateyes	LumiSolarProfessional	Area	Si CCD	up to $12,000 \times 20,000$		$2460 \times 1400 \times 1200$	250
Greateyes	LumiSolarOurdoor	Area	Si CCD	2048×2048			40
Hamamatsu	ORCA II	Area	Si CCD	1024×1024	Air or water cooled	$215 \times 110 \times 76$	
PCO	Sensicam qe	Area	Si CCD	1376×1040	Thermoelectric w/forced air	$210 \times 93 \times 78$	1.6
PCO	pco.4000	Area	Si CCD	4008×2672	Thermoelectric	$195 \times 135 \times 51$	1.9
Various	Modified SLR	Area	Si CCD	Various	None	Various	Various
Andor	Zyla 4.2 PLUS	Area	Si CMOS	2048×2048	Air or water cooled	$133 \times 82 \times 80$	1.0
Sony	Raspberry Pi NoilR Camera	Area	Si CMOS	3296×2512	None	$25 \times 23 \times 9$	0.003

4.4.2.2 Inspection procedure

Outdoor-EL-systems typically include a camera, portable power supply (battery) and computer. To eliminate the background light, the inspection is conducted at night or with a black shroud for the inspected PV module. Night or low light conditions improve the quality of EL-images. Day-light systems require advanced equipment and image processing. There are two approaches for EL-imaging: ground-level inspection and aerial inspection.

Figure 4.18: GreatEyes LumiSolarOutdoor measurement systems for field tests of PV modules. Image obtained from `http://www.costar.co.kr/`.

According to IEA PVPS [136], ground-level inspection includes fixed EL-cameras on portable constructions or smaller hand-held systems. Depending on the DC power sup-

ply, which fed the PV modules with current, a single PV module or a whole array of modules can be imaged at once. Since the PV modules are normally connected in series within an array, the limitation of the DC power supply corresponds to the voltage.

The recording times are high for manual systems, the productivity can be approximately about 0.2 MWp of inspected PV installation per night [136]. In order to increase the recording rate, the power supply and the string should be interconnected to a multi-box with several inputs and a remote controlled switch.

In the case of the inspection of roof-mounted PV systems, IEA PVPS [136] recommends the use of a telescopic tripod with a remote-controlled pivot arm. Since at night EL-camera's auto-focus do not work, the distance between the camera and the module under inspection must be measured by a distance sensor. Based on this measured distance, the focus length can be adjusted manually. Fig. 4.18 shows an example of a ground-level system.

Regarding to aerial inspection, they are conducted bye EL-cameras mounted on UAVs (unmanned aerial vehicles). According to IEA PVPS [136], not all the EL-cameras are suitable for aerial inspection. Aerial inspections require EL-cameras with higher sensitivities and lower exposure times. IEA PVPS [136] recommends mirror-less full-format cameras for this type of inspection. As with ground-level inspection, UAV should be equipped with distance sensor and remote-controlled focus length. Since the aerial inspection has battery-limited flight duration, IEA PVPS [136] also recommends a power supply with a multi-box for higher recording rate. According to them, these aerial systems have a productivity up to 1 MWp if inspected PV installation per night.

4.4.2.3 Evaluation

It is common and frequent that EL-images contain different types of cracks and defects in the solar cells. This situation makes it difficult to quantify the exact impact of each abnormality on the overall power losses of the PV module. Using an example (see Fig. 4.19), IEA PVPS [136] explain some of the different defects and abnormalities that can be found in a single PV module. According to IEA PVPS [136], temperature dis-homogeneity during firing the solar cell in the production stage gives rise to a gradient of the contact resistance of the cell's finger metallization from the cell centre to its border. Cells B2, C2 and D2 within Fig. 4.19 present this gradient, dark in the centre and bright at the borders. Not only patterns like gradients can be identified, but also homogeneous patterns. When a cell is not perfectly connected to its busbars (see cell E2), the cell is homogeneously dark. This is because the abnormal cell is not receiving the same amount of injected current than its neighbors due to the imperfect connection.

Fig. 4.19 also present interrupted fingers. They are present without cracks (almost all the cells within row 4) or they are induced by cracks (see cells B3 and D3). According to IEA PVPS [136], finger disconnection without cracks has a marginal impact on power losses and does not significantly degrade with time. In contrast, finger interruptions induced by cracks can be harmful because those cracks can further expand due to environmental exposure. Hence, more fingers can be further interrupted leading to a wear out failure. However, not

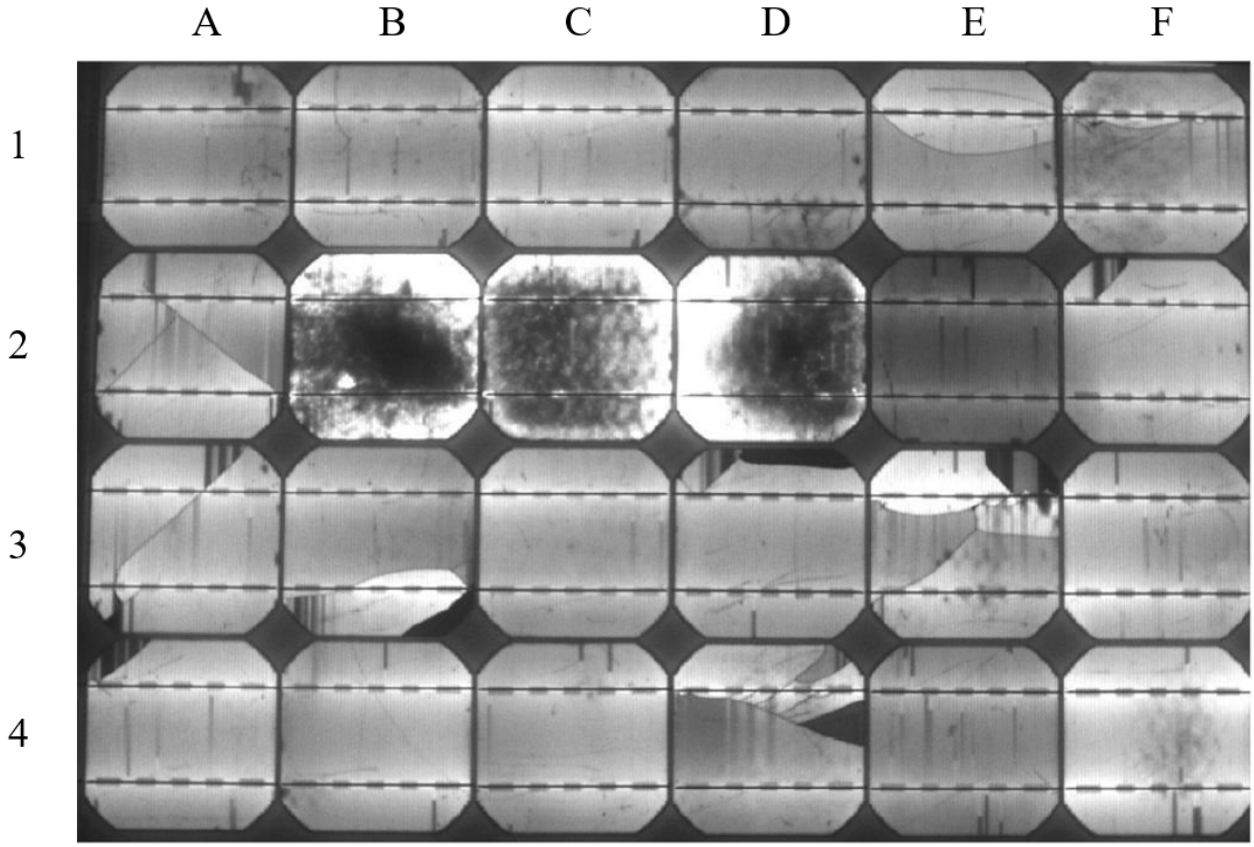

Figure 4.19: EL-image of a monocrystalline PV module with various defects. Image adapted from [136].

all cracks induce loss of power or disconnections. See for example cell A2 that contain a crack that is crossing almost the whole cell, but the cracks is still partially conductive.

According to IEA PVPS [136], with a proper visual inspection it is possible to recognize if a crack is due to an accidental localized pressure applied during installation or by hail impacts. In some cases cracks are due to wrong assembly of the PV module (see cell E3), such as cracks emanating from the busbars due to bad soldering. In other cases, cracks are caused by mechanical loads during transportation (see cell D4).

EL-imaging not only can identify cracks but also the presence of PID. Fig. 4.20 shows an example of a PV module with PID, which contain dark cells at its boundaries.

IEA PVPS [136] states that commonly observable defects and failures have been outlined in one of their previous works (see section 5.4 in [64]). They explain a classification of EL-images can be performed by comparison with the list of failures in [64], just for small studies. This qualitative assessment will not be sufficient for large sample quantities and quantitative techniques must be used. Currently, advanced image analysis tools are available in the internet as open source versions. According to IEA PVPS [136], these software packages provide a full suite of image processing and feature recognition utilities for EL-image analysis tasks. Furthermore, the combined information of EL-images and I-V curves can be used to determine ideality factors and loss current densities for each cell in a module image.

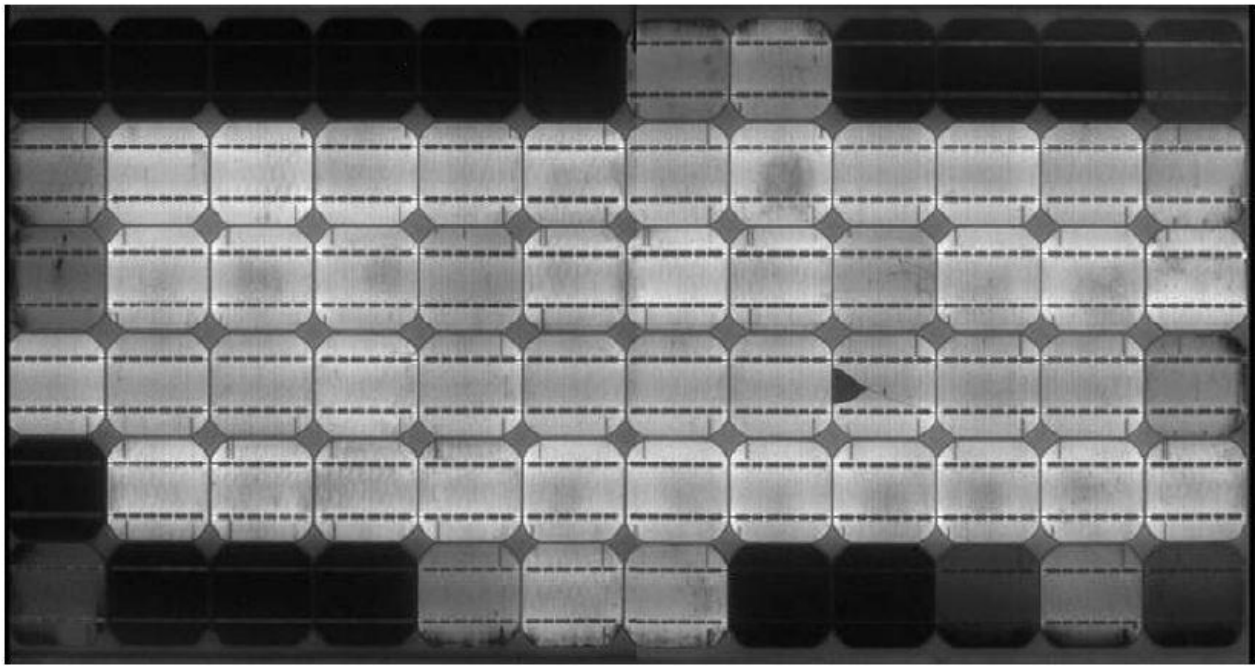

Figure 4.20: EL-image of a monocrystalline PV module with PID [136].

Additionally, IEA PVPS [136] indicates that advanced machine and statistical learning codes have become accessible for research topics. According to them, fault diagnosis for PV systems using Artificial Neural Networks (ANN) and graph-based semi-supervised learning have been demonstrated successfully using array of electrical parameters and environmental data. Although machine learning can improve data diagnosis and make the assessment faster, for the use of machine learning the amount of data must be high for better accuracy. In the case of supervised learning approaches, each cell needs to be manually classified. This task must be completed only once, but it must be done very with carefulness to minimized the error associated with human judgment.

Chapter 5

Inspection Data Collection Tool

5.1 Methodological Strategy

To define a strategy for PV module characterization, this thesis proposes the methodological steps shown in Fig. 5.1, which represents a block diagram that has four levels.

The first level is composed by:

- Theory about PV modules and components
- State-of-the-art of failure modes and degradation mechanisms of PV modules
- State-of-the-art of standards and/or guidelines for field testing of PV modules

The second level corresponds to the main criteria that includes scope and objectives.

The third level corresponds to the IDCTool, which is composed by:

- Form of field testing (survey)
- Equipment and tools used in the field
- Procedures for field testing

Finally the fourth level corresponds to the methodology for the analysis of the results that emerge from the IDCTool.

How are the levels interrelated? Level 2 places the main criteria to design the IDCTool for field testing. In this level, the scope (limitations and delimitations), combined with the objectives of this work, give form to this tool. The inputs needed by level 2 are the ones given by level 1. Level 1 supplies the main resources to create the IDCTool. In this level, the peculiarities of the study that is going to be carried out are captured. Such peculiarities can be the focus on the Atacama Desert, scale of applications, type of technologies, among

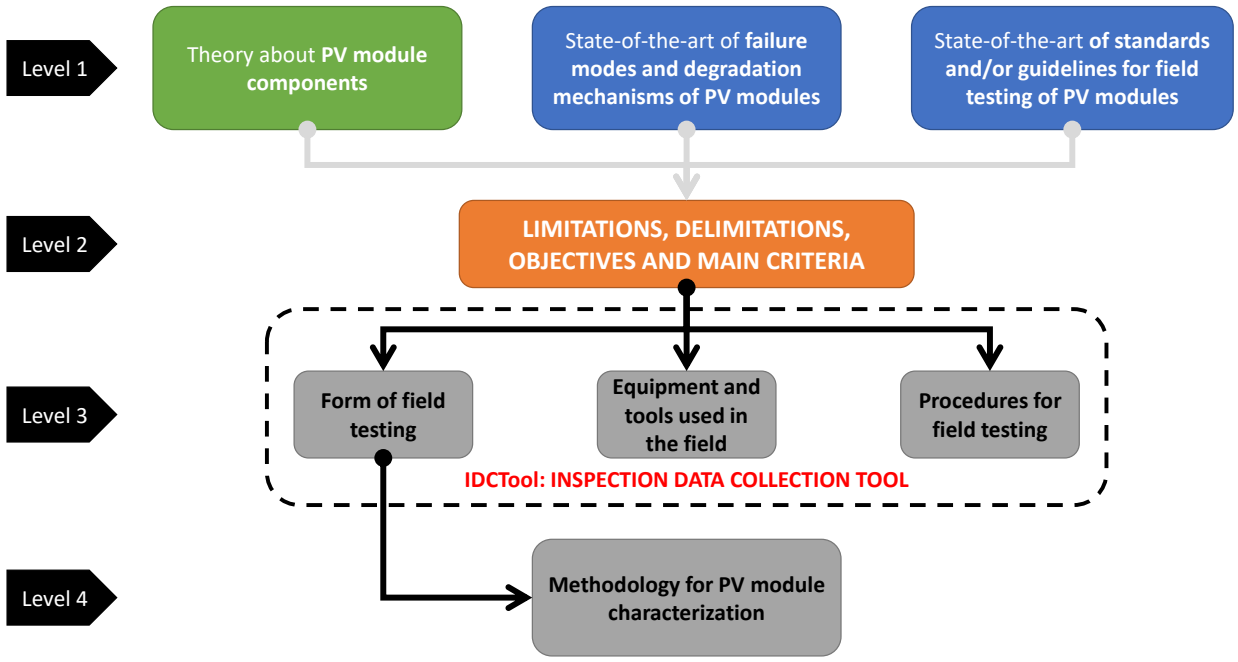

Figure 5.1: Methodological strategy for this work.

others. Thus, the survey, in level 3, is mainly based in the state-of-the-art of failure modes (level 1), the theory about PV modules and their components (level 1) and main criteria (level 2). The equipment and tools in combination with the procedures for field testing, in level 3, are mainly based in the state-of-the-art of standards and guidelines for field testing of PV modules (level 1) and main criteria (level 2).

Level 3 contains the products of this work, the survey form must be filled by the person responsible for the campaign, who will use the specified equipment and tools. Moreover, this thesis indicates the procedures in compliance with HSE requirements, so the worker can be safe while doing the inspection. Finally, level 4 corresponds to the methodology for analysis of the results. The analysis is strongly influenced by the structure of the survey. In this context, the methodology is thought to be robust for statistical analysis. Thus, for a minimum amount of data with statistical significance, robust conclusions and recommendations can be formulated based on the proposed methodology for analysis.

5.2 Main Criteria

The main criteria corresponds to the selection and organization of the relevant and key information from the state-of-the-art within Chapter 3 and Chapter 4, following the structure explained in Chapter 2. The information is defined as relevant in agreement with the scope (limitations and delimitations) and the objectives of this research work. Finally, this selection gives shape to the IDCTool (see section 5.3).

First of all, the delimitations made for this research work consider that the IDCTool is developed for (mono or multi) c-Si technology only, leaving out technologies such as thin-film (CIGS, a-Si and CdTe), concentrator PV (CPV), multi-junction cells and emerging PV (quantum dot cells, perovskite cells, organic cells, inorganic cells and dye-sensitized cells). This choice is based in two main reasons. One reason is that Si-wafer based PV technology accounted for about 94% of the total production in 2016 [139], while the other 6% was accounted by thin-film technology. The rest of the technologies are not yet marketable. The other reason is that the probability of finding PV modules based on thin-film technology within the Atacama Desert is low.

Another important delimitation is that the IDCTool is developed to be applied in PV modules operating in desert conditions. This choice was based on the main targets for PV R&D&I within the national solar program. Today, the development of a national solar power industry is on the way and all the efforts are focused into this task. In order to make an intelligent choice of technologies for this developing industry, it is important to understand how the available technologies operate within the conditions that the Atacama Desert presents. This desert has unique characteristics that are currently known by Chilean researchers due to projects concerning studies of the solar resource in the north of Chile. As stated in the introduction, one of the most significant characteristics is the UV-B irradiation. It is known that UV-B doses are 40% higher than the northern Africa doses, which can be detrimental to certain materials within certain PV technologies.

Finally, the last delimitation of this research work is the amount of details within the IDCTool. The aim of this tool is to create a database with information regarding the most typical failures or abnormalities that PV modules develop while they operate in the Atacama Desert. We are not interested in a full examination to scan all the issues that a single PV module may experience. A full scan will generate a huge amount of information that in the end may not be required, or will make the analysis of the data more complex. Furthermore, it is imperative to maintain a low, but sufficient, amount of details to examine a single PV module in a few minutes. The time is important because this tool is designed to make a scan of all (within the reasonable constraints) PV modules operating in the Atacama Desert until today.

Regarding to the inherent limitations of this research work, the main issue is the available budget. This limitation makes it necessary to select low-cost equipment, which may not have the required specifications regarding resolution and/or accuracy. Despite of this, the collected data can still provide meaningful, yet less comprehensive, statistics for failure analysis purposes. Nevertheless, specifications and budget must always be treated in balance. It is not recommended to buy the cheapest apparatus if the ranges of its specifications are too far from the ones required.

One of the most important objectives of this research work is the elaboration of recommendations through the analysis of the collected data. To accomplish this objective, it is important to have reliable and consistent conclusions about the information under analysis. Therefore, the IDCTool is designed to deliver a basic/minimum set of information to extract deductions by the means of statistical studies and comparison. Furthermore, the collected information can be analyzed via typical patterns of visual or thermal abnormalities, which

are explained with graphical examples. Likewise, I-V characteristic can be studied from a qualitative (shape of the curve) or quantitative (electrical parameter values) point of view.

5.3 Inspection Data Collection Tool

The IDCTool is the combination of the form of field testing (survey), the equipment and tools, and the procedures to acquire data in the field. Appendices A and B show the survey in English and Spanish language respectively. Appendix C indicates the supplementary documentation, which is the same survey presented in four different ways. Two of them are in fillable PDF format (in two languages) and the other two are in fillable xlsx format (in two languages). Regarding the equipment and tools, the minimum equipment necessary to proceed with the inspection is: iPad or tablet to fill the survey, an I-V tracer with its components (DC (clamp) ampere-meter and sensors for temperature and irradiance), and the thermal camera. In relation to the procedure, in general, the inspection starts with a checklist of the equipment and tools with their right configuration, followed by the filling of the survey for visual inspection, and ending with the acquirement of electronic records. The electronic records start with the thermal inspection due to the necessity of thermal equilibrium (thermal steady state condition), followed by the I-V curve measurements.

The next sections will cover the full explanation of everything mentioned above.

5.3.1 Fillable form (survey)

The survey is mainly based in the visual inspection data collection tool developed by NREL [17]. The addition of new types of damages (or the change of an existing one) into the survey is based in the review of failures in Chapter 3 and the information given by the international standards IEC PAS 62257-10 [121], IEC 61215-1[122] and ASTM E1799 [123]. The addition or modification of a failure was made in order to give priority to failures that occur in desert climates.

As an example of the survey, Fig. 5.2 shows an excerpt of the whole survey. This form is composed of 15 sections, which are explained in the list below.

1. *Site information* —it contains the basic information to geographically locate the inspected installation.

2. *Module data* —it contains the minimum information that any PV module should have printed in its label (at the back).

3. *Rear-side glass* —it identifies common damage types for the glass at the back of a bifacial PV module.

4. *Backsheet (polymer)* —it identifies the appearance, texture and damage types for the backsheet of non-bifacial modules only.

Visual inspection form

1. Site information | Folio #

Installation address:		Latitude :	
		Longitude :	
		Altitude :	
ID (Solar MAP):		Date (dd/mm/yy) :	/ /

BEGIN INSPECTION AT THE BACK SIDE OF THE MODULE

2. Module data

Photo taken of nameplate: ☐ yes ☐ no
Technology: ☐ mono-si ☐ multi-Si
Estimated deployment date (mm/yy) : /
Manufacturer :
Model # :
Serial # :
Nameplate: ☐ Nameplate missing

$P_{mpp\,[W]}$: 0 $V_{oc\,[V]}$: $I_{sc\,[A]}$:
$V_{mpp\,[V]}$: $I_{mpp\,[A]}$:

3. Rear-side glass ☐ applicable ☐ not applicable

Damage type				
Crazing (or other non-cracked damage) :	☐ non	☐ small, localized	☐ extensive
Cracks :	☐ non	☐ small, localized	☐ extensive
Shattered (tempered) :	☐ non	☐ small, localized	☐ extensive
Shattered (non-tempered) :	☐ non	☐ small, localized	☐ extensive
Chipped :	☐ non	☐ small, localized	☐ extensive

Figure 5.2: Excerpt from the complete filling form (survey) developed in this work.

5. *Wires* —it identifies the appearance and damage types for the external cabling (not considering the connectors or the cabling within the junction box).

6. *Connectors* —it identifies the type of connectors, their appearance and damage types.

7. *Junction box* —it identifies the appearance and damage type of the box itself, its lid, its adhesive and its wire attachments.

8. *Frame grounding* —it identifies the original state of the grounding's frame, its appearance and function (in the present).

9. *Frame* —it identifies the appearance and the damage types of the frame with the addition of the damage types of the adhesive of the frame.

10. *Frame-less edge seal* —bifacial and non-bifacial PV modules can have aluminum frame or not frame at all. For frame-less modules, this section identifies the appearance and the damage types of the seal.

11. *Glass/polymer (front)* —it identifies material, features, appearance and damage types of the front glass, polymer or composite.

12. *Encapsulant* —it identifies appearance and damage types for the encapsulant. In particular, the damage types covers delamination and discoloration.

13. *Metallization* —it identifies the appearance and the damage types of grid-lines, busbars, cell interconnect ribbon and string interconnect.

14. *Silicon cell* —it identifies the number of cells and strings within the PV module and the damage types for silicon cells.

15. *Electronic records* —it identifies the number of visual- and thermal-images with their respective names to organize electronic information. I-V curve measurements are also considered (amount of measurements, names and electrical parameters for each curve). Information regarding temperature and irradiance for thermal-images are also identified.

5.3.2 Equipment and tools

Figure 5.3 shows the minimum equipment and tools to proceed with the inspection of PV modules in the field. All the equipment and tools are described in detail in the following sections. The data-sheet for the thermal camera and the I-V tracer are shown in Appendices D and E, respectively. The most relevant information from each data-sheet will be also covered in the following sections. For further details, see the mentioned appendices.

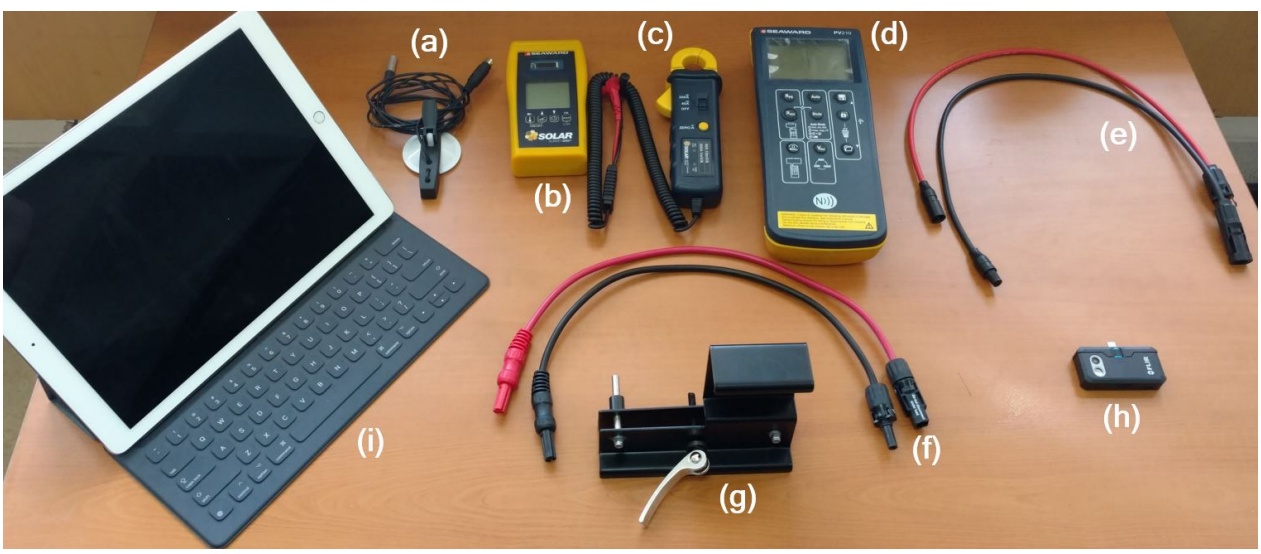

Figure 5.3: Minimum equipment and tools for data collection in the field. (a) Temperature sensors, (b) irradiance meter, (c) DC (clamp) ampere-meter, (d) I-V tracer, (e) MC3 to MC4 adapter leads, (f) MC4 test leads, (g) irradiance meter mounting bracket, (h) FLIR ONE pro camera and (i) iPad.

5.3.2.1 FLIR ONE pro

The FLIR ONE pro thermal camera (see Fig. 5.4) is a low cost camera for thermal imaging. Today, this camera can be bought at four hundred dollars at the official manufacturer or other stores like amazon, eBay, etc. In particular, this camera is certified with the iOS version which allows it to be used with an iPad. Although this camera has an optional version that is compatible with a tablet that runs with Android, there is no adapter or configuration that allows to use it with both operating systems, which means that it must be decided beforehand the type of tablet to be use. Due to its small dimensions ($68 \times 34 \times 14$ mm^3) and its light weight (36.5 g), it can be transported in the pocket and used in small places.

Figure 5.4: FLIR ONE pro camera.

The most important specifications of FLIR ONE pro camera are shown in Table 5.1. According to the requirements of thermal cameras for PV application in Table 4.3, the thermal spectral range of FLIR ONE pro is within the desired values. Likewise, the thermal sensitivity is another important parameter that the FLIR ONE pro fulfills ($150\ mK \leq 0.1\ K$). Regarding the object temperature range, FLIR ONE pro fulfills the requirements exceeding the upper limit by 280°C. In contrast, a few requirements are not in the desired range. According to Table 4.3, the accuracy (or absolute error measurements) should be less than 2 K, but FLIR ONE pro has an accuracy of $\pm 3\ K$. Likewise, the emissivity and reflected temperature should be adjustable, but they are not. The emissivity can be adjustable only in four values and the reflected temperature is fixed at 22°C.

In relation to the shutter, the spot meter resolution and measurement functions, the FLIR ONE pro is a very good option for thermal imaging. This camera can take one picture with 9 measurement functions working at the same time. Fig. 5.5 shows an example of this. The thermal-image contains 3 spot measurements, 3 rectangle-area measurements and 3 circle-area measurements. The spot meter resolution for spot measurements is within the desired thermal sensitivity, according to Table 4.3. The shutter can be automatically or manually

adjusted. Therefore, sharped thermal-images can be taken.

Figure 5.5: Thermal-image, taken with FLIR ONE pro, with 9 measurement functions working at the same time.

Regarding the recommendation of 3 cm of the module edge per pixel as maximum (see Table 4.3), which can be translated to 5×5 pixels per solar cell or a maximum IFOV of $30-32$ mm, the FLIR ONE pro fulfills the requirement with a pixel size of 12 μm. This pixel size can be translated to an IFOV of 0.012 mm, which is less than the upper limit. According to IEA PVPS (see Table 4.6), the thermal resolution of FLIR ONE pro is within the low class. This thermal resolution is typical for low cost cameras (see Table 4.7) and is within a reasonable resolution. Furthermore, IEA PVPS recommends that the visual resolution shall be higher than the thermal resolution for better details. FLIR ONE pro fulfills this requirement with a second lens (see Fig. 5.4) with a resolution of 1440×1080 (see Table 5.1), which is higher than its thermal resolution.

Finally, FLIR ONE pro has a battery life of approximately 1 hour with a charge time of 40 minutes. The camera brings a USB-C to USB-A lead to charge the battery with a 1 A power source.

Table 5.1: FLIR ONE pro specifications (see Appendix D).

Item	**Specification**
Thermal pixel size	12 μM
Thermal spectral range	8 - 14 μM
Thermal/visual resolution	160 × 120 / 1440 × 1080
HFOV / IFOV	55° ±1° / 43° ±1°
Focus	Fixed 15 cm - Infinity
Scene dynamic range	-20°C to 400°C
Accuracy	±3°C or ±5%
Thermal sensitivity	150 mK
Emissivity settings	Matte: 95%, Semi-Mate: 80%, Semi-Glossy: 60%, Glossy: 30% and $T_{refl} = 22$°C
Shutter	Automatic/Manual
Spot meter resolution	0.1°C

5.3.2.2 Seaward PV210

The solar PV tester and *I-V* curve tracer (see Fig. 5.6) provides efficient and effective test and diagnostic solution for PV systems in compliance with IEC 61829. The standard IEC 61829 (published in 2015) is a later version of IEC 60904 (published in 2006), which gives guidance for *I-V* curve measurements that take place outdoors. When the tracer is used in conjunction with the Solar Survey 200R (see Fig. 5.9) irradiance meter, the PV210 measurement data can be converted to STC, using either the PVMobile app (smart-phone) or SolarCert Elements software (PC). A high contrast display is clearly visible in direct sunlight and shows open-circuit voltage, short-circuit current, maximum power point voltage, current and power, as well as the fill factor of the PV module or system under test. Detailed and colored *I-V* and power curves can be viewed instantly once data is transferred to the PVMobile Android app using wireless NFC connectivity. The most important specifications from Appendix E are shown in Table 5.2.

The tracer comes with its own leads to connect the equipment to PV modules with MC4 connectors. MC4 connectors are the most typical connectors that PV modules use today. Before MC4 connectors were the most used, there were MC3 connectors. Since there is a possibility of finding PV modules with MC3 connectors, it is recommended to have leads to adapt MC3 connectors to MC4 connectors. Fig. 5.8 shows two leads (one for the positive pole and other for the negative pole of the PV module) to adapt both terminals of the PV module so it can be connected to the tracer. These adapter cables do not come with the

tracer, nor the PV210 kit. They were fabricated in Universidad de Chile, for this particular research work.

Figure 5.6: Seaward PV210 I-V tracer.

Table 5.2: Seaward PV210 specifications (see Appendix E).

Item	**Specification**
Voltage measurement (via 4 mm probes)	
Display and measurement range	30 V - 440 VAC/DC
Resolution	1 V
Accuracy	±(5% rdg + 2d)
Operating current (via DC current clamp)	
Measurement range	0.1 A - 40 A AC/DC
Resolution	0.1 A
Accuracy	±(5% rdg + 2d)
I-V curve	
Maximum power dissipation	10 kW
Number of points	Dynamic up to 128
MPP calculation max error	±(1.5% rdg + 40w)

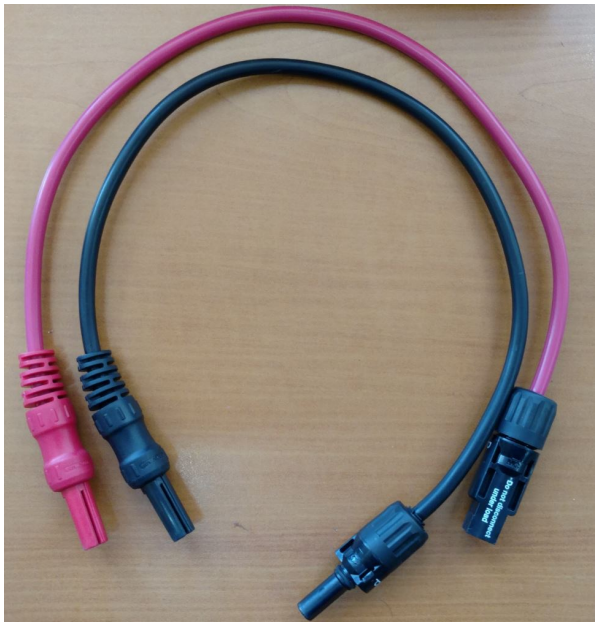

Figure 5.7: MC4 test leads.

Figure 5.8: MC3 to MC4 adapter leads.

Figure 5.9: Solar Survey 200R irradiance meter.

Standards IEC 60904-1 [124] and ASTM E1036 [131] specify that a PV reference device (or cell) must be used for correction to standard test conditions. The Solar Survey 200R irradiance meter shown in Fig. 5.9, which is part of the PV210 kit, contains a reference cell above the display. Within Fig. 5.9, the temperature sensors are shown at the left of the irradiance meter. The metallic thermocouple is for ambient temperature measurements, while the white rubber is for temperature measurements of the PV module. Since the tracer in conjunction with the irradiance meter compute the corrections for STC, a third temperature sensor for the reference cell within the irradiance meter is not required. An spectroradiometer is also not required due to the same argument.

Since the reference cell must acquire the same irradiance that the PV module, the PV210 kit brings a mounting bracket (see Fig. 5.10) to align the irradiance meter along the PV module. Additionally, the PV210 kit also brings a DC clamp meter (see Fig. 5.11) to measure the current (AC or DC) in real time.

Figure 5.10: Solar Survey 200R irradiance meter mounting bracket.

Figure 5.11: DC clamp meter from PV210 kit.

5.3.2.3 iPad

The last, but not least, equipment is an iPad. This device can be replaced by any other tablet, however, it must be ensured that the FLIR ONE pro camera version is compatible

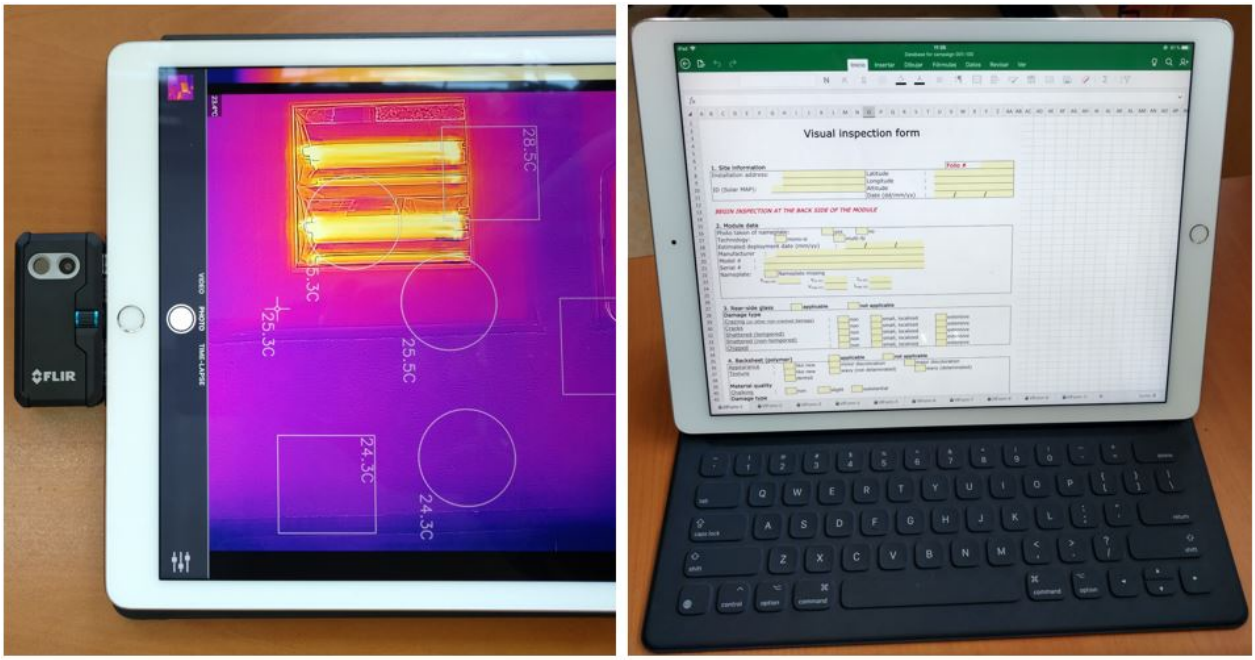

Figure 5.12: iPad to fill the visual inspection survey and to take thermal picture in combination with FLIR ONE pro.

with the tablet's operating system. As explained in section 5.3.2.1, this camera is compatible with both, iOS operating system and Android, but not simultaneously. So, when buying the camera, it is important to choose the appropriate operating system according to the tablet to be use. As it can be seen in Fig. 5.12, the iPad is used for two purposes. One purpose is to fill the visual inspection survey, and the second purpose is to take thermal pictures in combination with FLIR ONE pro.

5.3.3 Procedure for field testing

The sequence of the complete field inspection is as follows:

1. Equipment and tools checklist and optimization.
2. PV module criteria selection for inspection:
   (a) Perform a quick visual inspection and select at least 3 PV modules that are visually degraded or damaged.
   (b) If all PV modules are identical (no difference in visual appearance) then perform a random selection of at least 3 PV modules.
   (c) If time is not a restriction, then it is recommended to inspect all of the PV modules installed in the small power plant.
3. Once the modules to be inspected are chosen, carry out the following steps for each of the selected modules.
4. Perform a detailed visual inspection:
   (a) Fill the site information, date and folio within the survey.
   (b) Fill the module information within the survey and take a visual-image of the label.
   (c) Perform the visual inspection at the back of the PV module (fill the survey and take visual-images).
   (d) Perform the visual inspection at the front of the PV module (fill the survey and take visual-images).
5. Perform the thermal inspection:
   (a) If the PV module under inspection is not under operation, connect it to a resistive load and wait at least 15 minutes.
   (b) Check for environmental conditions requirements:
      i. Minimum irradiance shall be 600 Wm^{-2}. Module current shall be at least 30% of rated current.

ii. Cloud coverage shall be maximum 2 okta (use Appendix F).

iii. Wind speed shall be maximum 4 Bft or 28 km/h (use Annex E from IEC TS 62446-3 [62]).

iv. Soiling must be low. Clean the surface if it is required.

(c) Do the thermal inspection at the front surface of the PV module (fill the survey and take thermal-images):

i. Position the camera as perpendicular as possible to the PV module surface. Avoid object and personnel reflections.

ii. If an abnormality is identified, take a thermal-image with its corresponding visual-image (fill the survey).

(d) If it is not easy to identify abnormalities in the front, make a thermal inspection from the back of the PV module (follow the same instructions as in frontal thermal inspection).

(e) Fill the thermal parameters within the survey (ambient and module temperature).

6. Perform the I-V curve measurement(s):

(a) Assemble the mounting bracket at one edge of the PV module under inspection. Place the irradiance meter on the mounting bracket.

(b) Install the the module's temperature sensor at the back of the inspected PV module. It must be placed as near as possible to the center of the backsheet.

(c) Connect the I-V tracer to the PV module under inspection. If the module uses MC3 connectors, use de adapter leads.

(d) Synchronize the I-V tracer with the irradiance meter for STC corrections.

(e) Make a measurement and save it in the tracer. Write the name of the measurement and the corresponding electrical parameters within the survey.

(f) Take at least 4 measurements.

5.4 Characterization methodology

The methodology for the characterization of the inspected PV modules, as stated in level 4 of the diagram in Fig. 5.1, is directly related to the visual inspection survey. In this context, the analysis of the results is organized based on the structure of the visual inspection form. This means that the approach for the analysis is different for visual data, electrical data and thermal data. The survey organizes the results and facilitates the creation of a database for

statistical studies. The methodology for the analysis/characterization of the PV modules inspected is thought to have statistical significance. In this context, when the IDCTool is used for a minimum amount of PV modules, robust conclusions and recommendations can be developed with this work. The following paragraphs explain the PV characterization methodology.

Visual damage, electrical degradation, thermal behavior and thermal abnormalities are analyzed, using three different points of view, as follows:

1. the zone in which the affected PV module is installed,
2. the manufacturer of the affected PV module and,
3. the time of exposure of the affected PV module.

5.4.1 Visual analysis

Table 5.3 shows the analysis methodology for PV module characterization using the results that emerge from the IDCTool. Given a visual failure, the number of times that the defect occurs is considered the total universe to analyze the failure. Therefore, one visual defect can be found at most 95 times (maximum number of modules inspected). Using the total universe of the defect, the questions in Table 5.3 are answered during the analysis. Hence, zones are sorted from the one that presents the failure most frequently to the one that presents the failure less frequently. The same happens with the manufacturers and the exposure times.

5.4.2 Electrical analysis

Visual failures are given from section 3 to section 14 in the inspection survey. Section 15 gather information related to electronic records. Electronic records correspond to the number and the name of the visual and thermal photos taken in the inspection, including the information regarding to the maximum power (in W), open-circuit voltage (in V), short-circuit current (in A), the voltage (in V) and the current (in A) in the maximum power point, and the fill factor (in %) of the measured I-V curves. Furthermore, thermal information of the I-V curve measurements is also gathered including irradiance (in W/m^2), and temperatures from the module and the ambient (in °C).

To analyze the electrical information given by the I-V measurements, in order to answer the questions in Table 5.3, the information given by the I-V tracer must be corrected to STC. The correction must be in accordance with the state-of-the-art in chapter 4. Once the electrical parameters are corrected to STC, the following parameters must be calculated:

$$P_{mpp_{\mathrm{drop}}} = \frac{P_{mpp_{rated}} - P_{mpp_{STC}}}{P_{mpp_{rated}}} \times 100\% \tag{5.1}$$

$$DR_{P_{mpp}} = \frac{P_{mpp_{\text{drop}}}}{\text{years of operation (age)}} \tag{5.2}$$

$$I_{sc_{\text{drop}}} = \frac{I_{sc_{rated}} - I_{sc_{STC}}}{I_{sc_{rated}}} \times 100\% \tag{5.3}$$

$$DR_{I_{sc}} = \frac{I_{sc_{\text{drop}}}}{\text{years of operation (age)}} \tag{5.4}$$

$$V_{oc_{\text{drop}}} = \frac{V_{oc_{rated}} - V_{oc_{STC}}}{V_{oc_{rated}}} \times 100\% \tag{5.5}$$

$$DR_{V_{oc}} = \frac{V_{oc_{\text{drop}}}}{\text{years of operation (age)}} \tag{5.6}$$

$$FF = \frac{P_{mpp_{rated}}}{I_{sc_{rated}} \times V_{oc_{rated}}} \tag{5.7}$$

$$FF_{\text{drop}} = \frac{FF - FF_{STC}}{FF} \times 100\% \tag{5.8}$$

$$DR_{FF} = \frac{FF_{\text{drop}}}{\text{years of operation (age)}} \tag{5.9}$$

where rated power, current and voltage are parameters given by the manufacturers in their data-sheets, and STC power, current, voltage and fill factor are parameters measured by the I-V tracer that must be corrected to STC.

It should be noted that for zone and manufacturer analysis of the electrical parameters —the **degradation rate** of the maximum power ($DR_{P_{mpp}}$), short-circuit current ($DR_{I_{sc}}$), open-circuit voltage ($DR_{V_{oc}}$) and fill factor (DR_{FF}) must be calculated (see Table 5.3). However, for temporal analysis—the **absolute drop** of the maximum power ($P_{mpp_{\text{drop}}}$), short-circuit current ($I_{sc_{\text{drop}}}$), open-circuit voltage ($V_{oc_{\text{drop}}}$) and fill factor (FF_{drop}) must be calculated. The questions stated in Table 5.3 must be answered by sorting the zones from the one that presents the degradation rate less severely to the one that presents the degradation rate most severely. This should be done for each electrical parameter (power, current, voltage and fill factor). The same happens with the manufacturers and the exposure times. However, temporal analysis use degradation drop of the electrical parameters instead of degradation rate.

5.4.3 Thermal analysis

Thermal analysis is divided into three categories: (1) temperature deviation study, (2) hot-spot study and (3) thermal pattern study.

Temperature deviation study refers to the analysis of the temperature difference between the average operating temperature of the module (T_{mod}^{ave}) and the ambient temperature (T_{amb}) of the location where the module is installed. For each PV module inspected, the temperature difference (ΔT) must be calculated as follows:

$$\Delta T = T_{mod}^{ave} - T_{amb} \tag{5.10}$$

Using equation 5.10, the questions in Table 5.3 must be answered. In this context, zones must be sorted by the one that presents highest ΔT deviations to the one that present the lowest deviations. The same happens with the manufacturer and temporal analysis.

Hot-spot study refers to the analysis of the presence of hot-spots in the PV modules inspected. A hot-spot is considered an in-homogeneous (and localized) spot with a higher temperature with respect to its surroundings. According to the literature, a spot with higher temperature is considered a hot-spot if its temperature difference is higher than 10°C [140, 141]. A classification[1] is made for two types of hot-spots:

- Light hot-spot, which corresponds to a temperature difference of 10°C to 20°C
- Strong hot-spot, which corresponds to a temperature difference higher than 20°C.

By using the definition and classification of hot-spots stated above, the questions stated in Table 5.3 must be answered. Therefore, zones must be sorted by the one that presents highest number of PV modules with light (and strong) hot-spot to the one that presents the lowest number of light (and strong) hot-spots. The same happens with the manufacturer and temporal analysis.

Thermal pattern study refers to the analysis of thermal abnormalities that are already classified as common/typical thermal patterns found in PV modules. The matrix of thermal abnormalities in Appendix G considers 11 thermal patterns. One PV module can develop more than one pattern, but not all of them. For example, thermal pattern 1 and 2 of this matrix cannot be present in the same PV module. This is because the module cannot be in short-circuit and open-circuit condition at the same time.

Thermal images of each inspected PV module must be analyzed with the matrix of thermal abnormalities, then, the questions in Table 5.3 must be answered. In this context, for each thermal pattern (from 1 to 11), the zones are sorted from the one that presents the thermal pattern most frequently to the one that presents the thermal pattern less frequently. The same happens with the manufacturer and temporal analysis.

[1] It is not mentioned if this classification is for maximum power point operation or other condition. Since is not mentioned, it is more likely to be made for maximum power condition.

Table 5.3: Methodology for the analysis of PV module characterization.

Type of failure		**Zone analysis**	**Manufacturer analysis**	**Temporal analysis**
Visual		Which zone presents the visual damage more frequently?	Which manufacturer presents the visual damage more frequently?	Which exposure time presents the visual damage more frequently?
Electrical		Which zone presents the electrical degradation rate of V_{oc}, I_{sc}, P_{mpp} and FF more severely?	Which manufacturer presents the electrical degradation rate of V_{oc}, I_{sc}, P_{mpp} and FF more severely?	Which exposure time presents the electrical degradation of V_{oc}, I_{sc}, P_{mpp} and FF more severely?
Thermal	**Temperature deviation**	Which zone presents higher ΔT deviations?	Which manufacturer presents higher ΔT deviations?	Which exposure time presents higher ΔT deviations?
	Hot-spot	Which zone presents higher number of PV modules with light (and strong) hot-spots?	Which manufacturer presents higher number of PV modules with light (and strong) hot-spots?	Which exposure time presents higher number of PV modules with light (and strong) hot-spots?
	Thermal pattern	Which zone presents the thermal abnormality more frequently?	Which manufacturer presents the thermal abnormality more frequently?	Which exposure time presents the thermal abnormality more frequently?

Chapter 6

Field Test Campaign

The aim of the campaign in the Arica and Parinacota Region (north of Chile) is to elaborate recommendations based on the analysis of the results from this case of study. To be able to generate reliable conclusions about the effects of the climate on the PV module operating in the region, climate characterization of the different zones within the region is required. One of the main targets of the analysis from the campaign is to associate abnormalities due to material and environmental conditions interaction.

In the following sections, a characterization of Arica and Parinacota Region is given. This characterization is based on a description of the region, which includes administrative division and geomorphological division with its associated climate zones.

6.1 XV Arica and Parinacota Region [142]

XV Arica and Parinacota Region can be summarized into three different landscapes: valleys, desert and plateau (or highlands). The region has a total surface of 16,898.3 km^2 that corresponds to the 2.24% of the total surface of the country. According to the census of 2017, performed by Instituto Nacional de Estadísticas (INE), the population in the region is 226,068 inhabitants. The administrative division corresponds to two provinces with their capitals and four communes. The administrative division is shown in Table 6.1. The capital for the province of Parinacota is Putre, which has the communes of Putre and General Lagos. The capital for the province of Arica is also called Arica, which has the communes of Camarones and Arica.

Figure 6.1: Welcome to the new Arica and Parinacota Region. Image obtained from `http://www.pinterest.es/talytacc/`.

Table 6.1: Provinces and communes from Arica and Parinacota Region [142].

Provinces		**Communes**		
Name	**Capital**	**Name**	**Communal Headquarters**	**Surface** (km^2)
Arica	Arica	Arica	Arica	4,799.40
		Camarones	Cuya	3,927.00
Parinacota	Putre	Putre	Putre	5,902.50
		General Lagos	Visviri	2,244.40
		Total		**16,873.30**

The complete Arica and Parinacota Region is shown in Fig. 6.2. It can be seen that the commune of Arica is closer to the coast, while the commune of Camarones is in the middle of the intermediate depression. The communes of Parinacota (Putre and General Lagos) are closer to the mountains. Fig. 6.3 shows a satellite version of the same map to show the relief terrain.

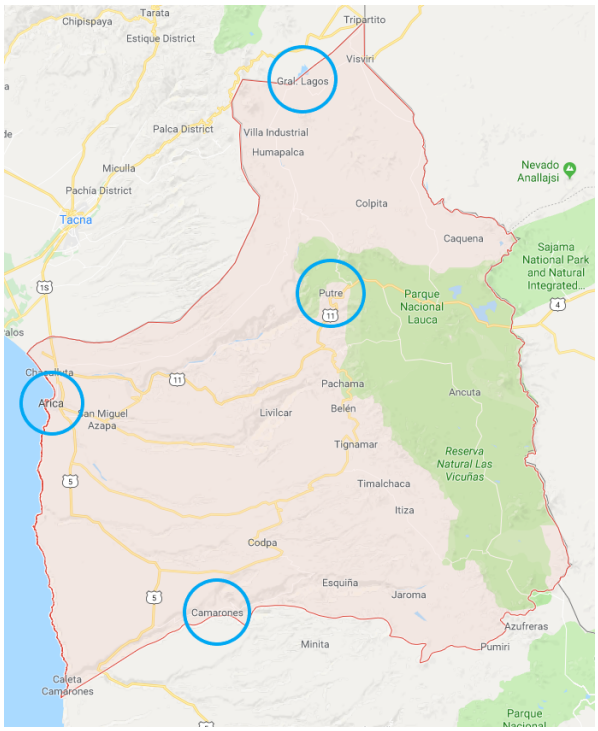

Figure 6.2: Google map of Arica and Parinacota Region. The four communes are shown inside a blue circle.

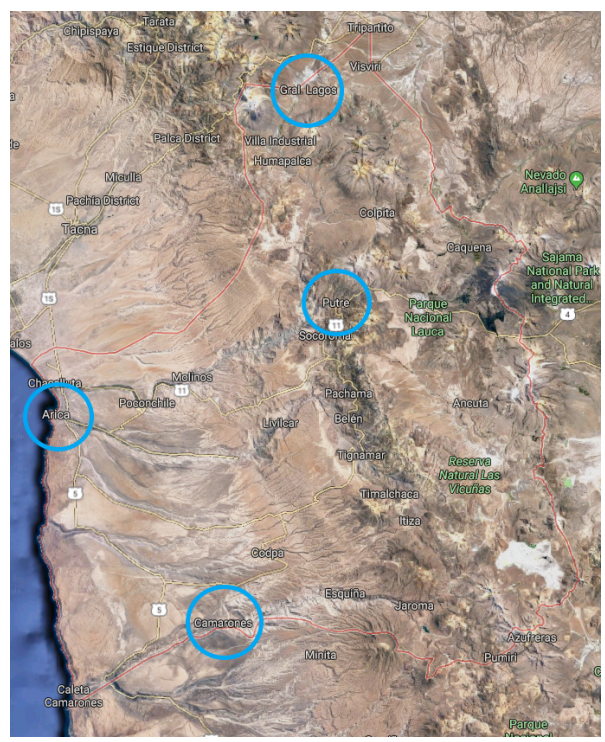

Figure 6.3: Satellite Google map of Arica and Parinacota Region. Communes are highlighted again.

6.1.1 Geomorphological division

The tectonic plates give birth to the Coastal mountain, Andes mountain, the coastal walls and the plateau. This derives in different environments such as the coastal edge, valleys, absolute desert, wetlands or bofedales (see Fig. 6.5), salares (see Fig. 6.6), and lower- and high-mountain range. The coastal edges are commonly arid while fertile valleys can be found in the lower-mountain range. Fig. 6.4 shows a geomorphological map of the Arica and Parinacota Region. It can be seen that the pampas and the salt fields are located between the Coastal mountain and the Andes mountain, while the coastal walls, as their name states, are located at the coast. A coastal wall (or coastal farellón) is a large cliff that is formed due to the abrupt fall of the Coastal mountain into the sea.

Branches of geomorphology study the factors that have strong influences in the form of the Earth's surface, such as the climate. Climatic geomorphology studies the climate influence in the development of the relief of the Earth's surface. Therefore, there is a relationship between the climate and the terrain of a specific zone. In the following section, the climate of different environments of the region will be explained following the geomorphological division.

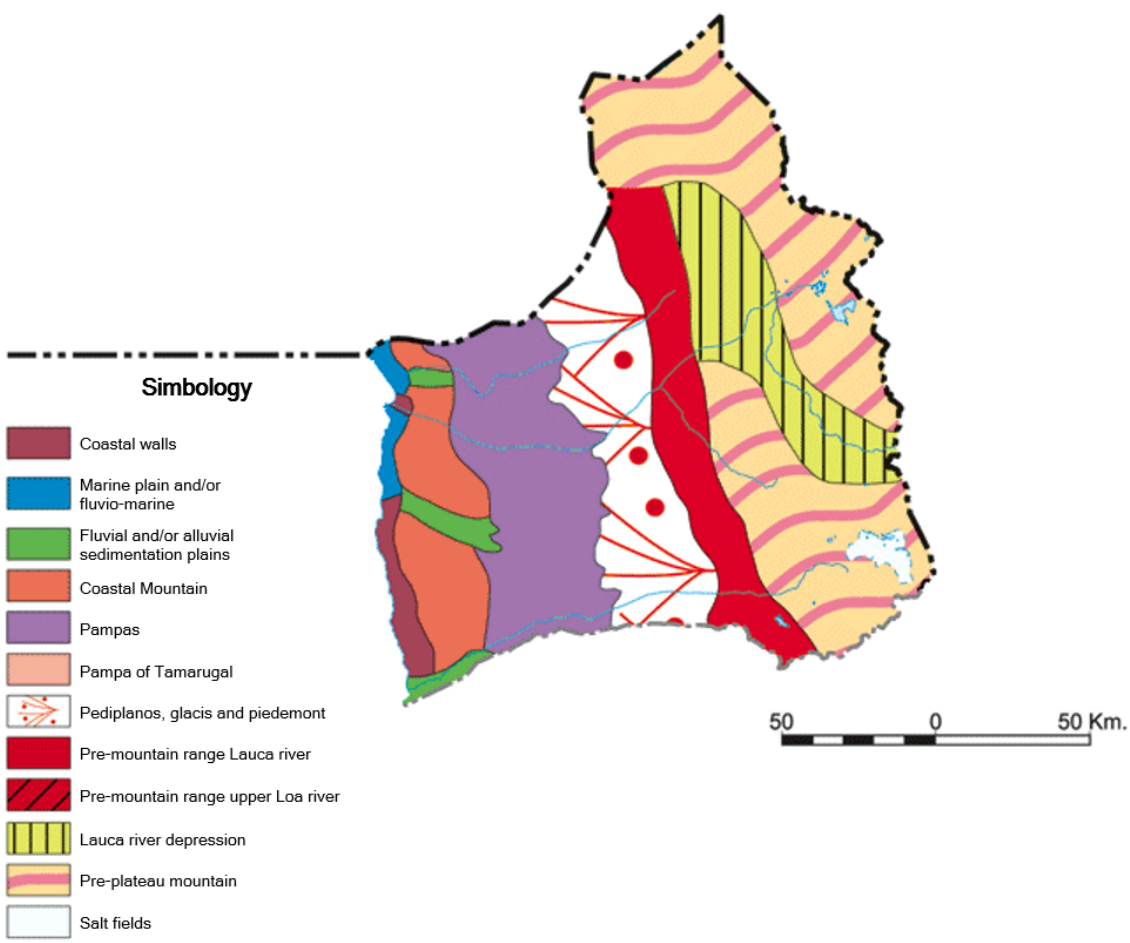

Figure 6.4: Geomorphological map of the Arica and Parinacota Region. Image adapted from `http://www.educarchile.cl/`

Figure 6.5: Wetlands in the Chungará Lake. Image obtained from `http://www.flickr.com/photos/jorgeleoncabello/`.

Figure 6.6: Salar of Surire. Image obtained from `http://geografia200ith.blogspot.cl/`.

6.1.2 Climate Zones

Due to the latitude, between the Ecuador and the Tropic of Capricorn, in the region predominate the southwest winds. The high pressure of the Pacific Ocean Anticyclone triggers the descent of warm air from the Ecuador, which enables permanent good weather and absence of precipitation in the littoral and intermediate depression. Although the precipitations in the littoral do not surpass the millimeter, concentrating only in winter, the tropical influence (masses of humid air) get to accumulate 300 millimeters annually in the highland region.

The phenomenon known as *Camanchaca* (superficial fog), which occurs in the coastal zone (see Fig. 6.7), is due to the cooling of the superficial warm air (less than 1,000 meters) that goes through the cold current of Humboldt. The progress of this fog is stopped by the coastal walls.

Due to the altitude of the region (up to 6,000 meters within the volcanoes), the temperature of the coastal zone (18°C) decreases towards the mountain zone (11°C). The average monthly temperatures of the region can reach -10°C and increase up to 26°C. Due to the effects of *El Niño* phenomenon, the marine waters increment their temperature that in turn increase the temperature of the coastal air in 1°C or 2°C. The effects of *La Niña* phenomenon has the opposite effect in the coastal air temperature.

According to the Köppen Classification, which was created by the German climatologist Wladimir Köppen, the region of Arica and Parinacota present four types of climates. The four climates corresponds to: Dry Arid with Abundant Cloudiness Climate (BWn), Normal Dry Arid Climate (BW), Hot Dry Arid Climate (BWh) and Hot Semi-Arid Climate (BSh). In the order presented before, the four climates extend from the coastal to the highlands.

The Köppen Classification uses as a first letter a capital letter (from A to E) to define the main climate of a zone. The following two letters indicate sub-groups of the main climate. Climates of type B are arid, which are mainly controlled by the dryness, not the temperature. The aridity not only indicates a deficit of precipitations, but also the loss of water within the soil.

Figure 6.7: Camanchaca phenomenon. Image obtained from `http://www.laderasur.cl/`.

Figure 6.8: Valley of Putre (highlands). Image obtained from `http://www.nosotrosloschilenos.org/`.

The arid climate is divided into two sub-groups. The Dry Arid (BW) climate, which is associated with the coastal zone, and the Dry Semi-Arid (BS) climate, which is associated with the highlands (see Fig. 6.8). The third letter indicates an important miscellaneous characteristic of the climate, where the n corresponds to frequently cloudy (coastal edge) and h corresponds to hot climate commonly found in the subtropics.

6.1.2.1 Dry arid with abundant cloudiness climate (BWn)

Includes the Coastal mountain and the littoral up to 1,000 meters of altitude with a width of 20-30 km. The thermal regime is influenced by the cold currents of Humboldt, moderating the ambient temperature that oscillates between 13°C and 22°C.

6.1.2.2 Normal dry arid climate (BW)

Is present between 1,000 to 2,000 meters of altitude with a width of 25-50 km. Includes the intermediate depression, a series of pampas and basins between the Coastal and Andes mountains. Its main characteristic is the permanent, stable and dry air mass that originates the aridity of the zone, clean skies, low humidity and a daily thermal oscillation up to 25°C.

6.1.2.3 Hot dry arid climate (BWh)

Is present in areas close to the Andes mountain, above the 2,000 meters and below 3,500-3,800 meters of altitude with a width of 35-45 km. The climate is characterized by an unstable air mass, which by the effects of altitude produce cloudy skies and precipitation every summer. Although the rain does not eliminate the desert characteristic of the area, it creates conditions for seasonal vegetation. The temperatures are relatively low, they do not surpass the 15°C.

6.1.2.4 Hot semi-arid climate (BSh)

Includes the zones within the 3,500-3,800 meters of altitude with a width of 50 km. The altitude makes the temperatures cold enough for snow precipitation. Above the 5,700 meters of altitude the snow is permanent. The climate is characterized by an unstable air mass, which by the effects of altitude produce cloudy skies and precipitation during the summer.

6.1.3 Ayllu Solar Map [143]

SERC Chile (Chilean Solar Energy Research Center) began an ambitious project in 2014 in the region of Arica and Parinacota to convert this area into a world reference in the use and production of solar energy. Currently, Chile is in the third place among the countries that

are more attractive for investment in NCRE (non-conventional renewable energies). Today, 12.5% of the electric energy matrix of the country corresponds to NCRE.

In the Quechua language, *ayllu* means "community", a word that corresponds to the basic concept that gave rise to this great project of SERC, which is called *Ayllu Solar*. According to the last cadastre that SERC carried out, there are at least 140 projects of solar generation installed in the region. In accordance with the cadastre, the projects are different in nature and size.

Big projects such as *El Águila 1* and *Pampa Camarones* are power plants that are connected to the main grid of the country and generate a considerable amount of energy. Medium and small scale projects use PV modules and thermal collectors to generate electricity and heat water to optimize agricultural and livestock productive systems. Latest data indicate that more than 200 thousands hectares of farming and 13 thousand of cattle exist in the region.

The cadastre performed by SERC is publicly available in its official web site (`http://www.ayllusolar.cl/`). The 140 projects currently known are mapped onto the map of the Arica and Parinacota Region as shown in Fig. 6.9. The information within this solar map was key to determine the places that were visited for inspections. Most of the sites inspected within Arica's campaign are part of the cadastre of SERC. Therefore, these sites are part of the solar map. However, a few inspected sites are not part of the cadastre.

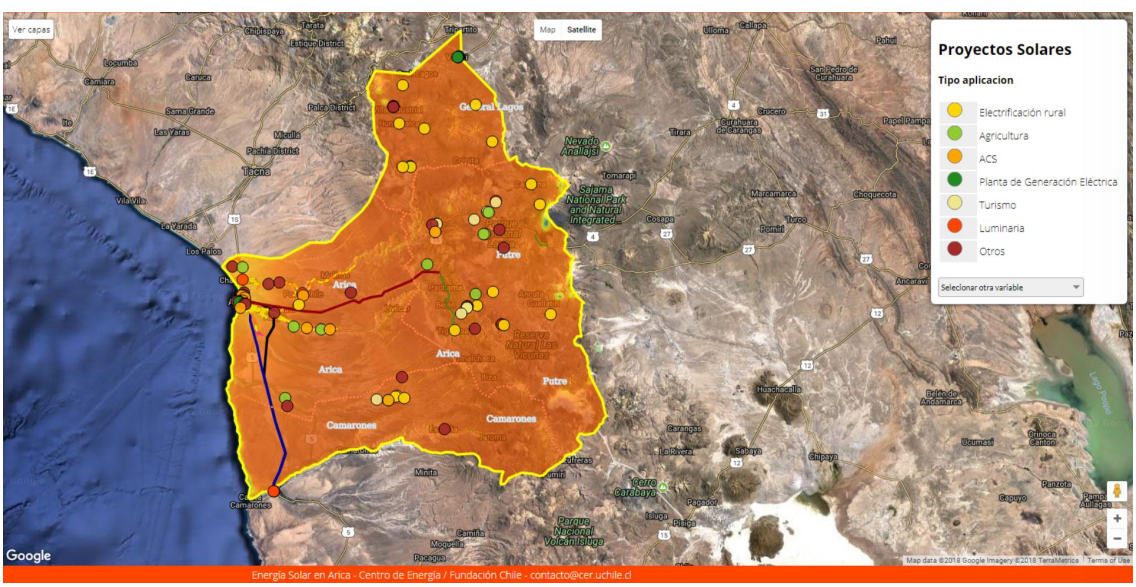

Figure 6.9: Ayllu Solar MAP. For more information, visit the web site `http://ernc2.dgf.uchile.cl/Arica/`.

6.2 Inspected zones

Fig. 6.10 shows the 15 sites that were visited for the campaign; most of these locations are part of Ayllu solar map. The locations are separated into 4 zones:

- Zone A: coastal region (locations 2 and 3).
- Zone B: city center region (locations 4, 5, 6, 7 and 8).
- Zone C: valley region (locations 9, 10, 11, 12, 13, 14 and 15).
- Zone D: desert region (location 1).

According to the classification listed above, similar locations are classified together. Here, due to the number of locations visited, the coastal and desert regions are the ones with less information. In contrast, the city and valley regions contain several locations. Within the 15 locations, 95 PV modules were inspected. The inspected modules were from 9 different manufacturers. Specifically for SUNEL manufacturer, two different models were found (SNM-M200(72) and SNM-P250(60)).

Table 6.2 shows a summary of the most important electrical parameters of the 10 different PV modules found within the 15 locations. The information was obtained from the data-sheets from the manufacturers. In particular, the series resistance of all modules were not found in the internet nor the data-sheet from the manufacturer. Series resistance's values in Table 6.2 were obtained from the database within the software SolarCert Elements from the company Seaward. This information is within this software because it is needed to transform measured I-V curves into STC I-V curves. Information regarding the series resistance of SUNEL, HANWHA and SIEMENS PV modules were not found anywhere. Hence, these values correspond to the simple average of the series resistance of the rest of the PV modules from the other manufacturers.

The 15 locations distributed within the four zones described above contain different number of installed PV modules from different manufacturers. Furthermore, each location has its own estimated deployment date. The last means that PV modules installed in different locations are exposed to different temporal intervals. Also, more than one system with different installation dates can be found in the same location. The differences among the four zones, hence locations, are described in Table 6.3.

From Table 6.3, it can be seen that zone A contains two locations with installed PV modules from SOLAR WORLD and ET TOWARDS EXCELLENCE. Each location has 6 PV modules, where location 2 is operating since 2013 and location 3 is operating since 2015. It is important to highlight that some locations have more than one system, where each system can have different PV modules and/or different estimated deployment date. The last happens within locations 7 (zone B), 14 (zone C) and 1 (zone D). Location 7 contains two different systems, one with PV modules from LUXOR and the other from JA SOLAR. The first one was installed in 2011 while the second one was installed in 2015. It must be highlighted that the only location using PV modules from two different manufacturers, in the same system, was location 1 in zone D (see the footnotes from Table 6.3).

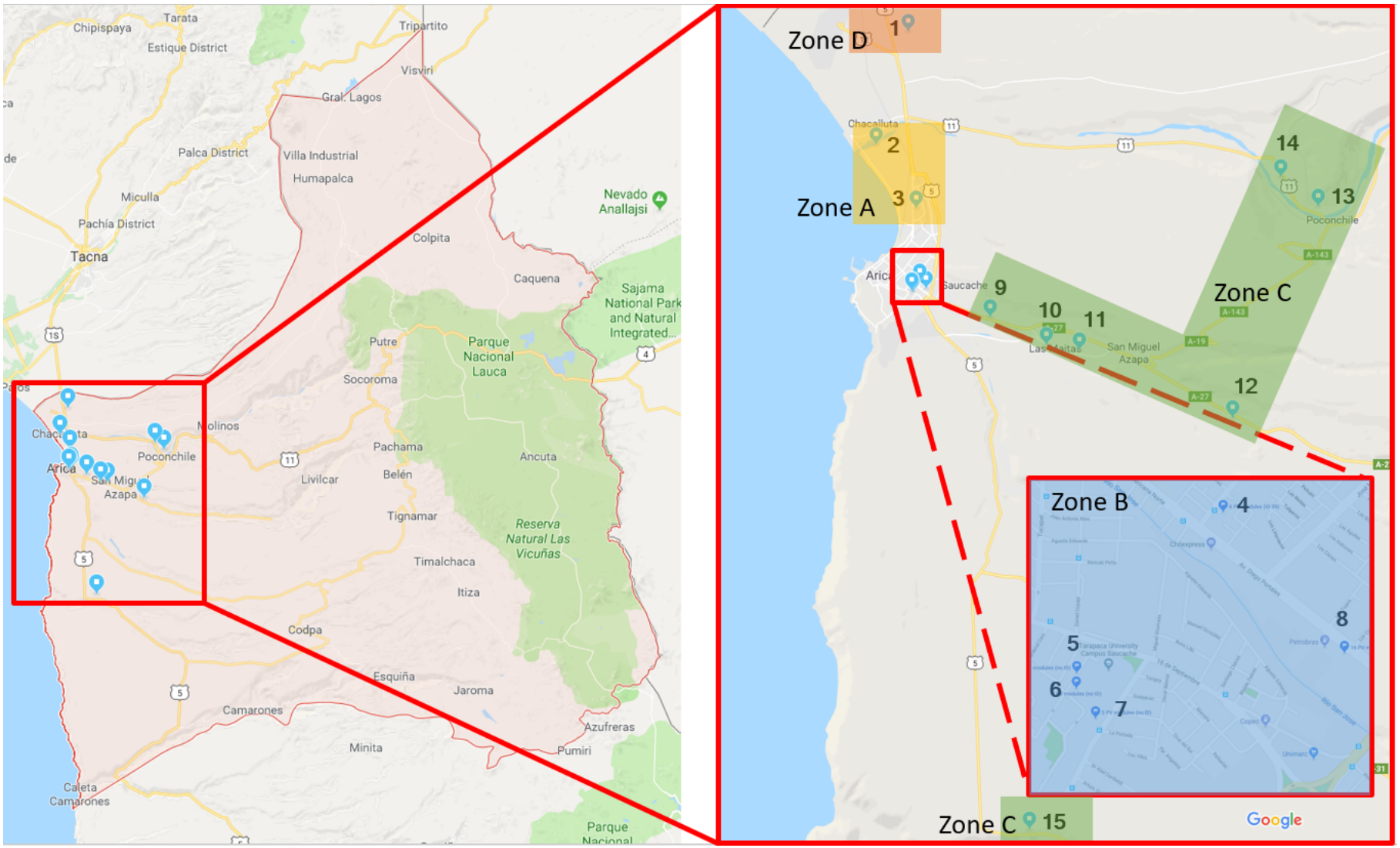

Figure 6.10: Mapping of the inspected sites within Arica's campaign.

Table 6.2: Summary of electrical parameters of all 10 PV modules models inspected in Arica.

Manufacturer	**Model**	V_{oc} **[V]**	V_{mpp} **[V]**	I_{sc} **[A]**	I_{mpp} **[A]**	P_{mpp} **[W]**	**TC** I_{sc} **[A/K]**	**TC** V_{oc} **[V/K]**	R_s
BP SOLAR	BP3160N	44.20	35.10	4.80	4.55	160	0.0031	-0.1591	0.618
LUXOR	LX-230P/156-60+	37.55	30.10	8.39	7.81	235	0.0050	-0.1187	0.276
SOLAR WORLD	Sunmodule SW 250 poly	37.60	30.50	8.81	8.27	252	0.0071	-0.1391	0.245
RISEN	SYP250P	37.30	30.30	8.90	8.27	251	0.0029	-0.1230	0.486
ET TOWARDS EXCELLENCE	ET-P660250WW	37.47	30.34	8.76	8.24	250	0.0035	-0.1273	0.252
JA SOLAR	JAP6-60-260/3BB	37.98	30.63	9.04	8.49	260	0.0052	-0.1253	0.253
SUNEL	SNM-M200(72)	48.48	37.19	5.89	5.36	199	0.0025	-0.1696	0.355
HANWHA SOLAR	HSL60P6-PB-1-250	37.70	30.40	8.79	8.23	250	0.0043	-0.1168	0.355
SUNEL	SNM-P250(60)	37.68	30.90	8.89	8.09	250	0.0035	-0.1243	0.355
SIEMENS	SM55	21.70	17.40	3.45	3.15	55	0.0012	-0.0770	0.355

Table 6.3: Summary of inspected zones.

Zone	Location			PV modules		
	Number	**Latitude**	**Longitude**	**Manufacturer**	**Number**	**Estimated deployment date**
A	2	-18.4136111	-70.3152778	SOLAR WORLD	6	2013
	3	-18.4460410	-70.2935220	ET TOWARDS EXCELLENCE	6	2015
B	4	-18.4840700	-70.2915800	ET TOWARDS EXCELLENCE	6	2015
	5	-18.4883630	-70.2956970	SIEMENS	2	No information
	6	-18.4887710	-70.2957020	BP SOLAR	1	No information
	7[1]	-18.4895600	-70.2951670	LUXOR	6	2011
				JA SOLAR	3	2015
	8	-18.4878280	-70.2881770	RISEN	16	2015
C	9	-18.5022550	-70.2529490	SUNEL(60)	8	2016
	10	-18.5166667	-70.2222222	SOLAR WORLD	2	2013
	11	-18.5193680	-70.2043570	SOLAR WORLD	6	2013
	12	-18.5544860	-70.1210200	SOLAR WORLD	4	No information
	13	-18.4454440	-70.0742150	SOLAR WORLD	6	2012
	14[2]	-18.4302340	-70.0948360	SUNEL(72)	1	2012
				SOLAR WORLD	6	2012
	15	-18.7665360	-70.2316310	SIEMENS	4	2005
D	1[3]	-18.3549320	-70.2977860	HANWHA SOLAR	4	2015
				RISEN	8	2015

[1] Two separated systems: (a) 6 modules from LUXOR installed in 2011 and (b) 3 modules from JA SOLAR installed in 2015.
[2] Two separated systems: (a) 6 modules from SOLAR WORLD installed in 2012 and (b) 1 module from SUNEL installed in 2012.
[3] One system with 12 modules, 4 from HANWHA SOLAR and 8 from RISEN. The system was installed in 2015.

6.3 Results and Analysis

The results and the analysis of the results emerged from Arica's Campaign are presented in this section. Applying the methodology in section 5.4, we have the following analysis.

6.3.1 Visual damage of rear-side glass

All (95) PV modules inspected in the campaign were manufactured with a polymeric backsheet. No module with rear glass was found in any of the (15) inspected locations.

6.3.2 Visual damage of backsheet (polymer)

The visual failures or defects searched in the backsheet of each PV module are defined in section 4 of the visual inspection form. Fig. 6.11 shows section 4 in particular.

4. Backsheet (polymer)			applicable		not applicable
Appearance :	like new		minor discoloration		major discoloration
Texture :	like new		wavy (not delaminated)		wavy (delaminated)
	dented		rugged		
Material quality					
Chalking :	non	slight	substantial		
Damage type					
Burn marks :	non	small, localized		extensive	
Bubbles :	non	small, localized		extensive	
Delamination :	non	small, localized		extensive	
Cracks/scratches :	non	small, localized		extensive	
Corrosion/weathering :	non	small, localized		extensive	

Figure 6.11: Section 4 (polymeric backsheet) of the visual inspection form.

Among all the defects in the survey that are related to the backsheet, PV modules were found to have:

- minor discoloration in their appearance,
- rugged texture,
- chalking: substantial and slight, and
- small and localized cracks and scratches.

PV modules with backsheets with major discoloration in their appearance, wavy or dented texture, burn marks, bubbles, delamination or corrosion/weathering were not found in the campaign.

Zone analysis

Table 6.4 shows the results of the visual defects of the backsheet found in the 95 PV modules inspected in Arica, sorted by zone. Likewise, Fig. 6.14 shows a bar graph that represents the information in Table 6.4, where each colored bar represents a zone. It can be seen that minor discoloration is only found in zone C, within the valley. It must be noted that there, modules were operating at high temperatures with an average of 55.99°C. An example of one of the modules presenting a minor discoloration on the front of the backsheet is shown in Fig. 6.12.

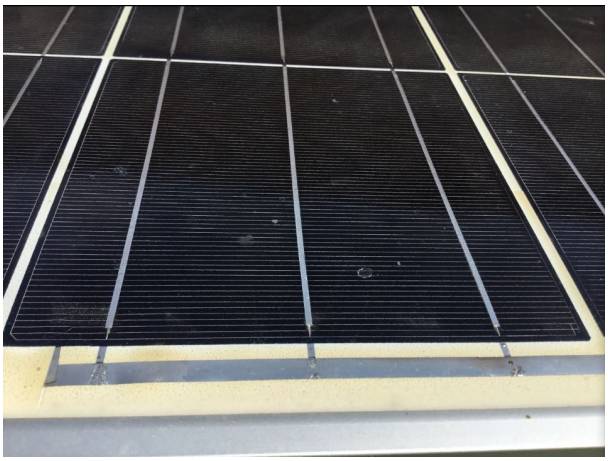

Figure 6.12: PV module, in zone C, operating at high temperature with minor discoloration of the backsheet.

Figure 6.13: Substantial chalking at the backsheet of a PV module operating in zone C.

Table 6.4: Backsheet failures/defects found in inspected PV modules, sorted by zone.

Zone	**Appearance**	**Texture**	**Chalking**		**Cracks/ scratches**
	Minor discoloration	**Rugged**	**Substantial**	**Slight**	**Small/ localized**
Zone A	0	6	0	6	0
Zone B	0	31	1	22	0
Zone C	8	5	3	0	0
Zone D	0	0	0	0	3
Total	8	42	4	28	3

In relation to chalking, this defect was found in three zones: A, B and C. PV modules with substantial chalking were found in zone B and C (4 modules in total). It must be noted that

those PV modules had the longest operating period (since 2005) of all 95 inspected modules. Fig. 6.13 shows an example of substantial chalking of the backsheet. PV modules with slight chalking at the backsheet were found at zones A and B, where zone B contains more number of modules with slight chalking than zone A, being 22 and 6, respectively.

Just 3 modules were found to have scratches at the back of the backsheet, all of them found in the same location (zone D). Fig. 6.15 shows an example of one of the three modules.

Regarding to the texture of the backsheet, this was inspected with bare hands. It was found that backsheet's texture was like new (very smooth) or rugged. Backsheets with rugged texture were found in 42 PV modules, which are installed in zone A, B and C. Most of these modules are in zone B (see Fig. 6.14), while zone A and C contain the less number of modules in equal amount.

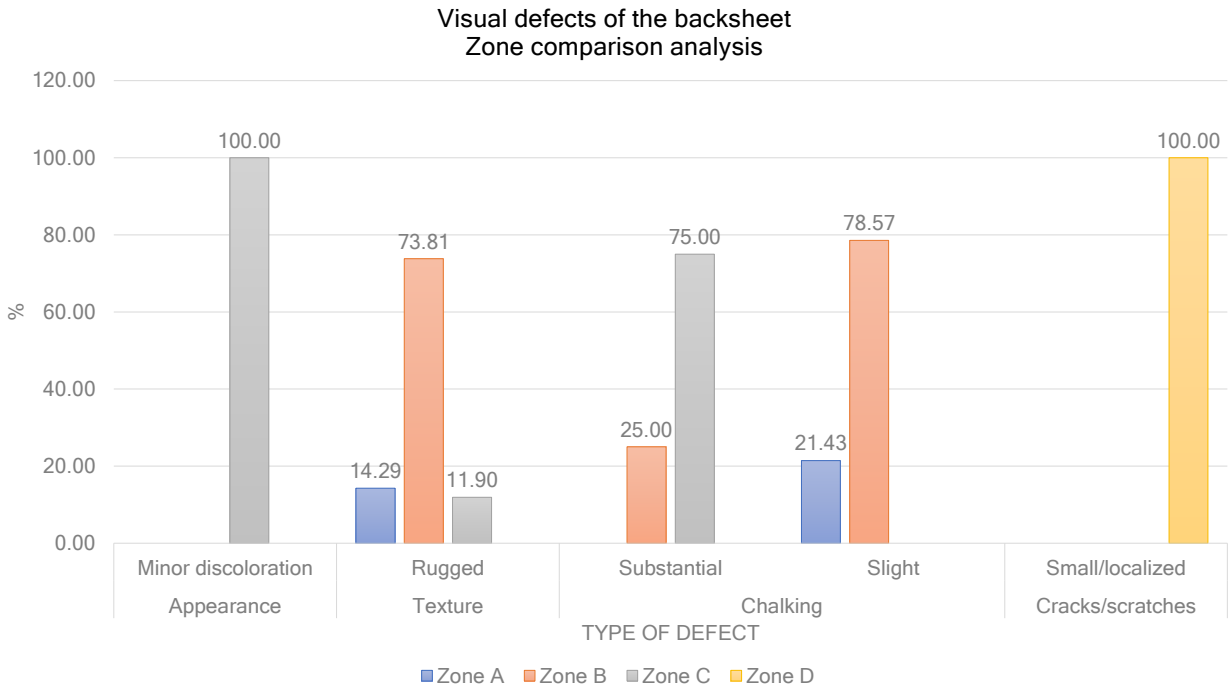

Figure 6.14: Zone comparison of backsheet failures/defects.

Manufacturer analysis

Table 6.5 shows the results of the visual defects of the backsheet found in the 95 PV modules inspected in Arica, sorted by manufacturer. Likewise, Fig. 6.16 shows a bar graph that represents the information in Table 6.5, where each colored bar represents a manufacturer. It can be seen that PV modules with minor discoloration on the front of the backsheet are all from SUNEL, specifically SNM-P250(60). In contrast to this situation, backsheets with rugged texture are found in several manufacturers. RISEN represents the 38.10% of all the PV modules with rugged texture, followed by ET TOWARDS EXCELLENCE (28.57%) and LUXOR (14.29%). SOLAR WORLD, HANWHA SOLAR and BP SOLAR were found to

have a smooth (like new) backsheet.

Figure 6.15: PV module with a scratched backsheet.

Table 6.5: Backsheet failures/defects found in inspected PV modules, sorted by manufacturer.

Manufacturer	**Appearance**	**Texture**	**Chalking**		**Cracks/ scratches**
	Minor discoloration	**Rugged**	**Substantial**	**Slight**	**Small/ localized**
SOLAR WORLD	0	0	0	6	0
RISEN	0	16	0	16	2
HANWHA SOLAR	0	0	0	0	1
ET	0	12	0	0	0
SIEMENS	0	4	4	0	0
LUXOR	0	6	0	6	0
JA SOLAR	0	3	0	0	0
SUNEL	8	1	0	0	0
BP SOLAR	0	0	0	0	0
Total	8	42	4	28	3

Substantial chalking was only found in PV modules from SIEMENS, but slight chalking was found in three different manufacturers. It must be noted again that SIEMENS modules are exposed since 2005, while the rest of the modules are exposed since 2011 or later. RISEN represents the highest percent (57.14%) of all the modules with slight chalking, followed by SOLAR WORLD (21.43%) and LUXOR (21.43%). Regarding to the PV modules with scratches in the backsheet, they were found in the same location. The 3 PV modules are from RISEN (66.67%) and HANWHA SOLAR (33.33%).

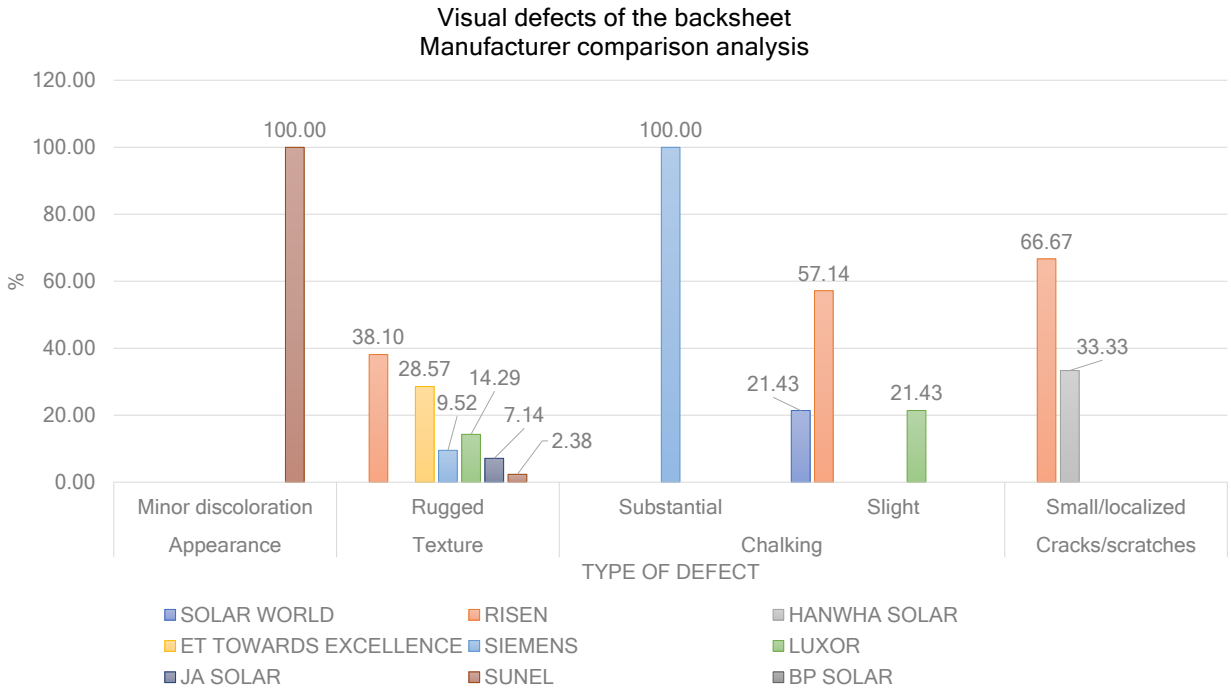

Figure 6.16: Manufacturer comparison of backsheet failures/defects.

Temporal analysis

Table 6.6 shows the results of the visual defects of the backsheet found in the 95 PV modules inspected in Arica, sorted by time exposure. Likewise, Fig. 6.17 shows a bar graph that represents the information in Table 6.6, where each colored bar represents a specific time interval. The longest exposure is a time interval of 13 years, which corresponds to the PV modules installed in 2005; and the shortest time exposure is 2 years, which corresponds to the PV modules installed in 2016. It can be seen that PV modules with minor discoloration of the backsheet have been operating only for 2 years. Again, it is important to highlight that those modules are operating all in the same place and are from the same manufacturer.

Fig. 6.17 shows that PV modules with rugged texture have been operating during different amounts of time, most of them (73.84%) are operating since 2015 (3 years). The rest of the affected PV modules (23.81%) are operating since longer periods of time, that is between 7 and 13 years of exposure. Regarding to PV modules with substantial chalking, they all have been operating since 2005 (13 years). It must be noted again, that those PV modules are all from the same manufacturer and zone. More than half (57.14%) of the PV modules

with slight chalking are mainly operating since 2015 (3 years), while the other half (42.86%) have an exposure time from 5 to 7 years. Finally, the 3 PV modules with scratches in the backsheet have been operating since 2015 (3 years).

Table 6.6: Backsheet failures/defects found in inspected PV modules, sorted by time exposure.

Exposure time [years]	**Appearance**	**Texture**	**Chalking**		**Cracks/ scratches**
	Minor discoloration	**Rugged**	**Substantial**	**Slight**	**Small/ localized**
13	0	4	3	0	0
7	0	6	0	6	0
6	8	1	0	0	0
5	0	0	0	6	0
3	0	31	0	16	3
2	8	0	0	0	0
Total	8	42	3	28	3

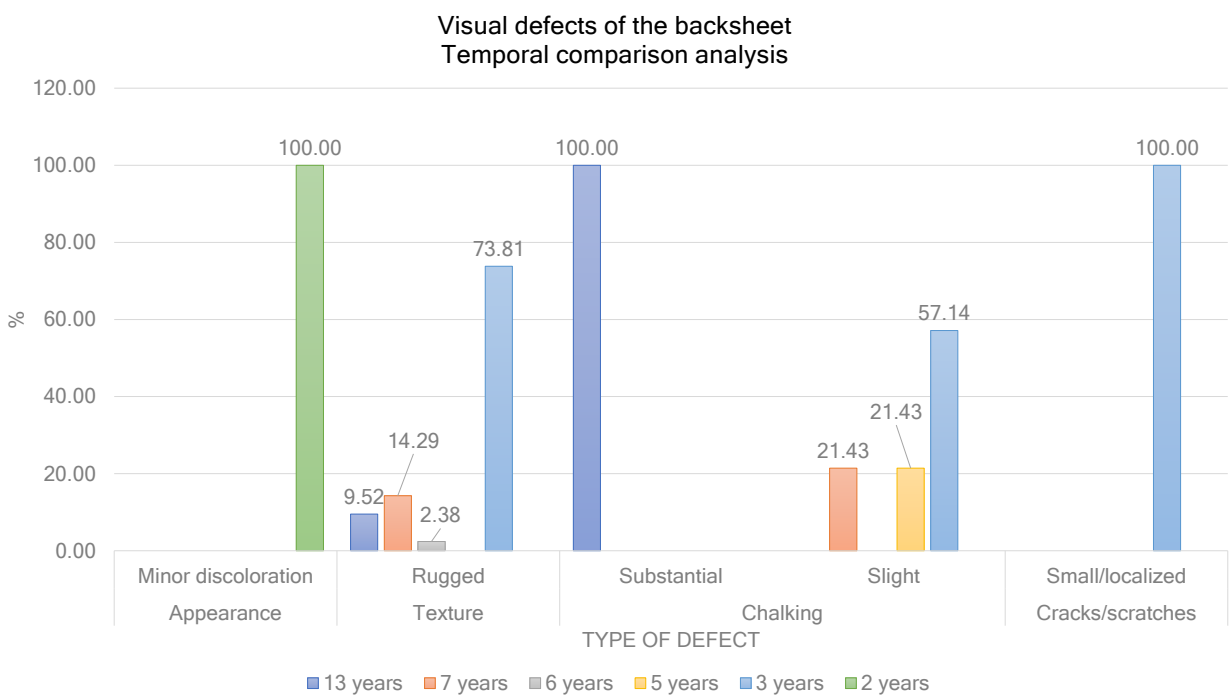

Figure 6.17: Temporal comparison of backsheet failures/defects.

6.3.3 Visual damage of wires

Fig. 6.18 shows the defects searched in wires. Wires, including their isolation, were all found to be like new. They were not pliable, neither degraded nor embrittled. The insulation was not found to be cracked nor disintegrated, neither burnt nor corroded. The wires, in all the installations, were protected from the UV irradiation by the PV modules themselves. Almost all installations also restrained their wires with plastic-cables ties around the supporting structure.

5. Wires		applicable	not applicable		
Appearance	:	like new	pliable, but degraded	embrittled	
Damage type	:	cracked/disintegrated insulation	burnt	corroded	
		cuts/marks			

Figure 6.18: Section 5 (wires) of the visual inspection form.

6.3.4 Visual damage of connectors

Fig. 6.19 shows the visual defects searched in connectors. Connectors were all found to be like new. They were not pliable, neither degraded, nor embrittled. The insulation was not found to be cracked nor disintegrated, neither burnt nor corroded. Connectors were also protected by UV irradiation in the same way that wires.

Only one location was found to contain a PV module with MC3 connectors. In this case in particular, the PV module was intervened for educational purposes. Hence, we do not know the connector used by the manufacturer. All the other PV modules used MC4 connectors. The only exception were all the modules from SIEMENS that were the oldest ones, and they did not use any connectors. The PV system that used PV modules from SIEMENS connects its modules directly within the junction boxes.

6. Connectors		applicable	not applicable			
Type	:	unsure	MC3	MC4	Tyco Solarlok	other
Appearance	:	like new	pliable, but degraded	embrittled		
Damage type	:	cracked/disintegrated insulation	burnt	corroded		

Figure 6.19: Section 6 (connectors) of the visual inspection form.

6.3.5 Visual damage of junction box

The visual failures or defects searched in the junction box of each PV module are defined in section 7 of the visual inspection form. Fig. 6.20 shows section 7 in particular.

Among all the defects in the survey that are related to the junction box, PV modules were found to have:

- the box itself weathered or burned,

- the lid of the box fell off or cracked and,

- the wire attachments within the box fell off.

PV modules with junction boxes with unsound structure, cracked or warped were not found. Loose lids were not found either, they were completely fell off. Defects in the adhesive were not found, neither pliable, degraded nor embrittled adhesive. The adhesive was always found to be well attached, neither loose, brittled nor fell off. Regarding to the wire attachments within the box, they were found to be fell off just for SIEMENS modules in one location. In the rest of the modules, wire attachments were not showing any defect, they were not loose, brittled nor fell off. The seal was always in perfect conditions for the junctions that could be opened (no wire attachments were found to be arced).

7. Junction box ☐ **applicable** ☐ **not applicable**

Junction box itself

Appearance : ☐ intact ☐ unsound structure

Damage type : ☐ weathered ☐ cracked ☐ burnt ☐ warped

Junction box lid

Damage type : ☐ intact/potted ☐ loose ☐ fell off ☐ cracked

Junction box adhesive ☐ **applicable** ☐ **not applicable**

Appearance : ☐ like new ☐ pliable, but degraded ☐ embrittled

Damage type : ☐ well attached ☐ loose/brittle ☐ fell off

Junction box wire attachments ☐ **applicable** ☐ **not applicable/observable**

Damage type : ☐ well attached ☐ loose/brittle ☐ fell off

Seal : ☐ good seal ☐ seal will break

Other : ☐ arced/started a fire

Figure 6.20: Section 7 (junction box) of the visual inspection form.

Zone analysis

Table 6.7 shows the results of the visual defects of the junction box found in the 95 PV modules inspected in Arica, sorted by zone. Likewise, Fig. 6.21 shows a bar graph that represents the information in Table 6.7, where each colored bar represents a zone. It can be seen that weathered junction boxes are only found in PV modules installed in zone B and C. From the 7 weathered boxes, 85.71% were found in zone B, and 14.29% in zone C. Fig. 6.22 shows an example of this defect, in this case, the junction box has a salty layer corroding the box.

Just one junction box was found burned, the affected PV module is installed in zone B. Fig. 6.23 shows the burned junction box from the inside. Regarding PV modules with the indent junction box without the lid, they were installed in zone B and C (5 modules in total, 2 from B and 3 from C). Only one PV module had the lid from the junction box cracked, the module was in zone C. Finally, PV modules with wire attachments from the junction box fell off were only found in zone C (4 modules in total). It must be highlighted that most of the defects found in junction boxes were from SIEMENS PV modules, this could be related to vandalism since they constitute the oldest system.

Table 6.7: Junction box failures/defects found in inspected PV modules, sorted by zone.

Zone	Box itself		Lid		Wire attachments
	Weathered	**Burnt**	**Fell off**	**Cracked**	**Fell off**
Zone A	0	0	0	0	0
Zone B	6	1	2	0	0
Zone C	1	0	3	1	4
Zone D	0	0	0	0	0
Total	7	1	5	1	4

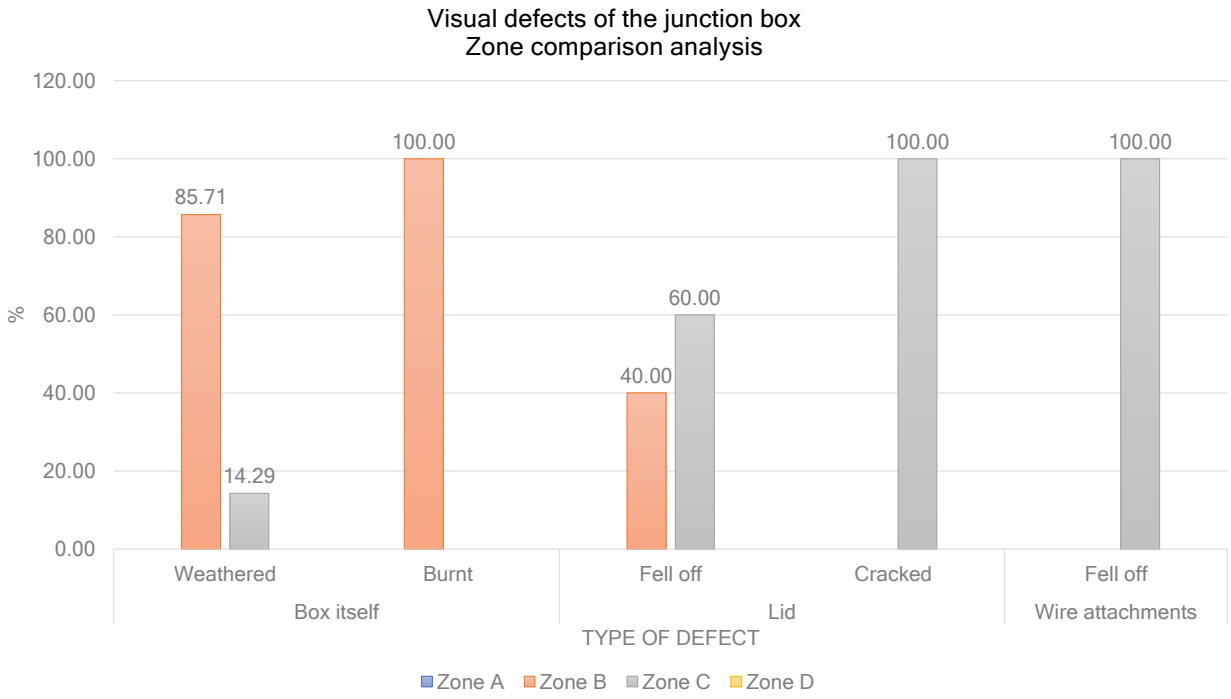

Figure 6.21: Zone comparison of junction box failures/defects.

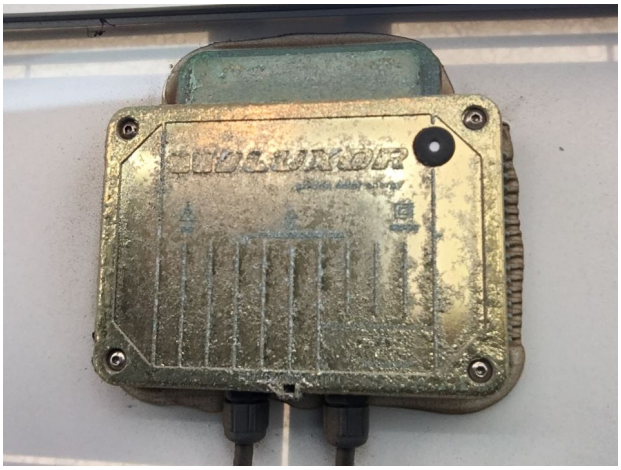

Figure 6.22: Weathered junction box of a PV module installed in the city.

Figure 6.23: Burnt junction box of a PV module from SIEMENS.

Manufacturer analysis

Table 6.8 shows the results of the visual defects of the junction box found in the 95 PV modules inspected in Arica, sorted by manufacturer. Likewise, Fig. 6.25 shows a bar graph that represents the information in Table 6.8, where each colored bar represents a manufacturer.

Figure 6.24: Lid from the box fell off.

It can be seen that only LUXOR, SOLAR WORLD and SIEMENS present defects in the junction box. As mentioned above, the burned box is from a SIEMENS PV modules. Likewise, the cracked box's lid is also from a SIEMENS PV module. The 4 modules with wire attachments of the box fell off are also from SIEMENS. Regarding the box's lid that were fell off, 3 were from SOLAR WORLD (60.00%), while 2 were from SIEMENS (40.00%). Finally, weathered junction boxes were mainly found in PV modules from LUXOR (85.71%). All modules from LUXOR were located in the same place in the middle of the city (see Fig. 6.22).

Table 6.8: Junction box failures/defects found in inspected PV modules, sorted by manufacturer.

Manufacturer	**Box itself**		**Lid**		**Wire attachments**
	Weathered	**Burnt**	**Fell off**	**Cracked**	**Fell off**
SOLAR WORLD	1	0	3	0	0
RISEN	0	0	0	0	0
HANWHA SOLAR	0	0	0	0	0
ET	0	0	0	0	0
SIEMENS	0	1	2	1	4
LUXOR	6	0	0	0	0
JA SOLAR	0	0	0	0	0
SUNEL	0	0	0	0	0
BP SOLAR	0	0	0	0	0
Total	7	1	5	1	4

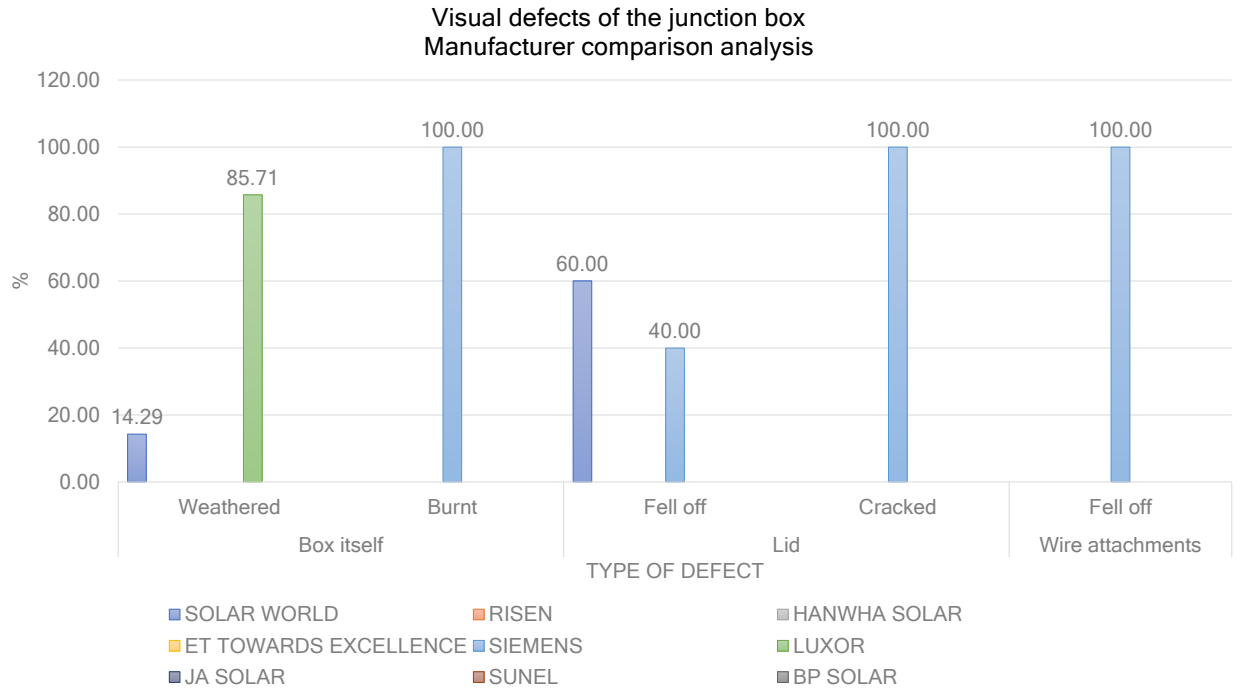

Figure 6.25: Manufacturer comparison of junction box failures/defects.

Temporal analysis

Table 6.9 shows the results of the visual defects of the junction box found in the 95 PV modules inspected in Arica, sorted by time exposure. Likewise, Fig. 6.26 shows a bar graph that represents the information in Table 6.9, where each colored bar represents a specific time interval.

It can be seen in both, Table 6.9 and Fig. 6.26, that burned junction box as a defect is not present in the temporal analysis. This is because the defect belongs to a SIEMENS module that was in location 5 (zone B). Therefore, it cannot be assessed because there is no estimated deployment date.

Fig. 6.26 shows that the PV modules operating the longest (13 years) are the only ones with cracked box's lid and box's wire attachments fell off. All corresponding to SIEMENS PV modules. Regarding the 3 PV modules with box's lid fell off, they have been operating since 2012 (6 years). Weathered junction boxes (7 in total) corresponds to module operating during 7 years (85.71%) and 6 years (14.29%).

Table 6.9: Junction box failures/defects found in inspected PV modules, sorted by time exposure.

Exposure time [years]	Box itself	Lid		Wire attachments
	Weathered	Fell off	Cracked	Fell off
13	0	0	1	4
7	6	0	0	0
6	1	3	0	0
5	0	0	0	0
3	0	0	0	0
2	0	0	0	0
Total	7	3	1	4

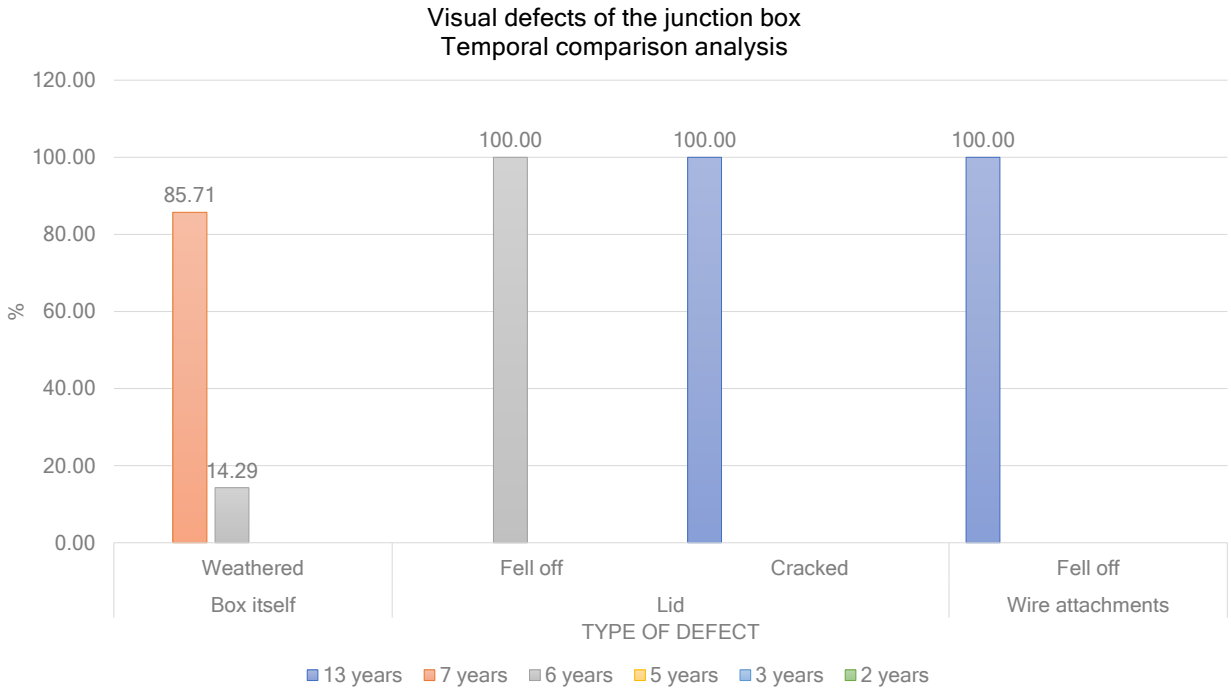

Figure 6.26: Temporal comparison of junction box failures/defects.

6.3.6 Visual damage of frame grounding

The visual failures or defects searched in the frame grounding of each PV module are defined in section 8 of the visual inspection form. Fig. 6.27 shows section 8 in particular.

8. Frame grounding applicable not applicable

Original state	:		wired ground		resistive ground		no ground		unknown
Appearance	:		not applicable		like new		minor corrosion		major corrosion
Function	:		well grounded		no connection				

Figure 6.27: Section 8 (frame grounding) of the visual inspection form.

Among all the defects in the survey that are related to the frame grounding, only minor corrosion in the appearance of the grounding of the frame was found.

When a frame was grounded, it was always by wire. No system was grounded by resistive ground. Only 7 PV modules were not grounded. The appearance of all the PV modules grounded via frame where like new or with minor corrosion, no major corrosion was found. When the PV module was grounded by the frame it was always well grounded (from a mechanical point of view).

Zone analysis

Table 6.10 shows the results of the visual defects of the frame grounding found in the 95 PV modules inspected in Arica, sorted by zone. Likewise, Fig. 6.28 shows a bar graph that represents the information in Table 6.10, where each colored bar represents a zone. It can be seen that the 18 PV modules with minor corrosion of the frame grounding (66.67%) are installed in zone A, while 33.33% are installed in zone B. Fig. 6.31 and Fig. 6.32 show the two types of corrosion of the frame grounding found in the campaign. One case corresponds to corrosion between the frame and the structure, while the other corresponds to corrosion between the bolt and the frame. Both cases correspond to frame grounding via wire.

Table 6.10: Frame grounding failures/defects found in inspected PV modules, sorted by zone.

Zone	**Appearance**
	Minor corrosion
Zone A	12
Zone B	6
Zone C	0
Zone D	0
Total	18

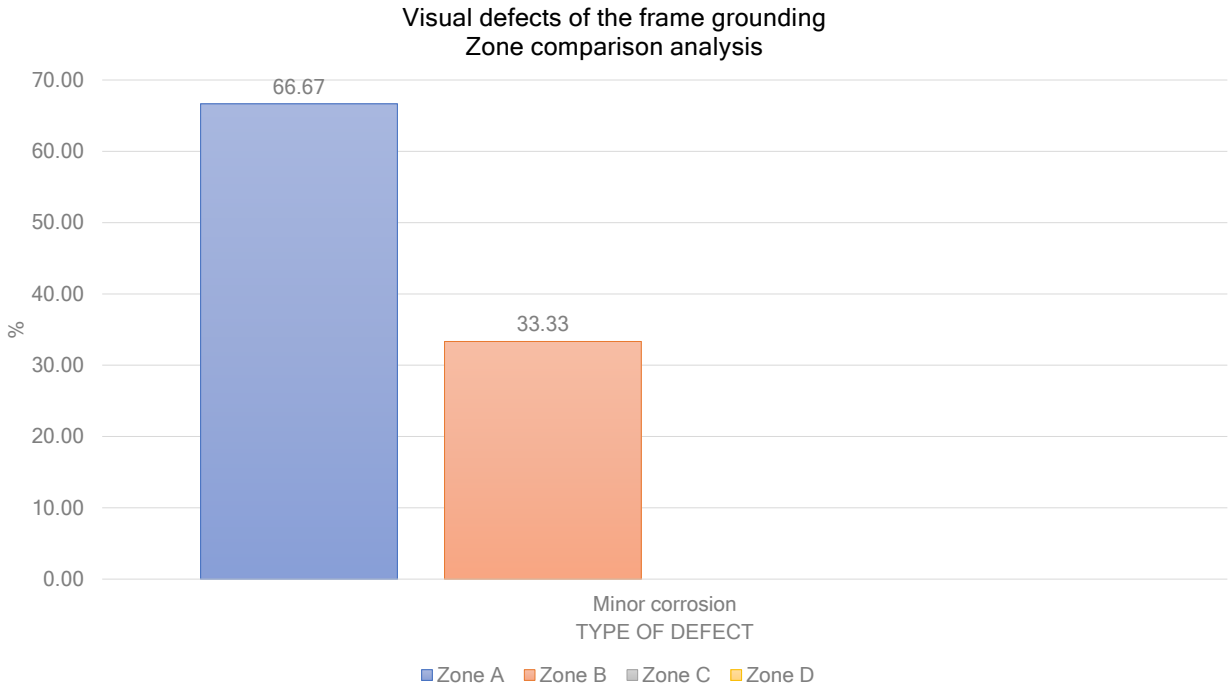

Figure 6.28: Zone comparison of frame grounding failures/defects.

Manufacturer analysis

Table 6.11 shows the results of the visual defects of the frame grounding found in the 95 PV modules inspected in Arica, sorted by manufacturer. Likewise, Fig. 6.29 shows a bar graph that represents the information in Table 6.11, where each colored bar represents a manufacturer.

Table 6.11: Frame grounding defects found in inspected PV modules, sorted by manufacturer.

Manufacturer	**Appearance**
	Minor corrosion
SOLAR WORLD	6
RISEN	0
HANWHA SOLAR	0
ET	12
SIEMENS	0
LUXOR	0
JA SOLAR	0
SUNEL	0
BP SOLAR	0
Total	18

It can be seen that frame corrosion is only found in PV modules from ET TOWARDS EXCELLENCE (66.67%) and SOLAR WORLD (33.33%).

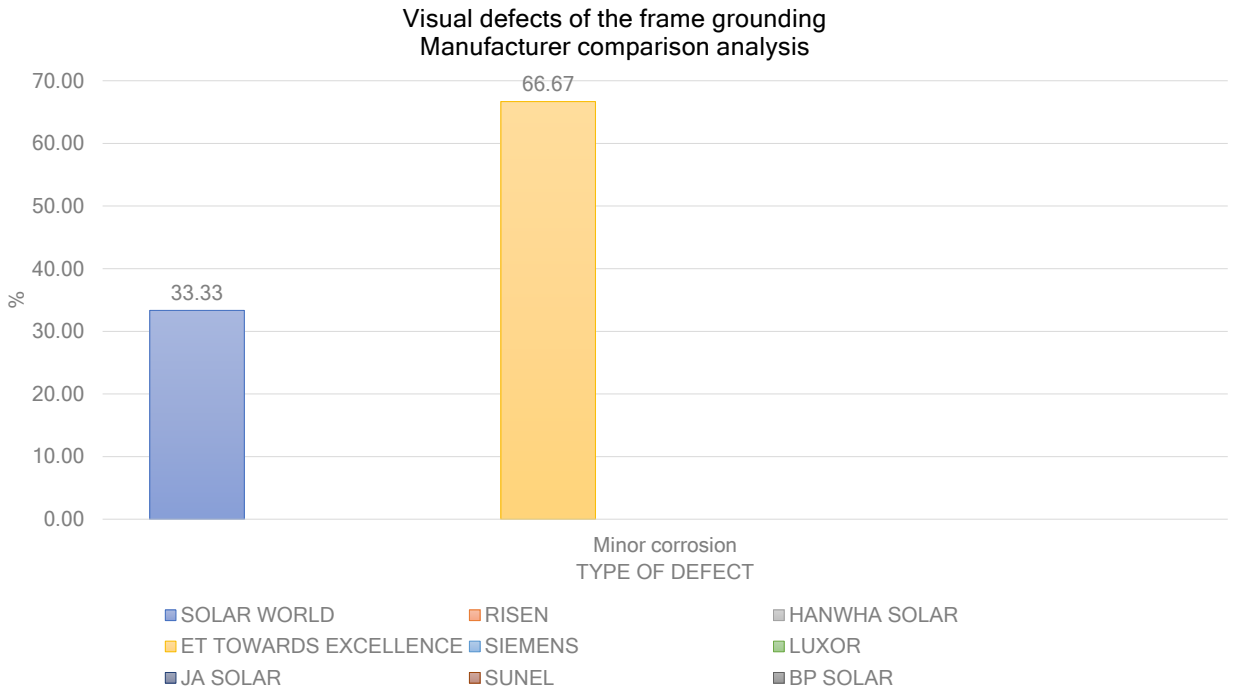

Figure 6.29: Manufacturer comparison of frame grounding failures/defects.

Temporal analysis

Table 6.12 shows the results of the visual defects of the frame grounding found in the 95 PV modules inspected in Arica, sorted by time exposure. Likewise, Fig. 6.30 shows a bar graph that represents the information in Table 6.12, where each colored bar represents a specific time interval. The graph indicates that PV modules with corrosion in the frame grounding have been operating since 2015 (66.67%) and 2013 (33.33%).

Table 6.12: Frame grounding defects found in inspected PV modules, sorted by time exposure.

Exposure time [years]	**Appearance**
	Minor corrosion
13	0
7	0
6	0
5	6
3	12
2	0
Total	18

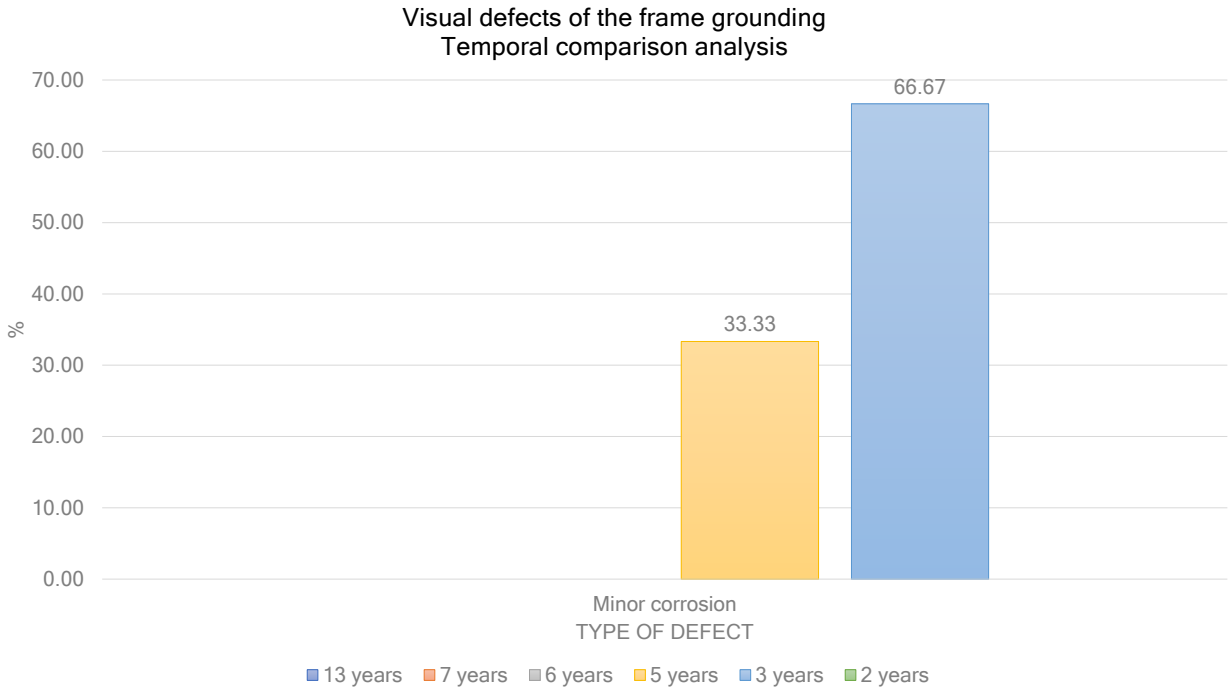

Figure 6.30: Temporal comparison of frame grounding failures/defects.

Figure 6.31: Frame grounded via structure, while structure is grounded via wire. Minor corrosion between structure and frame interface.

Figure 6.32: Frames interconnected with themselves by wires. Minor corrosion between the frame and the bolt.

6.3.7 Visual damage of frame

The visual failures or defects searched in the frame of each PV module are defined in section 9 of the visual inspection form. Fig. 6.33 shows section 9 in particular.

Among all the defects in the survey that are related to the frame, only minor corrosion in the appearance of the grounding of the frame was found.

9. Frame		applicable		not applicable			
Appearance	:	like new	damaged	missing			
Damage type	:	weathered	distorted/bended	detached	separated joints		
Frame adhesive							
Damage type	:	like new/not visible	degraded				

Figure 6.33: Section 9 (frame) of the visual inspection form.

When a frame was grounded, it was always by wire. No system was grounded by resistive ground. Only 7 PV modules were not grounded. The appearance of all the PV modules grounded via frame where like new or with minor corrosion; no major corrosion was found. When the PV module was grounded by the frame it was always well grounded (from a mechanical point of view).

Zone analysis

Table 6.13 shows the results of the visual defects of the frame found in the 95 PV modules inspected in Arica, sorted by zone. Likewise, Fig. 6.35 shows a bar graph that represents the information in Table 6.13, where each colored bar represents a zone. It can be seen that the 12 weathered frames were found in PV modules installed in zone C and D. Most of the modules with weathered frames are in zone D (66.67%). Zones A and B do not present any PV module with damaged frames. Regarding the adhesive of the frame, the 4 PV modules with degraded adhesive of the frame were found in zone C. It must be highlighted that all those PV modules are from SIEMENS and operating since 2005. The adhesive was found to be embrittled (see Fig. 6.34).

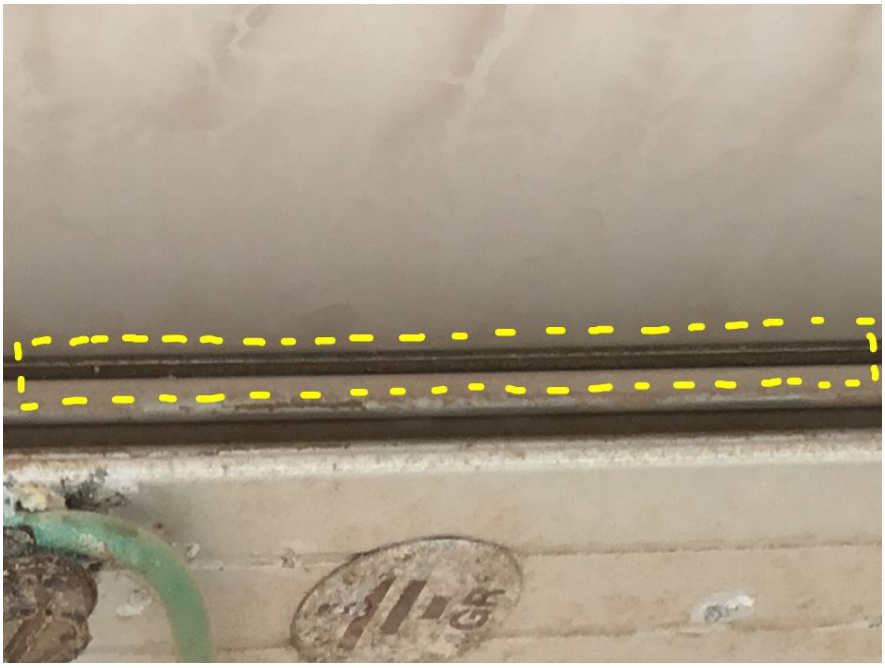

Figure 6.34: Embrittled frame adhesive of a SIEMENS PV module operating since 2005.

Table 6.13: Frame failures/defects found in inspected PV modules, sorted by zone.

Zone	Damage type	Frame adhesive
	Weathered	Degraded
Zone A	0	0
Zone B	0	0
Zone C	4	4
Zone D	8	0
Total	12	4

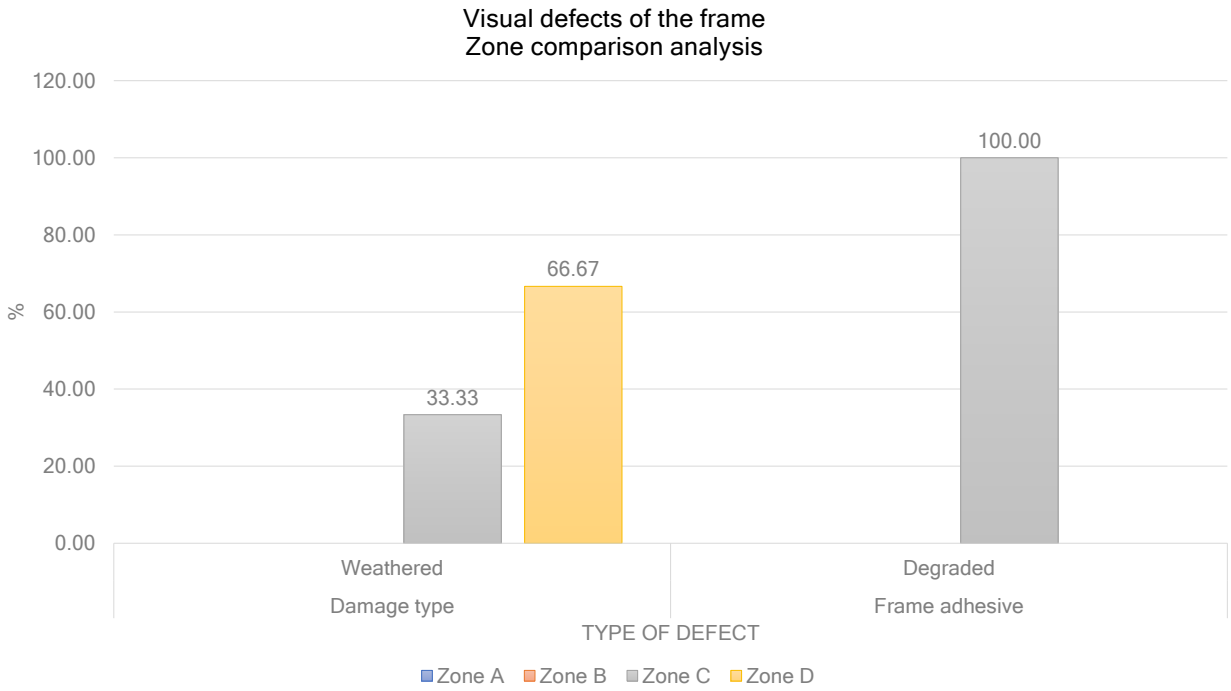

Figure 6.35: Zone comparison of frame failures/defects.

Manufacturer analysis

Table 6.14 shows the results of the visual defects of the frame found in the 95 PV modules inspected in Arica, sorted by manufacturer. Likewise, Fig. 6.36 shows a bar graph that represents the information in Table 6.11, where each colored bar represents a manufacturer. According to the graph, weathered frames were found in PV modules from RISEN, HANWHA SOLAR and SIEMENS in the same amount (33.33%). As mentioned before, PV modules with degraded adhesive (see Fig. 6.34) are all from SIEMENS manufacturer.

Table 6.14: Frame failures/defects found in inspected PV modules, sorted by manufacturer.

Manufacturer	Damage type	Frame adhesive
	Weathered	Degraded
SOLAR WORLD	0	0
RISEN	4	0
HANWHA SOLAR	4	0
ET	0	0
SIEMENS	4	4
LUXOR	0	0
JA SOLAR	0	0
SUNEL	0	0
BP SOLAR	0	0
Total	12	4

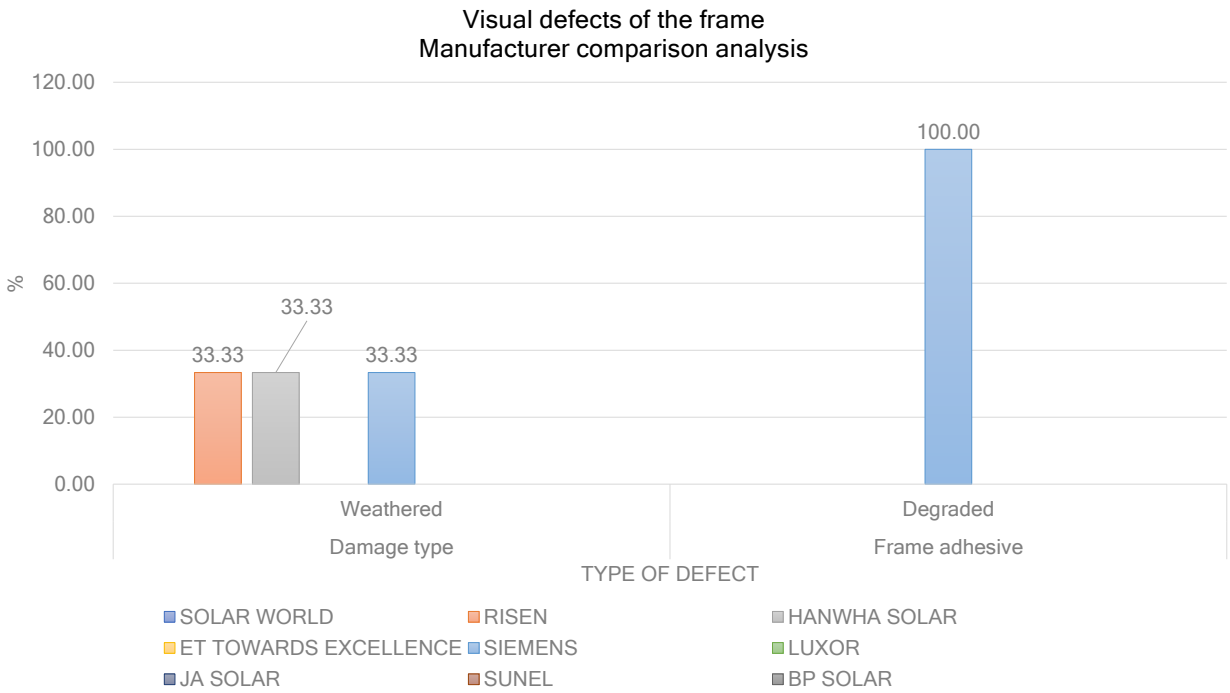

Figure 6.36: Manufacturer comparison of frame failures/defects.

Temporal analysis

Table 6.15 shows the results of the visual defects of the frame found in the 95 PV modules inspected in Arica, sorted by time exposure. Likewise, Fig. 6.37 shows a bar graph that represents the information in Table 6.15, where each colored bar represents a specific time interval. SIEMENS PV modules operating since 2005 (13 years) correspond to 33.33% of the 12 PV modules with degraded frames. The 8 left, which is the 66.67%, correspond to PV modules operating since 2015 (3 years). Fig. 6.38 and Fig. 6.39 show two examples of weathered frames found in Arica's campaign.

Table 6.15: Frame failures/defects found in inspected PV modules, sorted by time exposure.

Exposure time [years]	**Damage type**	**Frame adhesive**
	Weathered	**Degraded**
13	4	4
7	0	0
6	0	0
5	0	0
3	8	0
2	0	0
Total	12	4

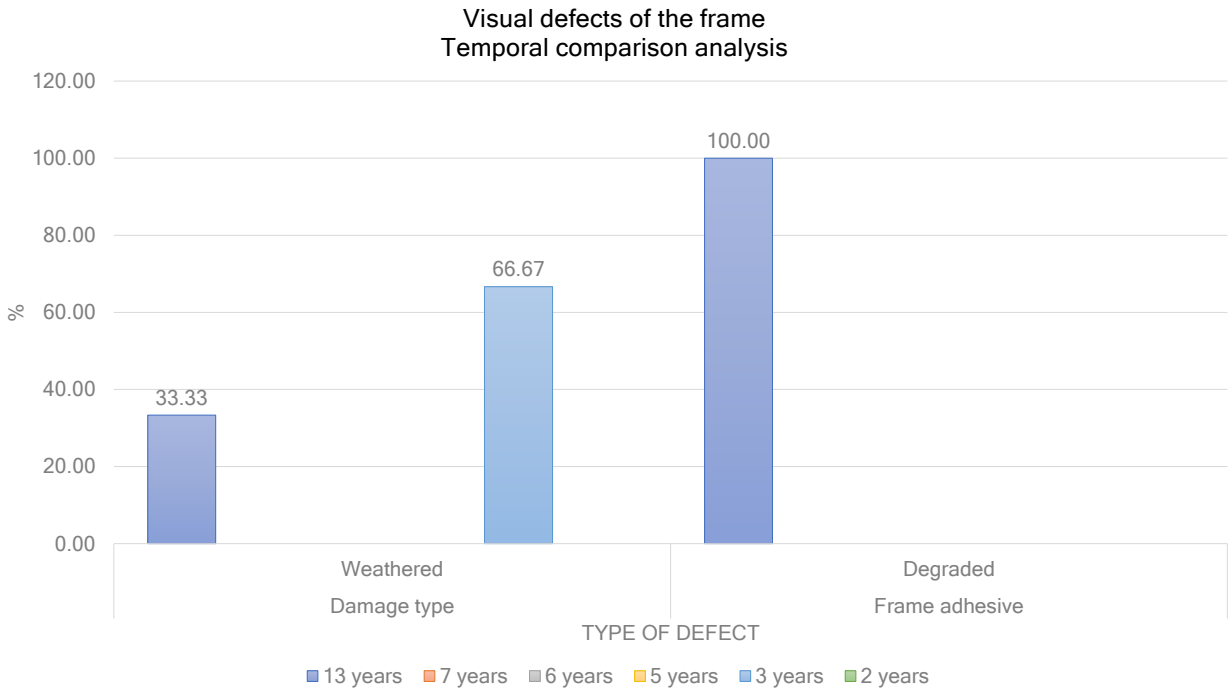

Figure 6.37: Temporal comparison of frame failures/defects.

Figure 6.38: Frame corroded at the edges.

Figure 6.39: Frame burned and corroded where it come into contact with the metallic supportive structure.

6.3.8 Visual damage of frame-less edge seal

All (95) PV modules inspected in the campaign were manufactured with aluminum frame. No frame-less module was found in any of the (15) inspected locations.

6.3.9 Visual damage of front glass

The visual failures or defects searched in the front glass of each PV module are defined in section 11 of the visual inspection form. Fig. 6.40 shows section 11 in particular.

11. Glass/polymer (front)											
				applicable				not applicable			
Material	:		glass		polymer			glass/polymer composite			unknown
Features	:		smooth		slightly textured			pyramid/wave texture			AR coating
Appearance	:		clean		lightly soiled			heavily soiled			weathered
Damage type											
Crazing (or other non-cracked damage)	:		non					small, localized			extensive
Cracks	:		non					small, localized			extensive
Shattered (tempered)	:		non					small, localized			extensive
Shattered (non-tempered)	:		non					small, localized			extensive
Chipped	:		non					small, localized			extensive
Milky discoloration	:		non					small, localized			extensive

Figure 6.40: Section 11 (front glass/polymer) of the visual inspection form.

In the campaign, only PV modules with front glass (not polymer) were found. Among all the defects in the survey that are related to the front glass, PV modules were found to have glass:

- slightly textured (instead of smooth),
- lightly or heavily soiled or weathered, and

- extensive or small/localized milky discoloration.

PV modules with front glass with crazing or cracks were not found. Furthermore, PV modules with shattered (tempered or non-tempered) or chipped front glass were also not found.

Zone analysis

Table 6.16 shows the results of the visual defects of the front glass found in the 95 PV modules inspected in Arica, sorted by zone. Likewise, Fig. 6.43 shows a bar graph that represents the information in Table 6.16, where each colored bar represents a zone. It can be seen that the 6 PV modules with textured glass were all found in zone A. Regarding to soiling, light soiling on glass was found in all zones except zone A, which only contain modules with heavy soiling. Zone C is the region with more modules with light soiling (44.23%), and zone D is the region with less affected modules (23.08%). Heavy soiling was found in all zones except in zone D, which only contain modules with light soiling. Zone B is the region with more modules with heavy soiling (38.56%), while zone A and C contain the same amount of modules (30.77% each).

Figure 6.41: Extensive milky discoloration of the front glass of a PV module in zone C.

Weathered glass was found in 2 PV modules in zone C, those modules were related with a combination of milky discoloration and soiling that it was impossible to remove from the glass surface. The only zone where milky discoloration of the glass was found was zone C.

2 modules presented extensive discoloration that are the ones with weathered glass (see Fig. 6.41), while 6 modules presented a localized milky discoloration at the bottom (see Fig. 6.42).

Figure 6.42 can be easily confused with soiling, but is a combination of milky discoloration and soiling. This can be detected when the surface of the glass is cleaned by a cloth, the soiling is easily removed but the discoloration remains. Due to the soiling, the milky discoloration does not look too white in the image.

Figure 6.42: Localized milky discoloration (at the bottom) of the front glass of a PV module in zone C.

Table 6.16: Front glass failures/defects found in inspected PV modules, sorted by zone.

Zone	**Features**	**Appearance**			**Milky discoloration**	
	Slightly textured	**Lightly soiled**	**Heavily soiled**	**Weathered**	**Extensive**	**Small / localized**
Zone A	6	0	12	0	0	0
Zone B	0	17	15	0	0	0
Zone C	0	23	12	2	2	6
Zone D	0	12	0	0	0	0
Total	6	52	39	2	2	6

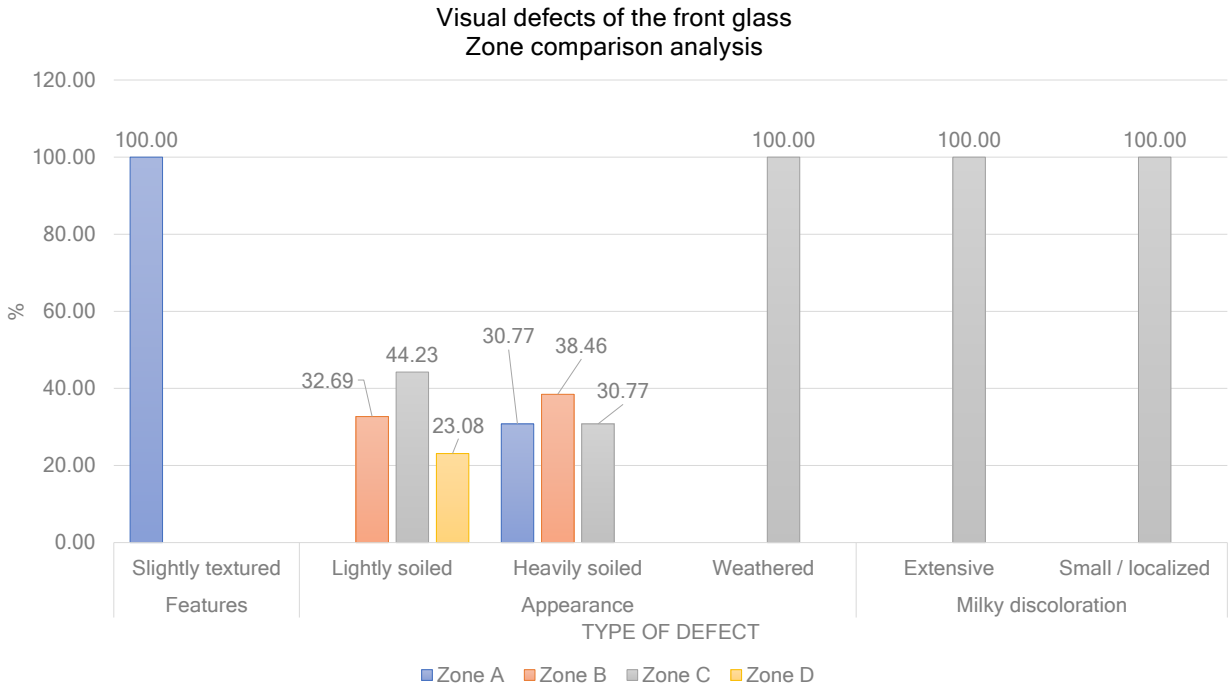

Figure 6.43: Zone comparison of front glass failures/defects.

Manufacturer analysis

Table 6.17 shows the results of the visual defects of the front glass found in the 95 PV modules inspected in Arica, sorted by manufacturer. Likewise, Fig. 6.46 shows a bar graph that represents the information in Table 6.17, where each colored bar represents a manufacturer. It can be seen that PV modules with textured glass are all from ET TOWARDS EXCELLENCE, but it must be noted that not all PV modules from ET TOWARDS EXCELLENCE have textured glass. The 52 modules with light soiling (see Fig. 6.44) are divided between RISEN (46.15%), SOLAR WORLD (19.23%), SUNEL (17.31%), HANWHA

Figure 6.44: PV module operating under light soiling in location 9 (zone B).

Figure 6.45: PV module operating under heavy soiling in location 11 (zone C).

SOLAR (7.69%), SIEMENS (7.69%) and BP SOLAR (1.92%). Regarding to modules with heavy soiling (see Fig. 6.45), they are mainly from SOLAR WORLD (46.15%) and ET TOWARDS EXCELLENCE (30.77%). The rest of the modules with heavy soiling are divided between LUXOR (15.38%) and JA SOLAR (7.69%). In relation to milky discoloration of the glass, only modules from SOLAR WORLD presented either extended or small (localized) discoloration. Finally, the two modules with weathered glass are from SOLAR WORLD.

Table 6.17: Front glass defects found in inspected PV modules, sorted by manufacturer.

Manufacturer	**Features**	**Appearance**			**Milky discoloration**	
	Slightly textured	**Lightly soiled**	**Heavily soiled**	**Weathered**	**Extensive**	**Small / localized**
SOLAR WORLD	0	10	18	2	2	6
RISEN	0	24	0	0	0	0
HANWHA SOLAR	0	4	0	0	0	0
ET	6	0	12	0	0	0
SIEMENS	0	4	0	0	0	0
LUXOR	0	0	6	0	0	0
JA SOLAR	0	0	3	0	0	0
SUNEL	0	9	0	0	0	0
BP SOLAR	0	1	0	0	0	0
Total	6	52	39	2	2	6

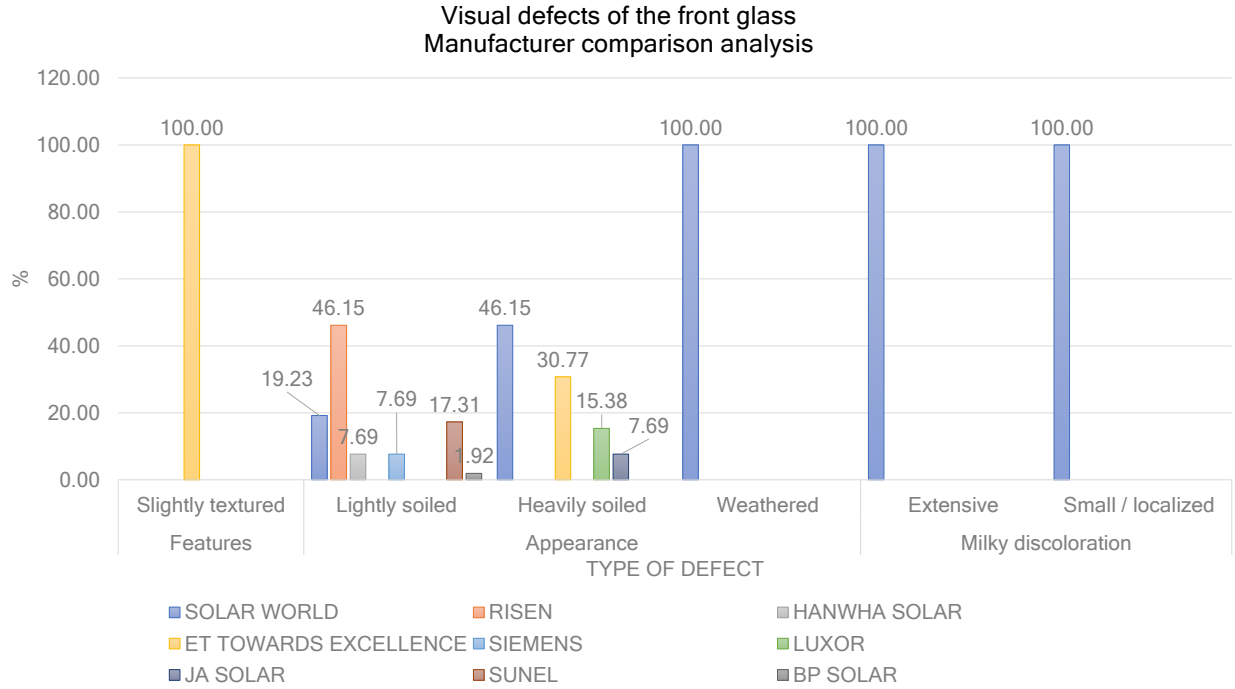

Figure 6.46: Manufacturer comparison of front glass failures/defects.

Temporal analysis

Table 6.18 shows the results of the visual defects of the front glass sorted by time exposure and Fig. 6.47 represents the same information. PV modules with textured glass have been operating since 2015 (3 years). Soiling is present in PV modules that have been operating since different installation dates: light soiling is mostly seen in modules installed in 2015 (59.57%), while is less seen in modules installed in 2005 (8.51%). Heavy soiling is seen mostly in modules installed in 2015 (38.46%) and 2013 (30.77%), and less in modules installed in 2011 and 2012 (15.38% each). The 2 modules with weathered glass have been operating for 5 years (2013), and the modules with milky discoloration have been operating during 5 years (extensive discoloration) and 6 years (localized discoloration).

Table 6.18: Front glass defects found in inspected PV modules, sorted by time exposure.

Exposure time [years]	Features	Appearance			Milky discoloration	
	Slightly textured	Lightly soiled	Heavily soiled	Weathered	Extensive	Small / localized
13	0	4	0	0	0	0
7	0	0	6	0	0	0
6	0	7	6	0	0	6
5	0	0	12	2	2	0
3	6	28	15	0	0	0
2	0	8	0	0	0	0
Total	6	47	39	2	2	6

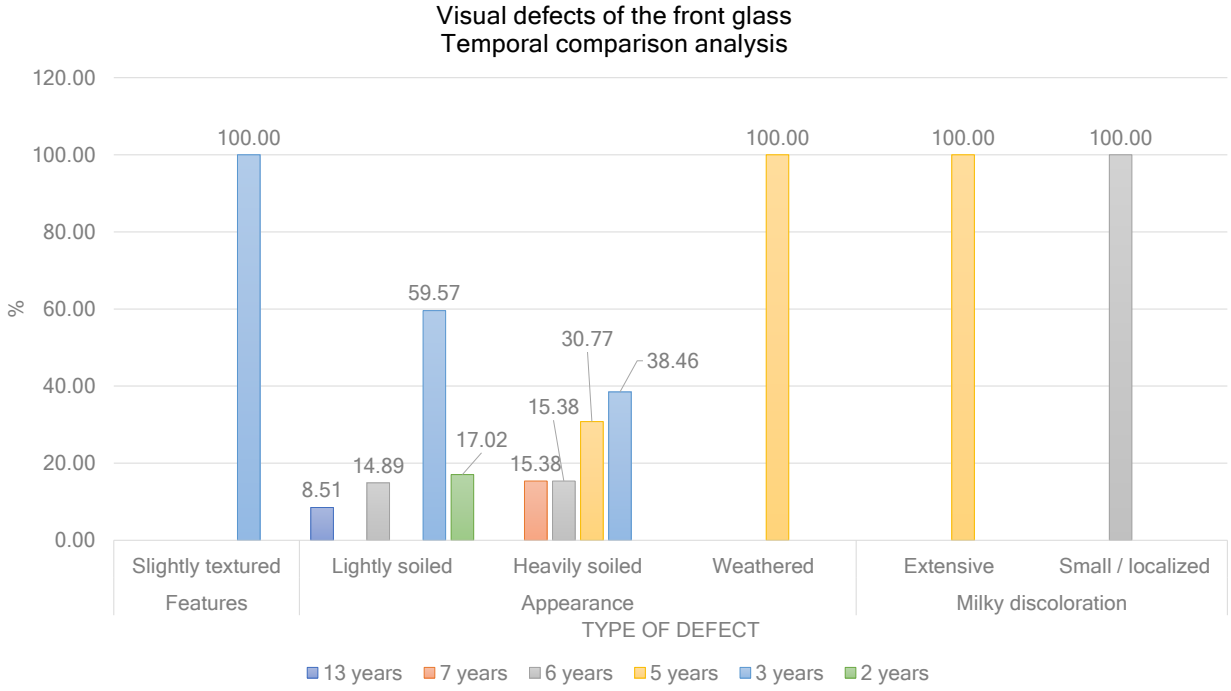

Figure 6.47: Temporal comparison of front glass failures/defects.

6.3.10 Visual damage of encapsulant

The visual failures or defects searched in the encapsulant of each PV module are defined in section 12 of the visual inspection form. Fig. 6.48 shows section 12 in particular.

12. Encapsulant (front) ☐ **applicable** ☐ **not applicable**

Appearance :	☐ like new	☐ light discoloration (yellow)	☐ dark discoloration (brown)		
Damage type					
Delamination :	☐ non	☐ from edges	☐ uniform	☐ corner(s)	☐ near the JB
	☐ between cells	☐ over cells	☐ near cell or string interconnect		
Discoloration :	☐ non	☐ light discoloration	☐ dark discoloration		
Discoloration location(s) :	☐ uniform	☐ module center	☐ module edged	☐ cell centers	
	☐ cell edges	☐ over gridlines	☐ between cells	☐ over busbars	

Figure 6.48: Section 12 (encapsulant) of the visual inspection form.

Among all the defects in the survey that are related to the encapsulant, PV modules were found to have:

- delamination over cells, and/or
- delamination over the busbars.

PV modules with discolored encapsulant were not found, neither light nor dark. Delamination was found only over cells and busbars, not other types.

The cases are not several, all (3) PV modules from JA SOLAR installed in 2015 in zone

Figure 6.49: PV module from JA SOLAR installed in 2015 in zone B. Delamination of encapsulant over the cells.

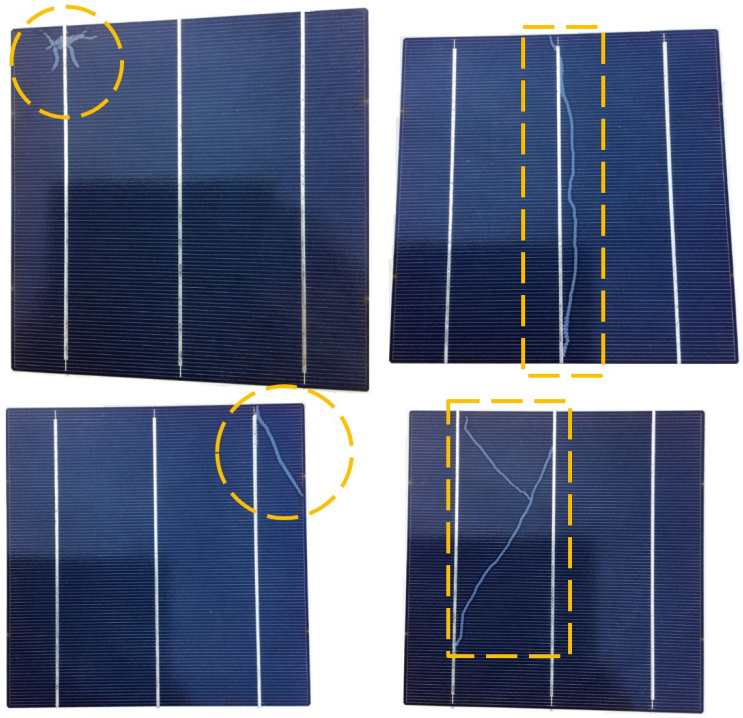

Figure 6.50: Another PV module from JA SOLAR with only 4 cells delaminated.

B (location 7) were found to present delamination over the cells, as shown in Fig. 6.49. The example given in Fig. 6.49 is the PV module from JA SOLAR that is in worst conditions, it is highly probable that the module was hit during transportation or installation. The other two modules from JA SOLAR have delamination in a smaller amount. The other case

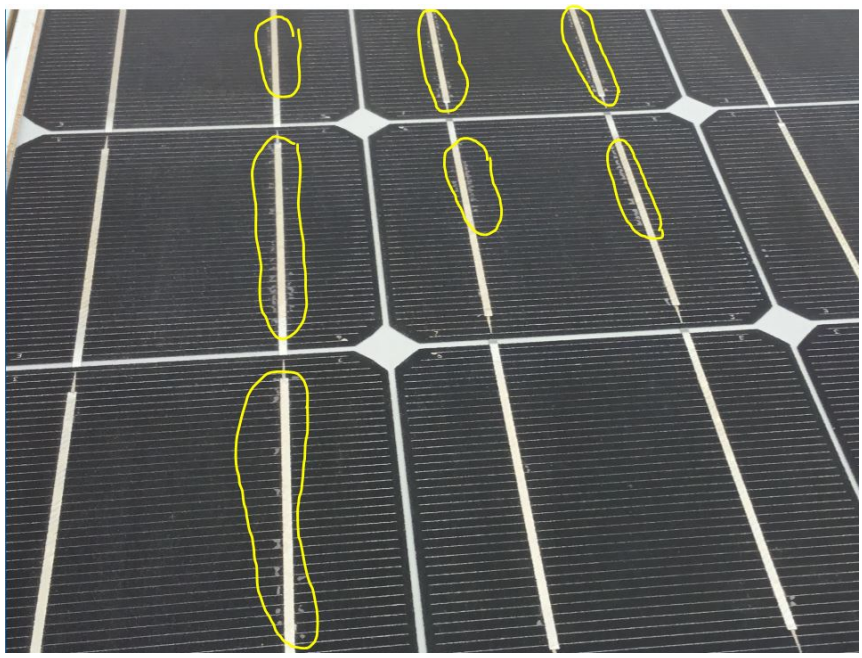

Figure 6.51: PV module from SIEMENS installed in 2005 in zone C. Delamination of encapsulant over the busbars.

is only one PV module from SIEMENS installed in 2005 in zone C (location 15), which has delamination over the cells and busbars (see Fig. 6.51). None other cases were found to have problems with the encapsulant.

6.3.11 Visual damage of metallization

The visual failures or defects searched in the metallization of each PV module are defined in section 13 of the visual inspection form. Fig. 6.52 shows section 13 in particular.

13. Metallization

Gridlines/fingers		☐	**not applicable/observable**			☐	**applicable**
Appearance	:	☐	like new	☐	light discoloration	☐	dark discoloration
Busbars	☐	**not applicable/observable**		☐	**applicable**		
Appearance	:	☐	like new	☐	light discoloration	☐	dark discoloration
Damage type	:	☐	obvious corrosion	☐	diffuse burn marks	☐	misaligned
Cell interconnect ribbon		☐	**not applicable/observable**			☐	**applicable**
Appearance	:	☐	like new	☐	light discoloration	☐	dark discoloration
Damage type	:	☐	obvious corrosion	☐	burn marks	☐	breaks
String interconnect		☐	**not applicable/observable**			☐	**applicable**
Appearance	:	☐	like new	☐	light discoloration	☐	dark discoloration
Damage type	:	☐	obvious corrosion	☐	burn marks	☐	breaks ☐ arc tracks (thin, small burns)

Figure 6.52: Section 13 (metallization) of the visual inspection form.

Among all the defects in the survey that are related to the metallization, PV modules were found to have:

- light discoloration over the grid-lines and/or
- light and/or dark discoloration over the cell interconnect ribbon.

PV modules with defects in the string interconnect and the busbars were not found. Regarding to defects in the grid-lines and cell interconnect ribbon, only discoloration was found. Corrosion or burn marks were not found.

Similar to encapsulant defects, metallization defects are not several either. The 10 affected PV modules were all installed in zone C. They are divided into 6 modules from SUNEL in location 9, and 4 modules from SIEMENS in location 15. 7 modules have light discoloration of the grid-lines, 3 from SUNEL and 4 from SIEMENS. 5 modules have discoloration in the cell interconnect ribbon, all from SUNEL manufacturer. The modules are divided into 2 with dark discoloration and 3 with light discoloration. Since SUNEL modules were installed in 2016, cell interconnect ribbon (dark and light) discoloration is found only in modules operating during 2 years. Finally, light discoloration of grid-lines shows up in modules operating during 2 years (3 from SUNEL), and modules operating during 13 years (4 from SIEMENS).

6.3.12 Visual damage of silicon solar cells

The visual failures or defects searched in the silicon solar cell of each PV module are defined in section 14 of the visual inspection form. Fig. 6.53 shows section 14 in particular.

14. Silicon cell ☐ applicable ☐ not applicable

Number of

cells in module :

cells in series/string :

strings in series :

Damage type

N° of cells with burn marks	:	☐	0	☐	1	☐	2	☐	3	☐	4	☐	5-10	☐ >10
N° of cells with cracks	:	☐	0	☐	1	☐	2	☐	3	☐	4	☐	5-10	☐ >10
N° of cells with moisture	:	☐	0	☐	1	☐	2	☐	3	☐	4	☐	5-10	☐ >10
N° of cells with snail tracks	:	☐	0	☐	1	☐	2	☐	3	☐	4	☐	5-10	☐ >10

Figure 6.53: Section 14 (silicon cell) of the visual inspection form.

No defects were found in any solar cell via bare eyes. No burn marks, cracks, moisture neither snail tracks. It is probable that PV modules with delamination over the cells contain micro-cracks along the delamination paths, but this can be studied using electroluminescence.

6.3.13 Electrical degradation of PV modules

Section 15 of the visual inspection form gather information related to electronic records. Electronic records correspond to the number and the name of the visual and thermal photos taken in the inspection, including the information regarding to the maximum power (in W), open-circuit voltage (in V), short-circuit current (in A), the voltage (in V) and the current (in A) in the maximum power point, and the FF (in %) of the measured I-V curves. Furthermore, thermal information of the I-V curve measurements is also gathered including irradiance (in W/m^2), and temperatures from the module and the ambient (in °C). All this information is shown in Fig. 6.54.

15. Electronic records ☐ applicable ☐ not applicable

Visual images recorded electronically ☐ applicable ☐ not applicable

Number of images recorded :

Name of each recorded image :

I-V curves recorded electronically ☐ applicable ☐ not applicable

Number of times recorded :

Name of each recording :

$P_{mpp\,[W]}$: 0 $V_{oc\,[V]}$: $I_{sc\,[A]}$: $V_{mpp\,[V]}$: $I_{mpp\,[A]}$: $FF_{[\%]}$:

Irradiance [W/m^2]: Ambient temperature [°C]:

Module temperature [°C]:

IR images recorded electronically ☐ applicable ☐ not applicable

Number of images recorded :

Name of each recorded image :

Figure 6.54: Section 15 (electronics records) of the visual inspection form.

The analysis for the electrical parameters is done applying the methodology given in section 5.4. The measured parameters are corrected to STC using the software SolarCert Elements from Seaward. This software requires the information shown in Table 6.2, which contains the nominal electrical parameters and the thermal coefficients for the inspected PV module. All given by the official data-sheet from the manufacturer. Regarding the data gathered from the 95 PV modules, 5 *I-V* curve measurements were made with an irradiance below 600 W/m^2, 3 measurements have random errors and 7 PV modules do not have information related to the estimated deployment date. For this reason, the 3 modules from JA SOLAR and 1 module from BP SOLAR are not analyzed. Hence, both manufacturers do not appear in this section. In total, the electrical parameters from only 81 of 95 PV modules are analyzed here.

6.3.13.1 Degradation of the open-circuit voltage

The summary of the voltage degradation drop (in %) and the voltage degradation rate (in %/year) values from the whole population under study is shown in Table 6.19. It can be seen that the maximum voltage drop corresponds to 11.25%. Although the maximum voltage drop is high, the population under study concentrates the voltage drop between 3.19% ± 2.24%. Hence, most of the absolute voltage drop is in the range 0.95-5.43%. Regarding to the voltage degradation rate, the maximum value is 3.03%/year, but most of the rates are in the range 0.21-1.55%/year.

Table 6.19: Minimum and maximum value, average and standard deviation of absolute open-circuit voltage degradation ($V_{oc_{drop}}$) and open-circuit voltage degradation rate ($DR_{V_{oc}}$) of the whole population under study (81 PV modules).

Parameter	$V_{oc_{drop}}$ **[%]**	$DR_{V_{oc}}$ **[%/year]**
Minimum value	0.02	0.01
Maximum value	11.25	3.03
Average	3.19	0.88
Standard deviation	2.24	0.67

Figure 6.55 shows the distribution of the voltage degradation rates in several intervals for each zone. The graph indicates that zone C, which contains the highest rate of degradation (3.03%/year), also maintains the lowest degradation rates in average in comparison to the other zones. 21 modules in zone C have a voltage degradation rate lower than 0.63%/year, and the other 9 modules have a higher voltage degradation rate distributed in a large range. Following this zone, zone D presents 7 modules with a voltage degradation rate in the range 0.34-0.63%/year having 2 modules below and 3 modules above this range. Hence, zone D is a region of lower voltage degradation rates.

Zones A and B concentrate their degradation rates mainly above 0.34%/year. However, both regions are slightly different, zone A has PV modules with lower voltage degradation rates than zone B. In zone A, 5 modules are below 0.63%/year, and 6 modules are in the range 0.98-1.62%/year. In zone B, 14 modules have a degradation rate in the range 0.39-0.98%/year, while 11 modules have a degradation rate in the range 0.98-2.26%/year.

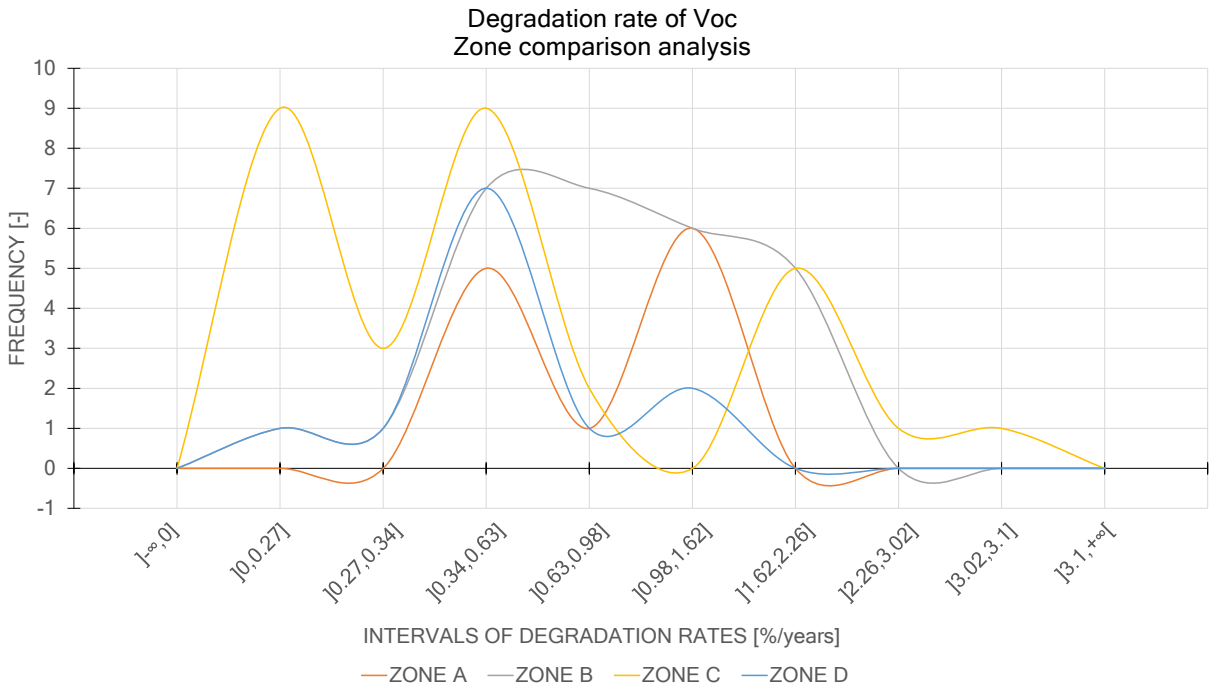

Figure 6.55: Zone analysis of the degradation rate of the open-circuit voltage.

Regarding the distribution of the voltage degradation rates for each manufacturer, it can be seen, in Fig. 6.56, that SOLAR WORLD is the manufacturer with the lowest degradation rates (lower than 0.63%/year), in average and absolute. Although 6 modules from RISEN have a voltage degradation rate above 0.98%/year, 14 modules are in the range 0.34-0.98%/year, and the remaining 4 are below 0.34%/year. Hence, RISEN is the second best evaluated, following SOLAR WORLD. SIEMENS and LUXOR have most of their modules with a voltage degradation rate lower than 0.63%/year.

Following those manufacturers, modules from HANWHA SOLAR have degradation rates mainly in the range 0.63-1.62%/year, and modules from ET TOWARDS EXCELLENCE are mainly in the range 0.98-1.62%/year. Finally, SUNEL is the manufacturer that has the highest absolute voltage degradation rate (3.03%/year), and most of their modules have high voltage degradation rates. Most of their modules have a degradation rate in the range 1.62-2.26%/year.

Figure 6.57 shows the same voltage degradation rates intervals analyzed before, but the distribution is for each interval of time exposure of the modules. According to this graph, the lowest degradation rates are for modules operating during 5 and 6 years, where the voltage degradation rate is mainly lower than 0.63%/year. Following those two exposure time intervals, the PV modules operating the longest (13 and 7 years) are the modules with

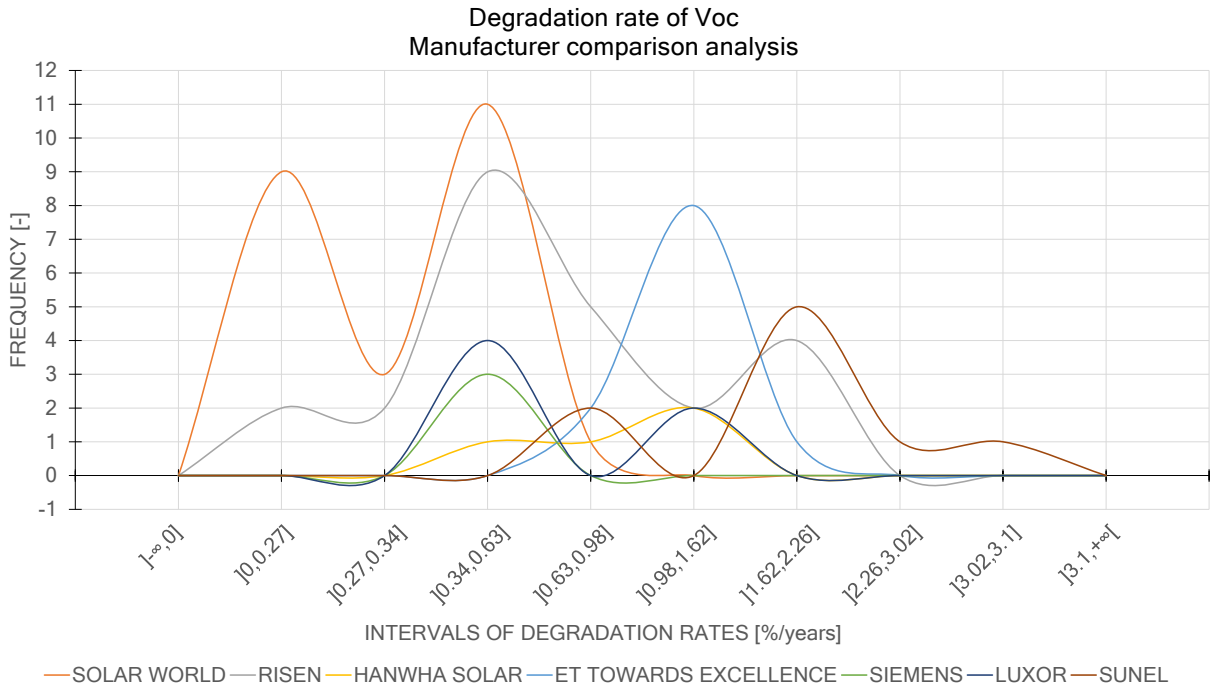

Figure 6.56: Manufacturer analysis of the degradation rate of the open-circuit voltage.

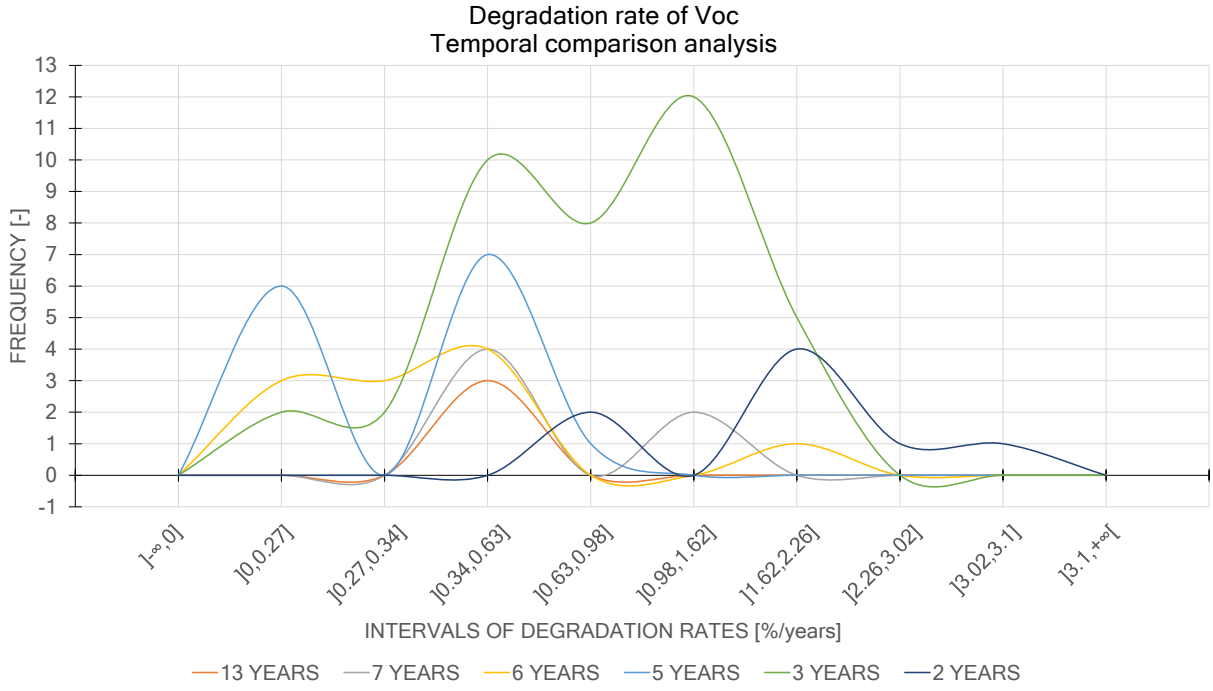

Figure 6.57: Temporal analysis of the degradation rate of the open-circuit voltage.

lower degradation rates. Most of the modules operating during 13 or 7 years have voltage degradation rates in the range 0.34-0.63%/year.

In relation to modules operating the shortest periods (3 and 2 years), they have higher voltage degradation rates. Modules operating since 2015 (3 years) have degradation rates mainly in the range 0.34-1.62%/year, being the highest rate below 2.26%/year. Modules installed in 2016 have degradation rates above 0.63%/year, where most rates are in the range 1.62-3.02%/year. Modules operating during 2 years have the highest degradation rate, which is 3.03%/year.

6.3.13.2 Degradation of the short-circuit current

In general, current degradation rates are higher than voltage degradation rates. The maximum voltage degradation rate from the 81 modules inspected is 3.03%/year, while the maximum current degradation rate for the same universe is 6.76%/year (see Table 6.20). In average, the voltage degradation rate is 0.88%/year while the current degradation rate is 2.30%/year. This can be seen comparing scale of the degradation rate intervals between voltage and current degradation rates. For the current, the first interval of degradation rates corresponds to the values below 0.63%/year. But for the voltage, four intervals of degradation rates are in that same range (below 0.63%/year). To see this, notice the intervals of degradation rates in the abscissa axis in the graphs from Fig. 6.55 and Fig. 6.58.

Table 6.20: Minimum and maximum value, average and standard deviation of absolute short-circuit current degradation ($I_{sc_{\mathrm{drop}}}$) and short-circuit current degradation rate ($DR_{I_{sc}}$) of the whole population under study (81 PV modules).

Parameter	$I_{sc_{\mathrm{drop}}}$ **[%]**	$DR_{I_{sc}}$ **[%/year]**
Minimum value	0.13	0.02
Maximum value	22.84	6.76
Average	8.80	2.30
Standard deviation	5.71	1.46

Table 6.20 indicates that the absolute short-circuit current drop is 22.84%, which is considered a very high value. Furthermore, most of the values are distributed in the range 8.80% $\pm$ 5.71% (3.09-14.51%). It can be seen that the degradation rate of the short-circuit current is also a high value (6.76%/year), which can be due to a high current drop in combination with short exposure times. According to Table 6.20, most of the degradation rates

of the short-circuit current are in the range 0.84-3.76%/year.

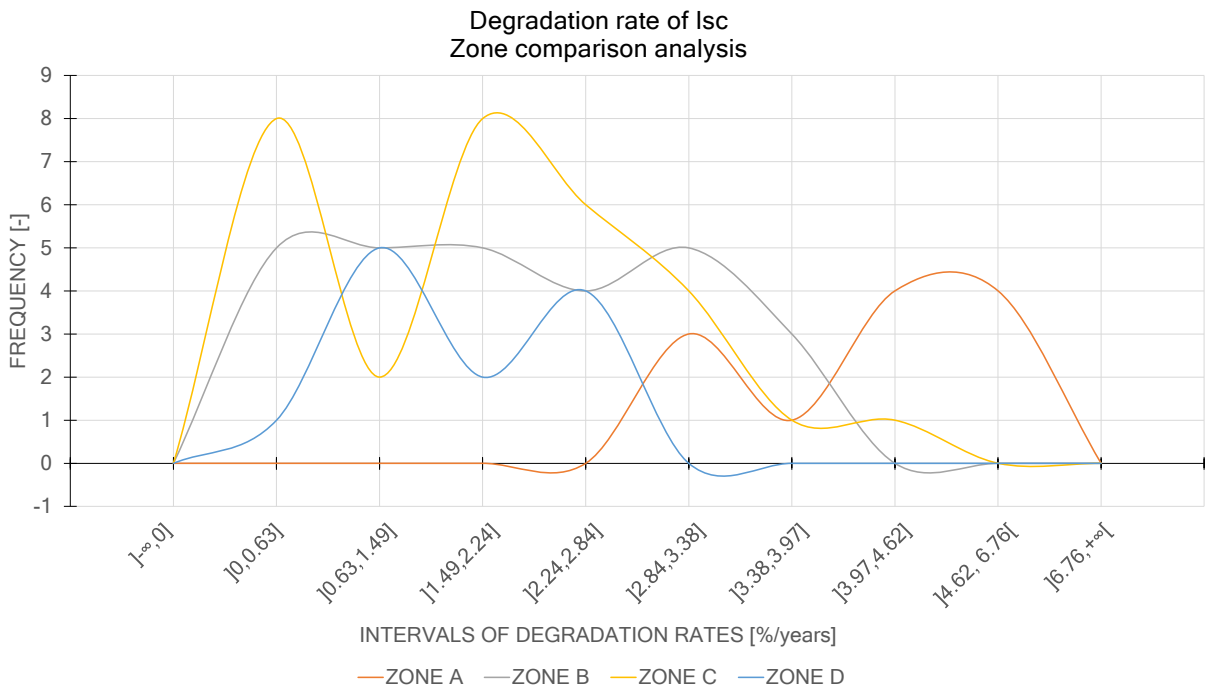

Figure 6.58: Zone analysis of the degradation rate of the short-circuit current.

At first sight, where Fig. 6.58 shows the distribution of the degradation rates of the current for each zone, it is easy to realize that zone A is the region with higher degradation rates of current. Degradation rates of the short-circuit current in zone A are higher than 2.84%/year, where the highest rates are above 4.62%/year, being 6.76%/year the highest of the 81 PV modules inspected. In contrast to zone A, zone D is the one with lower degradation rates. Zone D has modules with current degradation rates below 2.84%/year, where most rates concentrate in the range 0.63-2.84%/year.

Degradation rates of modules installed in zone B and zone C are distributed along a wide range, but both zones concentrate most of the degradation rates below 3.38%/year. Therefore, zone B and zone C are between zone D and A. In particular, most current degradation rates in zone C are below 0.63%/year and in the range 1.49-3.38%/year, while zone B has nearly half of the modules below 2.24%/year and the other half in the range 2.24-3.97%/year. In this situation, it is a difficult decision to sort zones B and C.

Figure 6.59 shows the current degradation rates in different intervals for all the manufacturers. It is clear that modules from SIEMENS, HANWHA SOLAR and LUXOR have the lowest current degradation rates, while those from ET TOWARDS EXCELLENCE have the highest current degradation rates. SIEMENS and LUXOR have degradation rates mainly lower than 0.63%/year, while the degradation rates of HANWHA SOLAR are mostly in the range 0.63-2.24%/year.

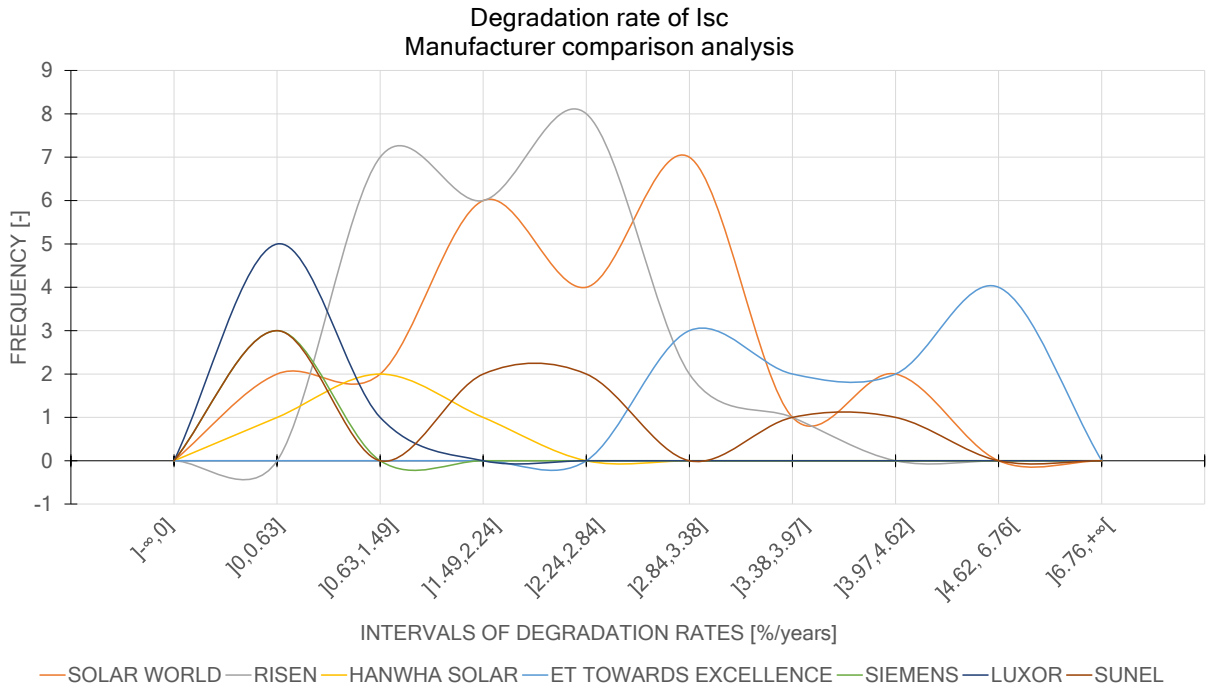

Figure 6.59: Manufacturer analysis of the degradation rate of the short-circuit current.

Regarding to modules from SOLAR WORLD, RISEN and SUNEL, the current degradation rates are distributed along a large range (from below 0.63 to 3.38%/year). Out of the three manufacturers, RISEN concentrates its current degradation rates in the range 0.63-2.84%/year, following SOLAR WORLD that concentrates its current degradation rates in the range 1.49-3.38%/year. On the other hand, modules from SUNEL are not so easy to sort. SUNEL does not concentrate its degradation rates in any interval.

Finally, modules from ET TOWARDS EXCELLENCE have degradation rates higher than 2.84%/year, where 4 out of 11 modules have current degradation rates higher than 4.62%/year.

From a temporal point of view, Fig. 6.60 shows that current degradation rates are in some cases concentrated in lower values for older modules, while in other cases the values are distributed along the whole intervals. As stated before, modules operating the longest periods (13 and 7 years) have the lowest current degradation rates, which are below 0.63%/year. Although the highest absolute current degradation rate is from a module operating during 3 years, 24 out of 39 modules that have been operating during 3 years have current degradation rates in the range 0.63-2.84%/year. Following those modules, modules operating during 6 years have degradation rates concentrated in the range 1.49-3.38%/year. Similar to modules operating during 6 years, the modules operating during 5 years also concentrate in the range 1.49-3.38%/year. However, 3 out of 14 modules have degradation rates below 1.49%/year, and 3 have degradation rates above 3.38%/year.

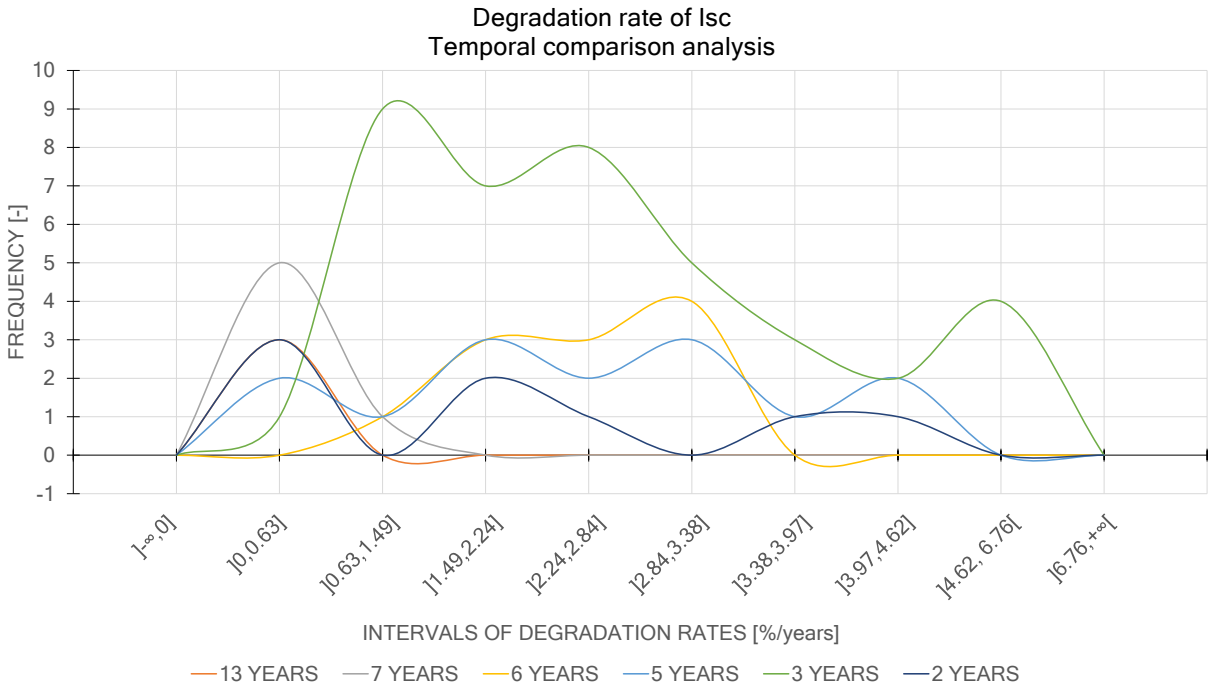

Figure 6.60: Temporal analysis of the degradation rate of the short-circuit current.

6.3.13.3 Degradation of the maximum power

In the previous paragraph we have seen the degradation of the open-circuit voltage and the short-circuit current. The maximum power degradation corresponds to the degradation of the voltage and the current at the maximum power point combined. Table 6.21 shows a critical maximum power drop of 39.08%, which corresponds to a voltage and current at the maximum power point drop of 31.56% and 10.99%, respectively. It is also interesting to see that the minimum power drop is 4.41%, while in the case of the open-circuit voltage and the short-circuit current the minimum drop was nearly 0%. Not only the maximum power drop is high, but the range in which the power drop concentrates (6.97-19.41%) is also considerable.

Table 6.21: Minimum and maximum value, average and standard deviation of absolute power degradation ($P_{mpp_{\mathrm{drop}}}$) and power degradation rate ($DR_{P_{mpp}}$) of the whole population under study (81 PV modules).

Parameter	$P_{mpp_{\mathrm{drop}}}$ **[%]**	$DR_{P_{mpp}}$ **[%/year]**
Minimum value	4.41	0.67
Maximum value	39.08	8.66
Average	13.19	3.55
Standard deviation	6.22	1.74

According to Jordan, Kurtz, VanSant and Newmiller [144], most common guarantees from manufacturers of PV modules indicate that after 25 years the PV module will generate 80% of the power rated in the nameplate. This can be translated into a maximum power degradation loss of 0.8%/year. From the 81 modules inspected, only one is within a typical guarantee, which corresponds to the PV module with the minimum power degradation (0.67%/year). The rest of the modules under study have higher power degradation rates with an average of 3.55%/year. Considering all the results, most of the power degradation rates are in the range 1.81-5.29%/year.

According to the graph shown in Fig. 6.61, it can be seen that the power degradation rate of the inspected modules, for each zone, is distributed along a wide range. Zone D has all its modules with power degradation rates within the range 1.26-4.46%/year, where 50% is in the range 3.12-4.07%/year. Following zone D is zone C, which has 70% (21 out of 30) of its modules with power degradation rates below 4.07%/year. Similar to zone C, zone B has 70.37% (19 out of 27) of its modules with power degradation rates below 4.07%/year. In the case of zone A, this region contains modules with very different power degradation rates. In this zone, 50% of the modules have degradation rates in the range 2.73-4.46%/year, while the rest is above 4.91%/year.

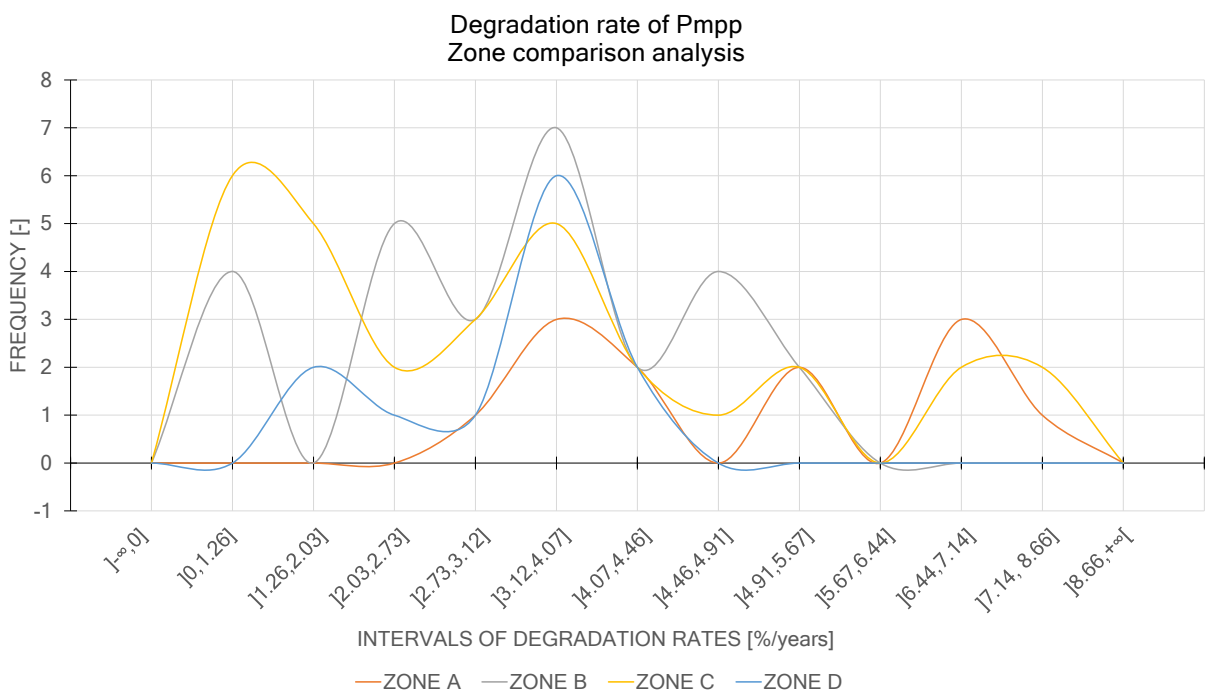

Figure 6.61: Zone analysis of the degradation rate of the maximum power.

In the case of the power degradation rates for each manufacturer, Fig. 6.62 shows the relevant distribution for each one of them. It can be seen that all SIEMENS modules, which have the longest operating period, have power degradation rates below 1.26%/year, including the module with the lowest power degradation rate (0.67%/year). Following SIEMENS is SOLAR WORLD, which has most of its modules (87.5%) with degradation rates below 4.07%/year.

Modules from LUXOR, which are 6 in total, are concentrated in two different ranges. 4

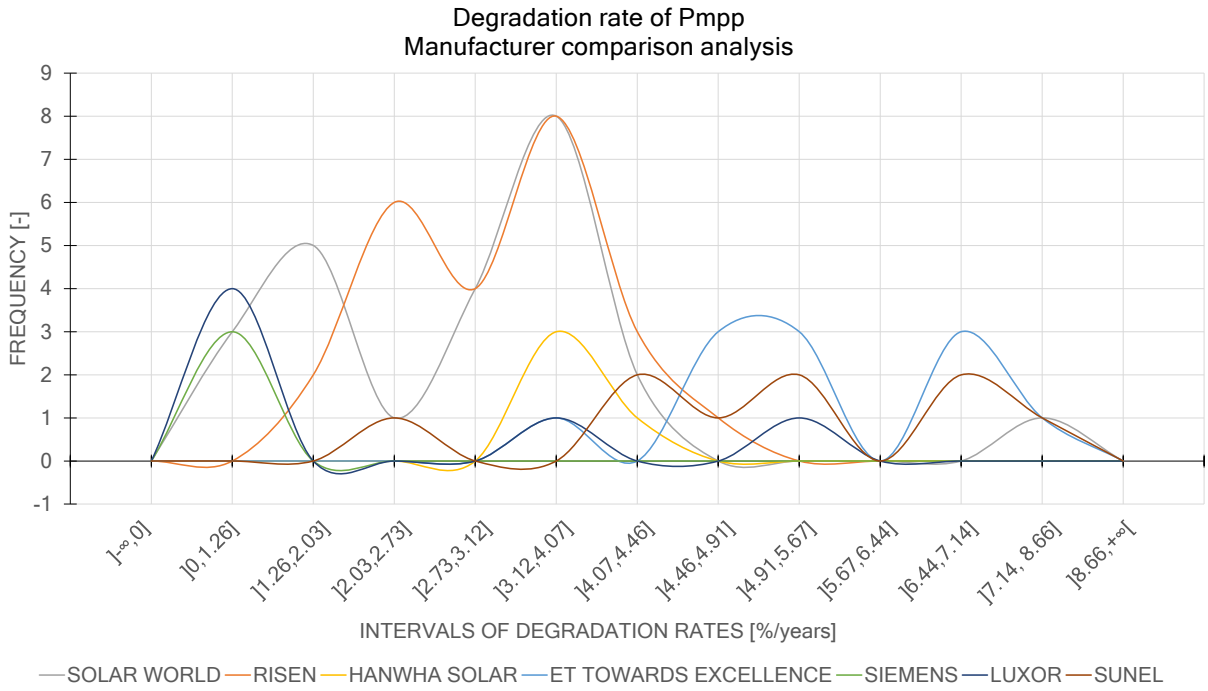

Figure 6.62: Manufacturer analysis of the degradation rate of the maximum power.

modules have power degradation rates below 1.26%/year, while the rest is above 3.12%/year. Following SOLAR WORLD and LUXOR is RISEN, 83.33% of their modules have power degradation rates in the range 1.26-4.07%/year, while 16.66% are in the range 4.07-4.91%/year. The next manufacturer is HANWHA SOLAR that has modules with power degradation rates in the range 3.12-4.46%/year. The highest power degradation rates are for modules from SUNEL and ET TOWARDS EXCELLENCE. Most of their modules have power degradation rates above 4.46%/year, where the highest value (8.66%/year) corresponds to a module from SUNEL.

According to the distribution of the power degradation rates for each interval of time exposure in the field, shown in Fig. 6.63, the modules operating the longest period of time (13 and 7 years) are the ones with power degradation rates below 1.26%/year, except for 2 modules operating during 7 years that have power degradation above 3.12%/year. Following the oldest modules, those operating during 6 years have power degradation rates in the range 1.26-4.07%/year.

The next modules correspond to those operating during 5 years, from which 78.57% have power degradation rates below 4.07%/year and one is above 7.14%/year. Regarding to modules operating during 3 years, their power degradation rates are very different. There are three ranges of accumulation, 61.53% of the modules have power degradation rates in the range 1.26-4.07%/year, 28.20% in the range 4.07-5.67%/year and the rest above 6.44%/year. Finally, modules operating during 2 years have power degradation rates above 4.07%/year.

It can be seen that the power degradation rate values are inversely proportional to the exposure time, i.e., at shorter periods of exposure, the degradation rate is higher. This is obvious when we look at the equation 5.2. From this we can conclude that modules

probably have fast initial degradation in the first years, and during their lives they do not degrade so fast. Hence, with more years of exposure, the power degradation rate tends to decrease. This may happen because PV modules are tested individually by the manufacturers. However, when modules are installed in a power plant, they are affected by the electrical interconnections with other modules, inverters, transformers, etc. Since the interconnection does not change, the module stabilizes itself.

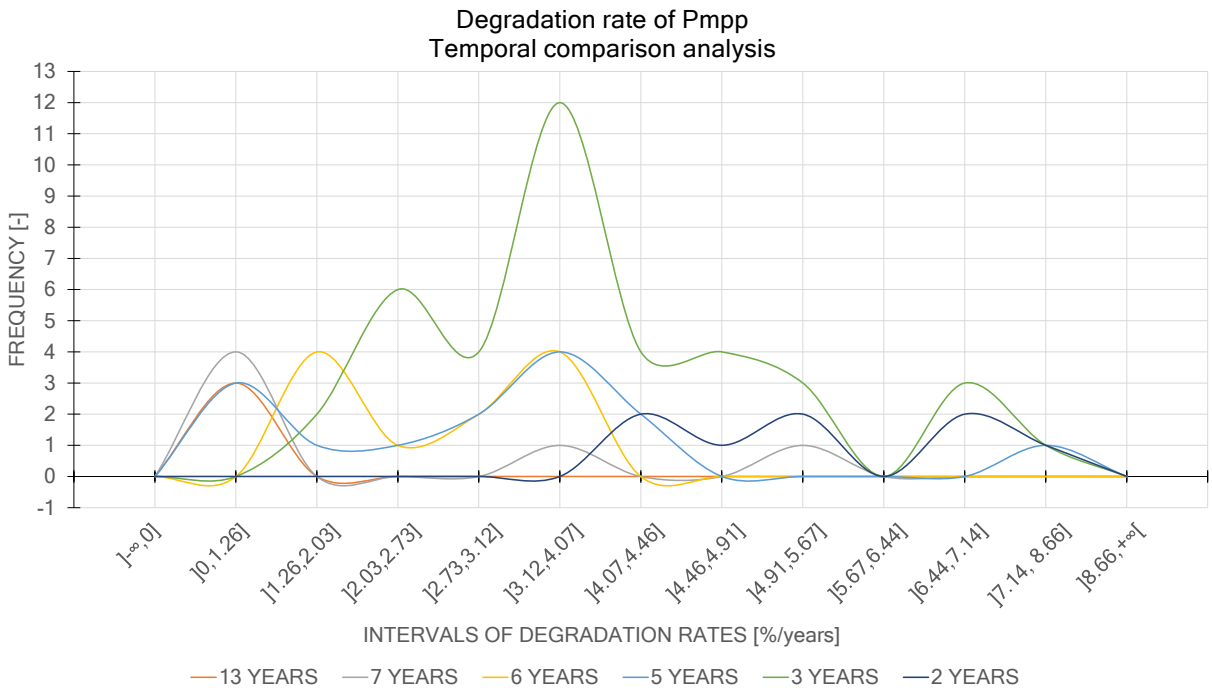

Figure 6.63: Temporal analysis of the degradation rate of the maximum power.

6.3.13.4 Degradation of the fill factor

Something peculiar happens with the degradation of the fill factor, which is not seen in the other variables. 8 PV modules (6 from SOLAR WORLD, 1 from ET TOWARDS EXCELLENCE and 1 from SUNEL) show fill factors higher than the fill factor calculated with the information of the nameplate. Due to this strange situation, the minimum values for the fill factor degradation and rate are negatives. 34.35% is the maximum drop for the fill factor, and most of the values are in the range -0.86%/-10.02%. Regarding the degradation rates of the fill factor, the maximum value is 6.87%/year and most of the values are between -0.15%/year and 2.83%/year.

Figure 6.64 shows the distribution of the degradation rate of the fill factor for each of the 4 zones. The graph clearly shows that the lowest degradation rates for the fill factor are for modules installed in zone A, where all the modules have degradation rates below 1.02%/year. The next zone with lower rates corresponds to zone B, where 85.18% of the installed modules have the degradation rates of the fill factor below 1.35%/year. In the case of zone C, 66.66% of the installed modules have a degradation rate of the fill factor below 1.16%/year, and 30% above 3.71%/year. Zone C has the module with the highest degradation rate of the fill factor,

which is 6.87%/year. Zone D corresponds to the region with higher degradation rates of the fill factor. In this zone the rates are in the range 1.35-3.71%/year.

Table 6.22: Minimum and maximum value, average and standard deviation of absolute fill factor degradation (FF_{drop}) and fill factor degradation rate (DR_{FF}) of the whole population under study (81 PV modules).

Parameter	FF_{drop} **[%]**	DR_{FF} **[%/year]**
Minimum value	-5.63	-1.28
Maximum value	34.35	6.87
Average	4.58	1.34
Standard deviation	5.44	1.49

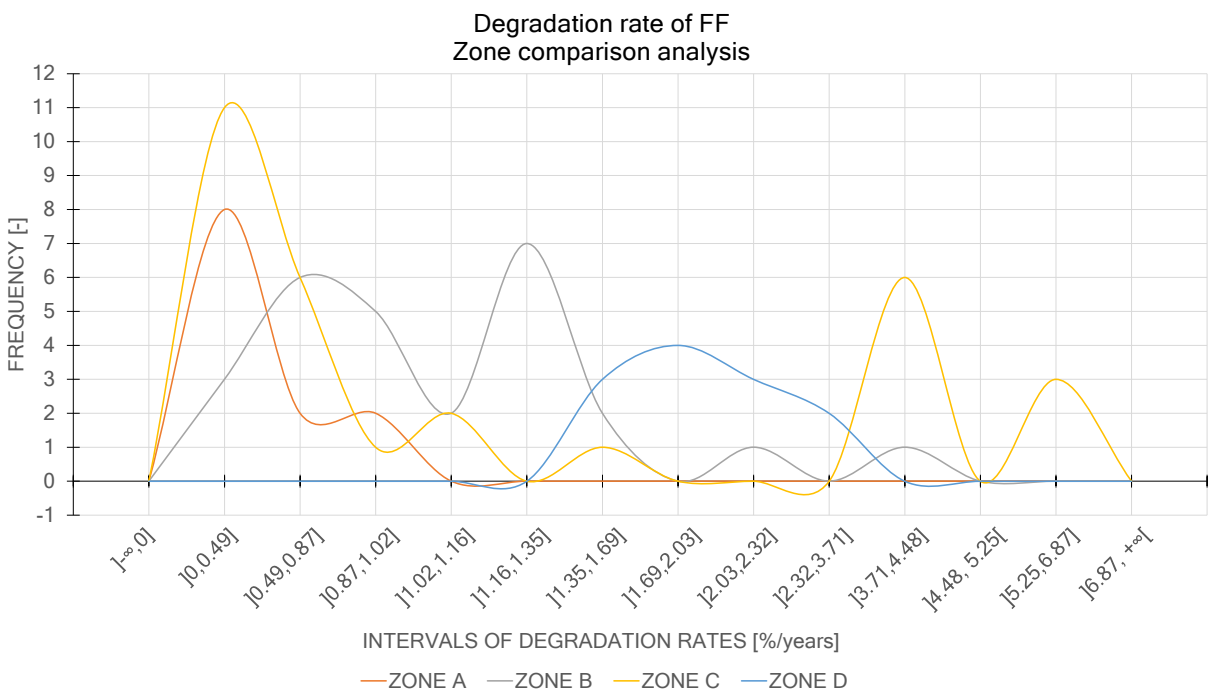

Figure 6.64: Zone analysis of the degradation rate of the fill factor.

In relation to the distribution of the degradation rates of the fill factor for each manufacturer, Fig. 6.65 indicates that the PV modules with lower degradation rates correspond to SOLAR WORLD. 79.16% of the modules from SOLAR WORLD have degradation rates below 0.87%/year. Like SOLAR WORLD, SIEMENS also has low degradation rates for the fill factor (also below 0.87%/year).

RISEN and ET TOWARDS EXCELLENCE have modules with a wide range of degradation rates, 45.83% of the modules from RISEN have degradation rates below 1.16%/year,

and 50% are in the range 1.16%.03%/year. Similarly, 63.63% of the modules from ET TOWARDS EXCELLENCE have degradation rates below 1.02%/year, and 36.36% are in the range 1.16-1.69%/year.

Following the order, modules from HANWHA SOLAR have relatively high degradation rates of the fill factor. All the modules from HANWHA SOLAR have degradation rates in the range 2.03-3.71%/year. The module with highest degradation rates of the fill factor corresponds to module from SUNEL. All the modules have degradation rates above 3.71%/year, where the highest is 6.87%/year. Finally, modules from LUXOR are difficult to sort among the others, because 66.66% (4 out of 6) of the modules have low degradation rate (below 1.02%/year), and the rest is above 2.03%/year.

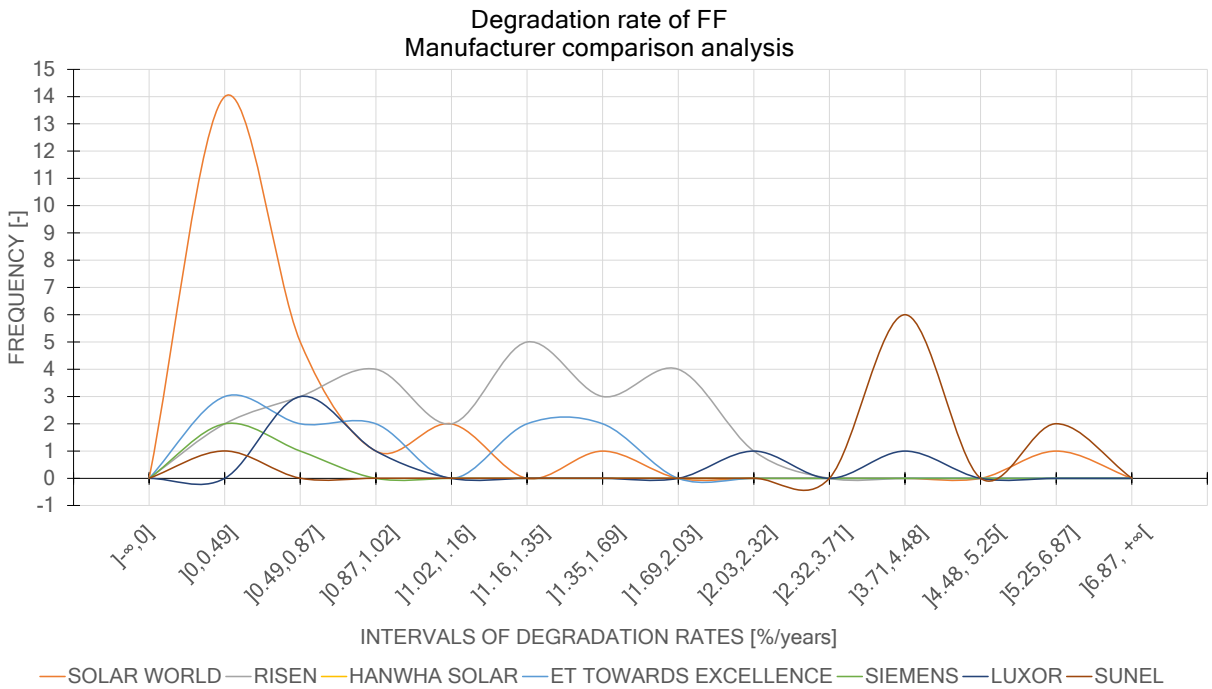

Figure 6.65: Manufacturer analysis of the degradation rate of the fill factor.

In relation with the temporal analysis, Fig. 6.66 shows the distribution of the degradation rates of the fill factor for each exposure period. The oldest PV modules (13 years of operation) and the modules operating during 6 years have the lowest degradation rates (below 0.87%/year). Modules operating during 5 years also have low rates, 85.71% of the modules have degradation rates of the fill factor below 1.16%/year. Regarding to modules operating during 7 years, they have degradation rates concentrated in two different ranges: 66.66% is below 1.02%/year, and 33.33% is above 2.03%/year.

It is evident that modules operating the shortest period (2 years) have the highest degradation rates of fill factor, which are above 3.71%/year. In the case of modules operating during 3 years, it is difficult to sort them among others. The distribution of the degradation rates for modules operating during 3 years indicates that 46.15% of the modules have degradation rates of the fill factor below 1.16%/year, while 53.84% are in the range 1.16-3.71%/year. But no matter what, the rates are better than the ones for modules operating during 2 years.

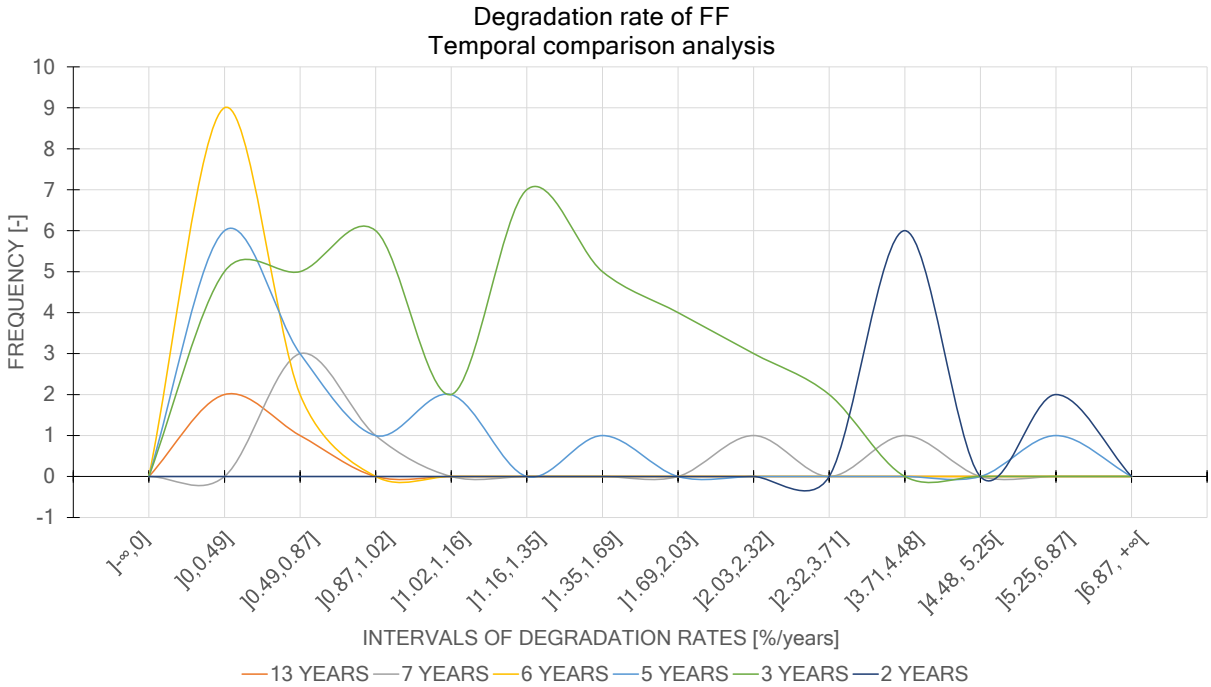

Figure 6.66: Temporal analysis of the degradation rate of the fill factor.

6.3.14 Thermal abnormalities of PV modules

The thermal analysis is done in accordance with the methodology given in section 5.4. In the following sections, the results and analysis of thermal data are presented.

6.3.14.1 Temperature difference deviations

Regarding to temperature measurements made in the campaign, it is important to understand a few facts. The thermal camera FLIR One Pro is capable to obtain several parameters, where temperature is the most relevant variable to be observed. Every pixel of the thermal-images from this camera contains information regarding temperatures. Therefore, thermal-images are very useful to determine the temperature of operation of the inspected PV module. In the other hand, the I-V tracer possess a specific sensor for ambient temperatures. Therefore, it is best to obtain the ambient temperature from the tracer.

With the above being said, the average operating temperature of the module is obtained using the software FLIR Tools. This software can translate any pixel of the image into a temperature, and calculate the average temperature. Thus, the operating temperature of the module corresponds to the calculation of the average of all the pixels of the surface of the module from the thermal-image. On the other hand, thermal-images and I-V curve measurements were taken, for each PV module, consecutively with a few minutes of difference. Since the time between both processes is small, the value of the ambient temperature measured by the I-V tracer is used. With this in mind, the temperature difference $T_{mod}^{ave} - T_{amb}$ is calculated for each PV module as is specified by the methodology of analysis. The average

ambient temperature of a location or a zone is not calculated, because it is not possible to obtain a reliable value. The last is due to the possible micro-climates for each location, the distance and the distribution of the locations for each zone, and the time delay of the measurements for all the modules within a zone.

From the 95 PV modules, only 90 modules are analyzed because the measurements of the other 5 modules were taken under bad climate conditions. Figure 6.67 shows in a qualitative manner how scattered is the temperature difference between T_{mod}^{ave} and T_{amb}. We have four trends, one for each zone. Since each zone contains different amount of PV modules, each trend contains different amount of data points. Y axis plots temperature differences, but for clarification the trends are shifted in this axis, so each trend can be observed independently. The number at the end of each trend corresponds to the average of the dispersion of the data points of the trends. This number is in degrees Celsius unit.

According to the graph in Fig. 6.67, zone C has modules with higher deviations. In average, modules from zone C operate 13.59°C above its ambient temperature. In the other end is zone B, with modules with less deviations. In average, modules in zone B operate 9.21°C above its ambient temperature. In the middle we find zones A and D. In average, modules of zone D have deviations of temperature of 0.97°C more than modules in zone A.

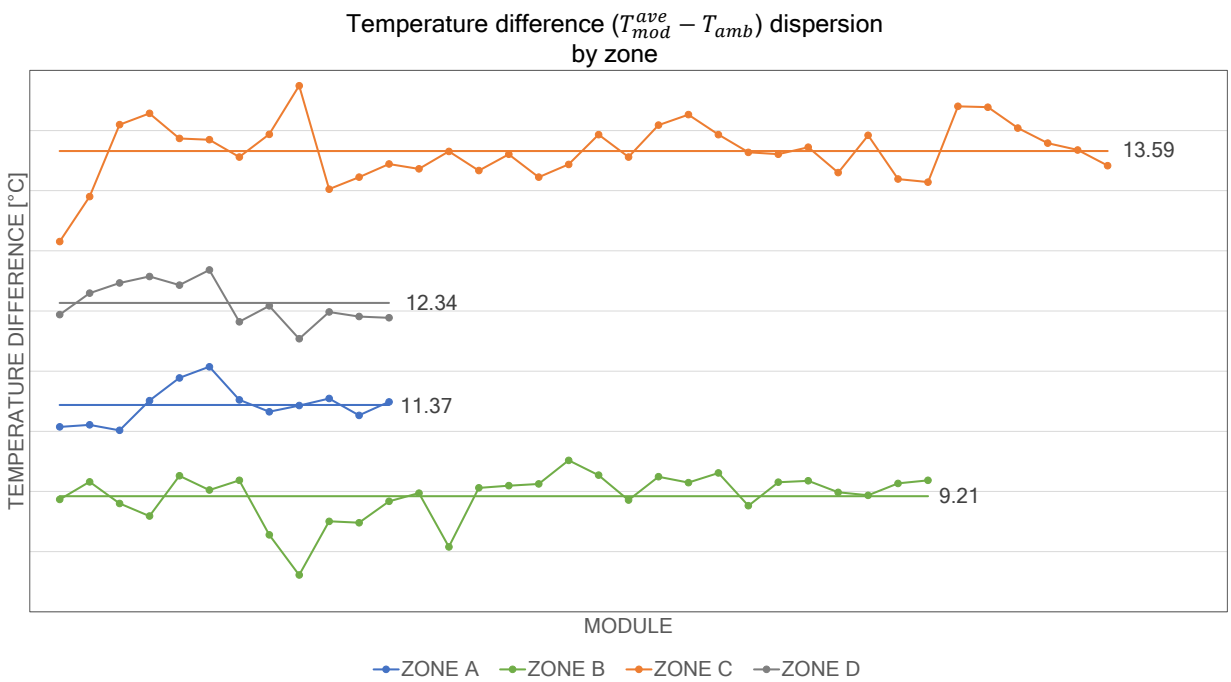

Figure 6.67: Dispersion of the temperature difference $T_{mod}^{ave} - T_{amb}$ for each zone.

The statistical data given in Fig. 6.68 gives us more insights. In this graph, the Y axis shows temperature difference $T_{mod}^{ave} - T_{amb}$. Notice that each group is represented by a "box" and two "whiskers". The portion between the bottom whisker (local minimum) and the bottom of the box (first quartile) are the first 25% of the data points (lowest values). The range from the first quartile to the mid-line inside the box (the median) contains the next 25% of the data points. From the median to the top of the box (third quartile), lies another 25%. Lastly, the distance between the top of the box and the end of the second whisker (local

maximum) contains the final 25% of the data points. Furthermore, the mean is denoted by the "x" marker in the middle of the box (value highlighted in yellow), while the median is denoted by a line within the box (highlighted in red). Outliers are points that are displayed beyond the end of each whisker.

According to the Fig. 6.68, the most disperse temperature differences are within zone C (with a deviation of 4,87°C). This zone also presents the highest temperature difference (24.15°C), where half of the values are above 13.46°C, with an average of 13.59°C. Zone D is the following zone with higher temperature differences. Here, half of the PV modules operate 11.35°C above their ambient temperature, with an average of 12.34°C of temperature differences. Finally, it can be easily seen that temperature differences in zone A are higher than in zone B. In this regard, zone A has higher local maximum (15.88°C>15.17°C), higher median (11.59°C>10.42°C) and higher average (11.37°C>9.21°C).

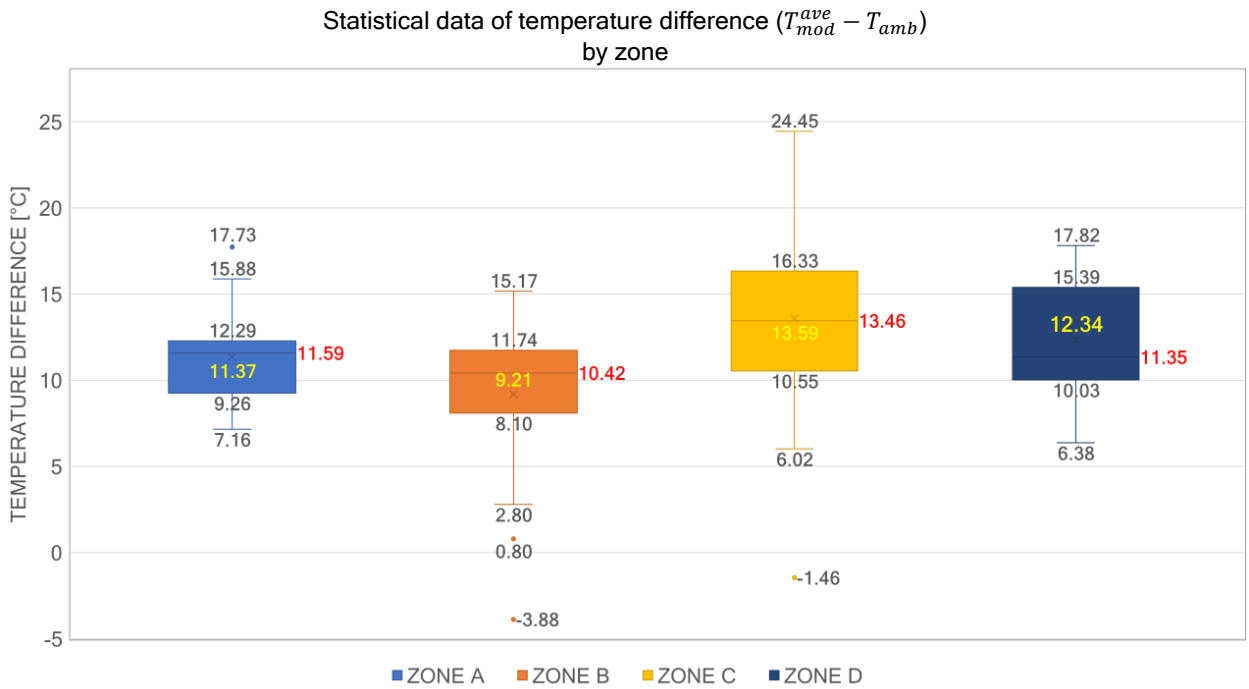

Figure 6.68: Statistics of the temperature difference $T_{mod}^{ave} - T_{amb}$ for each zone.

Regarding the manufacturers, Fig. 6.69 and Fig. 6.70 show the same information analyzed in the paragraph above but sorted by manufacturer. It can be seen that most of the PV modules under study correspond to modules from SOLAR WORLD and RISEN. For the same reason, the standard deviation of the temperature difference $T_{mod}^{ave} - T_{amb}$ is higher for those two manufacturers (see Fig. 6.70).

According to the dispersion of the data points and the average of the temperature difference $T_{mod}^{ave} - T_{amb}$ shown in Fig. 6.69, in average all the modules operate above its ambient temperature. Modules from RISEN and LUXOR have the lowest temperature difference in average. Both manufacturers have modules operating 9.71°C and 10.04°C above its ambient temperature, respectively. In the other end, modules from SUNEL and SOLAR WORLD have the highest temperature difference in average. Modules from SUNEL operate 14.93°C

above its ambient temperature, while modules from SOLAR WORLD operate 12.45°C above its ambient temperature.

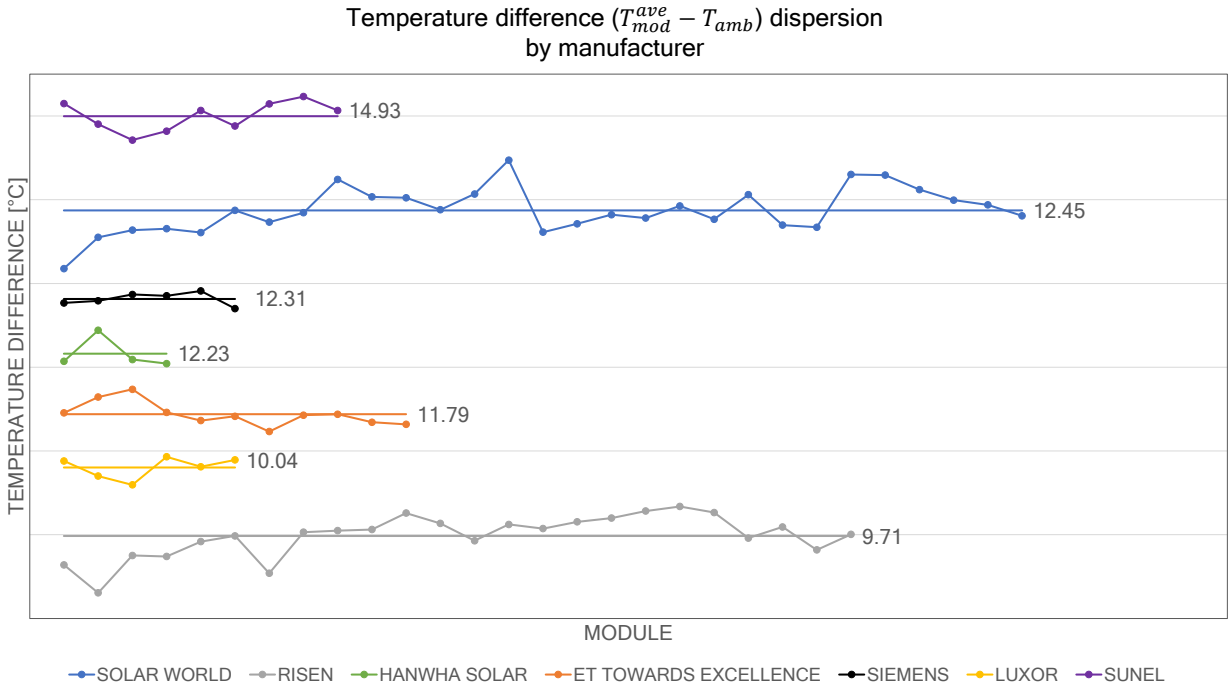

Figure 6.69: Dispersion of the temperature difference $T_{mod}^{ave} - T_{amb}$ for each manufacturer.

Statistics, shown in Fig. 6.70, indicate the same trend discussed above. SOLAR WORLD and SUNEL have the highest maximum temperature difference (24.45°C and 19.64°C, respectively), and modules from SUNEL have a high minimum temperature difference (9.25°C). Following those two manufacturers is SIEMENS. Modules from SIEMENS do not have a high maximum temperature difference (14.22°C) in comparison to the other manufacturers, but the minimum and the average temperature difference (10.00°C and 12.31°C, respectively) are considered high in relation with the 4 remaining manufactures. Also, the standard deviation is low for SIEMENS (1.40°C), this means that almost all the modules operate 12.31°C above its ambient temperature.

Modules from HANWHA SOLAR are very similar to modules from SIEMENS and are very difficult to sort. Modules from HANWHA SOLAR have a higher maximum temperature difference (17.82°C), but also a higher standard deviation (3.24°C), and most of the temperature difference data points of HANWHA SOLAR trend in Fig. 6.69 are below the average, while in the trend of SIEMENS are above the average. Hence, deviations between the operating temperature of modules and their corresponding ambient temperature are lower for modules from HANWHA SOLAR than for SIEMENS. Also, according to the median, half of the PV modules from HANWHA SOLAR have temperature differences lower than 10.62°C.

Following modules from HANWHA SOLAR are the modules from ET TOWARDS EXCELLENCE and LUXOR. ET TOWARDS EXCELLENCE is very close to HANWHA SOLAR, but the lower standard deviation (2.73°C) indicates that temperature differences are nearer to the average temperature difference, which is lower for ET TOWARDS EXCELLENCE (11.79°C) than for HANWHA SOLAR (12.23°C). Also, ET TOWARDS EXCEL-

LENCE has a lower minimum temperature difference (7.63°C) than HANWHA SOLAR (9.87°C). Average operating temperatures from LUXOR clearly have lower deviations from their respective ambient temperatures since the maximum, minimum and average temperature difference (12.61°C, 5.91°C and 10.04°C, respectively) are lower than the values measured for ET TOWARDS EXCELLENCE. Finally, RISEN is the manufacturer with modules that operate with temperatures closer to the ambient temperature. Although their maximum temperature difference (16.74°C) is higher than for SIEMENS and LUXOR, the average temperature difference is the lowest (9.71°C), and half of the PV modules have temperature differences below 10.79°C.

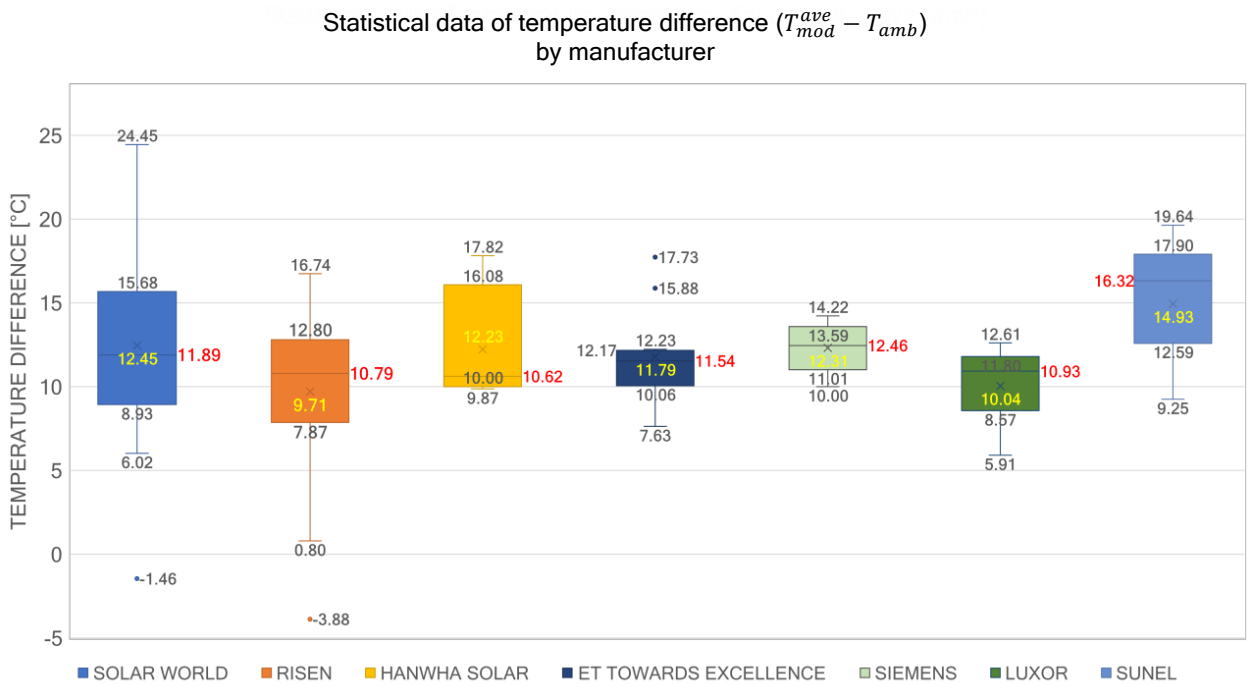

Figure 6.70: Statistics of the temperature difference $T_{mod}^{ave} - T_{amb}$ for each manufacturer.

In terms of exposure time, Fig. 6.71 and Fig. 6.72 show the behavior of temperature difference $T_{mod}^{ave} - T_{amb}$ according to the exposure time of modules. The trend of the temperature differences dispersion for each exposure time indicates that modules exposed by 2 or 6 years are, in average, operating 14.56°C and 14.22°C, respectively, above their ambient temperature. Modules operating during 3 or 7 years have, in average, the lowest temperature deviation with respect to their ambient temperatures. They operate 10.56°C and 10.04°C, respectively, above their ambient temperature. Modules exposed by 13 and 5 years have temperature deviations in the middle.

Statistics from the trends in Fig. 6.71 that are shown in Fig. 6.72 indicates that modules operating during 2 or 6 years have a high maximum temperature difference (19.64°C and 24.45°C, respectively) and the minimum temperature difference is also high (9.25°C and 7.25°C, respectively). Additionally, half of the PV modules have temperature differences above 14.69°C and 13.53°C, respectively.

Sorting the remaining 4 exposure times is not easy. It seems that modules operating during 5 years operate with higher deviations from their ambient temperature, than modules

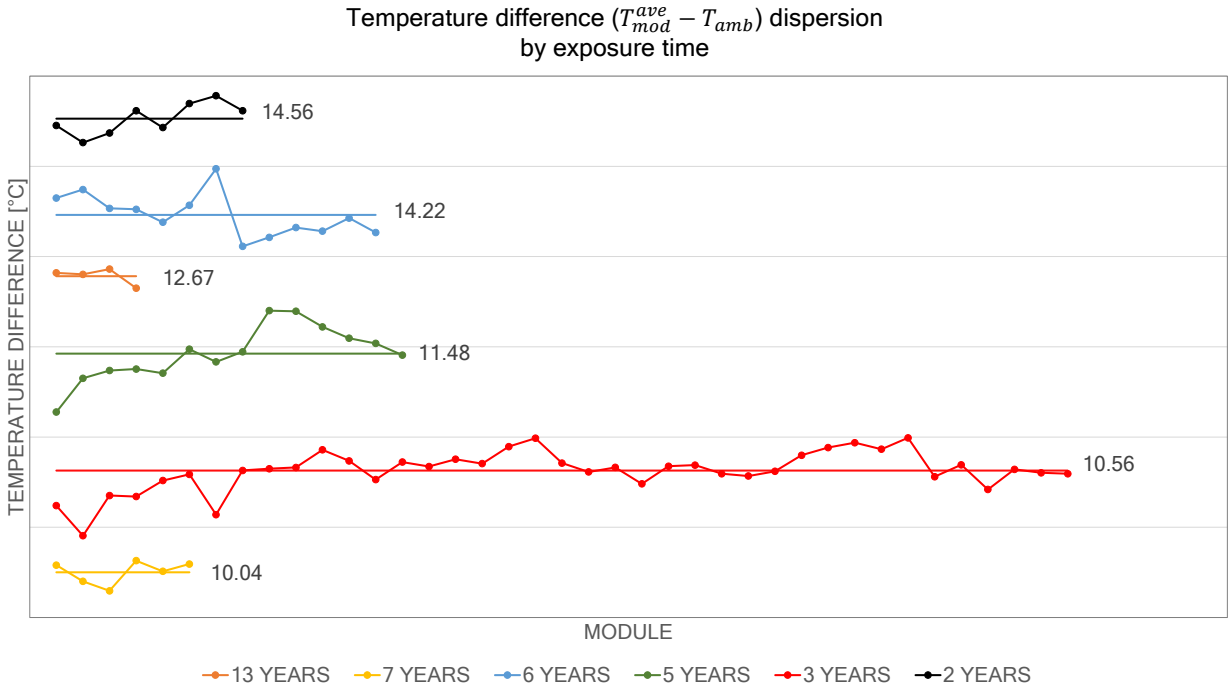

Figure 6.71: Dispersion of the temperature difference $T_{mod}^{ave} - T_{amb}$ for each exposure time.

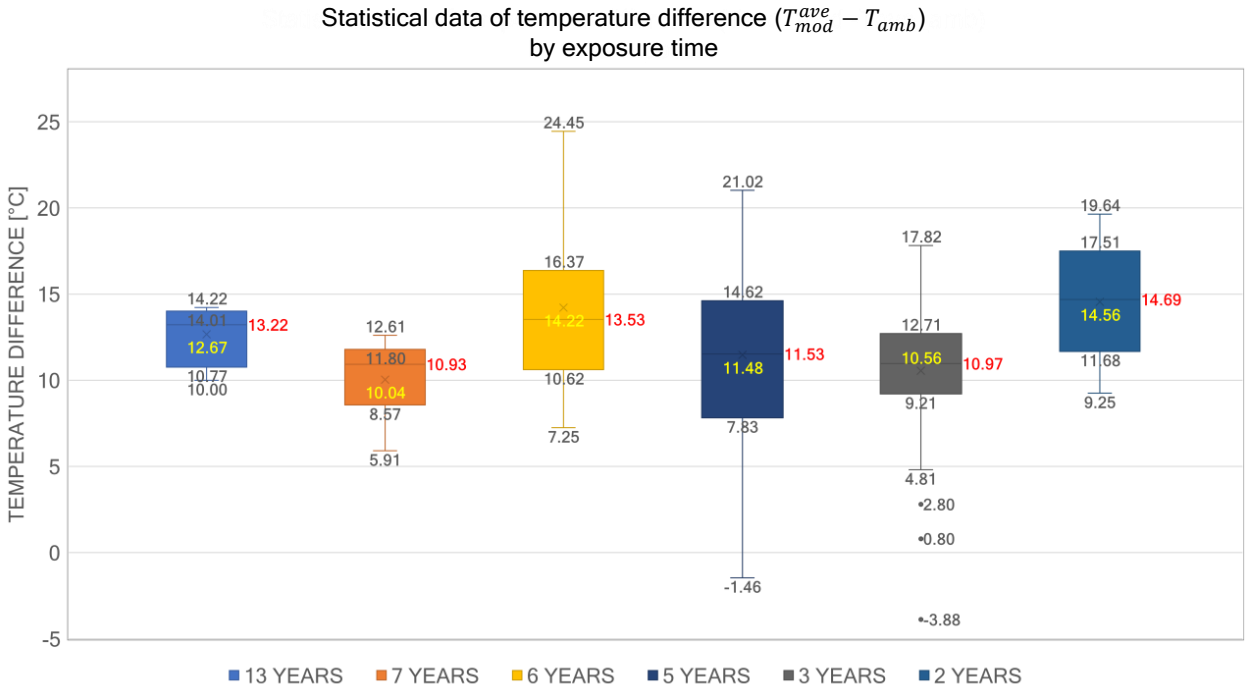

Figure 6.72: Statistics of the temperature difference $T_{mod}^{ave} - T_{amb}$ for each exposure time.

operating during 13 years. According to the average and the deviation of the temperature differences for both times of exposures, most deviations for modules operating during 5 years concentrate in the range 5.64-17.32°C, while modules operating during 13 years concentrate in the range 11.07-14.27°C. Since the maximum temperature difference for modules operating during 13 years is 14.22°C, and for modules operating 5 years is 21.02°C, modules of 5 years old seem to present higher temperature differences.

According to the values of the average and the standard deviation of the temperature differences from modules of 3 or 7 years old, modules of 3 years of operation concentrate their temperature differences in the range 6.19-14.93°C, while modules of 7 years of operation concentrate their temperature differences in the range 8.03-12.77°C. Since the standard deviation of modules operating during 7 years is low (2.37°C), and the average and the maximum temperature difference are lower than for modules of 3 years of operation (10.04°C<10.56°C and 12.61°C<17.82°C, respectively), modules operating during 7 years present lower deviations of their operating temperature with respect to their ambient temperature.

6.3.14.2 Modules with hot cells

When taking into account the definition and classification of hot-spots in the methodology of analysis (section 5.4), we only found homogeneous hot cells and no hot-spots in the results given by the IDCTool. To study the modules with hot cells we use the classification that is made for hot-spots, but we change hot-spot for hot cell. In this context, a hot cell is an homogeneous heat, instead of a spot heat. In this regard, it is important to clarify that:

- A cell at 10-20°C higher than its neighbors is no harm. It will depend on the operating temperature of the module if this temperature difference is a problem or not. For example, if the module is operating at 70°C, then 20°C or more is a problem because the polymers are near their melting points (90°C for EVA).

- Temperature differences between cells are higher when the module is in short-circuit conditions, than when it is operating at its maximum power point. This happens because the current difference at short-circuit condition is higher than at maximum power point.

Understanding the above statements, we can study the number of modules with hot cells. We use the classification of hot-spots and classify the hot cells as strong hot cell (>20°C) or light hot cell (10-20°C). Fig. 6.73 shows the number of modules with hot cells in each zone and the total number of hot cells for all the modules. The hot cells are separated by their temperature difference (10-20°C or >20°C).

The total amount of PV modules installed in zone A, B, C and D are 12, 30, 36 and 12 PV modules, respectively (90 PV modules in total). In Fig. 6.73, it can be seen that all modules in zone A have hot cells with temperature difference of 10-20°C. The 12 modules have 30 hot cells in total. From those 12 modules, only 8 contain hot cells with a temperature difference higher than 20°C. The 8 modules have 12 hot cells in total. In the case of zone D, 10 out of 12 modules have 28 hot cells in total with a temperature difference of 10-20°C, and only 5

modules have in total 5 hot cells with temperature differences above 20°C.

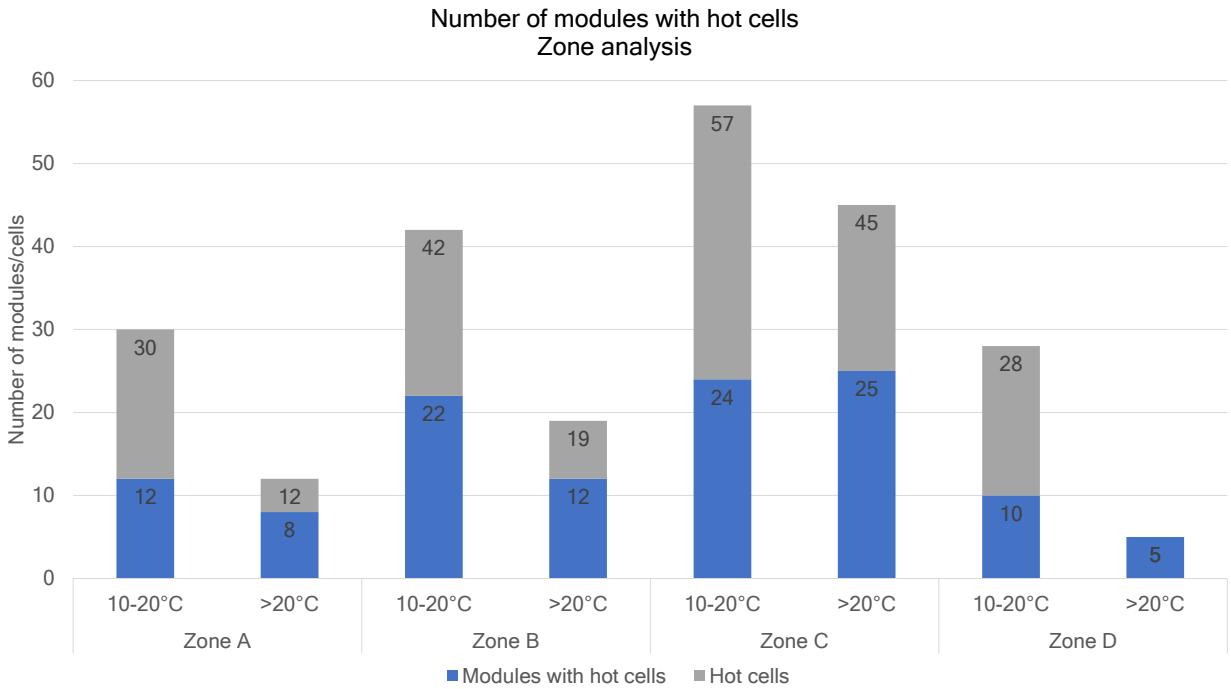

Figure 6.73: Number of modules per zone time with hot cells. The number of hot cells with temperature differences above 20°C and between 10-20°C is specified.

In zone B and C, which are the ones with higher number of modules, more than 65% of the modules contain hot cells. Considering that both zones have a similar amount of modules, both have a similar amount of modules with hot cells with temperature differences of 10-20°C, 22 and 24 modules in zone B and C, respectively. Modules from zone C contain in average more hot cells than modules from zone B. In total the 22 modules in zone B have 42 hot cells, while the 24 modules in zone C have 57 hot cells. Regarding hot cells with temperature differences higher than 20°C, zone C has almost the double amount of modules with hot cells. From the 30 modules of zone B, 12 have in total 19 hot cells. From the 36 modules of zone C, 25 have in total 45 hot cells.

The same information is now sorted by manufacturer in Fig. 6.74. In this case, the 90 PV modules correspond to 29 and 24 modules from SOLAR WORLD and RISEN, respectively; 11 and 9 modules from ET TOWARDS EXCELLENCE and SUNEL, respectively; SIEMENS and LUXOR have 6 modules each; and 4 modules from HANWHA SOLAR. It can be seen that more than 75% of the modules from SOLAR WORLD have hot cells with temperature differences of 10-20°C, while 86% have hot cells higher than 20°C. 22 modules have in total 48 hot cell with 10-20°C of temperature difference, while 25 modules have 47 hot cells with temperature differences higher than 20°C. RISEN has more than 80% of its modules with a total of 44 hot cells with temperature differences higher than 20°C, but only 8 (30%) of its modules with a total of 10 hot cells with temperature differences higher than 20°C.

All the modules from HANWHA SOLAR have in total 10 hot cells with temperature differences of 10-20°C, and only one module with only one hot cell with a temperature difference higher than 20°C. Regarding to the modules of ET TOWARDS EXCELLENCE, 9 out

of 11 have in total 25 hot cells with a temperature difference of 10-20°C, and 6 modules have in total 11 hot cells with a temperature difference above 20°C. Among the 9 modules from SUNEL, 7 have in total 19 hot cells with temperature differences of 10-20°C, and 5 modules have in total 6 hot cells with temperature differences above 20°C. Finally, half of the modules from LUXOR have in total 6 hot cells with temperature differences of 10-20°C, and the other half with a total of 4 cells with a temperature difference higher than 20°C. SIEMENS only has 2 modules with a total of 2 hot cells with a temperature difference of 10-20°C.

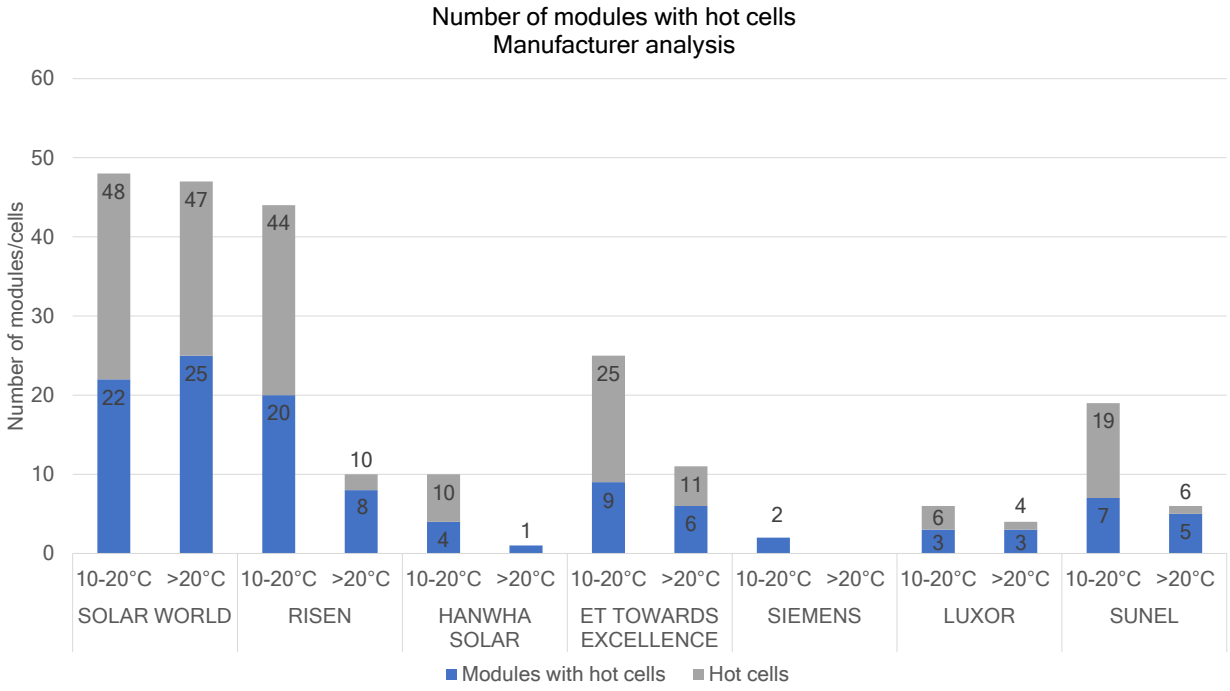

Figure 6.74: Number of modules per manufacturer with hot cells. The number of hot cells with temperature differences above 20°C and between 10-20°C is specified.

Regarding the age of the modules, Fig. 6.75 shows the number of modules with hot cells sorted by time of exposure. From the whole sample universe, 39 modules are 3 years old, 14 modules are 5 years old, 13 modules are 6 years old, 8 modules are 2 years old, 6 modules are 7 years old and 4 modules are 13 years old. From modules installed in 2015, 33 of them have in total 79 hot cells with a temperature difference of 10-20°C, while 15 modules have in total 22 hot cells with a temperature difference above 20°C. From the 14 modules of 5 years old, 12 have a total of 26 hot cells with ΔT =10-20°C and 11 modules have a total of 20 hot cells with ΔT>20°C.

Modules operating for 6 years have more modules with hot cells with a temperature difference above 20°C than in the range 10-20°C. 8 modules have a total of 18 hot cells with ΔT =10-20°C and 12 modules with a total of 24 hot cells with ΔT>20°C. From the 8 modules operating during 2 years, 6 have a total of 18 hot cells with ΔT =10-20°C and 4 modules have a total of 5 hot cells with ΔT>20°C. Finally, half of the modules operating during 7 years have in total 6 hot cells with ΔT =10-20°C and the other half have a total of 4 hot cells with ΔT>20°C. SIEMENS has only one module with one hot cell with ΔT =10-20°C.

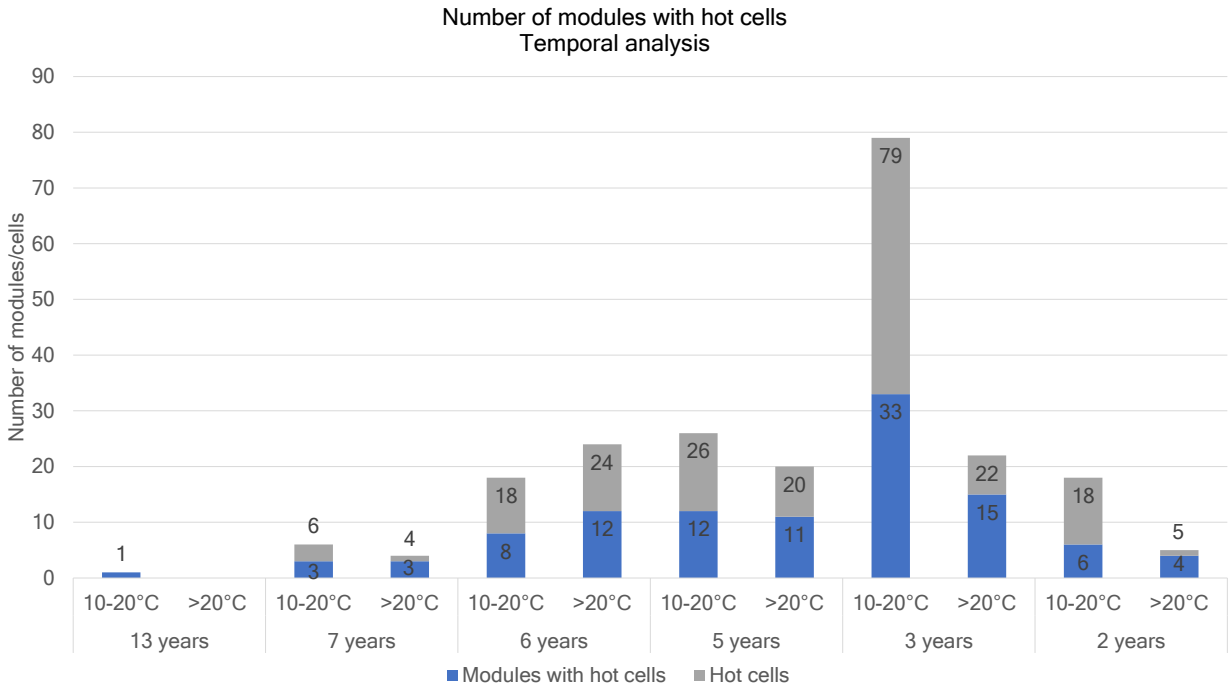

Figure 6.75: Number of modules per exposure time with hot cells. The number of hot cells with temperature differences above 20°C and between 10-20°C is specified.

6.3.14.3 Thermal abnormalities

The matrix of thermal abnormalities in Appendix G considers 11 thermal patterns. From the 95 PV modules, only 90 were inspected under corrected environmental conditions. Within the 90 modules inspected, 89 present at least one thermal pattern. Only the modules from BP SOLAR did not show any thermal abnormality. The remaining 89 modules present one abnormality (e.g. pattern 7) or two abnormalities (e.g. pattern 8 and 11). According to Table 6.23, 6 modules present pattern 2 or 7 but it cannot be determined. Among the 11 thermal abnormalities shown in the matrix in Appendix G, only the pattern 2, 7, 8 and 11 were found.

It must be highlighted that modules were under short-circuit conditions when the thermal-image was taken. In this context, modules with the pattern 2 are not defected. Also, to be able to determine a thermal pattern of a thermal-image, not only the thermal pattern of the image was taken into account, but also the electrical parameters. Since some thermal patterns are similar and can be confused with each other, the electrical parameters, the form of the I-V curve and the visual-images were a helpful hint to distinguish between those similar thermal patterns.

Figure 6.76 shows the thermal patterns found in each of the 90 PV modules, where modules are sorted by zone. In zone A, half of the modules (60) present a short-circuit pattern and the other half (6) present uncertain pattern. It cannot be determined if those 6 modules have a short-circuit pattern or PID, even observing the electrical and visual data. Fig. 6.79 shows a thermal-image of 5 modules with undetermined thermal pattern. Regarding

to zone B, 75.86% of the modules present a short-circuit pattern, 2 modules present PID (see Fig. 6.80), 2 modules present a very hot cell, 1 module shows a short-circuit pattern and also pointing heating due to bird drop. In zone C, 77.77% of the modules present the short-circuit pattern while the remaining 22.22% present hot cells. Finally, in zone D all the modules present the patchwork pattern due to short-circuit condition.

Table 6.23: Thermal abnormalities found in 89 of 95 PV modules inspected.

Thermal pattern	**Number of modules presenting the pattern**
Pattern 2	68
Pattern 7	2
Pattern 8	10
Pattern 2 and 11	1
Pattern 8 and 11	2
Pattern 2 or 7	6
Pattern 1, 3, 4, 5, 6, 9 or 10	0

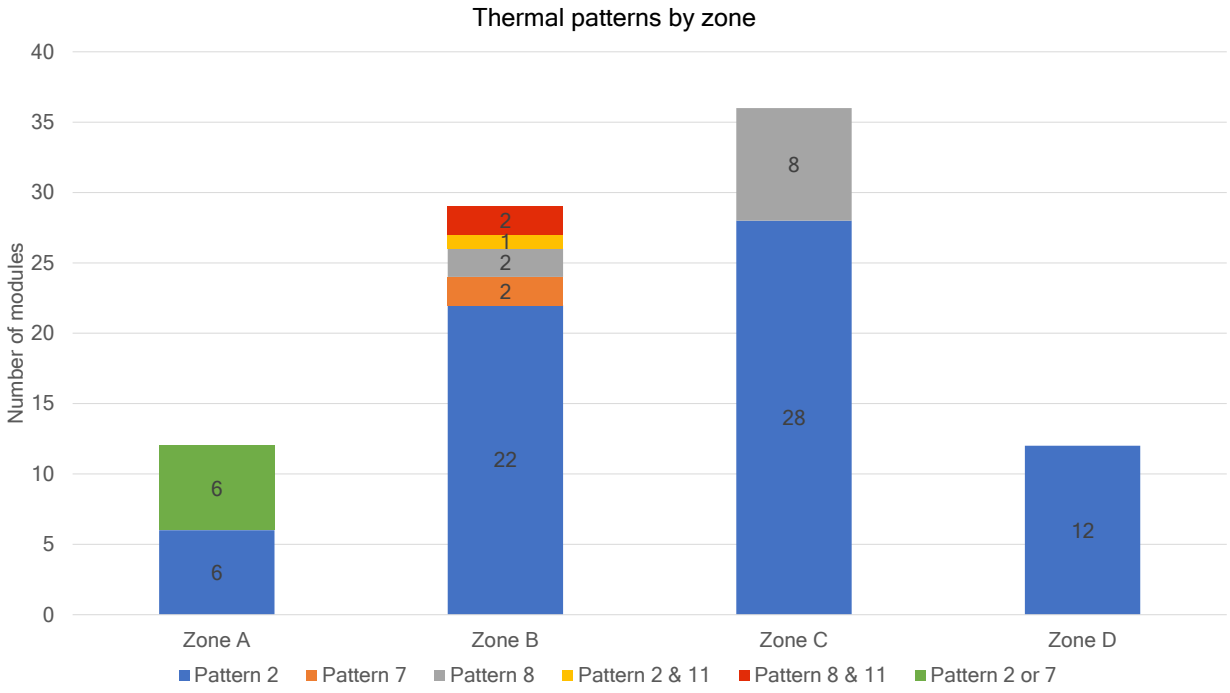

Figure 6.76: Thermal patterns found within 89 PV modules. Modules are sorted by zone.

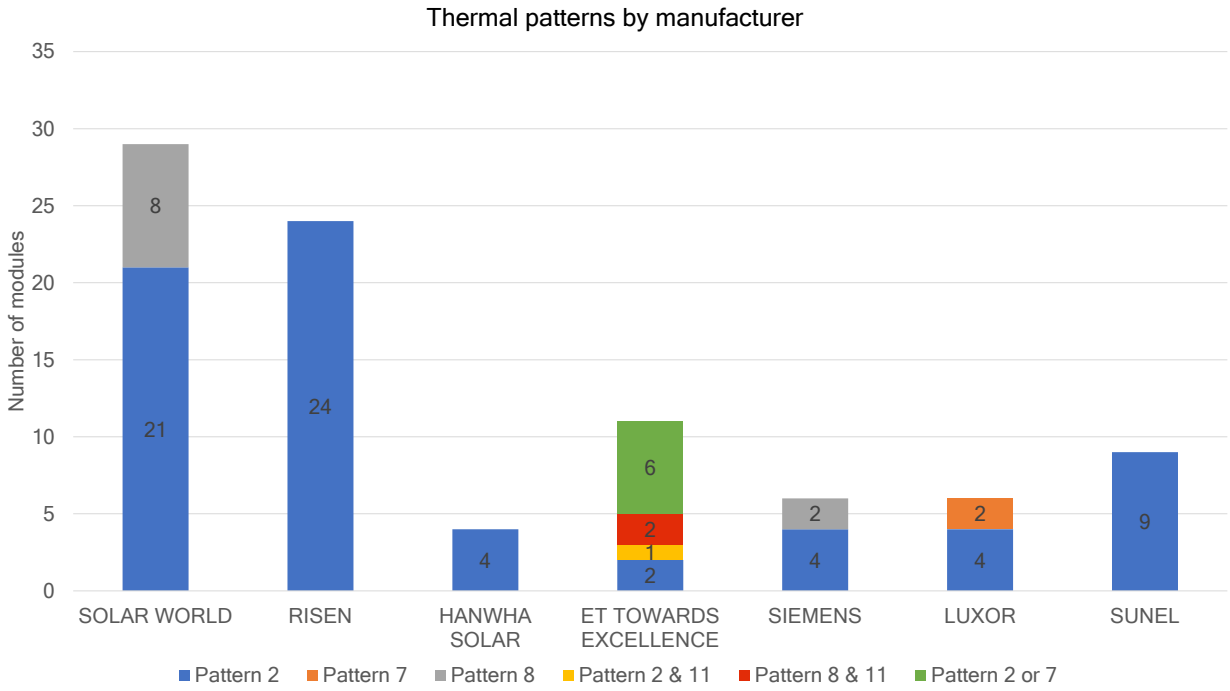

Figure 6.77: Thermal patterns found within 89 PV modules. Modules are sorted by manufacturer.

Figure 6.78: Thermal (left) and visual (right) image of a SIEMENS module stored in a laboratory in a university. The pattern shows a clear hot cell (pattern 8).

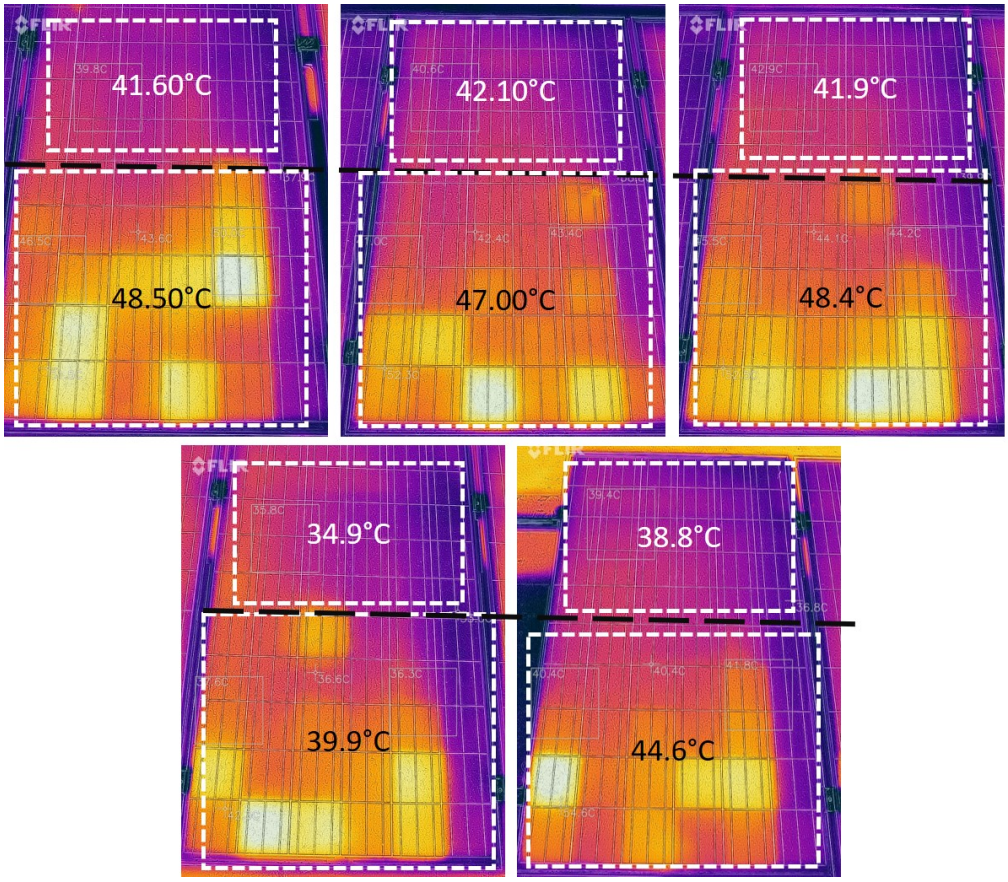

Figure 6.79: Five from the six modules with uncertain thermal pattern (pattern is 2 or 7). Modules are in zone A, from manufacturer ET TOWARDS EXCELLENCE installed in 2015. The average temperature of the lower the upper half is shown.

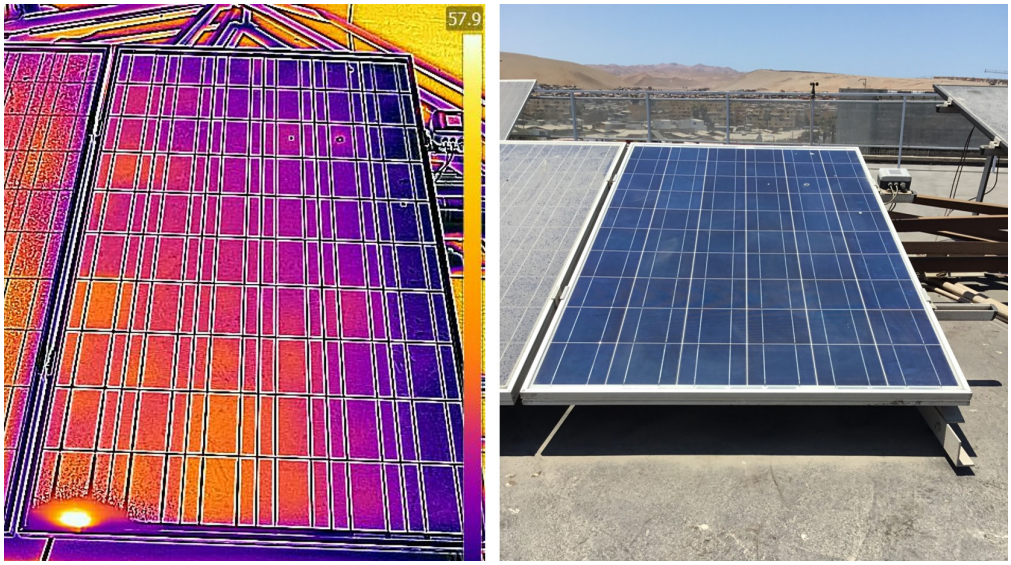

Figure 6.80: Thermal (left) and visual (right) image of a LUXOR module installed in zone B in 2011. The module presents PID (pattern 7) with a degraded I-V curve and a FF of 53.27%.

In Fig. 6.77, the modules are sorted by manufacturer. It can be seen that modules from RISEN, HANWHA SOLAR and SUNEL only present a patchwork pattern due to the short-circuit condition. Modules from SOLAR WORLD and SIEMENS mostly present a patchwork pattern, but 8 modules from SOLAR WORLD and 2 from SIEMENS present hot cells (see Fig. 6.78 and Fig. 6.83). Regarding to modules from LUXOR, 2 modules present PID while the remaining 4 present a patchwork pattern. Modules from ET TOWARDS EXCELLENCE show several types of thermal abnormalities, 2 modules present hot cells and pointing heating due to bird dropping and 1 module present patchwork and pointing heating patterns. From the remaining 8 modules of ET TOWARDS EXCELLENCE, 2 modules have patchwork pattern due to the short-circuit conditions while 6 modules cannot be determined between patchwork pattern or PID.

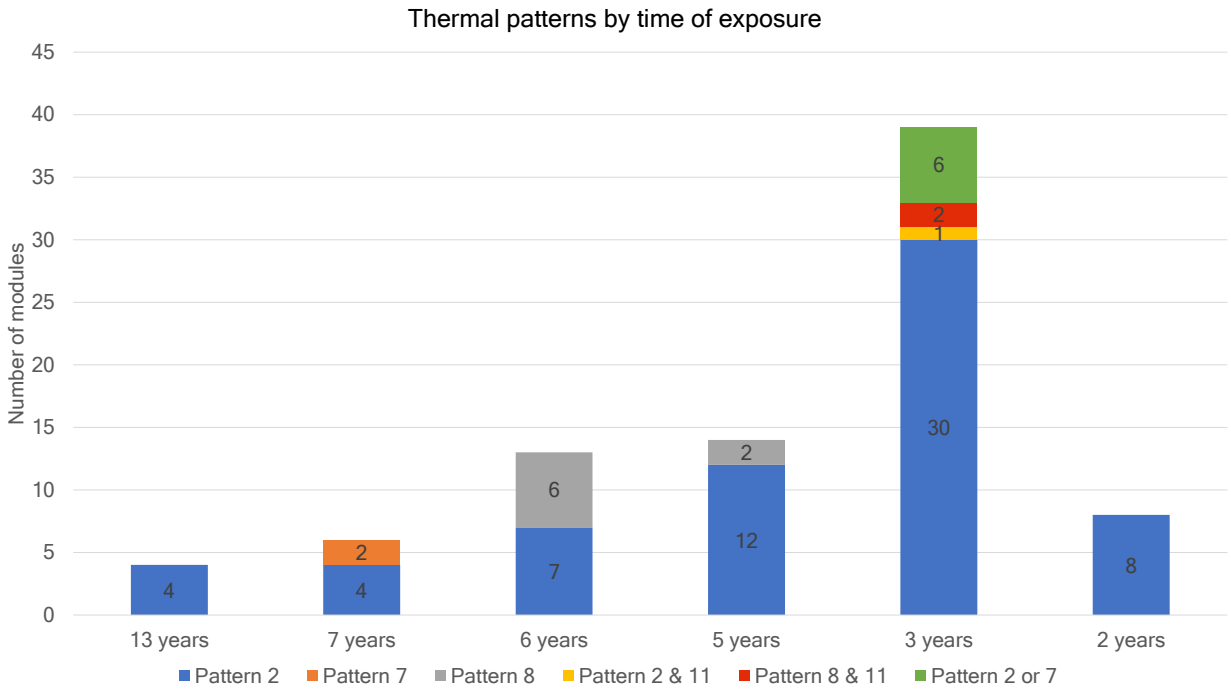

Figure 6.81: Thermal patterns found within 89 PV modules. Modules are sorted by exposure time.

Finally, modules with thermal abnormalities are sorted by time of exposure in Fig, 6.81. It can be seen that the oldest and youngest modules (13 and 2 years of operation) present a patchwork pattern due to the short-circuit condition. Modules operating during 6 and 5 years present a patchwork pattern or hot cells. Almost half of the modules operating during 6 years shows a patchwork pattern while other half show hot cells. In the case of modules operating during 5 years, only 2 from 14 present a pattern of hot cells while the remaining 12 shows a patchwork pattern. Regarding the modules operating 7 years, 2 present PID while the remaining 4 shows a short-circuit pattern. Finally, modules of 3 years old present several patterns, 76.92% of the modules present a patchwork pattern, 6 modules cannot be determined between the patchwork pattern or PID, 2 modules present hot cells (see Fig. 6.82) and heating pointing and 1 modules present a patchwork pattern and pointing heating.

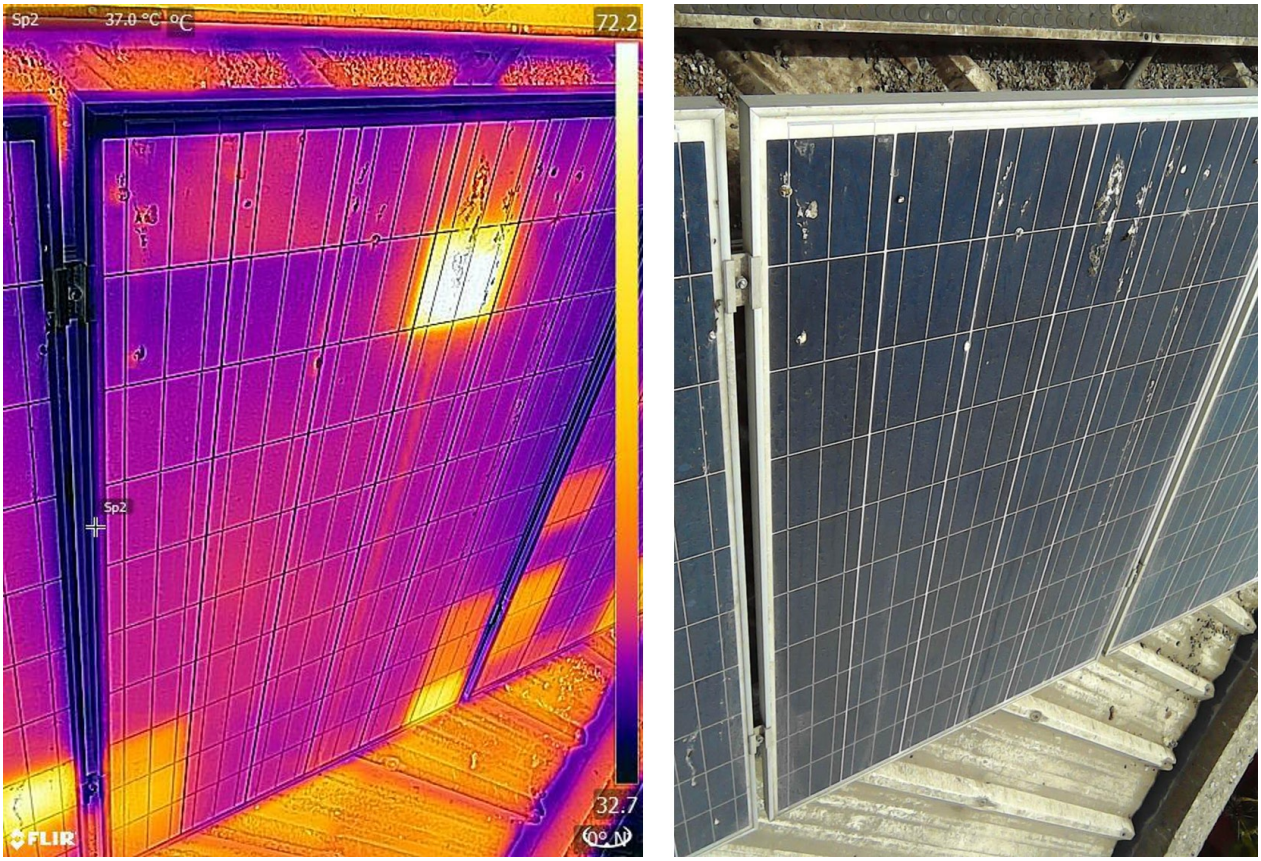

Figure 6.82: Thermal (left) and visual (right) image of a module from ET TOWARDS EXCELLENCE installed in zone B in 2015. This module present a hot cell (pattern 8) and pointing heating due to bird dropping (pattern 11) simultaneously.

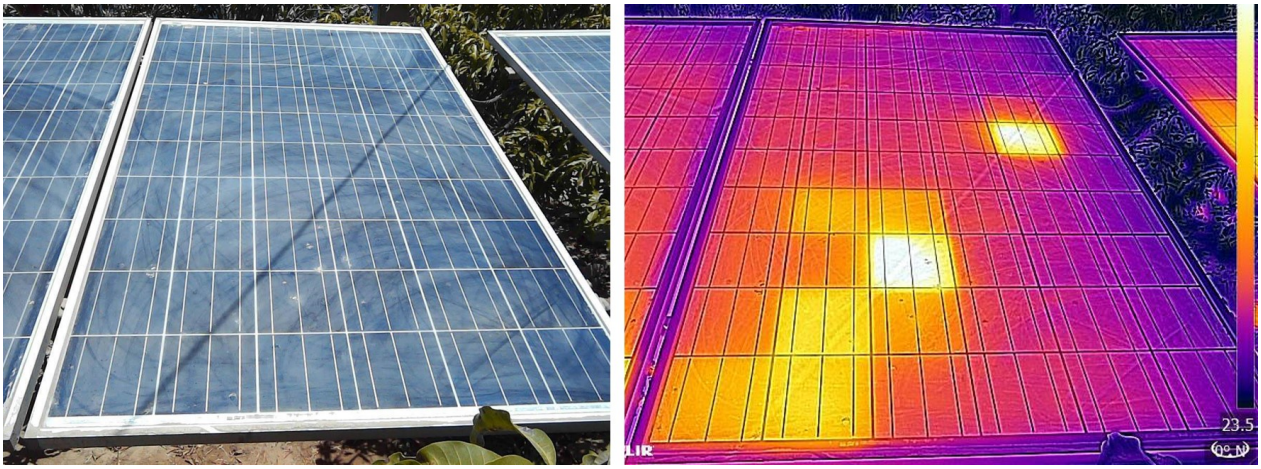

Figure 6.83: Thermal (right) and visual (left) image of a module from SOLAR WORLD installed in zone C in 2013. The module present hot cells in the same direction as the shadow on the surface due to a cable over the module

6.3.15 Relevant cases/modules in the campaign

6.3.15.1 Case 1

One of the two interesting cases among the 95 PV modules inspected corresponds to a PV module from LUXOR in the location 7 (zone B). This module was installed in the roof of a building of a university, it was part of a system of 6 modules (all from LUXOR) and this module was connected at one of the ends of the system. The estimated deployment date, according to a professor of the university, was 2011. The system was operating before the inspection was undertaken.

According to the visual inspection, the material of the backsheet presents slight chalking (see Fig. 6.87), the junction box is weathered (see Fig. 6.86) and the glass is slightly soiled. The visual-image in Fig. 6.85 shows the module after cleaning, the left module in the visual-image is not cleaned and is slightly soiled. From the electrical parameters shown in Table 6.24, it can be seen that the module is severely degraded. The fill factor is reduced in 28.61%. A fill factor below 60% is considered a degraded module and it should be replaced.

Table 6.24: Rated and measured electrical parameters of the module. Calculation of degradation drop and degradation rate.

Parameter	**Rated from manufacturer**	**Measured and corrected to STC**	**Degradation drop**	**Degradation rate**
V_{oc}	37.55 V	33.46 V	10.90%	1.56%/year
I_{sc}	8.39 A	8.16 A	2.79%	0.40%/year
P_{mpp}	235.00 W	149.83 W	36.69%	5.24%/year
FF	0.75	0.53	28.61%	4.09%/year

The electrical characteristics of the module, shown in Fig. 6.84, indicates that the fill factor is mostly degraded due to a critical open voltage drop of 10.9% and power drop of 36.69%. The combination of the degradation of the voltage and the power makes the knee of the curve extremely rounded. Regarding to the thermal-image in Fig. 6.85, it indicates hotter cells at the bottom and at the left of the module. According to Table 6.25, in short-circuit condition the module operates at 11.5°C above its ambient temperature. The maximum temperature found in the module corresponds to 44.2°C, this means that there are no cells with temperature differences above 10°C.

Table 6.25: Measured temperatures from module and location and number of hot cells of the module.

Ambient temperature °C	**Module temperature** °C			**Number of hot cells**	
	Maximum	**Average**	**Minimum**	**10-20°C**	**>20°C**
27.79	44.2	39.4	32.7	0	0

Due to the fill factor degradation, the form of the curve, the severe voltage drop and the distribution of the hottest cells in the module, it is more likely that the modules suffer from potential induce degradation.

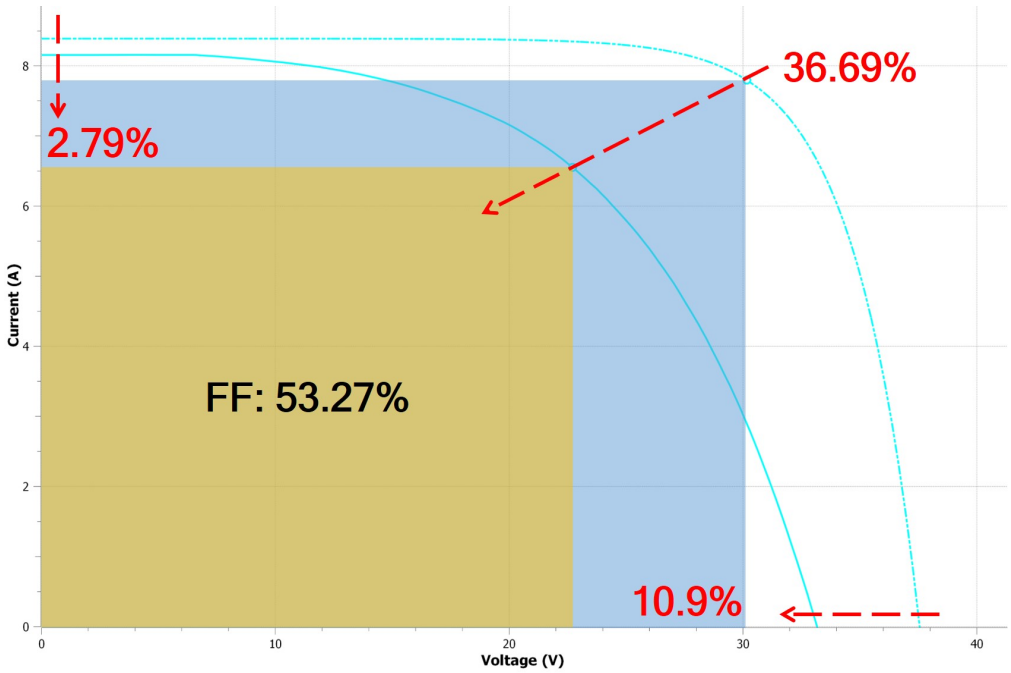

Figure 6.84: I-V curve and measured electrical parameters corrected to STC indicated over the curve for the module.

Figure 6.85: Thermal (left) and visual (right) image of the module. Pattern in combination with I-V curve indicates PID pattern.

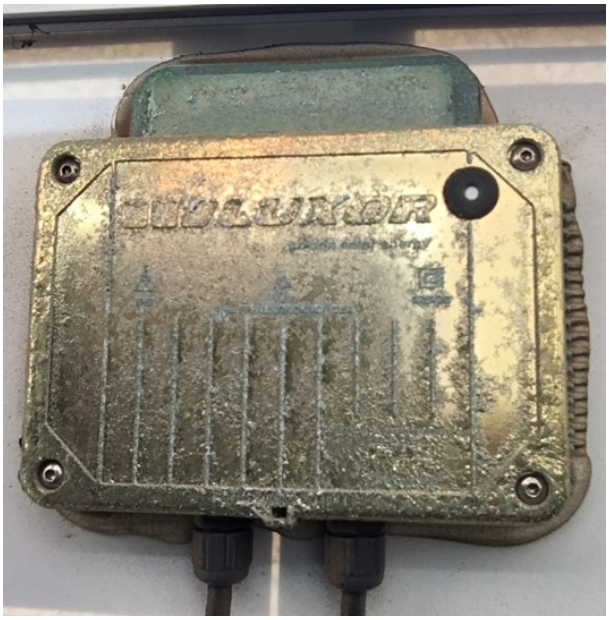

Figure 6.86: Weathered junction box of the module, it has like salt or some kind of corrosion.

Figure 6.87: Module present slight chalking of the backsheet.

6.3.15.2 Case 2

The second interesting case corresponds to a module from SOLAR WORLD installed in the location 11 (zone C) with an estimated deployment date of 2013. For this module in particular, thermal-images and I-V curve measurement were taken twice: one thermal-image and one I-V curve was taken when the module was with heavy soiling and with shadowing from its surroundings and the other thermal-image and I-V curve was taken when the module was clean without shadowing.

Figure 6.89 shows heavy shadowing at the bottom left corner of the module due to a tree. The heavy soiling maintain a low and homogeneous temperature of the module with only two hot cells. The I-V curve shown in Fig. 6.88 indicates that bypass diodes are operating, probably due to the the shadowing. Due to soiling, the current drop is critical (58.12%) leading to a power loss of 75.31%.

Table 6.26: Rated and measured electrical parameters of the cleaned module without shadowing. Calculation of degradation drop and degradation rate.

Parameter	**Rated from manufacturer**	**Measured and corrected to STC**	**Degradation drop**	**Degradation rate**
V_{oc}	37.60 V	36.95 V	1.74%	0.35%/year
I_{sc}	8.81 A	7.68 A	12.82%	2.56%/year
P_{mpp}	252.00 W	153.66 W	7.82%	5.24%/year
FF	0.76	0.49	34.35%	6.87%/year

Table 6.27: Measured temperatures from module and location and number of hot cells of the module. Data measured for the cleaned module without shadowing.

Ambient temperature °C	**Module temperature** °C			**Number of hot cells**	
	Maximum	**Average**	**Minimum**	**10-20°C**	**>20°C**
28.78	98.5	49.1	38.9	2	3

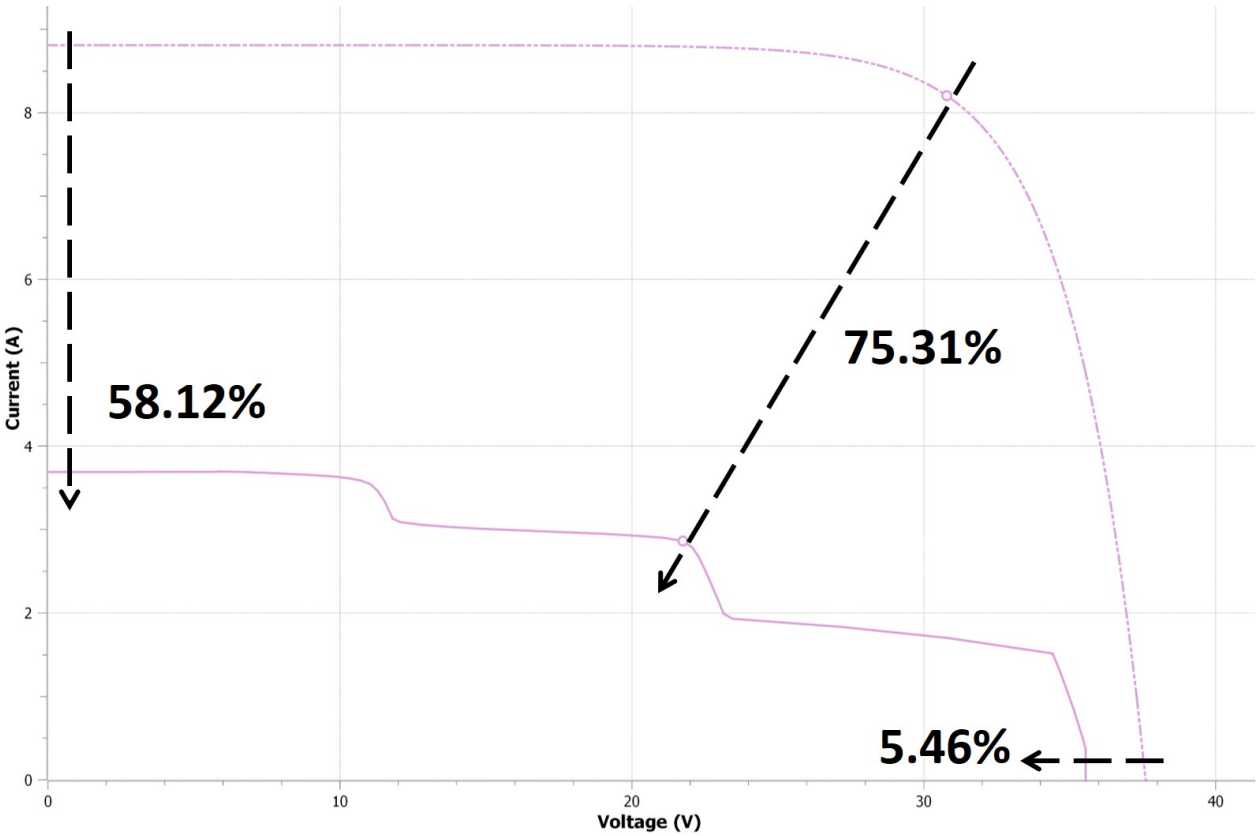

Figure 6.88: I-V curve of the module with heavy soiling and shadowing.

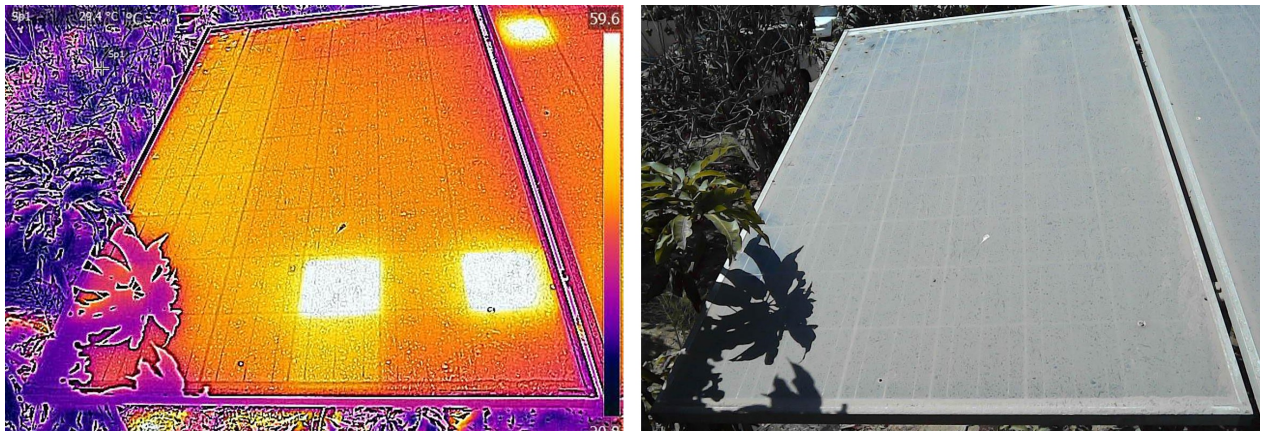

Figure 6.89: Thermal (left) and visual (right) image of the module with heavy soiling and shadowing.

After the module is cleaned, interesting facts are found. Even though the module is cleaned and there is no shadowing when the I-V curve is measured, one bypass diode is still operating and it can be seen due to the sharp step in Fig. 6.90. The voltage drop of the sharp step corresponds to approximately 12 V, because the prolongation of the curve has an open-circuit voltage near 25 V. This voltage drop corresponds to 1/3 of the module's voltage, so 1 of 3 bypass diode is conducting. Also, the short-circuit current drop, shown in Table 6.26, is 12.82% even when the surface of the module is clean. Due to the low short current and the operating bypass diode, the fill factor of the module (49.99%) is extremely low and should be replaced. Furthermore, the power loss is very high (39.08%) and the power degradation rate (5.24%/year) is critically away from the value accepted in the industry (0.7-1.0%/year)

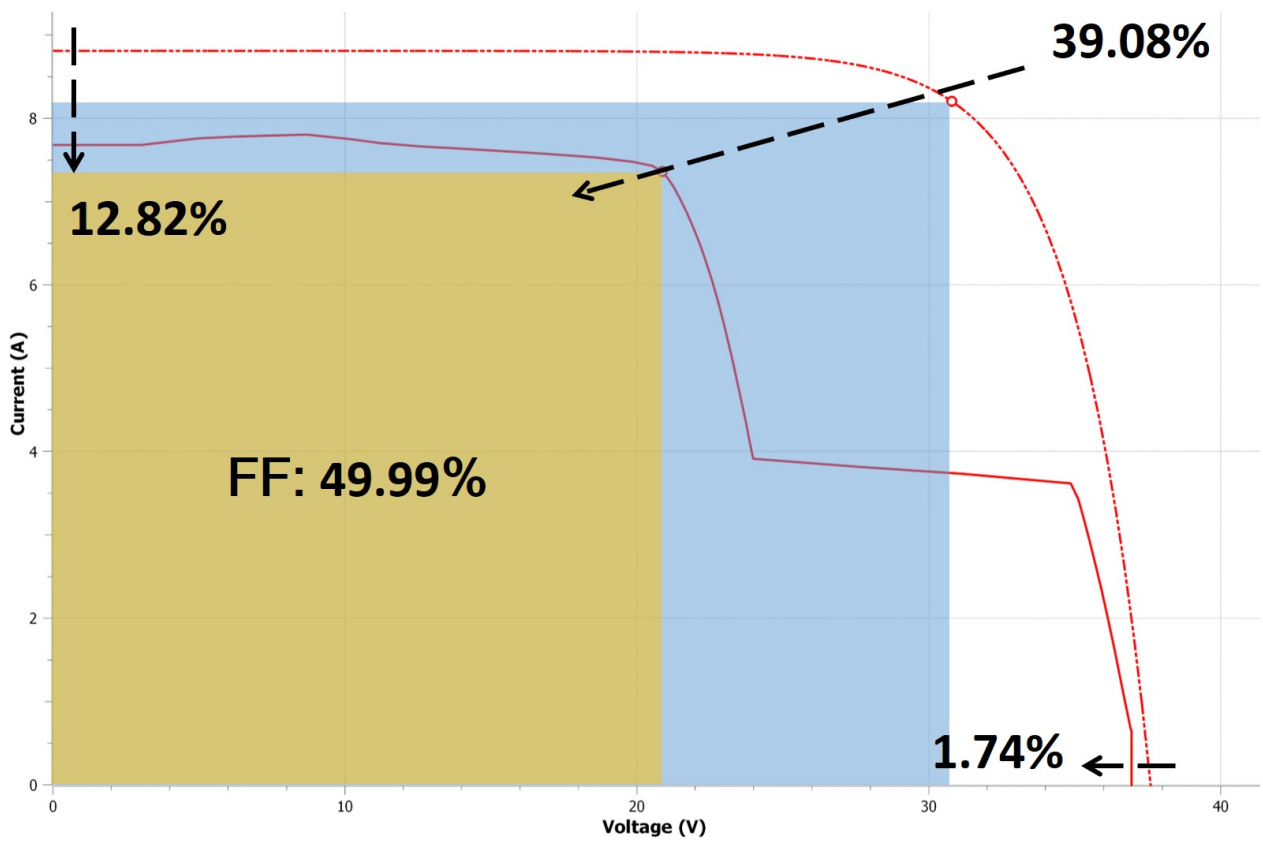

Figure 6.90: I-V curve and measured electrical parameters corrected to STC indicated over the curve for the cleaned module without shadowing.

Not only the electrical parameters show interesting behavior after cleaning, but temperatures and thermal patterns also change. According to Fig. 6.89 and Fig. 6.91, the number of hot cells increase and change without shadowing. Table 6.27 indicates 5 hot cells, which are clearly visible in the thermal-image of Fig. 6.91, 2 cells are 10-20°C above the average module temperature and 3 cells are >20°C above the average module temperature. The hottest cell in the upper left corner is operating at 98.5°C (see Table 6.27), which is detrimental for he module because the melting point of the EVA encapsulant is near the 90°C. Furthermore, the module is operating with an average temperature of 49.1°C, which corresponds to 20.32°C above the ambient temperature.

Figure 6.91: Thermal (left) and visual (right) image of the cleaned module without shadowing.

6.4 Discussion and Recommendations

Regarding the defects found in the campaign, recommendations can be made but with certain restrictions. It must be noticed that, due to the small amount of PV modules inspected, the "Law of large numbers" cannot be used to generalize the phenomena found in this campaign. Nevertheless, the following discussion and recommendations can be applied to the particular locations visited. In this context, the arguments here cannot be used for other situations neither locations.

Starting with visual damage, chalking of the backsheet seems to be related with locations in the city and young PV modules (3 years of operation). Chalking, which corresponds to a chemical degradation, may be triggered by chemical components of the air in combination with coastal winds. In this case, the city is very close to the coastal area, hence, it is difficult to separate the origin of the failure. In the city we have high amount of contamination due to public and private transportation that it is combined with salty winds from the coast. For theses cases is highly recommended to design PV modules for special conditions (such as corrosive environments).

The presence of minor corrosion mainly in PV modules installed in the city and the coastal area may be also related to the composition of the air due to the given the reasons stated above. Like the situation with chalking, minor corrosion of the frame is also found in young PV modules. The visited installations were found to have stainless steel screws in contact with the aluminum frame for the grounding connection. It is known that stainless steel and aluminum have sufficient difference in potential to provide significant galvanic corrosion, which in this case is worsened by the coastal air. As a recommendation for this situation, it is best to use screws made from a material that has a small difference potential with aluminum.

Soiling was found in all visited locations being strongly present in PV modules from the city and the valley. Although studies must be carried out to specify the composition of the soiling, it is highly probable that the soiling of the PV modules installed in the city has

different composition than from the soiling of PV modules operating in the valley. Soiling in the valley was light while in the city was sometimes heavy and sometimes light. Since the frequency (and presence) of cleaning is unknown, it cannot be concluded that modules in the city suffer from a stickier soiling than in the valley. The classic solution for soiling will be cleaning, but depending on the composition of the soiling it is possible to select a proper coating for the glass in the design of the PV module.

In relation to the degradation of electrical parameters, it was found that in average, independently of the location, short-circuit current degradation was 2.75 times higher than the degradation of the open-circuit voltage. This situation may be related to the sensibility of the electrical parameters to irradiance and temperature. Most of the inspected modules had slight or heavy soiling and it is unknown if modules are cleaned (and its frequency). Irradiance affects the current linearly, therefore, the soiling impacts heavily on the current. Regarding the voltage, it is known that this parameter is simultaneously affected by lots of factors in the field such as saturation current (recombination), temperature of operation, irradiance, PID, etc. In this context, it is highly difficult to associated the origin of the voltage degradation to certain climatic properties if the location or other factors. What it can be said from the campaign is that voltage seems to be more stable than current.

According to the typical warranties offered by the manufacturers in the solar industry, the power degradation of all the PV modules inspected (except by one module) were outside the established range (0.7-1.0%/year). The power degradation was 4.13 times higher than the short-circuit current degradation and 1.49 times higher than the open-circuit degradation. It was also seen that degradation rates were higher for young modules than for the ones operating for several years. In this context, it seems that PV modules have a fast initial degradation in the first years and during their lives they do not degrade so fast. One of the hypothesis for this situation is that new PV modules should "settle" themselves in their new condition/environment. This means that they must operate under restrained conditions that are demanded by the series-parallel connections; the inverter topology; instantaneous situations such as over-voltage, high irradiance (more than 1000 W/m^2); etc. Manufacturers test their modules as single units under different accelerated environmental chambers to simulate their response for the next 30 years of operation, but it is known that such tests do not reflect the reality. The recommendation for the study of the design on PV modules would be to perform initial degradation tests for each component/material of the PV module, for the module as a whole, and in addition the initial degradation of the module under more realistic conditions (considering connection topologies, peak radiation, etc.).

It was seen that 8 PV modules from the study presented higher measured FF than rated FF, where the rated fill factor was calculated using the information of the nameplate. The detailed results from the database show that in these PV modules the degradation of the P_{mpp} was nearly the same as the I_{sc}. Therefore, taking into account the degradation of V_{oc}, the decrease of $V_{oc} \times I_{sc}$ was higher than the decrease of P_{mpp}. Hence, the FF increased. On the other hand, the degradation of the FF, in average, was higher than the degradation of the V_{oc} but lower than the degradation of I_{sc} and P_{mpp}. Regardless of which electrical parameter was the one that degraded the most or was least degraded, the rate of degradation of all electrical parameters was higher for young PV modules. In this context, the recommendations to study this situation are the same as those given in the paragraph immediately above.

Relative to the deviation of the average operating temperature of modules from the ambient temperature of their respective locations ($T_{mod}^{ave} - T_{amb}$), it was found that the maximum deviation was 24.45°C from a module operating during 6 years in the valley. Likewise, modules in the valley were, in average, the ones with higher temperature deviations. This situation is not surprising because modules operating in the valley are exposed to warmer winds than module operating near the coastal zone or the city (also near the coast). Furthermore, the valley is one of the region with more vegetation, which leads to frequent or even permanent shading that in turn leads to hot-spots and higher operating temperatures. As mentioned at the beginning of this section, the valley present lots of PV modules with light soiling. In this context, in-homogeneous soiling can be also the reason for higher operating temperature of modules. Recommendations to avoid high temperatures due to soiling and other effects are mentioned in next paragraphs.

In relation to the thermal patterns found in the inspected modules, most of the them were associated to a patchwork pattern. In this specific thermal inspection, the patchwork pattern is not a failure or defect because the thermal inspection was done with the module under short-circuit conditions. On the other hand, the most relevant cases, which were two, presented PID pattern. It can be seen in the matrix for thermal abnormalities of PV modules (in Appendix G) that the PID pattern is commonly mistaken with patchwork pattern. Therefore, it is difficult to select which is the right pattern that is shown by the measured thermal-image.

Regarding the operation and maintenance of the PV systems visited in the campaign, several problems were recognized. Based on those issues, recommendations can be made. People living from the agriculture outside the city and people living in the city have different lifestyles and behaviors. In this context, the same can be said for the manner in which they spend energy.

Specifically for farmers in the valley, we have the following problems in the operation and maintenance of their PV systems:

- PV systems operate during short periods of time in the day, when farmers need to water their plants. They normally water their plants in the morning for a few hours. This means that during most part of the day, the PV system is not supplying energy. However, the system continuously generate energy due to the presence of sunlight.

- Lots of PV systems were installed in the same year through a government initiative (2010-2014). Most PV systems were designed to feed a water pumping machine to pump water for the farmers. During the first years of operation, several farmers had technical problems with their water pumps and until today they have not found spare parts in the national market. These systems have not been operated for years but PV modules are still interconnected and generating energy without a load to dissipate this energy.

- Other initiatives have been made by other governments to help farmers with other agricultural applications. In this context, new PV systems were installed beside old PV systems without interconnecting the systems. In this situations, some farmers stopped using their old systems without disassembling them or giving them new usage.

The situations described above force the PV module to constantly generate energy, due to the presence of sunlight, without a load (because is not present, working or operating) to dissipate its generated energy. When a PV module cannot deliver its energy as an electric current,the module dissipate it as heat. This means that PV modules operating without a load are always warmer than the ones operating with a load.

The previous situation is worsened by the movement of the sun and changes in the ambient temperature during the entire day. Within 24 hours, the sun is "present" only during 10-12 hours. If a PV module do not have a proper load, then it will be heated up while the sun is present and it will cold down during the night. The effects of the ambient temperature have the same impact on the PV module because the temperature of the ambient increase and decrease with the presence of the sun in the same manner.

The thermal stress of PV modules is an effect that must be taken into account when modules are designed. All materials in the module expand or contract due to temperature changes (or stress). Depending on the CTE, material expand or contract at different rates. The aluminum of the frame and the polymers of the backsheet have, typically, the highest CTE while the silicon and the glass have the smallest CTE. The copper of the ribbon is normally in the middle. Therefore, thermal stress is capable of breaking the weld between ribbon and silicon, breaking the interconnections between solar cells and even cause delamination.

Solutions or recommendations in relation to thermal stress can be applied to PV module design, PV system design or to final-client (e.g. farmers) behavior. In the context of PV module design, more than one robust busbar (for redundancy) is applied to avoid an open-circuit in case of broken interconnections. Also, manufacturers are changing from the typical solder with tin and flux to solder pastes. Solder paste is an effective alternative to solder-coated copper ribbon during the stringing and tabbing process. Theses pastes allow lower process temperature and, cost and material optimization (due to precision).

For PV system design, cooling systems can be applied but they can be expensive and complex. Some alternatives can include latent air-cooled method (natural or forced convection), water-cooled method (circulating water), etc. In the case of farmers, the PV system can be designed to also feed a part of the consumption of electricity of a household and not only to feed water irrigation. In this case, so that the system does not increase its capacity, the electrical consumption of the household must be outside the periods of water irrigation. Another solution is the use of batteries, but they can be expensive. Lead-acid batteries need to be maintained regularly and last longer than other technologies.

It is difficult that farmers change their water plant schedule because, for example, it is more efficient to water plants in the early morning (or late evening) so the water do not evaporate too fast. However, farmers can be educated to understand that they can have a positive impact in the lifetime of their systems. They can, for example, cover the PV system with a reflective cover to darken the solar cells to simulate the night when they are not using the system (for long or short periods of time).

The following problems were found for PV systems in the valley (for agricultural uses) or in the city (for electricity consumption):

1. System owners do not clean PV modules with the regularity that is needed. This causes accumulation of soiling to start as slight accumulation until it looks like a heavy coating of dust. Due to the inclination of the PV modules most part of the dust accumulates at the bottom of the PV modules.

2. PV systems are installed anywhere without a proper study of shading. A few systems were constantly shaded by trees that were too close to the system.

3. Some PV systems use PV modules from different manufacturers. That means that PV modules from different manufacturers (and possibly different nominal power) are interconnected.

Situations shown in point 1 and 2 causes to solar cells within PV modules to receive different amount of solar radiation. This means that solar cells are generating different amounts of electrical current within the same PV module. This situation causes "current mismatch" and can easily induce hot-spots because shadowed cells dissipate part of the energy generated by the cells that are not shadowed. This situation also occur in the case of point 3, but the current mismatch is not at cell-level but at module-level. When two interconnected modules have different electrical characteristic, which can happen even if they have the same power rating, there is a mismatch in the output current of the modules. Therefore, in a system with multiple interconnected modules, the modules with lower output current dissipate (as heat) part of the generated current of the system. The current mismatch may be enhanced by interconnecting modules of different manufacturers because not all of them use the same PV cells or encapsulating materials.

Solutions or recommendations in relation to current mismatch at cell-level and module-level are several. The first one, which is the most obvious, is to clean PV modules. Small PV systems, such as the ones that farmers use to feed a water pump, can be easily cleaned. Water must be demineralized and should never be applied under pressure onto the module's surface. To take off the dust with the water it is recommended to use a manual windshield wiper and avoid to scrape with cloth.

It is also recommended to trim trees and bushes regularly to avoid permanent shading of the PV modules. In this context, it is best to make an study or assessment of the best place to install the PV system. It is clearly better to have the system in a place with no trees or any plant, but this is not always possible. Finally, regarding to PV modules of different manufacturers, it is recommended to have small systems with only one manufacturer. In the case of larger system, it is possible to use several manufacturers and separate PV arrays in different inverters or in one inverter with several power trackers.

The last but not least important problem that was found in the campaign is related to security. In general, small systems (typically 6 PV modules) do not have any means for protection of DC current, which is one of the most important items regarding security. These small systems uses an inverter that can be turn on and turn off, without any mechanical equipment to isolate the DC generation. In this context, within the inverter (even when it is turned off) there is always 180 VDC alive. This situation can be dangerous even for a certificated maintenance operator with proper personal protection equipment and can be worst for people that use the system and do not have proper training. Although the inverter

is always under shadow because is installed under the PV modules, it is exposed to the environmental conditions 24h/365d. Finally, these systems do not have fences to isolate the system from near people or children.

Security is a key factor to avoid inappropriate operation and/or maintenance of the system. A bad maintained or operated system can lead to fire as one of the ultimate catastrophic failures. It is highly important to separate the system by the means of a fence and place a high-voltage danger sigh to prevent people. Only trained people should be permitted to enter and inspect the PV system. Also, the PV system should be maintained regularly by a trained person. The inverter should be inside a box with proper ventilation and should have proper protection for DC and AC sides.

Chapter 7

Conclusions and Recommendations for Future Work

7.1 Conclusions

In this thesis a design of an Inspection Data Collection Tool to evaluate PV modules is proposed. The proposal is based on the state-of-the-art in the field and the definition of a set of criteria for its use in small scale PV solutions. The implementation involves the development of a survey, equipment and tools, procedure for testing and analysis. IDCTool was used for a field campaign in the Arica and Parinacota Region, which is representative for desert climate conditions. Consequently, regarding the 9 specific objectives of this research work, all of them were fully and successfully carried out. The obtained results were analyzed following the proposed procedure. Thus, the main conclusions and future work were developed.

Almost 18 failures modes with their respective degradation modes were reviewed by the use of most recent research work with high impact in the scientific community. According to the experiences in Chile, since 2014, in relation to PV operation and maintenance, the most significant failures are the ones related to the encapsulant degradation (such as discoloration), PID and hot-spots. In the other hand, six standards and three guidelines were reviewed in relation to the field inspection methods. Among those standards and guidelines are the ones developed by technical committees such as IEC and ASTM and highly recognizable and respectable institutions such as NREL and IEA PVPS. While the inspection survey was basically developed with the NREL visual inspection tool and the state-of-the-art of failures of PV modules, the procedures to carry out the field inspection of the PV modules was completely based on the reviewed standards and guidelines. According to the experience lived while doing Arica's campaign, we can state that the visual inspection survey was very complete. Failures not covered in the survey were not found, but also several failures covered by survey were not found in any of the inspected PV modules. The latter seems to suggest that visual inspection is not a very good tool to find failures or defects, but it is necessary when electrical or thermal defects are found. Thus, the visual inspection is a very good tool analyze the possible origin of electrical/thermal abnormalities. Likewise, the visual

inspection survey was very useful to extract information in a way that was easy to construct a database in excel. Thus, this survey is also an excellent tool for statistical treatment of the information.

Regarding to the used equipment and tools for the inspection, following observations can be said. The equipment and tools used were enough to perform the inspection tasks. They were light weight, occupied little space (everything fits inside a bag of $30 \times 20 \times 20\ cm^3$), were easy to use and the I-V tracer, which was the device that takes the longest to make a measurement, only took less than a minute to perform a single measurement. The autonomy of the FLIR ONE pro camera and iPad were enough to work with the devices at least 8 hours and inspect 21 modules in the best day. Plastic tie cables and cable cutter were used innumerable times to free the cables from the structure and to place them again in their initial position. This is very important, because the facility must remain exactly as it was at the beginning of the inspection. Sometimes it was difficult to separate the MC4 connectors with bare hands and it was necessary to use a special tool to unplug them.

In relation to the design of the procedure for field testing, its implementation was successful and useful. However, several processes can be done differently or can be improved. It is known that it is possible to bring all the equipment necessary to perform the inspection of a PV module almost anywhere, due to the aforementioned reasons. However, this does not mean that it will be possible to perform the desired inspection.

With the above being said, three types of installations were found in the field: (1) modules installed on inclined structures at ground level, (2) modules installed in inclined structures elevated at least 2 meters from the floor and (3) modules installed on structures without inclination onto the roof. In the latter case, modules could not be inspected at all because it was not possible to have access to the MC4 connectors to measure the electrical parameters. In the case 2, the inspection was possible if there was a ladder available at the installation. Although it was possible to perform the inspection, it was difficult to have a good angle with the camera and to clean the entire module. The first case was not a problem from any point of view. In Arica's campaign most of the inspected location were type 2 with available ladder, the rest was type 1 (mostly certified small PV plants) and only one location was type 3. Therefore, it is desirable to build a structure to hold the camera steady in a specific angle and at a specific distance from the module. This structure should be something that can be folded for storage and transportation and it should have way to anchor the structure to the frame when it is used. To place the structure at the module's frame, a small folding ladder should be used in the case of installation of type 2.

According to the field testing procedure in section 5.3.3, if the module under inspection is not operating, it must be connected to a load. During Arica's campaign, some locations had PV systems that were not operating because the load was not working (e.g. a defective water pump) or because it was not the time of the day to use the load (e.g. water agricultural plantations). In both cases the only solution was to short-circuit the modules to have a thermal equilibrium point to take thermal-images. Also, PV plants connected to the grid have their 15 kW (or higher) inverters protected and far from the PV modules. In those cases, it is complicated to have access to the inverter and in most cases, due to safety reasons, it is best to shut down the whole installation at the beginning of the inspection. Hence, we

have again the problem of the load and we must short-circuit the PV module. Thermal-images of short-circuited modules can show defects when those defects are strong. The last means a short-circuited module with a really hot cell will not show a patchwork pattern, because the temperature difference between the hottest cell is extremely high compared with the temperature difference of normal current mismatch. The problem is that we cannot recognize smaller temperature differences and we do not know the temperature operation of the module in its maximum power point. It will be useful to have a small and light weight programmable resistance/load to connect to each module, so the module can operate at its maximum power point while the thermal inspection is performed.

Regarding the methodology for analysis, it can be said that the results from Arica's campaign are standardized and they can be used to characterize PV modules. This is mainly due to the structure of the inspection survey that facilitates the development of a small database to treat the gathered data for statistical studies. In this context, the methodology for the analysis of the results gives, as it can be seen in the analysis section of this work, treated-data that can be observed and studied by tendencies. Such tendencies are easily comprehended by statistic parameters. Thus, it was possible to make conclusions and recommendations based in the analysis. However, like it was point out in the discussion section of this work, due to the lack number of PV modules inspected, the phenomena found in the campaign cannot be generalized by the lack of robust statistical significance. However, a set of data with robust statistical significance is made by inspecting more and more PV modules. Thus, increasing this initial small database.

In relation to the case study, this was carried out in Arica and Parinacota Region. Most of the inspected locations were from the Arica's commune. The 15 locations that were visited were separated into 4 zones for proper study. Zone A was the coastal region (with 2 locations), zone B was the city center region (with 5 locations), zone C was the valley region (with 7 locations) and zone D was the desert region (with 1 location). Considering the whole campaign, 95 PV modules were inspected in total. From the 95 PV modules, 30 were from SOLAR WORLD, 12 from ET TOWARDS EXCELLENCE, 6 from SIEMENS, 1 from BP SOLAR, 6 from LUXOR, 3 from JA SOLAR, 24 from RISEN, 9 from SUNEL and 4 from HANWHA SOLAR. Among all the inspected modules, the ones with longer exposures in the field were the ones installed in 2005 (13 years of operation) and the ones with shorter exposures were installed in 2016 (2 years of operation).

According to the campaign's results, frame-less PV modules or with rear-glass were not inspected. All the inspected modules had front glass, rear-polymeric backsheet and aluminum frame. Considering the 18 failures modes reviewed in the state-of-the-art, the total inspected universe (95 PV modules and 15 locations) did not show any failure or defect in their wires, connectors or solar cells. The solar cells in particular were not found to have any visual defect, but this does not mean that cells were not cracked. Only severe cracks can be detected with the naked eye. For micro-crack of solar cells inspection, EL imaging is necessary.

Soiling in the glass was the most common visual failure with 52 cases of slight soiling and 39 cases of heavy soiling. The following visual defects that appeared the most were minor corrosion of the frame grounding (18 cases) and weathered/corroded frame (12 cases). Among the visual failures that appeared the least, the most interesting were: yellowing of the

inner layer of the backsheet (8 cases), weathered junction box (7 cases), milky discoloration of the glass (6 cases) and delamination of the EVA-encapsulant (4 cases).

Regarding the degradation of the electrical parameters, most degraded parameters were: (a) the maximum power with a maximum drop of 39.08% and a average drop of 13.19±6.22% and (b) the short-circuit current with a maximum drop of 22.84% and an average drop of 8.80±5.71%. When data is sorted by the largest to the smallest drop value, it appears that the degradation of P_{mpp} is strongly related with the degradation of I_{sc}. Likewise, the current degradation seems to be highly related to soiling among the all possible failures. With regards to the fill factor, its maximum drop (34.35%) is even larger than the short-circuit current drop. However, the average drop of the fill factor is almost half (4.53±5.44%) compared with the average drop of the current. The least affected parameters corresponds to the open-circuit voltage which has a maximum degradation drop of 11.25% with an average drop of 3.19±2.24%. It seems that the degradation of the FF and the V_{oc} is strongly related to PID. This cannot be concluded in general, because only two PV modules are found to suffer from PID.

In relation to temperature operation of the modules and their ambient temperatures, the largest temperature difference found was 24.45°C with an average difference of 11.67°C. There also seems to be a relation between the modules that operate with higher temperature with respect to their ambient temperature and the modules with hottest cells. The hottest cell from the whole inspected universe was found to be operating around the 99.4°C, while in average the hottest cells were operating at 64.0°C. Regarding the thermal abnormalities of the inspected modules, 68 of them showed a patchwork pattern. Since the thermal inspection was performed with modules under short-circuit condition, modules with patchwork pattern are not faulty. Among the remaining modules, 2 modules showed a PID pattern and 12 modules showed severely homogeneous hot cells. Only 3 modules presented pointing heating due to bird dropping, but the temperature difference was always below 10°C. Hence, modules with pointing heating were not considered to have hot-spots by definition. Finally, 6 modules had undetermined thermal pattern because it was not possible to distinguish between PID or patchwork pattern. However, electrical parameters of the modules suggested patchwork over PID.

Finally, recommendations based on the analysis of the results from the campaign were done. Such recommendations were linked to the state of the PV module according to the analysis in combination with current practices of operation and maintenance that were informed by the owners of the visited locations. Also, site conditions were also taken into account in the recommendations. As stated in the above paragraphs, recommendations with robust statistical significance is possible by using the IDCTool and the analysis methodology for a minimum amount of PV modules.

7.2 Recommendations for Future Work

The tool developed in this research can be improved in several parts. Changes in the procedure for field testing and the equipment can be made. The following suggestions are based

on specific problems that the responsible of the campaign underwent while performing its tasks.

- *PV module selection criteria and small scale application*: the IDCTool is thought for small scale applications, thus, all PV modules installed should be inspected if possible. According to the selection criteria if the latter is not possible, the selection comes from a quickly visual inspection of the entire PV system. In the other hand, it was shown, in this research, that visual inspection by itself is not a good tool to search for probable failures of PV modules. It is, therefore, not efficient use visual inspection as a selection criteria. In this context, it would be best to use a drone with a thermal camera (UAV). Since the purpose of the UAV is to select PV modules that will be further inspected, is not necessary to have an extremely high resolution. Also, it must be taken into account the autonomy of the UAV (battery charge/discharge time) and the costs.

- *Field testing procedure*: it is highly recommended to take thermal pictures when PV modules are operating in their maximum power point than when they are short-circuited. In this context, it is even better if the thermal pictures are taken when the module is operating in their "real environment". Real environment refers to a PV module connected to its neighbors and to its respective load (such as a water pump). In this context, it is best to change part of the procedure for field testing that is given in this research. After the PV modules are chosen for the inspection (e.g. with a drone), it is best to make the visual inspection and the thermal inspection of the selected modules while the system is operating in its normal conditions (e.g. feeding the public grid or a particular water pump). Once both inspection are done, the inverter must be shut down and the DC generator must be mechanically and electrically isolated. The next inspection should be the measurement of the I-V curve with the module disconnected from its neighbors. This changes must be evaluated because the thermal and electrical inspection would be done with a higher interval, in which the environmental conditions can change. However, this recommendation is not the only one that can be implemented. Another option is the use of a variable resistive load to be able to connect a load to a single PV module. The advantages of this option, with respect to the previous one, are mainly two:

  1. A single PV module can be operated at short-circuit, open-circuit and maximum power condition and for each condition a thermal-image can be taken.

  2. For a PV module under inspection, the thermal an electrical inspection can be taken one after the other with no interval in between. Hence, environmental conditions would be very similar.

  Both proposed changes must be assessed in terms of increase of time for field testing and of amount of thermal-image for later post-processing and analysis.

- *Ambient and module temperature*: it was explained that in this research the ambient temperature was measured for each PV module under study with the I-V tracer. With this procedure, the ambient temperature for a location was measured by a small amount of data points (depending on the number of inspected PV modules) with a high interval in between. For example, for a small PV plant of 15 kW, 16 PV modules were

inspected from 9:00 AM to 4:00 PM. Then, if the ambient temperature for the location is calculated, the value is an average of the 7 hours using 16 data points. In this context, it would be best to measure the temperature of the location continuously while several modules are inspected. Regarding the module temperature, the I-V tracer from Seaward obtains the module operating temperature with only one sensor at the back of the PV module. In this context, an evaluation (or study) must be carried out to evaluate the precision of such method.

- *Standardized images*: to improve the quality and standardization of (visual or thermal) images taken during the inspection, it would be best to develop a structure to support the cameras (at least the thermal camera) as orthogonal and close as possible to the surface of the PV module under inspection. The distance must be calculated so the whole PV module is capture. This structure should be lightweight for transportation and be fold-able for storage.

- *Details of the survey*: an assessment or study must be carried out to determine the increase in time in filling the survey if the following details are added:

  1. Location characteristics: presence of vegetation, type of soil, among others.

  2. PV structure: topology, total number of PV modules, unique or several manufacturers of PV modules, type of rack (mounted at ground level, mounted and elevated, roof, ballasted, etc.), among others.

  3. Operation and maintenance: mode of use, frequency of use, mode of maintenance and frequency of maintenance.

  These parameters are expected to provide more insights to understand the origin of the failures of the PV modules and how these failures are related to the environmental conditions and their operation and maintenance.

- *Wind*: make an study/assessment of the advantages of including the measurement of the velocity and the direction of the wind. This can give more insights to understand the operating temperature of the PV modules.

- *Position of PV module*: research the advantages and disadvantages of including the information regarding to the geometrical position of an inspected PV module respect to its neighbors and the direction of the wind to have a better understanding of the heat dissipation and its operating temperature. Evaluation must consider the increase in time for field inspection.

- *IDCTool for large scale*: it is possible to extend this research work for testing in large PV plants. In this context, time must be evaluated because this tool is thought to be for small scale application with exhaustive inspection. This comes from the objectives of this research work, because information resulted from the analysis is used as input for criteria of technology selection and for development of standards. Operation and maintenance contractors for PV plants have their own monitoring system, which is installed for preventive and corrective maintenance in the plant. The objectives for

large PV asset is to maintain a certain performance for the return of investment. In this context, a PV module with large degradation is simply replaced. Therefore, the IDCTool may be a good tool to complement the work of an O&M team, but not to replace it.

Bibliography

[1] R. R. Cordero et al. "Ultraviolet radiation in the Atacama Desert". In: *Antonie van Leeuwenhoek* (Mar. 2018). DOI: 10.1007/s10482-018-1075-z. URL: https://doi.org/10.1007%2Fs10482-018-1075-z.

[2] Marc Köntges. *Assessment of Photovoltaic Module Failures in the Field*. Sankt Ursen: International Energy Agency, Photovoltaic Power Systems Programme, 2017. ISBN: 978-3-906042-54-1.

[3] Daniel Inns. *Research and product development at DuPont Photovoltaic Solutions*. Accessed June 11, -2. 2016. URL: http://www2.pv.unsw.edu.au/videos/daniel-inns-11march2016/slides/Daniel-Inns-UNSW-2016_03.pdf.

[4] Harry Wirth. "Crystalline Silicon PV Module Technology". In: *Semiconductors and Semimetals*. Elsevier, 2013, pp. 135–197. DOI: 10.1016/b978-0-12-381343-5.00003-3. URL: https://doi.org/10.1016/b978-0-12-381343-5.00003-3.

[5] ISE Fraunhofer Institute for Solar Energy Systems. *PHOTOVOLTAICS REPORT*. Accessed June 11, -2. 2017. URL: https://www.ise.fraunhofer.de/content/dam/ise/de/documents/publications/studies/Photovoltaics-Report.pdf.

[6] Konrad Mertens. *Photovoltaics: Fundamentals, Technology and Practice*. Wiley, 2013. ISBN: 9781118634165. URL: http://a.co/dXmMBpa.

[7] Subash Mahajan. *Principles of Growth and Processing of Semiconductors*. McGraw-Hill Science/Engineering/Math, 1998. ISBN: 0070396051. URL: http://a.co/ecYSCAX.

[8] Antonio Luque (Editor) and Steven Hegedus (Editor). *Handbook of Photovoltaic Science and Engineering*. Wiley, 2003. ISBN: 0471491969. URL: http://a.co/aQkOQ2R.

[9] Francesca Ferrazza. "Crystalline Silicon". In: *Solar Cells*. Elsevier, 2013, pp. 69–86. DOI: 10.1016/b978-0-12-386964-7.00004-4. URL: https://doi.org/10.1016/b978-0-12-386964-7.00004-4.

[10] Shaoqing Xiao and Shuyan Xu. "High-Efficiency Silicon Solar Cells—Materials and Devices Physics". In: *Critical Reviews in Solid State and Materials Sciences* 39.4 (Apr. 2014), pp. 277–317. DOI: 10.1080/10408436.2013.834245. URL: http://dx.doi.org/10.1080/10408436.2013.834245.

[11] Corsin Battaglia, Andres Cuevas, and Stefaan De Wolf. "High-efficiency crystalline silicon solar cells: status and perspectives". In: *Energy Environ. Sci.* 9.5 (2016), pp. 1552–1576. DOI: 10.1039/c5ee03380b. URL: https://doi.org/10.1039%2Fc5ee03380b.

[12] D. Yogi Goswami. *Principles of Solar Engineering, Third Edition*. CRC Press, 2015. ISBN: 9781466563797. URL: http://a.co/hQ0EJ0M.

[13] Jürgen Werner. *Photovoltaik I*. URL: http://www.ipv.uni-stuttgart.de/.

[14] Dirk-Holger Neuhaus and Adolf Münzer. "Industrial Silicon Wafer Solar Cells". In: *Advances in OptoElectronics* 2007 (2007), pp. 1–15. DOI: 10.1155/2007/24521. URL: https://doi.org/10.1155%2F2007%2F24521.

[15] Musa T. Zarmai et al. "A review of interconnection technologies for improved crystalline silicon solar cell photovoltaic module assembly". In: *Applied Energy* 154 (Sept. 2015), pp. 173–182. DOI: 10.1016/j.apenergy.2015.04.120. URL: https://doi.org/10.1016/j.apenergy.2015.04.120.

[16] Musa Tanko Zarmai. "Modelling of Solder Interconnection's Performance in Photovoltaic Modules for Reliability Prediction". Accessed June 11, -2. PhD thesis. University of Wolverhampton, Feb. 2016. URL: https://wlv.openrepository.com/wlv/bitstream/2436/617782/1/Zarmai_PhD+Thesis.pdf.

[17] Corinne E. Packard, John H. Wohlgemuth, and Sarah R. Kurtz. *Development of a Visual Inspection Data Collection Tool for Evaluation of Fielded PV Module Condition*. Tech. rep. National Renewable Energy Laboratory 15013 Denver West Parkway Golden, Colorado 80401: NREL National Renewable Energy Laboratory, Aug. 2012.

[18] Shan Jiang et al. "Encapsulation of PV Modules Using Ethylene Vinyl Acetate Copolymer as the Encapsulant". In: *Macromolecular Reaction Engineering* 9.5 (Mar. 2015), pp. 522–529. DOI: 10.1002/mren.201400065. URL: https://doi.org/10.1002/mren.201400065.

[19] Ulf Blieske and Gunther Stollwerck. "Glass and Other Encapsulation Materials". In: *Semiconductors and Semimetals*. Elsevier, 2013, pp. 199–258. DOI: 10.1016/b978-0-12-381343-5.00004-5. URL: https://doi.org/10.1016/b978-0-12-381343-5.00004-5.

[20] A. El Amrani et al. "Solar Module Fabrication". In: *International Journal of Photoenergy* 2007 (2007), pp. 1–5. DOI: 10.1155/2007/27610. URL: https://doi.org/10.1155/2007/27610.

[21] DuPont. *DuPont™Tedlar®PVF Based Backsheets – Performance comparison vis-avis PVDF and PET based backsheets*. Accessed June 11, -2. 2016. URL: https://www.sunfueltechnology.com/wp-content/uploads/2017/02/TedlarR-based-backsheets-SunFuel.pdf.

[22] Günther Nölle. *Technik der Glasherstellung (German Edition)*. Wiley-VCH, 2009. ISBN: 3527309411. URL: http://a.co/cBlVL5L.

[23] Eric J. Schneller et al. "Manufacturing metrology for c-Si module reliability and durability Part III: Module manufacturing". In: *Renewable and Sustainable Energy Reviews* 59 (June 2016), pp. 992–1016. DOI: 10.1016/j.rser.2015.12.215. URL: https://doi.org/10.1016/j.rser.2015.12.215.

[24] Michelle Poliskie. *Solar Module Packaging: Polymeric Requirements and Selection*. CRC Press, 2016. ISBN: 9781439850749. URL: http://a.co/fhXIyx1.

[25] FABRICO™. *Acrylic Foam Tape Enhances Edge & Junction Box Seals in Solar Panel Manufacturing*. Accessed June 11, -2. URL: http://www.fabrico.com/sites/default/files/Import_6/Import/BJS_Application_Sheet_Acrylic_Foam_Tape.pdf.

[26] Dow Corning. *PV Junction Box Potting Agents, Bonding and Sealing*. Dow Corning Corporation. Dow Corning Corporation. Corporate Center. 2200 W. Salzburg Rd. PO Box 994 Auburn MI 48611.

[27] Joseph M. Kuitche, Rong Pan, and GovindaSamy TamizhMani. "Investigation of Dominant Failure Mode(s) for Field-Aged Crystalline Silicon PV Modules Under Desert Climatic Conditions". In: *IEEE Journal of Photovoltaics* 4.3 (May 2014), pp. 814–826. DOI: 10.1109/jphotov.2014.2308720. URL: https://doi.org/10.1109/jphotov.2014.2308720.

[28] David Berman, Sergey Biryukov, and David Faiman. "EVA laminate browning after 5 years in a grid-connected, mirror-assisted, photovoltaic system in the Negev desert: effect on module efficiency". In: *Solar Energy Materials and Solar Cells* 36.4 (Apr. 1995), pp. 421–432. DOI: 10.1016/0927-0248(94)00198-7. URL: https://doi.org/10.1016/0927-0248(94)00198-7.

[29] Sanjay Mohan Shrestha et al. "Determination of Dominant Failure Modes Using FMECA on the Field Deployed c-Si Modules Under Hot-Dry Desert Climate". In: *IEEE Journal of Photovoltaics* 5.1 (Jan. 2015), pp. 174–182. DOI: 10.1109/jphotov.2014.2366872. URL: https://doi.org/10.1109/jphotov.2014.2366872.

[30] Karan Rao Yedidi. "Failure and Degradation Modes of PV modules in a Hot Dry Climate: Results after 16 years of field exposure". MA thesis. ARIZONA STATE UNIVERSITY, Dec. 2013.

[31] Jaya Krishna Mallineni. "Failure and Degradation Modes of PV modules in a Hot Dry Climate: Results after 4 and 12 years of field exposure". MA thesis. ARIZONA STATE UNIVERSITY, Dec. 2013.

[32] Adam Alfred Suleske. "Performance Degradation of Grid-Tied Photovoltaic Modules in a Desert Climatic Condition". MA thesis. ARIZONA STATE UNIVERSITY, Dec. 2010.

[33] Jaspreet Singh, Jonathan Belmont, and GovindaSamy TamizhMani. "Degradation analysis of 1900 PV modules in a hot-dry climate: Results after 12 to 18 years of field exposure". In: *2013 IEEE 39th Photovoltaic Specialists Conference (PVSC)*. IEEE, June 2013. DOI: 10.1109/pvsc.2013.6745149. URL: https://doi.org/10.1109/pvsc.2013.6745149.

[34] Alberto Dolara et al. "Investigation on Performance Decay on Photovoltaic Modules: Snail Trails and Cell Microcracks". In: *IEEE Journal of Photovoltaics* 4.5 (Sept. 2014), pp. 1204–1211. DOI: 10.1109/jphotov.2014.2330495. URL: https://doi.org/10.1109/jphotov.2014.2330495.

[35] Sadok Mohammed, Benyoucef Boumediene, and Benmedjahed Miloud. "Assessment of PV Modules Degradation based on Performances and Visual Inspection in Algerian

Sahara". In: *International Journal of Renewable Energy Research-IJRER* 6.1 (Jan. 2016), pp. 106–116.

[36] Jing Fan. *Snail Trail Formation Mechanism: Modeling and Accelerated Aging Tests*. Accessed June 11, -2. 2016. URL: http://www.dupont.cn/content/dam/dupont/products-and-services/solar-photovoltaic-materials/solar-photovoltaic-materials-landing/documents/2016-snec-study-on-snail-trail-formation-jing-fan-dupont.pdf.

[37] M. Köntges et al. *Snail tracks (Schneckenspuren), worm marks and cell cracks*. Accessed June 11, -2. 2012. URL: http://iea-pvps.org/index.php?id=223&eID=dam_frontend_push&docID=1272.

[38] Ines Duerr et al. "Silver Grid Finger Corrosion on Snail Track affected PV Modules – Investigation on Degradation Products and Mechanisms". In: *Energy Procedia* 98 (Nov. 2016), pp. 74–85. DOI: 10.1016/j.egypro.2016.10.083. URL: https://doi.org/10.1016/j.egypro.2016.10.083.

[39] Rajiv Dubey et al. *All-India Survey of Photovoltaic Module Reliability: 2014*. Tech. rep. National Centre for Photovoltaic Research and Education (NCPRE), IIT Bombay & National Institute of Solar Energy (NISE), Gurgaon, Mar. 2016.

[40] Sylke Meyer et al. "Snail Trails: Root Cause Analysis and Test Procedures". In: *Energy Procedia* 38 (2013), pp. 498–505. DOI: 10.1016/j.egypro.2013.07.309. URL: https://doi.org/10.1016/j.egypro.2013.07.309.

[41] S. Meyer et al. "Silver nanoparticles cause snail trails in photovoltaic modules". In: *Solar Energy Materials and Solar Cells* 121 (Feb. 2014), pp. 171–175. DOI: 10.1016/j.solmat.2013.11.013. URL: https://doi.org/10.1016/j.solmat.2013.11.013.

[42] Peng Peng et al. "Microscopy study of snail trail phenomenon on photovoltaic modules". In: *RSC Advances* 2.30 (2012), p. 11359. DOI: 10.1039/c2ra22280a. URL: https://doi.org/10.1039/c2ra22280a.

[43] S. Meyer et al. "Polymer foil additives trigger the formation of snail trails in photovoltaic modules". In: *Solar Energy Materials and Solar Cells* 130 (Nov. 2014), pp. 64–70. DOI: 10.1016/j.solmat.2014.06.028. URL: https://doi.org/10.1016/j.solmat.2014.06.028.

[44] Han-Chang Liu et al. "A Defect Formation as Snail Trails in Photovoltaic Modules". In: *Energy and Power Engineering* 07.08 (2015), pp. 348–353. DOI: 10.4236/epe.2015.78032. URL: https://doi.org/10.4236/epe.2015.78032.

[45] S. Richter et al. "Understanding the Snail Trail Effect in Silicon Solar Modules on Microstructural Scale". eng. In: *27th European Photovoltaic Solar Energy Conference and Exhibition*. WIP, 2012. DOI: 10.4229/27theupvsec2012-4bv.3.7. URL: http://www.eupvsec-proceedings.com/proceedings?paper=21086.

[46] Sarah Kajari-Schroder et al. "Spatial and directional distribution of cracks in silicon PV modules after uniform mechanical loads". In: *2011 37th IEEE Photovoltaic Specialists Conference*. IEEE, June 2011. DOI: 10.1109/pvsc.2011.6186082. URL: https://doi.org/10.1109/pvsc.2011.6186082.

[47] J. Wendt et al. "The Link between Mechanical Stress Induced by Soldering and Micro Damages in Silicon Solar Cells". eng. In: *24th European Photovoltaic Solar Energy Conference*. WIP-Munich, 2009. DOI: 10.4229/24theupvsec2009-4av.3.40. URL: http://www.eupvsec-proceedings.com/proceedings?paper=4723.

[48] M. Sander et al. "Investigations on crack development and crack growth in embedded solar cells". In: *Reliability of Photovoltaic Cells, Modules, Components, and Systems IV*. Ed. by Neelkanth G. Dhere, John H. Wohlgemuth, and Kevin W. Lynn. SPIE, Sept. 2011. DOI: 10.1117/12.893662. URL: https://doi.org/10.1117/12.893662.

[49] Tonio Buonassisi. *Fundamentals of Photovoltaics. 2.627/2.626*. Massachusetts Institute of Technology: MIT OpenCourseWare. Oct. 2013. URL: https://ocw.mit.edu. License: Creative Commons BY-NC-SA.

[50] R. Sarjila et al. "Parameter Extraction of Solar Photovoltaic Modules Using Gravitational Search Algorithm". In: *Journal of Electrical and Computer Engineering* 2016 (2016), pp. 1–6. DOI: 10.1155/2016/2143572. URL: https://doi.org/10.1155/2016/2143572.

[51] Afshin Izadian, Arash Pourtaherian, and Sarasadat Motahari. "Basic model and governing equation of solar cells used in power and control applications". In: *2012 IEEE Energy Conversion Congress and Exposition (ECCE)*. IEEE, Sept. 2012. DOI: 10.1109/ecce.2012.6342639. URL: https://doi.org/10.1109/ecce.2012.6342639.

[52] J.W. Bishop. "Computer simulation of the effects of electrical mismatches in photovoltaic cell interconnection circuits". In: *Solar Cells* 25.1 (Oct. 1988), pp. 73–89. DOI: 10.1016/0379-6787(88)90059-2. URL: https://doi.org/10.1016/0379-6787(88)90059-2.

[53] IEC. "Terrestrial photovoltaic (PV) modules - Design qualification and type of approval —Part 2: Test Procedures". In: 61215-2 (2016).

[54] Jong-Rok Lim et al. "Correlation between Reverse Voltage Characteristics and Bypass Diode Operation with Different Shading Conditions for c-Si Photovoltaic Module Package". In: *JSTS:Journal of Semiconductor Technology and Science* 15.5 (Oct. 2015), pp. 577–584. DOI: 10.5573/jsts.2015.15.5.577. URL: https://doi.org/10.5573/jsts.2015.15.5.577.

[55] O. Breitenstein et al. "Shunt types in crystalline silicon solar cells". In: *Progress in Photovoltaics: Research and Applications* 12.7 (2004), pp. 529–538. DOI: 10.1002/pip.544. URL: https://doi.org/10.1002/pip.544.

[56] Otwin Breitenstein, Wilhelm Warta, and Martin Langenkamp. *Lock-in Thermography: Basics and Use for Evaluating Electronic Devices and Materials*. Springer Berlin Heidelberg, 2010. DOI: 10.1007/978-3-642-02417-7. URL: https://doi.org/10.1007/978-3-642-02417-7.

[57] O. Breitenstein. "Understanding the current-voltage characteristics of industrial crystalline silicon solar cells by considering inhomogeneous current distributions". In: *Opto-Electronics Review* 21.3 (Jan. 2013). DOI: 10.2478/s11772-013-0095-5. URL: https://doi.org/10.2478/s11772-013-0095-5.

[58] Otwin Breitenstein et al. "Understanding junction breakdown in multicrystalline solar cells". In: *Journal of Applied Physics* 109.7 (Apr. 2011), p. 071101. DOI: 10.1063/1.3562200. URL: https://doi.org/10.1063/1.3562200.

[59] P. Somasundaran and R. Gupta. "Evaluation of Shunt Losses in Industrial Silicon Solar Cells". In: *International Journal of Photoenergy* 2016 (2016), pp. 1–9. DOI: 10.1155/2016/8029608. URL: https://doi.org/10.1155/2016/8029608.

[60] DuPont. *Mitigating Strategies for Hot Spots in Crystalline Silicon Solar Panels*. Accessed June 11, -2. 2015. URL: http://www.dupont.com/content/dam/dupont/products-and-services/solar-photovoltaic-materials/solar-photovoltaic-materials-landing/documents/DEC-Mitagating-Strategies-for-Hot-Spots.pdf.

[61] Sinisa Djordjevic, David Parlevliet, and Philip Jennings. "Detectable faults on recently installed solar modules in Western Australia". In: *Renewable Energy* 67 (July 2014), pp. 215–221. DOI: 10.1016/j.renene.2013.11.036. URL: https://doi.org/10.1016/j.renene.2013.11.036.

[62] IEC. "Photovoltaic (PV) Systems –Requirements for testing, documentation and maintenance —Part 1: Grid connected systems –Documentation, commissioning tests and inspection". In: 62446-3 (2016).

[63] Jae-Seong Jeong, Nochang Park, and Changwoon Han. "Field failure mechanism study of solder interconnection for crystalline silicon photovoltaic module". In: *Microelectronics Reliability* 52.9-10 (Sept. 2012), pp. 2326–2330. DOI: 10.1016/j.microrel.2012.06.027. URL: https://doi.org/10.1016/j.microrel.2012.06.027.

[64] Marc Köntges. *Performance and reliability of photovoltaic systems subtask 3.2: Review of failures of photovoltaic modules : IEA PVPS task 13 : external final report IEA-PVPS*. Sankt Ursen: International Energy Agency, Photovoltaic Power Systems Programme, 2014. ISBN: 978-3-906042-16-9.

[65] F. Kraemer et al. "Mechanical stress analysis in photovoltaic cells during the string-ribbon interconnection process". In: *2014 15th International Conference on Thermal, Mechanical and Mulit-Physics Simulation and Experiments in Microelectronics and Microsystems (EuroSimE)*. IEEE, Apr. 2014. DOI: 10.1109/eurosime.2014.6813853. URL: https://doi.org/10.1109/eurosime.2014.6813853.

[66] Uichi Itoh et al. "Solder Joint Failure Modes in the Conventional Crystalline Si Module". In: *Energy Procedia* 55 (2014), pp. 464–468. DOI: 10.1016/j.egypro.2014.08.010. URL: https://doi.org/10.1016/j.egypro.2014.08.010.

[67] Joseph M. Kuitche, Govindasamy Tamizh-Mani, and Rong Pan. "Failure modes effects and criticality analysis (FMECA) approach to the crystalline silicon photovoltaic module reliability assessment". In: *Reliability of Photovoltaic Cells, Modules, Components, and Systems IV*. Ed. by Neelkanth G. Dhere, John H. Wohlgemuth, and Kevin W. Lynn. SPIE, Sept. 2011. DOI: 10.1117/12.894301. URL: https://doi.org/10.1117/12.894301.

[68] Jason Strauch et al. *PV Module Arc Fault Modeling and Analysis*. NREL Photovoltaic Module Reliability Workshop 2011. Accessed June 11, -2. 2011. URL: https://www.nrel.gov/docs/fy14osti/60170.pdf.

[69] O.S. Sastry et al. "Performance analysis of field exposed single crystalline silicon modules". In: *Solar Energy Materials and Solar Cells* 94.9 (Sept. 2010), pp. 1463–1468. DOI: 10.1016/j.solmat.2010.03.035. URL: https://doi.org/10.1016/j.solmat.2010.03.035.

[70] Lawrence Dunn, Michael Gostein, and Bill Stueve. *Literature Review of the Effects of UV Exposure on PV Modules*. NREL Photovoltaic Module Reliability Workshop 2013. Accessed June 11, -2. 2013. URL: https://www.nrel.gov/docs/fy14osti/60167.pdf.

[71] F. J. Pern and A. W. Czanderna. "EVA degradation mechanisms simulating those in PV modules". In: *AIP Conference Proceedings*. AIP, 1992. DOI: 10.1063/1.42901. URL: https://doi.org/10.1063/1.42901.

[72] A.W. Czanderna and F.J. Pern. "Encapsulation of PV modules using ethylene vinyl acetate copolymer as a pottant: A critical review". In: *Solar Energy Materials and Solar Cells* 43.2 (Sept. 1996), pp. 101–181. DOI: 10.1016/0927-0248(95)00150-6. URL: https://doi.org/10.1016/0927-0248(95)00150-6.

[73] F. J. Pern. "Ethylene-vinyl acetate (EVA) encapsulants for photovoltaic modules: degradation and discoloration mechanisms and formulation modifications for improved photostability". In: *Angewandte Makromolekulare Chemie* 252.1 (Dec. 1997), pp. 195–216. DOI: 10.1002/apmc.1997.052520114. URL: https://doi.org/10.1002/apmc.1997.052520114.

[74] Tsuyoshi Shioda. *Delamination failures in long-term field-aged PV modules from point of view of encapsulant*. Accessed June 11, -2. 2013. URL: https://energy.gov/sites/prod/files/2014/01/f7/pvmrw13_openingsession_shioda_mitsui.pdf.

[75] John Wohlgemuth. *Use of Field Observations to Assess PV Module Reliability*. 3rd Atlas/NIST Workshop on PV Materials Durability. Accessed June 11, -2. 2015. URL: https://www.nist.gov/sites/default/files/documents/el/building_materials/Use-of-Field-Observations-to-Assess-PV-Module-Reliability-John-Wohlgemuth.pdf.

[76] Fernando D. Novoa, David C. Miller, and Reinhold H. Dauskardt. "Adhesion and debonding kinetics of photovoltaic encapsulation in moist environments". In: *Progress in Photovoltaics: Research and Applications* 24.2 (July 2015), pp. 183–194. DOI: 10.1002/pip.2657. URL: https://doi.org/10.1002/pip.2657.

[77] Ahmed Bouraiou et al. "Experimental evaluation of the performance and degradation of single crystalline silicon photovoltaic modules in the Saharan environment". In: *Energy* 132 (Aug. 2017), pp. 22–30. DOI: 10.1016/j.energy.2017.05.056. URL: https://doi.org/10.1016/j.energy.2017.05.056.

[78] Reinhold Dauskardt. *Thermo-Mechanical Degradation Mechanisms Relevant for Field Failures and Solar Lifetimes*. Accessed June 11, -2. 2016. URL: https://www.nist.gov/sites/default/files/documents/el/building_materials/Thermo-Mechanical-

Degradation-Mechanisms-Relevant-for-field-Failures-and-Solar-Lifetimes-Reinhold-Dauskardt.pdf.

[79] G. Dhere and B. Pandit. "STUDY OF DELAMINATION IN ACCELERATION TESTED PV MODULES". In: *17th European Photovoltaic Solar Energy Conference, Munich, Germany*. Florida Solar Energy Center /University of CEntral Florida, Oct. 2001, pp. 572–575.

[80] Eduardo Lorenzo et al. "Performance analysis of a 7-kW crystalline silicon generator after 17 years of operation in Madrid". In: *Progress in Photovoltaics: Research and Applications* (May 2013), n/a–n/a. DOI: 10.1002/pip.2379. URL: https://doi.org/10.1002%2Fpip.2379.

[81] G. Oreski and G.M. Wallner. "Aging mechanisms of polymeric films for PV encapsulation". In: *Solar Energy* 79.6 (Dec. 2005), pp. 612–617. DOI: 10.1016/j.solener.2005.02.008. URL: https://doi.org/10.1016/j.solener.2005.02.008.

[82] Fernando D. Novoa, David C. Miller, and Reinhold H. Dauskardt. "Environmental mechanisms of debonding in photovoltaic backsheets". In: *Solar Energy Materials and Solar Cells* 120 (Jan. 2014), pp. 87–93. DOI: 10.1016/j.solmat.2013.08.020. URL: https://doi.org/10.1016/j.solmat.2013.08.020.

[83] Chiao-Chi Lin et al. "Depth profiling of degradation of multilayer photovoltaic backsheets after accelerated laboratory weathering: Cross-sectional Raman imaging". In: *Solar Energy Materials and Solar Cells* 144 (2016), pp. 289–299. ISSN: 0927-0248. DOI: https://doi.org/10.1016/j.solmat.2015.09.021. URL: http://www.sciencedirect.com/science/article/pii/S0927024815004547.

[84] Namsu Kim et al. "Study on the degradation of different types of backsheets used in PV module under accelerated conditions". In: *Solar Energy Materials and Solar Cells* 120.Part B (2014), pp. 543–548. ISSN: 0927-0248. DOI: https://doi.org/10.1016/j.solmat.2013.09.036. URL: http://www.sciencedirect.com/science/article/pii/S092702481300514X.

[85] G ORESKI and G WALLNER. "Delamination behaviour of multi-layer films for PV encapsulation". In: *Solar Energy Materials and Solar Cells* 89.2-3 (Nov. 2005), pp. 139–151. DOI: 10.1016/j.solmat.2005.02.009. URL: https://doi.org/10.1016/j.solmat.2005.02.009.

[86] Ethan Wang et al. "Failure Modes Evaluation of PV Module via Materials Degradation Approach". In: *Energy Procedia* 33 (2013), pp. 256–264. DOI: 10.1016/j.egypro.2013.05.066. URL: https://doi.org/10.1016/j.egypro.2013.05.066.

[87] Ababacar Ndiaye et al. "Degradations of silicon photovoltaic modules: A literature review". In: *Solar Energy* 96 (Oct. 2013), pp. 140–151. DOI: 10.1016/j.solener.2013.07.005. URL: https://doi.org/10.1016/j.solener.2013.07.005.

[88] Hongjie Hu et al. *Typical Photovoltaic Backsheet Failure Mode Analysis under Different Climates in China*. 10th SNEC PV POWER EXPO. Accessed June 11, -2. 2016. URL: http://www.dupont.com/content/dam/dupont/products-and-services/solar-photovoltaic-materials/solar-photovoltaic-materials-

landing/documents/Typical-PV-Backsheet-Failure-Mode-Analysis-under-Different-Climates-in-China-DuPont.pdf.

[89] W. Gambogi et al. "Weathering and durability of PV backsheets and impact on PV module performance". In: *Reliability of Photovoltaic Cells, Modules, Components, and Systems VI*. Ed. by Neelkanth G. Dhere, John H. Wohlgemuth, and Kevin W. Lynn. SPIE, Sept. 2013. DOI: 10.1117/12.2024491. URL: https://doi.org/10.1117%2F12.2024491.

[90] W. Gambogi et al. "A Comparison of Key PV Backsheet and Module Performance from Fielded Module Exposures and Accelerated Tests". In: *IEEE Journal of Photovoltaics* 4.3 (May 2014), pp. 935–941. DOI: 10.1109/jphotov.2014.2305472. URL: https://doi.org/10.1109/jphotov.2014.2305472.

[91] Gregoria Illya et al. "Backsheet Degradation under Salt Damp Heat Environments - Enabling Novel and Innovative Solar Photovoltaic Systems Design for Tropical Regions and Sea Close Areas". In: *Procedia Engineering* 139 (2016), pp. 7–14. DOI: 10.1016/j.proeng.2015.09.233. URL: https://doi.org/10.1016/j.proeng.2015.09.233.

[92] Fei Liu, Long Jiang, and Shuying Yang. "Ultra-violet degradation behavior of polymeric backsheets for photovoltaic modules". In: *Solar Energy* 108 (Oct. 2014), pp. 88–100. DOI: 10.1016/j.solener.2014.06.027. URL: https://doi.org/10.1016%2Fj.solener.2014.06.027.

[93] Andreas Schneider. *An overview on crystalline silicon solar cell module defects*. Accessed June 11, -2. 2015. URL: http://sercchile.cl/wp-content/uploads/2015/03/2.4-ANDREAS-SCHNEIDER-bifi-PSDA-Antofagasta-Chile-2015.pdf.

[94] Chris Barry. *Why Glass Sometimes Breaks*. NREL Photovoltaic Module Reliability Workshop 2010. Accessed June 11, -2. 2010. URL: https://www.nrel.gov/docs/fy14osti/60171.pdf.

[95] James Webb and James Hamilton. *Physical Properties of Glass and the Requirements for Photovoltaic Modules*. NREL Photovoltaic Module Reliability Workshop 2011. Accessed June 11, -2. 2011. URL: https://www.nrel.gov/docs/fy14osti/60170.pdf.

[96] David DeGraaff et al. *Degradation Mechanisms in Si Module Technologies Observed in the Field; Their Analysis and Statistics*. NREL 2011 Photovoltaic Module Reliability Workshop Golden, Colorado. Accessed June 11, -2. 2011. URL: https://www.irishellas.com/files/Degradation-Mechanisms-in-Si-Module.pdf.

[97] Christopher R. Cording. "Optimizing photovoltaic module glass reliability". In: *Reliability of Photovoltaic Cells, Modules, Components, and Systems*. Ed. by Neelkanth G. Dhere. SPIE, Aug. 2008. DOI: 10.1117/12.795120. URL: https://doi.org/10.1117/12.795120.

[98] Lawrence L. Kazmerski et al. "Fundamental Studies of Adhesion of Dust to PV Module Surfaces: Chemical and Physical Relationships at the Microscale". In: *IEEE Journal of Photovoltaics* 6.3 (May 2016), pp. 719–729. DOI: 10.1109/jphotov.2016.2528409. URL: https://doi.org/10.1109%2Fjphotov.2016.2528409.

[99] Claudio Ferrara and Daniel Philipp. "Why Do PV Modules Fail?" In: *Energy Procedia* 15 (2012), pp. 379–387. DOI: 10.1016/j.egypro.2012.02.046. URL: https://doi.org/10.1016/j.egypro.2012.02.046.

[100] Paula Sánchez-Friera et al. "Analysis of degradation mechanisms of crystalline silicon PV modules after 12 years of operation in Southern Europe". In: *Progress in Photovoltaics: Research and Applications* 19.6 (Jan. 2011), pp. 658–666. DOI: 10.1002/pip.1083. URL: https://doi.org/10.1002/pip.1083.

[101] Syed A.M. Said and Husam M. Walwil. "Fundamental studies on dust fouling effects on PV module performance". In: *Solar Energy* 107 (Sept. 2014), pp. 328–337. DOI: 10.1016/j.solener.2014.05.048. URL: https://doi.org/10.1016%2Fj.solener.2014.05.048.

[102] Rajiv Dubey et al. *All-India Survey of Photovoltaic Module Degradation: 2013*. Tech. rep. National Centre for Photovoltaic Research and Education (NCPRE), IIT Bombay & Solar Energy Centre, Gurgaon, Mar. 2014.

[103] Elam A Leed and Carlo G Pantano. "Computer modeling of water adsorption on silica and silicate glass fracture surfaces". In: *Journal of Non-Crystalline Solids* 325.1-3 (Sept. 2003), pp. 48–60. DOI: 10.1016/s0022-3093(03)00361-2. URL: https://doi.org/10.1016/s0022-3093(03)00361-2.

[104] Ethan Wang et al. "Accelerated Aging Tests on PV Grounding Connections". In: *Energy Procedia* 12 (2011), pp. 578–585. DOI: 10.1016/j.egypro.2011.10.078. URL: https://doi.org/10.1016%2Fj.egypro.2011.10.078.

[105] D. Jordan and S. Kurtz. "3 - Photovoltaic module stability and reliability". In: *The Performance of Photovoltaic (PV) Systems*. Ed. by Nicola Pearsall. Woodhead Publishing, 2017, pp. 71–101. ISBN: 978-1-78242-336-2. DOI: https://doi.org/10.1016/B978-1-78242-336-2.00003-3. URL: http://www.sciencedirect.com/science/article/pii/B9781782423362000033.

[106] Davide Polverini et al. "Polycrystalline silicon PV modules performance and degradation over 20 years". In: *Progress in Photovoltaics: Research and Applications* (Apr. 2012), n/a–n/a. DOI: 10.1002/pip.2197. URL: http://dx.doi.org/10.1002/pip.2197.

[107] Pramod Rajput et al. "Degradation of mono-crystalline photovoltaic modules after 22 years of outdoor exposure in the composite climate of India". In: *Solar Energy* 135 (Oct. 2016), pp. 786–795. DOI: 10.1016/j.solener.2016.06.047. URL: https://doi.org/10.1016/j.solener.2016.06.047.

[108] M.A. Munoz et al. "Early degradation of silicon PV modules and guaranty conditions". In: *Solar Energy* 85.9 (Sept. 2011), pp. 2264–2274. DOI: 10.1016/j.solener.2011.06.011. URL: https://doi.org/10.1016/j.solener.2011.06.011.

[109] David C. Miller and John H. Wohlgemuth. "Examination of a junction-box adhesion test for use in photovoltaic module qualification". In: *Reliability of Photovoltaic Cells, Modules, Components, and Systems V*. Ed. by Neelkanth G. Dhere and John H. Wohlgemuth. SPIE, Oct. 2012. DOI: 10.1117/12.929793. URL: https://doi.org/10.1117/12.929793.

[110] John Wohlgemuth et al. *Failure Modes of Crystalline Si Modules*. NREL Photovoltaic Module Reliability Workshop 2010. Accessed June 11, -2. 2010. URL: https://www.nrel.gov/docs/fy14osti/60171.pdf.

[111] Claudia Buerhop et al. *ÜberprKüfung der QualitKät von Photovoltaik-Modulen mittels Infrarot-Aufnahmen*. Tech. rep. National Renewable Energy Laboratory 15013 Denver West Parkway Golden, Colorado 80401: ZAE Bayern e.V., Oct. 2007.

[112] Alessandra Colli. "Failure mode and effect analysis for photovoltaic systems". In: *Renewable and Sustainable Energy Reviews* 50 (Oct. 2015), pp. 804–809. DOI: 10.1016/j.rser.2015.05.056. URL: https://doi.org/10.1016%2Fj.rser.2015.05.056.

[113] Juris Kalejs. *Junction Box and Wiring Issues in Reliability*. NREL Photovoltaic Module Reliability Workshop 2012. Accessed June 11, -2. 2012. URL: https://www.nrel.gov/docs/fy14osti/60169.pdf.

[114] Wei Luo et al. "Potential-induced degradation in photovoltaic modules: a critical review". In: *Energy & Environmental Science* 10.1 (2017), pp. 43–68. DOI: 10.1039/c6ee02271e. URL: https://doi.org/10.1039/c6ee02271e.

[115] Volker Naumann, Dominik Lausch, and Christian Hagendorf. "Sodium Decoration of PID-s Crystal Defects after Corona Induced Degradation of Bare Silicon Solar Cells". In: *Energy Procedia* 77 (Aug. 2015), pp. 397–401. DOI: 10.1016/j.egypro.2015.07.055. URL: https://doi.org/10.1016/j.egypro.2015.07.055.

[116] Dominik Lausch et al. "Potential-Induced Degradation (PID): Introduction of a Novel Test Approach and Explanation of Increased Depletion Region Recombination". In: *IEEE Journal of Photovoltaics* 4.3 (May 2014), pp. 834–840. DOI: 10.1109/jphotov.2014.2300238. URL: https://doi.org/10.1109/jphotov.2014.2300238.

[117] Volker Naumann et al. "Explanation of potential-induced degradation of the shunting type by Na decoration of stacking faults in Si solar cells". In: *Solar Energy Materials and Solar Cells* 120 (Jan. 2014), pp. 383–389. DOI: 10.1016/j.solmat.2013.06.015. URL: https://doi.org/10.1016/j.solmat.2013.06.015.

[118] Volker Naumann et al. "The role of stacking faults for the formation of shunts during potential-induced degradation of crystalline Si solar cells". In: *physica status solidi (RRL) - Rapid Research Letters* 7.5 (Mar. 2013), pp. 315–318. DOI: 10.1002/pssr.201307090. URL: https://doi.org/10.1002/pssr.201307090.

[119] Volker Naumann et al. "Potential-induced Degradation at Interdigitated Back Contact Solar Cells". In: *Energy Procedia* 55 (2014), pp. 498–503. DOI: 10.1016/j.egypro.2014.08.015. URL: https://doi.org/10.1016/j.egypro.2014.08.015.

[120] Swanson et al. "The surface polarization effect in high-efficiency silicon solar cells". In: Jan. 2005, p. 410.

[121] IEC. "Recommendations for renewable energy and hybrid systems for rural electrification —Part 10: Silicon solar module visual inspection guide". In: PAS 62257-10 (2017).

[122] IEC. "Terrestrial photovoltaic (PV) modules - Design qualification and type of approval —Part 1: Test Requirements". In: 61215-1 (2016).

[123] ASTM International. "Standard Practice for Visual Inspections of Photovoltaic Modules". In: E1799 (2012). DOI: 10.1520/e1799-12. URL: https://doi.org/10.1520/e1799-12.

[124] IEC. "Photovoltaic devices —Part 1: Measurement of the photovoltaic current-voltage characteristics". In: 60904-1 (2006).

[125] IEC. "Photovoltaic devices —Part 2: Requirements for photovoltaic reference devices". In: 60904-2 (2015).

[126] IEC. "Photovoltaic devices —Part 7: Computation of the spectral mismatch correction for measurements of photovoltaic devices". In: 60904-7 (2008).

[127] IEC. "Photovoltaic devices —Part 10: Methods of linearity measurement". In: 60904-10 (2009).

[128] IEC. "Photovoltaic devices —Part 3: Measurement principles for terrestrial photovoltaic (PV) solar devices with reference spectral irradiance data". In: 60904-3 (2016).

[129] IEC. "Photovoltaic devices —Procedures for temperature and irradiance corrections to measured I-V characteristics". In: 60891 (2009).

[130] ISO. "General requirements for the competence of testing and calibration laboratories". In: 17025 (2017).

[131] ASTM International. "Standard Test methods for Electrical Performance of Nonconcentrator Terrestrial Photovoltaic Modules and Arrays Using Reference Cells". In: E1036 (2015). DOI: 10.1520/e1036-15. URL: https://doi.org/10.1520/e1036-15.

[132] ASTM International. "Standard Test Method for Determination of the Spectral Mismatch Parameter Between a Photovoltaic Device and a Photovoltaic Reference Cell". In: E973 (2016). DOI: 10.1520/E0973-16. URL: https://doi.org/10.1520/E0973-16.

[133] ASTM International. "Specification for Physical Characteristics of Nonconcentrator Terrestrial Photovoltaic Reference Cells". In: E1040 (2016). DOI: 10.1520/e1040-10r16. URL: https://doi.org/10.1520/e1040-10r16.

[134] ASTM International. "Standard Test Method for Electrical Performance of Photovoltaic Cells Using Reference Cells Under Simulated Sunlight". In: E948 (2016). DOI: 10.1520/E0948-16. URL: https://doi.org/10.1520/E0948-16.

[135] ASTM International. "Standard Specification for Solar Simulation for Photovoltaic Testing". In: E927 (2015). DOI: 10.1520/E0927-10R15. URL: https://doi.org/10.1520/E0927-10R15.

[136] Ulrike Jahn et al. *Review on Infrared and Electroluminescence Imaging for PV Field Applications*. Sankt Ursen: International Energy Agency, Photovoltaic Power Systems Programme, 2017. ISBN: 978-3-906042-53-4.

[137] InfraTec GmbH. "Field of view calculator". In: (). Accesed June 11, -2. URL: http://www.infratec.eu/thermography/infrared-camera/variocamr-high-definition.html.

[138] Christiana Honsberg and Stuart Bowden. *PV Education*. Accessed June 11, -2. 2017. URL: http://www.pveducation.org/.

[139] ISE Fraunhofer Insitude for Solar Energy Systems. *PHOTOVOLTAIC REPORT*. Accessed June 11, -2. 2017. URL: https://www.ise.fraunhofer.de/content/dam/ise/de/documents/publications/studies/Photovoltaics-Report.pdf.

[140] John A. Tsanakas, Long Ha, and Claudia Buerhop. "Faults and infrared thermographic diagnosis in operating c-Si photovoltaic modules: A review of research and future challenges". In: *Renewable and Sustainable Energy Reviews* 62 (Sept. 2016), pp. 695–709. DOI: 10.1016/j.rser.2016.04.079. URL: https://doi.org/10.1016/j.rser.2016.04.079.

[141] Gabriel Takyi. "Correlation of Infrared Thermal Imaging Results with Visual Inspection and Current-Voltage Data of PV Modules Installed in Kumasi, a Hot, Humid Region of Sub-Saharan Africa". In: *Technologies* 5.4 (Oct. 2017), p. 67. DOI: 10.3390/technologies5040067. URL: https://doi.org/10.3390/technologies5040067.

[142] Jaime Hernández et al. *Biodiversidad Terrestre de la Región de Arica y Parinacota*. Maval Ltda, 2014. ISBN: 9789561908475.

[143] Rodrigo Palma Behnke. *La fuerza del sol*. BigBang Productora de Contenidos, 2017. ISBN: 9789563931549.

[144] Dirk C. Jordan et al. "Compendium of photovoltaic degradation rates". In: *Progress in Photovoltaics: Research and Applications* 24.7 (Feb. 2016), pp. 978–989. DOI: 10.1002/pip.2744. URL: https://doi.org/10.1002/pip.2744.

[145] Solmetric. *Guide to interpreting I-V curve measurements of PV arrays*. Accessed June 11, -2. 2010. URL: http://resources.solmetric.com/get/Guide%5C%20to%5C%20Interpreting%5C%20I-V%5C%20Curves.pdf.

[146] IEC. "Photovoltaic (PV) Systems –Requirements for testing, documentation and maintenance —Part 3: Photovoltaic modules and plants –Outdoor infrared thermography". In: TS 62446-3 (2017).

Appendices

Appendix A

Visual Inspection Form (English version)

Visual inspection form

1. Site information Folio # :_____

Installation address :_____	Latitude :_____
_____	Longitude :_____
ID (Solar MAP) :_____	Altitude :_____
	Date (dd/mm/yy) :_____

BEGIN INSPECTION AT THE BACK SIDE OF THE MODULE

2. Module data

Photo taken of nameplate: ☐ yes ☐ no
Technology: ☐ mono Si ☐ multi Si
Estimated deployment date (mm/yy) :_____
Manufacturer :_____
Model # :_____
Serial # :_____
Nameplate: ☐ nameplate missing

$P_{mpp\ [W]}$:_____ $V_{oc\ [V]}$:_____ $I_{sc\ [A]}$:_____
$V_{mpp\ [V]}$:_____ $I_{mpp\ [A]}$:_____

3. Rear-side glass ☐ applicable ☐ not applicable

Damage type

Crazing (or other non-cracked damage)	:	☐ non	☐ small, localized	☐ extensive
Cracks	:	☐ non	☐ small, localized	☐ extensive
Shattered (tempered)	:	☐ non	☐ small, localized	☐ extensive
Shattered (non-tempered)	:	☐ non	☐ small, localized	☐ extensive
Chipped	:	☐ non	☐ small, localized	☐ extensive

4. Backsheet (polymer) ☐ applicable ☐ not applicable

Appearance : ☐ like new ☐ minor discoloration ☐ major discoloration
Texture : ☐ like new ☐ wavy (not delaminated) ☐ wavy (delaminated)
☐ dented

Material quality

Chalking : ☐ non ☐ slight ☐ substantial

Damage type

Burn marks	:	☐ non	☐ small, localized	☐ extensive
Bubbles	:	☐ non	☐ small, localized	☐ extensive
Delamination	:	☐ non	☐ small, localized	☐ extensive
Cracks/scratches	:	☐ non	☐ small, localized	☐ extensive
Corrosion/weathering	:	☐ non	☐ small, localized	☐ extensive

5. Wires ☐ applicable ☐ not applicable

Appearance : ☐ like new ☐ pliable, but degraded ☐ embrittled
Damage type : ☐ cracked/disintegrated insulation ☐ burnt ☐ corroded
☐ cuts/marks

Page 1/3

6. Connectors ☐ applicable ☐ not applicable

Type	:	☐ unsure	☐ MC3	☐ MC4	☐ Tyco Solarlok	☐ other
Appearance	:	☐ like new	☐ pliable, but degraded		☐ embrittled	
Damage type	:	☐ cracked/disintegrated insulation			☐ burnt	☐ corroded

7. Junction box ☐ applicable ☐ not applicable

Junction box itself					
Appearance	:	☐ intact	☐ unsound structure		
Damage type	:	☐ weathered	☐ cracked	☐ burnt	☐ warped
Junction box lid					
Damage type	:	☐ intact/potted	☐ loose	☐ fell off	☐ cracked
Junction box adhesive		☐ applicable		☐ not applicable	
Appearance	:	☐ like new	☐ pliable, but degraded		☐ embrittled
Damage type	:	☐ well attached	☐ loose/brittle	☐ fell off	
Junction box wire attachments		☐ applicable		☐ not applicable/observable	
Damage type	:	☐ well attached	☐ loose/brittle	☐ fell off	
Seal	:	☐ good seal	☐ seal will leak		
Other	:	☐ arced/started a fire			

8. Frame grounding ☐ applicable ☐ not applicable

Original state	:	☐ wired ground	☐ resistive ground	☐ no ground	☐ unknown
Appearance	:	☐ not applicable	☐ like new	☐ minor corrosion	☐ major corrosion
Function	:	☐ well grounded	☐ no connection		

Photos taken of : ☐ back, label and junction box

CONTINUE INSPECTION AT THE FRONT SIDE OF THE MODULE

9. Frame ☐ applicable ☐ not applicable

Appearance	:	☐ like new	☐ damaged	☐ missing	
Damage type	:	☐ weathered	☐ distorted/bended	☐ detached	☐ separated joints
Frame adhesive					
Damage type	:	☐ like new/not visible	☐ degraded		

10. Frameless edge seal ☐ applicable ☐ not applicable

Appearance	:	☐ like new	☐ discolored	☐ visibly degraded
Damage type	:	☐ squeezed/pinched out		☐ moisture penetration
		☐ delaminated (small, localized)		☐ delaminated (extensive)

11. Glass/polymer (front) ☐ applicable ☐ not applicable

Material	:	☐ glass	☐ polymer	☐ glass/polymer composite	☐ unknown
Features	:	☐ smooth	☐ slightly textured	☐ pyramid/wave texture	☐ AR coating
Appearance	:	☐ clean	☐ lightly soiled	☐ heavily soiled	☐ weathered
Damage type					
Crazing (or other non-cracked damage)	:	☐ non	☐ small, localized	☐ extensive	
Cracks	:	☐ non	☐ small, localized	☐ extensive	
Shattered (tempered)	:	☐ non	☐ small, localized	☐ extensive	
Shattered (non-tempered)	:	☐ non	☐ small, localized	☐ extensive	
Chipped	:	☐ non	☐ small, localized	☐ extensive	
Milky discoloration	:	☐ non	☐ small, localized	☐ extensive	

12. Encapsulant (front) ☐ applicable ☐ not applicable

Appearance : ☐ like new ☐ light discoloration (yellow) ☐ dark discoloration (brown)

Damage type

Delamination : ☐ non ☐ from edges ☐ uniform ☐ corner(s) ☐ near junction box
☐ between cells ☐ over cells ☐ near cell or string interconnect

Discoloration : ☐ non ☐ light discoloration ☐ dark discoloration

Discoloration location(s) : ☐ uniform ☐ module center ☐ module edges ☐ cell centers
☐ cell edges ☐ over gridlines ☐ between cells ☐ over busbars

13. Metallization

Gridlines/fingers ☐ not applicable/observable ☐ applicable

Appearance : ☐ like new ☐ light discoloration ☐ dark discoloration

Busbars ☐ not applicable/observable ☐ applicable

Appearance : ☐ like new ☐ light discoloration ☐ dark discoloration

Damage type : ☐ obvious corrosion ☐ diffuse burn marks ☐ misaligned

Cell interconnect ribbon ☐ not applicable/observable ☐ applicable

Appearance : ☐ like new ☐ light discoloration ☐ dark discoloration

Damage type : ☐ obvious corrosion ☐ burn marks ☐ breaks

String interconnect ☐ not applicable/observable ☐ applicable

Appearance : ☐ like new ☐ light discoloration ☐ dark discoloration

Damage type : ☐ obvious corrosion ☐ burn marks ☐ breaks ☐ arc tracks (thin, small burns)

14. Silicon cell ☐ applicable ☐ not applicable

Number of

cells in module :_____

cells in series/string :_____

strings in parallel :_____

Damage type

N° of cells with burn marks :	☐ 0	☐ 1	☐ 2	☐ 3	☐ 4	☐ 5-10	☐ >10
N° of cells with cracks :	☐ 0	☐ 1	☐ 2	☐ 3	☐ 4	☐ 5-10	☐ >10
N° of cells with moisture :	☐ 0	☐ 1	☐ 2	☐ 3	☐ 4	☐ 5-10	☐ >10
N° of cells with snail tracks :	☐ 0	☐ 1	☐ 2	☐ 3	☐ 4	☐ 5-10	☐ >10

Photos taken of : ☐ front side

END OF VISUAL INSPECTION

15. Electronic records ☐ applicable ☐ not applicable

Visual images recorded electronically ☐ applicable ☐ not applicable

Number of images recorded :_____

Name of each recorded image :_____

I-V curves recorded electronically ☐ applicable ☐ not applicable

Number of times recorded :_____

Name of each recording :_____

$P_{mpp\ [W]}$:_____ $V_{oc\ [V]}$:_____ $I_{sc\ [A]}$:_____

$FF_{[\%]}$:_____ $V_{mpp\ [V]}$:_____ $I_{mpp\ [A]}$:_____

IR images recorded electronically ☐ applicable ☐ not applicable

Number of images recorded :_____

Name of each recorded image :_____

_____

Irradiance [W/m^2] :_____ Ambient temperature [°C] :_____

Module temperature [°C] :_____

Page 3/3

Appendix B

Visual Inspection Form (Spanish version)

Formulario de inspección visual

1. Información del sitio **Folio # :_____**

Dirección de instalación :_____	Latitud :_____
_____	Longitud :_____
ID (MAPA solar) :_____	Altitud :_____
	Fecha (dd/mm/aa) :_____

COMENZAR LA INSPECCIÓN POR LA PARTE TRASERA DEL MÓDULO

2. Información del módulo

Foto de la etiqueta tomada: ☐ si ☐ no
Tecnología: ☐ mono Si ☐ multi Si
Fecha estimada de instalación :_____
Fabricante :_____
Modelo # :_____
Serie # :_____
Etiqueta ☐ Sin etiqueta
$P_{mpp\ [W]}$:_____ $V_{oc\ [V]}$:_____ $I_{sc\ [A]}$:_____
$V_{mpp\ [V]}$:_____ $I_{mpp\ [A]}$:_____

3. Vidrio trasero ☐ aplica ☐ no aplica

Tipo de daño

Grietas (otros daños no-quebrado)	:	☐ no tiene	☐ pequeño, localizado	☐ extensivo
Quebraduras	:	☐ no tiene	☐ pequeño, localizado	☐ extensivo
Destrozado (templado)	:	☐ no tiene	☐ pequeño, localizado	☐ extensivo
Destrozado (no-templado)	:	☐ no tiene	☐ pequeño, localizado	☐ extensivo
Picado	:	☐ no tiene	☐ pequeño, localizado	☐ extensivo

4. Backsheet (polímero) ☐ aplica ☐ no aplica

Apariencia : ☐ como nuevo ☐ decoloración menor ☐ decoloración mayor
Textura : ☐ como nuevo ☐ arrugado (no delaminado) ☐ arrugado (delaminado)
☐ abollado

Calidad del material

Polvillo : ☐ no tiene ☐ ligero ☐ considerable

Tipo de daño

Quemaduras	:	☐ no tiene	☐ pequeño, localizado	☐ extensivo
Burbujas	:	☐ no tiene	☐ pequeño, localizado	☐ extensivo
Delaminación	:	☐ no tiene	☐ pequeño, localizado	☐ extensivo
Quebraduras/rasguños	:	☐ no tiene	☐ pequeño, localizado	☐ extensivo
Corrosión/desgaste	:	☐ no tiene	☐ pequeño, localizado	☐ extensivo

5. Cables ☐ aplica ☐ no aplica

Apariencia : ☐ como nuevo ☐ flexible, pero degradado ☐ fragilizado
Tipo de daño : ☐ aislación quebrada/desintegrada ☐ quemado ☐ corroído
☐ cortes/marcas

Página 1/3

6. Conectores ☐ aplica ☐ no aplica

Tipo	:	☐ inseguro ☐ MC3 ☐ MC4 ☐ Tyco Solarlok ☐ otro
Apariencia	:	☐ como nuevo ☐ flexible, pero degradado ☐ fragilizado
Tipo de daño	:	☐ aislación quebrada/desintegrada ☐ quemado ☐ corroído

7. Caja de conexiones (JB) ☐ aplica ☐ no aplica

JB propiamente		
Apariencia	:	☐ intacto ☐ estructura no firme
Tipo de daño	:	☐ erosionado ☐ quebrado ☐ quemado ☐ torcido
Tapa de JB		
Tipo de daño	:	☐ intacto/conservado ☐ suelto ☐ caído ☐ quebrado
Adhesivo de JB		☐ aplica ☐ no aplica
Apariencia	:	☐ como nuevo ☐ flexible, pero degradado ☐ fragilizado
Tipo de daño	:	☐ bien pegado ☐ suelto/fragilizado ☐ caído
Conexiones dentro de JB		☐ aplica ☐ no aplica/observable
Tipo de daño	:	☐ bien conectado ☐ suelto/fragilizado ☐ caído
Sello	:	☐ bien sellado ☐ sello cederá
Otro	:	☐ arqueado/inició un incendio

8. Conexión a tierra del marco ☐ aplica ☐ no aplica

Estado original	:	☐ conectado a tierra ☐ tierra resistiva ☐ sin tierra ☐ desconocido
Apariencia	:	☐ no aplica ☐ como nuevo ☐ corrosión menor ☐ corrosión mayor
Funcionamiento	:	☐ bien conectado a tierra ☐ no conectado a tierra

Fotos tomadas de: ☐ parte trasera, etiqueta y JB

CONTINÚE LA INSPECCIÓN POR LA PARTE FRONTAL DEL MÓDULO

9. Marco ☐ aplica ☐ no aplica

Apariencia	:	☐ como nuevo ☐ dañado ☐ ausente
Tipo de daño	:	☐ erosionado ☐ deformado/doblado ☐ despegado ☐ junturas separadas
Adhesivo del marco		
Tipo de daño	:	☐ como nuevo/no visible ☐ degradado

10. Sellante del contorno (sin marco) ☐ aplica ☐ no aplica

Apariencia	:	☐ como nuevo ☐ decolorado ☐ visiblemente degradado
Tipo de daño	:	☐ exprimido/pellizcado ☐ penetración de humedad
		☐ delaminado (pequeño, localizado) ☐ delaminado (extensivo)

11. Vidrio/polímero (frontal) ☐ aplica ☐ no aplica

Material	:	☐ vidrio ☐ polímero ☐ compuesto de vidrio/polímero ☐ desconocido
Características	:	☐ liso ☐ levemente texturizado ☐ textura pirámide/onda ☐ cubierta AR
Apariencia	:	☐ limpio ☐ ligeramente sucio ☐ considerablemente sucio ☐ erosionado
Tipo de daño		
Grietas (otros daños no-quebrado)	:	☐ no tiene ☐ pequeño, localizado ☐ extensivo
Quebraduras	:	☐ no tiene ☐ pequeño, localizado ☐ extensivo
Destrozado (templado)	:	☐ no tiene ☐ pequeño, localizado ☐ extensivo
Destrozado (no-templado)	:	☐ no tiene ☐ pequeño, localizado ☐ extensivo
Picado	:	☐ no tiene ☐ pequeño, localizado ☐ extensivo
Decoloración blanca	:	☐ no tiene ☐ pequeño, localizado ☐ extensivo

12. Encapsulante (frontal) ☐ aplica ☐ no aplica

Apariencia : ☐ como nuevo ☐ decoloración leve (amarillo) ☐ decoloración oscura (café)

Tipo de daño

Delaminación : ☐ no tiene ☐ desde bordes ☐ uniforme ☐ esquina(s) ☐ cerca de JB
☐ entre celdas ☐ sobre celdas ☐ cerca de celdas o interconexión de strings

Decoloración : ☐ no tiene ☐ decoloración clara ☐ decoloración oscura

Locación(es) decoloración : ☐ uniforme ☐ centro módulo ☐ bordes módulo ☐ centros celdas
☐ lados celdas ☐ sobre gridlines ☐ entre celdas ☐ sobre busbars

13. Metalización

Gridlines/fingers ☐ no aplica/observable ☐ aplica

Apariencia : ☐ como nuevo ☐ decoloración clara ☐ decoloración oscura

Busbars ☐ no aplica/observable ☐ aplica

Apariencia : ☐ como nuevo ☐ decoloración clara ☐ decoloración oscura

Tipo de daño : ☐ corrosión obvia ☐ quemaduras difusas ☐ desalineadas

Interconexión celdas (ribbon) ☐ no aplica/observable ☐ aplica

Apariencia : ☐ como nuevo ☐ decoloración clara ☐ decoloración oscura

Tipo de daño : ☐ corrosión obvia ☐ quemaduras ☐ quebraduras

Interconexión string ☐ no aplica/observable ☐ aplica

Apariencia : ☐ como nuevo ☐ decoloración clara ☐ decoloración oscura

Tipo de daño : ☐ corrosión ☐ quemaduras ☐ quebraduras ☐ marcas de arco (delgadas, pequeñas)

14. Celda de silicio ☐ aplica ☐ no aplica

Número de

celdas en módulo :_____

celdas en serie/strings :_____

strings en paralelo :_____

Tipo de daño

N° de celdas con quemaduras	:	☐ 0	☐ 1	☐ 2	☐ 3	☐ 4	☐ 5-10	☐ >10
N° de celdas quebradas	:	☐ 0	☐ 1	☐ 2	☐ 3	☐ 4	☐ 5-10	☐ >10
N° de celdas con humedad	:	☐ 0	☐ 1	☐ 2	☐ 3	☐ 4	☐ 5-10	☐ >10
N° de celdas con snail tracks	:	☐ 0	☐ 1	☐ 2	☐ 3	☐ 4	☐ 5-10	☐ >10

Fotos tomadas de: ☐ parte frontal

FIN DE LA INSPECCIÓN VISUAL

15. Datos electrónicos ☐ aplica ☐ no aplica

Imágenes visuales tomadas electrónicamente ☐ aplica ☐ no aplica

Número de imágenes tomadas :_____

Nombre de cada imagen :_____

Curvas I-V tomadas electrónicamente ☐ aplica ☐ no aplica

Número de veces tomada :_____

Nombre de cada toma :_____

$P_{mpp\ [W]}$:_____ $V_{oc\ [V]}$:_____ $I_{sc\ [A]}$:_____

$FF_{[\%]}$:_____ $V_{mpp\ [V]}$:_____ $I_{mpp\ [A]}$:_____

Imágenes térmicas tomadas electrónicamente ☐ aplica ☐ no aplica

Número de imágenes tomadas :_____

Nombre de cada imagen :_____

_____

Irradiancia [W/m^2] :_____ Temperatura ambiente [°C] :_____

Temperatura módulo [°C] :_____

Página 3/3

Appendix C

Supplementary Data Files

C.1 Description

The survey from the IDCTool is a fillable document, which can be completed using Adobe Reader (PDF version) or using Microsoft Excel (spreadsheet version). The survey is developed in English, but a translation in Spanish is also given. The provided documents are the following:

1. Fillable survey in PDF format. The survey is in English language.
2. Fillable survey in PDF format. The survey is in Spanish language.
3. Fillable survey in xlsx format. The survey is in English language.
4. Fillable survey in xlsx format. The survey is in Spanish language.

C.2 File names

The following files, which corresponds to the survey in two different languages and formats, are attached in the CD-ROM:

1. Fillable_visual_inspection_form_(english_version).pdf
2. Fillable_visual_inspection_form_(spanish_version).pdf
3. Fillable_visual_inspection_form_(english_version).xlsx
4. Fillable_visual_inspection_form_(spanish_version).xlsx

Appendix D

FLIR ONE Pro Camera Datasheet

FLIR ONE® PRO

The FLIR ONE Pro gives you the power to find invisible problems faster than ever. Combining a higher-resolution thermal sensor able to measure temperatures up to 400 °C (752 °F)with powerful measurement tools and report generation capability, the FLIR ONE Pro will work as hard as you do. Its revolutionary VividIR™ image processing lets you see more details and provide your customers with proof that you solved their problem right the first time. The updated design includes the revolutionary OneFit™ adjustable connector to fit your phone, without taking the phone out of its compatible protective case. An improved FLIR ONE app lets you measure multiple temperatures or regions of interest at once and stream to your smartwatch for remote viewing. Whether you're inspecting electrical panels, looking for HVAC problems, or finding water damage, the new FLIR ONE Pro is a tool no serious professional should be without.

VividIR IMAGE PROCESSING

See It & Solve It - Sharpest Mobile Thermal Imaging Performance Lets You Detect Problems with Precision and Accuracy, then Document Your Fix for the Customer

- Most advanced image resolution enhancement detects the thermal details you need to find problems fast
- With 160 x 120 thermal resolution, FLIR ONE Pro uses FLIR's highest resolution micro thermal camera and can measure temperatures as high as 400 °C (752 °F)
- FLIR MSX® embosses visible edges from the 1440 x 1080 HD camera onto thermal imagery to create a sharper, easier to understand picture

OneFit CONNECTOR

Leave Your Case On - Adjustable Connector Means You Don't Have to Choose Between Thermal Vision and Safeguarding Your Device when Using Compatible Protective Cases

- Adjust length of USB-C and Lightning connector up to an additional 4 mm
- Reversible connectors for Android and iOS
- Secure the FLIR ONE to your mobile device while keeping your phone safe

HARD-WORKING APP

Work Like a Pro - Work-Based Features Include Advanced Capabilities for More Professional Problem Solving and Functionality

- Use multiple real-time spot meters and regions of interest
- Access real-time thermal tips and tricks in the FLIR ONE app followed by professional reporting through FLIR Tools
- See around corners and in awkward spaces by connecting to your Apple Watch or Android smartwatch

Specifications

General	FLIR One Pro
Certifications	MFi (iOS version), RoHS, CE/FCC, CEC-BC, EN61233
Operating temperature	0 °C – 35 °C (32 °F to 95 °F) , battery charging 0 °C to 30 °C (32 °F to 86 °F)
Non-operating temperature	-20 °C to 60 °C (-4 °F to 140 °F)
Size	68mm W x34mm H x14mm D (2.7in x 1.3in x .6in)
Weight	36.5g
Mechanical shock	Drop from 1.8m (5.9ft)
Video	
Thermal and visual cameras with MSX	
Thermal sensor	Pixel size 12μM, 8 – 14μM spectral range
Thermal resolution	160x120
Visual resolution	1440x1080
HFOV / VFOV	55 ° ± 1 ° / 43 ° ± 1 °
Frame rate	8.7Hz
Focus	Fixed 15cm – Infinity
Radiometry	
Scene dynamic range	-20 °C to 400 °C (-4 °F to 752 °F)
Accuracy	±3 °C (5.4 °F) or ±5%, typical Percent of the difference between ambient and scene temperature. Applicable 60s after start-up when the unit is within 15 °C to 35 °C (59 °F to 95 °F) and the scene is within 5 °C to 120 °C (41 °F to 248 °F)
Thermal sensitivity (MRTD)	150mK
Emissivity settings	Matte: 95%, Semi-Matte: 80%, Semi-Glossy: 60%, Glossy: 30% Reflected background temperature is 22 °C (72 °F)
Shutter	Automatic/Manual
Power	
Battery life	Approximately 1h
Battery charge time	40min
Interfaces	
Video	Male Lightning (iOS), Male USB-C (Android)
Charging	Female USB-C (5V/1A)
App	
Video and still image display/capture	Saved as 1440x1080
File formats	Photo – radiometric jpeg Video – MPEG-4 (file format MOV (iOS), MP4 (Android))
Capture modes	Video, Photo, Time lapse
Palettes	Gray (white hot), Hottest, Coldest, Iron, Rainbow, Contrast, Arctic, Lava and Wheel.
Spot meter	Off / °C / °F. Resolution 0.1 °C / 0.1 °F
Adjustable MSX distance	0.3m – Infinity
Battery charge monitor	0 – 100%

CORPORATE HEADQUARTERS
FLIR Systems, Inc.
27700 SW Parkway Ave.
Wilsonville, OR 97070
PH: +1 877.773.3547

SANTA BARBARA
FLIR Systems, Inc.
6769 Hollister Ave.
Goleta, CA 93117
PH: +1 805.690.6600

CHINA
FLIR Systems Co., Ltd
Room 502, West Wing, Hanwei Building
No. 7 Guanghua Ave.
Chaoyang District, Beijing 100004, China
Phone: +86 10-59797755

EUROPE
FLIR Systems, Inc.
Luxemburgstraat 2
2321 Meer
Belgium
PH: +32 (0) 3665 5100

www.flir.com
NASDAQ: FLIR

17-2333-OEM-FLIROne_Pro_Datasheet_US

Appendix E

Seaward PV210 Kit Datasheet

SEAWARD

PV210

Solar PV tester and I-V curve tracer

The PV210 provides a highly efficient and effective test and diagnostic solution for PV systems, carrying out all commissioning tests required by IEC 62446 and performing fast and accurate measurement of I-V curves in accordance with IEC 61829. When used in conjunction with the Solar Survey 200R irradiance meter, the PV210 measurement data can be converted to STC, using either the PVMobile app or SolarCert Elements software, allowing direct comparison with the PV module manufacturer's published data.

With direct connection to individual PV modules or strings using the supplied lead sets, tests can be conducted easily and within a matter of seconds at the press of a single button.

A high contrast display is clearly visible in direct sunlight and shows open circuit voltage, short circuit current, maximum power point voltage, current and power, as well as the fill factor of the PV module or system under test, and insulation resistance (as part of an auto sequence or a discrete probe to probe measurement). If the measured curve deviates from the expected profile, the PV210 alerts the user to this, identifying the need for further analysis.

Detailed and color I-V and power curves, can be viewed instantly once data is transferred to the PVMobile Android app using wireless NFC connectivity. PVMobile displays measured I-V and power curves for visual analysis of the curve shape, enabling common problems such as shading, defective cells or poor electrical connections to be identified.

Key Features

- Lightweight, handheld and fast
- Affordable and efficient PV diagnostic tool
- Easy and fast push button operation
- All-in-one commissioning tests and I-V curve tracing, in accordance with international standards IEC 62446: 2016 and IEC 61829: 2015
- Instantly view detailed I-V curves in the field using the PVMobile Android app
- Convert I-V curve measurements to STC using the PVMobile app or SolarCert Elements software
- Instantly send PDF reports from the field back to the office using the PVMobile Android app
- Tests individual PV modules or strings
- Clear results display, even in direct sunlight
- Wirelessly receives irradiance and temperature measurements from Solar Survey 200R
- Full traceability of system performance
- Compatible with SolarCert Elements v2 software

Electrical/Analysis Test Functions

- I-V curve tracing, in accordance with IEC 61829
- Earth/ground continuity
- Insulation resistance (auto short circuit test and point-to-point)
- AC/DC voltage measurement
- Open circuit voltage up to 1000VDC
- Maximum power point voltage up to 1000VDC
- Short circuit current up to 15ADC
- Maximum power point current up to 15ADC
- Automatic fill factor calculation
- Operating current (using supplied current clamp) up to 40A
- DC power up to 40kW

PV210 Users

- PV system installers
- PV O&M technicians
- PV module manufacturers

Download your FREE guide to PV testing at www.seaward-groupusa.com/pvguide

www.seaward-groupusa.com/PV210
For USA, Canada and Central America
Tel: +1 (813) 886 - 2775
or email sales@seaward-groupusa.com
Head Office Tel: +44 (0) 191 587 8741

Technical Specifications

Earth continuity / resistance measurement

Display range	0.00 to 199Ω
Measurement range	0.01 to 199Ω
Accuracy	±(2% rdg + 5d)
Resolution	0.01Ω maximum
Open circuit test voltage	4VDC, nominal
Test leads zero	Zero up to 10Ω, by Zero button
Number of measurements	5,000 x 1 second tests
Audible / visible warning	≥ 30VAC/DC at inputs
User protection	Test inhibited if ≥ 30VAC/DC at inputs

Insulation resistance (auto short circuit test)

Display range	0.05 - 200MΩ
Measurement range	0.05 - 200MΩ
Accuracy	±(5% rdg + 5d) 0.05 - 100MΩ ±(10% rdg + 5d) 101 - 200MΩ
Resolution	0.01MΩ maximum
Open circuit test voltage	250, 500, 1000V (as per IEC 61557-2)
Test current	1mA nominal as per IEC 61557-2
Short circuit test current	<2mA
Number of measurements	5,000 x 1 second tests
Audible / visible warning	≥ 30VAC/DC at inputs
User protection	Test inhibited if ≥ 30VAC/DC at inputs

Insulation resistance (point to point)

Display range	0.05 to 300MΩ
Measurement range	0.05 to 300MΩ
Accuracy	±(5% rdg + 5d)
Resolution	0.01MΩ maximum
Open circuit test voltage	250, 500, 1000V (as per IEC 61557-2)
Short circuit test current	<1mA
Number of measurements	5,000 x 1 second tests
Audible / visible warning	≥ 30VAC/DC at inputs
Circuitry protection	Test inhibited if ≥ 30VAC/DC at inputs

Voltage measurement (via 4mm probes)

Display range	30V – 440VAC/DC
Measurement range	30V – 440VAC/DC
Resolution	1V
Accuracy	±(5% rdg + 2d)

Vo/c voltage measurement (via PV test leads)

Display range	0.0V – 1000VDC
Measurement range	5.0V – 1000VDC
Resolution	0.1V
Accuracy	±(0.5% rdg + 2d)
Enunciators	DC voltage polarity correct or reversed

Is/c current measurement (via PV test leads)

Display range	0.0A – 15.0ADC
Measurement range	0.5A – 15.0ADC
Resolution	0.1A
Accuracy	±(1% rdg + 2d)

Operating current (via DC current clamp)

Display range	0.0A – 40.0A AC/DC
Measurement range	0.1A – 40.0A AC/DC
Resolution	0.1A
Accuracy	±(5% rdg + 2d)

DC power

Display range	0.0W – 40.0kW
Measurement range	10W – 40.0kW
Resolution	10W max
Accuracy	±(6% rdg + 2d)

I-V curve

Maximum power dissipation	10kW
Number of points	Dynamic up to 128
MPP calculation max error	±(1.5% rdg + 40w)

General Specifications

Case dimensions and weight

Weight	2.3lb (unit)
Dimensions	10.4 x 4.2 x 2.3”
Display	Custom LCD with backlight
Power source	6 x 1.5V AA cells
Battery life	>1000 test sequences
Auto power down	User programmable
Onboard memory	Up to 999 complete test datasets

Connectivity

USB download to PC (CSV format)

Wireless ‘Solarlink™’ to Survey 200R (915MHz) (range c. 30m / 100ft)

NFC transfer of data to PVMobile Android app

iOS devices not supported

App compatibility

Compatible with Android version 4.2 (Jelly Bean) or later

iOS devices not supported

Software compatibility

Compatible with SolarCert Elements v2 software or later

(English language only)

Services

2 year warranty (subject to terms and conditions, register your product at **www.seaward-groupusa.com/register-product**)

Go to **www.seaward-groupusa.com/service-center** for more information about our services and calibration

Appendix F

Cloud Coverage Chart (okta scale)

According to American Meteorology Society the cloudiness es define as "that portion of the sky cover that is attributed to clouds, usually measured in tenths or eighths of sky covered". An *okta* is unit used to express the extent of cloud cover. 1 okta is equal to one eighth of the sky.

Table F.1: Cloud coverage, also known as cloudiness or cloudage, chart (in okta). Adapted from `https://worldweather.wmo.int/`

Image	**Oktas**	**Definition**	**Category**
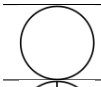	0	Sky clear	Fine
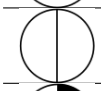	1	1/8 of sky covered or less, but not zero	Fine
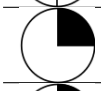	2	1/4 of sky covered	Fine
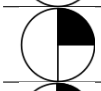	3	3/8 of sky covered	Partly cloudy
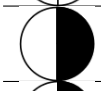	4	1/2 of sky covered	Partly cloudy
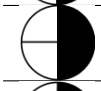	5	5/8 of sky covered	Partly cloudy
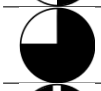	6	3/4 of sky covered	Cloudy
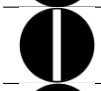	7	7/8 of sky covered or more, but not 8/8	Cloudy
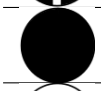	8	Sky completely covered	Overcast
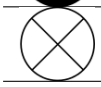	(9)	Sky is obscured by fog or similar	Obscured

Appendix G

Matrix for thermal abnormalities of PV modules

The following matrix contains several thermal abnormalities that are assessable by thermal pattern. For each thermal pattern, a description is given with additional information (comments in the last column) when it is possible. The third column presents the possible reasons, or the source of the problem, which can be several. When the possible reasons are different, they are listed. The fourth column shows how the electrical parameters are effected or related to the thermal pattern. When possible, the different electrical changes are related to specific thermal issues if they are listed in column three. Regarding to class of abnormality (CoA) in the fifth column, this is based on the classification shown by Table 4.5 from IEC 62446-3 [62]. Kontges et al. [64] also created a scale of safety, which in this work is related with the CoA from IEC 62446-3 in the way shown by Table G.1.

Table G.1: Relationship between the safety category from Kontges et al. [64] and CoA from IEC 62446-3 [62].

Safety category [64]	**Description**	**Analogous to CoA**
A	Failure has no effect on safety	1
B(f,e,m)	failure may cause fire (f), electrical shock (e), physical danger (m), if a following failure and/or a second failure occurs	2
C(f,e,m)	failure causes direct safety problem (definition of f,e,m see safety category B)	3

The matrix presented in this appendix is created based on the information given by Kontges et al. [64]; Jahn et al. [136]; Tsanakas, Ha and Buerhop [140]; Solmetric [145]; IEC 62446-1 [146] and IEC 62446-3 [62].

Thermal pattern example	Description	Possible reasons	Electrical parameters	CoA	Comments
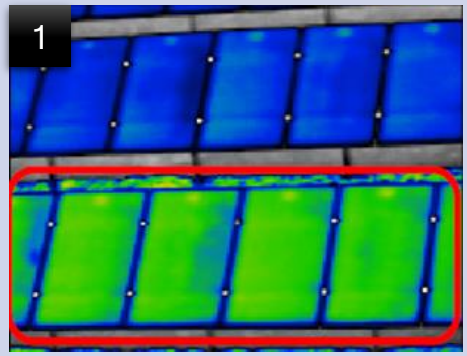	Modules uniformly warmer than the rest of the modules	a. Module is in open circuit because is not correctly connected or because is not connected at all. b. The junction box can be open circuited.	Not applicable. The module is fully functional and its electrical parameters are not compromised.	1-2	The module surface is warmer in an uniform way and the temperature of the junction box is similar to the rest of the solar cells. Recommendations are: - Check external wiring. - Check wiring within the junction box. Stress factors: non.
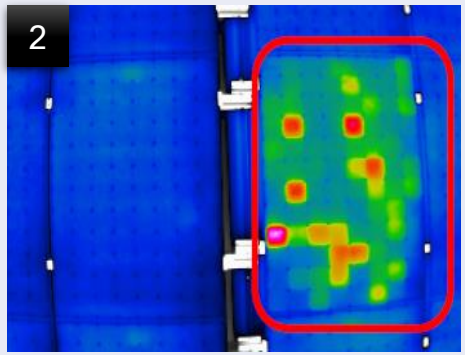	Module contains several hot cells in a random pattern (patchwork pattern)	a. The module is in short circuit condition. b. All bypass diodes are short circuited. c. The module is not correctly connected.	Not applicable.	1-2	This type of fault can be confused with: - Broken front glass (3) - PID (7) - Single hot cell (8) - Mismatch Recommendations are: - Check external wiring. - Check wiring within junction box. - Check bypass diodes. Stress factors: electrical.
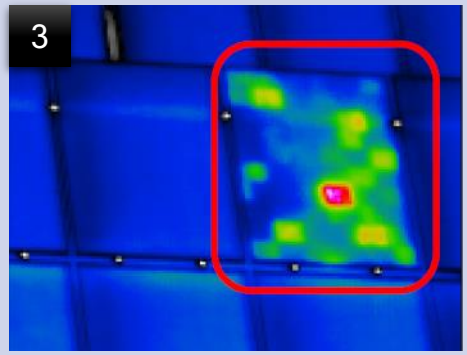	Module contains several hot cells in a random pattern (patchwork pattern)	Module has its front glass broken.	In the first weeks, the module can show normal behavior.	3	Due to the front glass being broken, the isolation resistance is lost. Risk of ground fault or electric shock. This type of fault can be confused with: - Module in short circuit condition (2) - PID (7) - Single hot cell (8) - Mismatch Stress factors: thermal cycling, temperature, humidity.

Thermal pattern example	Description	Possible reasons	Electrical parameters	CoA	Comments
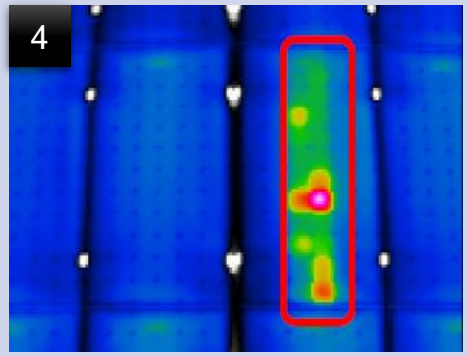	One substring shows a patchwork pattern	The substring is in short circuit condition due to: a. he substring is internally short circuited. b. The associated bypass is short circuited.	If M is the number of substrings-bypass diodes on the module and N the faulty ones, the power and voltage losses are $(N/M) \times 100\%$. Reduction of V_{oc}, V_{mpp} and P_{mpp}. 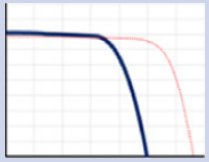	2	For more than one substring short circuited, this type of fault can be easily mistaken with: - Module in short circuit condition (2) - PID (7) - Single hot cell (8) - Mismatch Stress factors: electrical.
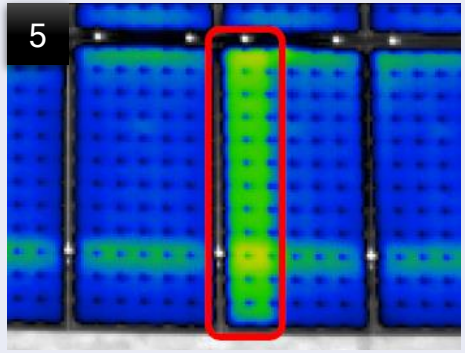	One substring is uniformly warmer than the rest of the module	The substring is in open circuit condition due to: a. Cell interconnect ribbon interruption and/or b. Open circuited cell (due to defects or severely broken)	If M is the number of substrings-bypass diodes on the module and N the faulty ones, the power and voltage losses are $\left(\frac{N}{M}\right) \times 100\%$. V_{oc}, V_{mpp} and P_{mpp} are reduced. 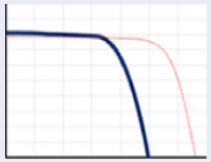	2-3	In contrast with the fault type 4, the substring is uniformly heated (NOT patchwork pattern is shown). The junction box is hotter than the rest of the module, because the bypass diode of the faulty substring is dissipating heat due to the current of the healthy substrings. At higher number of faulty substrings, more bypass diode dissipate heat. Therefore, the junction box will be more heated. Stress factors: electrical.
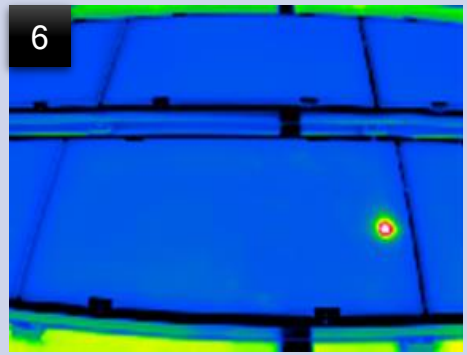	Heated junction box	a. Increased contact resistance within the junction box. b. Low resistive bypass diodes.	The increase in the contact resistance will lead to an increase in the series resistance (R_s) of the module. The FF will be reduced, 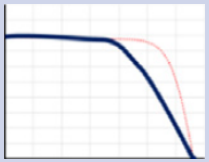	2-3	When the load is increased, the higher the contact resistance, the higher the temperature difference of the junction box in comparison with the rest of the module. The heat can also be due to low resistive bypass diodes that carry a significant current although they must be in reverse bias condition.

Thermal pattern example	Description	Possible reasons	Electrical parameters	CoA	Comments
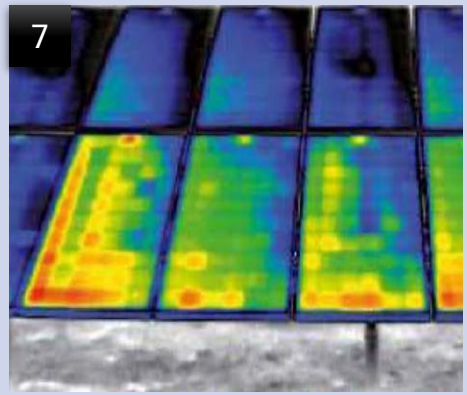	Several single cells are warmer, lower parts close to the bottom of the module are hotter than middle or upper parts	Massive shunts caused by PID and/or polarization	Massive shunts decrease V_{oc} (1). Rounding of the knee (2) is the effect of aging due to PID fault. 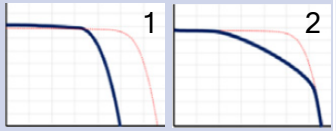	1	The temperature difference of medium degraded cell is higher than severely degraded ones. The power loss is severe but majorly recoverable by applying reverse voltage or changing the grounding conditions. Stress factors: temperature, relative humidity, electrochemical.
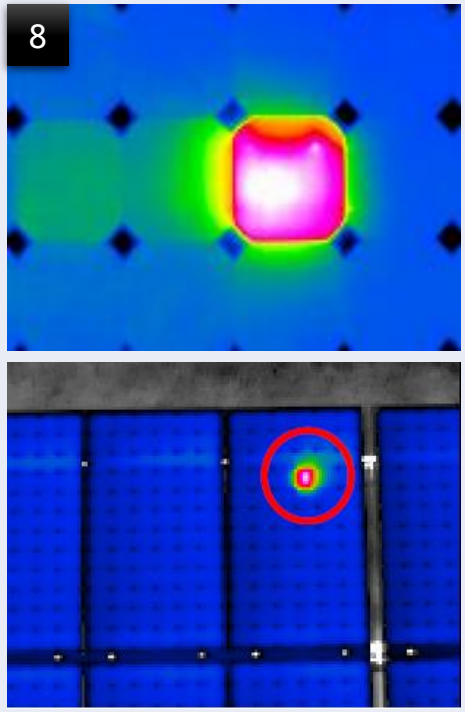	Single solar cell warmer	a. Total/partial shadow on cell b. Shunted cell c. Delaminated cell d. Broken cell *e.* I_{sc} mismatch	a. Total shadowed cells decrease V_{oc} (2) while total/partial shaded cells create steps (3). b. Shunted cells decrease V_{oc} (2) and R_{sh} (1). c. Delamination acts like shadowing. d. Broken cells create steps (3) and severely cracked cells reduce the open circuit voltage (2). *e.* I_{sc} mismatch can slightly decrease R_{sh}, but severe mismatch can activate a bypass diode (3). 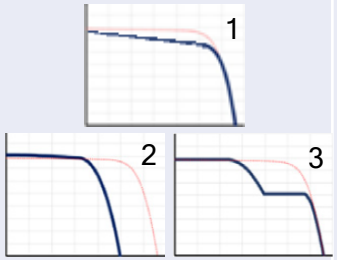	2-3	Short-circuit current from cells will have some mismatch, due to manufacturing variation or partial shading. Regular mismatch can be detected by a slight increase in R_{sh} while critical shading is detected with steps on the IV characteristic. Shunt current can be dominated by one hotspot of a single cell, or may arise from several small shunts. Therefore, one single cell can impact the shunt resistance. The temperature of the cell increase with the number of cell within the associated substring. Also with load and cell efficiency. If the temperature is extremely high and the reason is not shadowing, it is most likely to be a broken cell. Might lead to irreversible damage of cell, encapsulant or bypass diodes. Stress factors: thermal cycling, mechanical load

Thermal pattern example	Description	Possible reasons	Electrical parameters	CoA	Comments
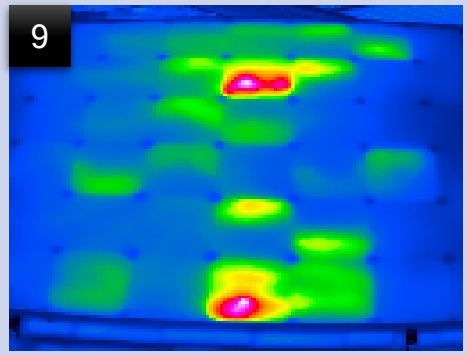	Part of a cell warmer	Broken cell	Inactive parts lead to steps (3), severely damage cells lead to V_{oc} reduction (1). More cracks lead to R_s increase (2). 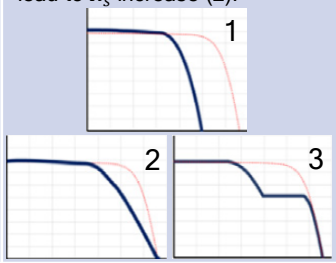	2	Similar characteristics, between cell cracks and broken ribbons (see fault type 10). The amount of power loss depend on crack pattern and size. Stress factors: thermal cycling, mechanical load.
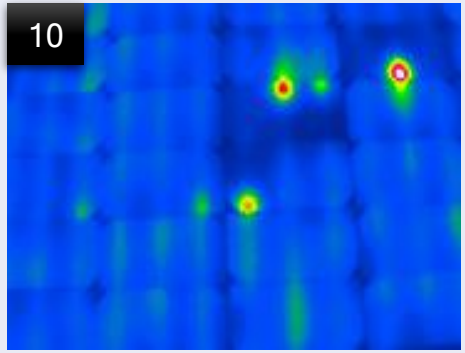	Warmer interconnections	a. Broken interconnecting ribbon(s) b. Faulty or displaced soldering	The series resistance increase. If all ribbons fail at the same cell, the power loss is proportional to the substring. 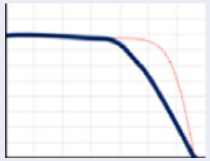	2-3	The temperature difference can be extreme, depend on the number of faulty interconnects. When all ribbons from one cell fail, the substring is open and the current from other substrings flows through the bypass diode. Stress factors: thermal cycling, mechanical load.
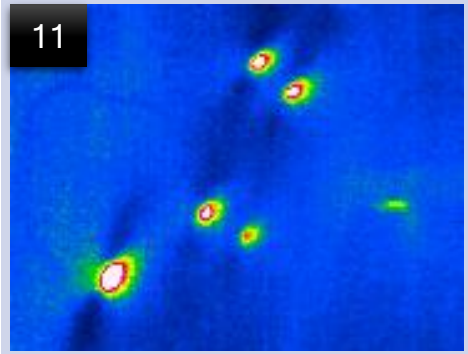	Pointed heating	a. Small and localized shunts/short circuits. b. Partly shadowing (bird dropping, etc.)	Shunts reduce V_{oc} (3). Major partial shading produce steps (2), minor partial shading slightly reduce the shunt resistance (1). 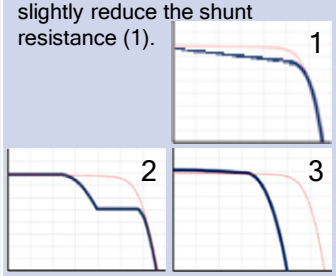	2	Shunt current can be dominated by one hotspot of a single cell, or may arise from several small shunts. Therefore, one single cell can impact the shunt resistance. Temperature difference is much lower than other faults. The shunt resistance can also be decreased. Stress factors: thermal cycling, mechanical load.